UC Berkeley
UC Berkeley Electronic Theses and Dissertations

Title
Probing Bacterial Cell Envelope Structure and Dynamics with Metabolic Reporters

Permalink
https://escholarship.org/uc/item/62d3q92h

Author
Rodriguez-Rivera, Frances Paola

Publication Date
2016

Peer reviewed|Thesis/dissertation

eScholarship.org Powered by the California Digital Library
University of California

Probing Bacterial Cell Envelope Structure and Dynamics with Metabolic Reporters

by

Frances Paola Rodríguez-Rivera

A dissertation submitted in partial satisfaction of the

requirements for the degree of

Doctor of Philosophy

in

Chemistry

in the

Graduate Division

of the

University of California, Berkeley

Committee in charge:

Professor Carolyn R. Bertozzi, Chair
Professor Matthew B. Francis
Professor Sarah A. Stanley

Fall 2016

Probing Bacterial Cell Envelope Structure and Dynamics with Metabolic Reporters

©2016

By Frances Paola Rodríguez-Rivera

Abstract

Probing Bacterial Cell Envelope Structure and Dynamics with Metabolic Reporters

By

Frances Paola Rodríguez-Rivera

Doctor of Philosophy in Chemistry

University of California, Berkeley

Professor Carolyn R. Bertozzi, Chair

The complexity of the bacterial cell envelope along with the clinical implications arising from biological discoveries have produced steady research over the last century. Orchestration of cell envelope biosynthesis requires the coordination of proteins, carbohydrates, glycolipids and lipids alike. The majority of these biomolecules are not encoded genetically and their dynamics can be challenging to interpret from standard genetic and biochemical approaches. Throughout my doctoral studies, I have endeavored into developing chemical reporters to visualize individual components of the bacterial cell envelope in live cells. This chemical biology strategy allowed the discovery of front-line tuberculosis drug effects on cell envelope dynamics, mapping of the cell envelope assembly during cell growth and division, as well as tracking individual glycolipids during *in vivo* mycobacterial infection. These investigations are the subject matter of this dissertation.

In the first chapter, I discuss a suite of chemical approaches to label the non-protein components of the bacterial surface. In particular, covalent and non-covalent modifications are described based on specificity towards labeling individual components from the cell envelope as well as examples of species-specific strategies. This overview of the literature sets the stage for improving metabolic reporters that can reveal underlying molecular processes concerning bacterial cell envelope structure and dynamics. The lessons learned from this survey are utilized to provide the framework for rational design of metabolic reporters outlined in the following chapters.

Chapter 2 describes the visualization of mycomembrane dynamics in real time in live bacteria. Metabolic labeling of trehalose mycolates associated with the cell envelope directly reports on mycomembrane fluidity. This strategy revealed that mycomembrane fluidity correlates with mycolic acid structure in Actinobacteria, and the glycolipids in Mycobacteria are nearly immobile. Our platform sets the stage for interrogation of mycomembrane fluidity as a proxy for increased susceptibility in mycobacteria during drug treatment.

The work presented in Chapter 3 relates to the study of cell envelope dynamics during cell growth in live mycobacteria visualized by metabolic labeling. Development of molecular tools revealed the subcellular organization trehalose monomycolates with super resolution microscopy. Pulse-chase experiments revealed that mycobacteria significantly remodel their cell envelope during front-line tuberculosis drug treatment. This work reveals the underlying dynamics in cell wall biogenesis of pathogenic *Mycobacterium marinum* and provides insight

into immediate stress responses. These findings also enhance our understanding of mycobacterial cell envelope structure and dynamics and have implications for development of new drug cocktails.

In Chapter 4, the investigation of cell envelope assembly during actinobacterial growth and division is described. Actinobacteria divide by a process called "V-snapping", where daughter cells remained joined until rapid snapping to form the characteristic V-shape. However, the exact cell envelope layer that undergoes rupture during V-snapping and the temporal landscape for this process remains unclear. Unnatural cell wall reporters amenable to ligation of fluorophores by bioorthogonal chemistry were used to visualize how cell envelope organization is coordinated in actinobacteria. Dynamics of the cell envelope revealed that new peptidoglycan and arabinogalactan are actively biosynthesized during septation, but non-covalently membrane-bound glycolipids are only mobilized to the septum right before V-snapping occurs. We propose that peptidoglycan undergoes mechanical rupture to facilitate millisecond V-snapping.

Finally, Chapter 5 describes the investigation of trehalose glycolipids during infection in the *M. marinum*-zebrafish model. In efforts to characterize *in vitro* dynamics of these glycolipids, fast turnover was observed and this phenomenon was correlated to the release of outer membrane vesicles. Super resolution microscopy shed light on the ultrastucture of glycolipids within the cell envelope. Metabolic labeling of trehalose mycolates revealed dynamic trafficking of such species during infection *in cellulo* and *in vivo*, where outer membrane vesicles could play an important role during early host-pathogen interactions.

This dissertation is dedicated to my sister Claudia.

Table of Contents

Appendix

List of Figures

List of Schemes

Acknowledgements

I could not have navigated the graduate school landscape without indispensable contributions from family friends, mentors and collaborators. First and foremost, I need to acknowledge my parents, Dr. Mercedes Rivera Borrero and Dr. René Rodríguez del Villar, who not only have been the inspiration and foundation for many of my professional endeavors, they have also advised me to exceed expectations, dream big and work hard. You are the primary reason behind every success that I have had. I am indebted to my sister Claudia, who epitomizes resilience and strives for perfection; this dissertation is dedicated to you.

Noelia, Isamar, Nashicel and Karla, the most loyal of friends, you have been there for me for so many years, no matter the physical distance. I have made several achievements in part possible through your support and sanity checks. On the academic side, Professors Mayra Pagán, Ivan Dmochowski, James Chambers, and James Heath helped me cultivate many skills as a young researcher and have provided steady support throughout the years, I thank you.

To my advisor Prof. Carolyn Bertozzi, thank you for fostering such a unique research environment within your lab. Your unwavering enthusiasm and support of scientific creativity and independence have molded the scientist that I am today. As a superb scientist, teacher, and writer, I have tried to assimilate many of your practices into my own line of work. Thank you for encouraging my research interests within and outside your areas of expertise, your wisdom and your generous advice. I will always approach science passionately, with awe and curiosity largely instilled by you. I credit Prof. Matt Francis and Prof. Chris Chang for exposing me to different flavors of Chemical Biology during my first-year rotations. I also credit Prof. Sarah Stanley and her research group for many valuable lessons when addressing scientific questions in the host-pathogen arena.

I thank Prof. Sloan Siegrist and Prof. Ben Swarts for teaching me the ropes and the wonders of chemical microbiology as a naïve graduate student. I am very fond of my scientific conversations with Doug Fox and CJ Cambier as well as their mentorship; I could not imagine more creative and unconventional people to brainstorm ideas with. To an outstanding collaborator, Peyton Shieh, I will remember you as one of the geniuses I had the pleasure of working with during my time in the Bertozzi group. In the lab, Mireille Kamariza, and outside of the lab, Prof. Lalita Ramakrishnan, Prof. Dan Portnoy, John Ngo and Prof. Roger Tsien, Xiaoxue (Snow) Zhou and Prof. Julie Theriot, Payton Weidenbacher and Prof. Peter Kim, Alex Eskandarian and Prof. John McKinney, Maikel Boot and Prof. Wilbert Bitter, Hoong Lim and Prof. Tom Bernhardt, and Josh Yoon and Prof. W.E. Moerner, have shaped my scientific views and how I approach research with an even more skeptical eye. In particular, I would like to thank Snow and Julie Theriot for teaching me ever-increasing scientific rigor and setting the bars of excellence as high as possible.

To my podmates, the witty Peter Robinson, the stealthy Matt Zhou, the no-BS Sam Keyser, and the young Jedi Corleone Delaveris, I am grateful for your company and brain-time, there is no question we recruit the best people! From my 817 days, Gaby de Almeida, you were my role model for "work hard, play hard" and I deeply appreciate your honest advice during this journey. To my mentees Olga Sokolovskaya and Sam Keyser, I am a very proud cheerleader and cannot wait to see what you will achieve in the future!

Asia Avelino, I want to express my gratitude for your untiring support in the last five years. You have been instrumental throughout my PhD, from providing free consolation hours to

spontaneous bobba runs. Olga, Sia, Karen, Cheryl, Meridee, and Maryann, thanks for being essential parts of the Bertozzi Lab engine, without you we could have been doomed to fail.

Lauren Wagner, Paresh Agarwal, Chelsea Gordon, Brenda Beahm, Brian Belardi, Lissette Andrés, Jason Hudak, Jessica Kramer, Marjoke Debets, Justin Kim, Junwon Choi, thank you for teaching me so many valuable lessons in graduate school; you will be dearly missed. Elliot Woods, Fred "Niceee" Tomlin, Neil Rumachik, Jason Tsai, Ulla Gerling-Driessen, Rachel Willand-Charnley, Ben Schumann, Han Xiao and Yi-Chang Liu, you have been fantastic colleagues and please stay in touch!

I would be absolutely remiss if I did not acknowledge Mason Appel, Ioannis Mountziaris, David Spiciarich and Nathan Yee from my cohort. Their dear friendship, relentless support and constructive criticism have been unparalleled, I could not imagine going through grad school without you.

To Kanwal, Ioana, Anna, Karla, Attar, Tony, Kelly, Cheri, Pete, Alex, Jigar, Willie, meeting and growing closer to you was no coincidence. I will forever cherish every memory from Berkeley that you were a part of, like jumping out of a perfectly working airplane to hiking the Half Dome in Yosemite. All of you have been part of the best years of my life.

Finally, Andrew. You have been my strongest pillar and I cannot find enough words to describe your monumental contribution to every aspect of my life for the last five years. You have been a truly admirable figure with the perfect humor and excess wit that I so often need. To such a brilliant man, I love you and I can't wait for what's next!

Chapter 1

Chemical Approaches to Label the Non-Protein Components of the Bacterial Cell Envelope

Chapter 1. Chemical Approaches to Label the Non-Protein Components of the Bacterial Cell Envelope

INTRODUCTION

The bacterial cell surface is the first line of defense against extracelluar stresses within the biological milieu and supports the basic processes of growth, division, and secretion. A significant proportion of cellular resources are dedicated to maintaining and remodeling the bacterial cell envelope. In turn, this barrier preserves cellular fitness by selective permeation of solutes over potential damaging agents as well as cell lysis. The essentiality and accessibility of the cell envelope have rendered it highly druggable as evidenced by the number of antibiotics that target it.[1,2] However, components of the cell envelope also play important roles in pathogenesis as they can mediate the very first interactions with a host during infection. To understand the underlying mechanisms of biosynthesis and host-pathogen interactions from a cell envelope perspective, it is imperative to understand the dynamics of individual components in their native environment.

Most bacteria can be classified in three categories in respect to the structure of the cell envelope: Gram-negative, Gram-positive and mycobacteria[3] (Figure 1.1). Architecture of the cell wall includes an inner membrane followed by a layer of peptidoglycan (PG), which is thicker in Gram-positive bacteria and mycobacteria. Gram-negatives display a characteristic outer membrane that is elaborated with lipopolysaccharides (LPS), capsular polysaccharides (CPS) and glycoproteins (Figure 1.1A). In comparison, Gram-positive organisms construct a thick PG layer modified with teichoic acids, as well as CPS and glycoproteins (Figure 1.1B). Similar to Gram-positives, mycobacteria biosynthesize a thick PG layer, but it is modified with unique glycan structures such as arabinogalactan and mycolic acids (Figure 1.1C). The mycobactecterial outer membrane, or mycomembrane, accommodates mycolylated arabinogalactan as well as non-covalently associated glycolipids, such as those derived from trehalose, which are hallmarks of the mycobacterial cell envelope.[4,5] In sum, the bacterial cell surface is primarily composed of non-genetically encoded products.

The complexity of the bacterial cell envelope along with the clinical implications arising from biological discoveries have produced steady research over the last century. Orchestration of cell envelope biosynthesis requires the coordination of proteins, carbohydrates, glycolipids and lipids alike. The majority of these biomolecules are not encoded genetically and their dynamics can be challenging to interpret from genetic and biochemical approaches. Thus, significant efforts have been devoted to chemically modifying the bacterial cell envelope. In this chapter, I discuss chemical approaches to label the non-protein components of the bacterial surface in different species. In particular, covalent and non-covalent modifications are described based on specificity towards labeling individual components from the cell envelope as well as species-specific examples. These approaches have become powerful tools to interrogate cell envelope structure, biosynthesis as well as interactions with the host during pathogenesis.

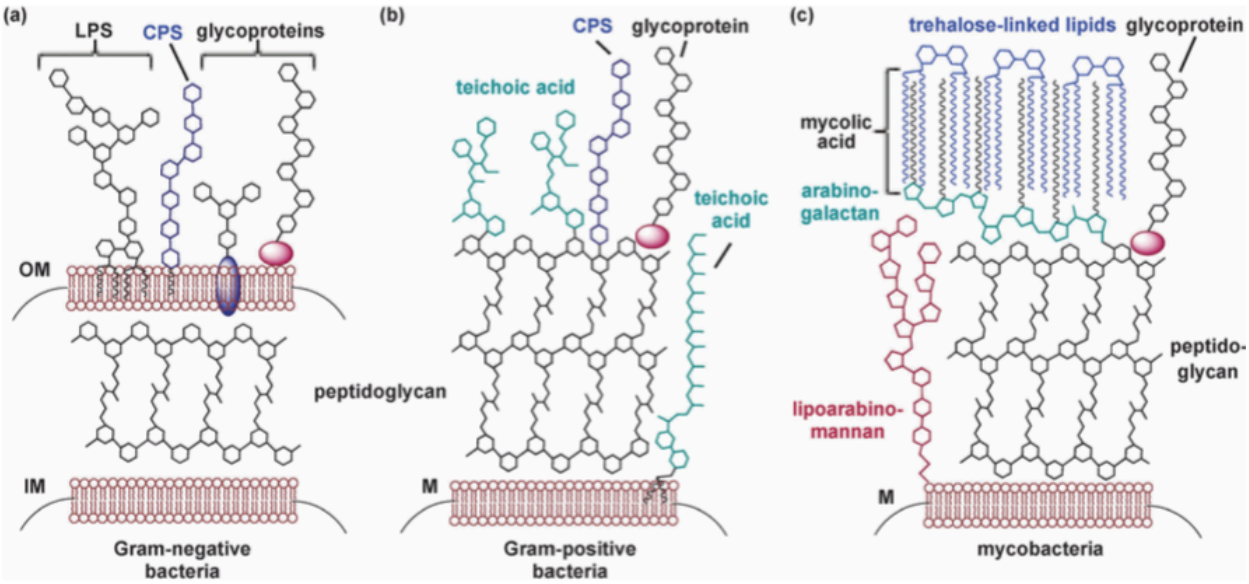

Figure 1.1 Bacterial cell envelopes for Gram-negative, Gram-positive and mycobacterial species. This figure highlights the differences in composition and structure between Gram-negative (a), Gram-positive (b) and mycobacterial species (c). Inner membrane (IM), outer membrane (OM), lipopolysaccharides (LPS), capsular polysaccharides (CPS). Reproduced with permission from reference.[6] Copyright 2014, The Royal Society of Chemistry.

CHEMICAL METHODS TO LABEL THE BACTERIAL CELL ENVELOPE

Agnostic small molecule probes for non-covalent and covalent modification

Small hydrophobic molecules have been useful to reveal structural information of the bacterial cell surface. For example, membrane intercalators should be agnostic to the surrounding cell wall components, but physical properties of these molecular probes can bias non-specific interactions according to size, charge, and hydrophobicity features. Early work using lipophilic fluorophore conjugates that nonspecifically intercalate into the mycomembrane of mycobacteria suggested a heterogeneous cell surface landscape.[7,8] Structural features of both selected fluorophore and lipid tail were found to influence localization of lipophilic conjugates to different subcellular regions.[7] The observed phenomena are further complicated by strong interactions between probe and glycolipids such as cardiolipin,[8] which could alter the structural organization of lipid domains. Among this class of compounds, FM-4-64 dye has been utilized to elucidate lipid spiral architecture and role in cell division of *Bacillus subtilis*, which has forced the revision of the fluid mosaic model for bacterial membranes.[9] Due to non-specific interactions, these compounds are mostly used as markers for cell membranes in fluorescence colocalization studies.

Commercially available amine-reactive dyes can tag any biomolecule within the cell wall that has a good appended nucleophile. In comparison to membrane intercalators, covalent attachment of fluorophore can illuminate long-term dynamics with spatiotemporal resolution of the modified biomolecule. For this reason, many groups have selected this strategy for tracking

proteins in the bacterial cell envelope, but these reagents cannot discriminate between exposed amines in proteins, lipids, or glycans.[10–13] Virtually all amine functional groups can be modified during labeling, where accessibility might determine preference towards more exposed functionalities. This labeling strategy requires removal of all proteins from the growth media, slightly basic pH, and excess reagent to account for competing hydrolysis of labeling reagent in order to increase the labeling efficiency. Such stringent conditions might affect the physiology of the cell and therefore the outcome of the visualization method. From using this strategy, we have learned about the nature of polar inert murein[10] and helical orientation of cell surface proteins in *Escherichia coli*,[11] as well as differential susceptibilities to antibiotics in *Mycobacterium smegmatis* by measuring asymmetry and cell elongation rate.[13]

Other efforts for covalent modification have focused on oxidation of cell surface glycans followed by installation of a visualizable handle, commonly used for tagging mammalian glycans.[14,15] Periodate oxidation of carbohydrates introduces aldehydes than can be ligated with amine or hydrazide reagents that are installed on glycoproteins, glycolipids or higher order glycopolymers (arabinogalactan, lipoarabinomannan, etc.). Russell and coworkers discovered the trafficking of mycobacterial cell envelope components within infected macrophages utilizing this method.[16,17] However, non-specific oxidation of bacterial cell surface glycans could negatively impact interactions with host receptors that are crucial for pathogenesis. Taken together, agnostic small molecule probes are useful tools to illuminate the bacterial cell surface, but lack the specificity to modify individual component of the cell envelope.

Drug-inspired molecular probes

The bacterial cell envelope is the target of several successful antibiotics, but these have also expanded our understanding of underlying molecular processes of cell wall biosynthesis. Most prominent is the PG layer, almost ubiquitous among bacterial organisms, which determines the cell's shape and protects it from turgor pressure.[18–20] For these reasons, PG structure and biosynthesis has been an area of extensive study for many years.[21–25] The peptidoglycan polymer consists of a repeating disaccharide unit (*N*-acetylglucosamine and *N*-acetylmuramic acid, GlcNAc and MurNAc, respectively) that harbors short peptides. The peptide chains, composed of mostly D-amino acids (up to pentamers), are crosslinked and can vary among bacterial species. This meshwork affords the intrinsic rigidity to the cell wall and can sustain impressive turgor pressures.

Many enzymes are involved in the biosynthesis of PG, which are located both in the cytosol and the periplasm (Gram-negative) or extracytoplasm (Gram-positive) (Figure 1.2). D-alanine is processed by D-alanyl-D-alanine ligase to form the first committed D-ala-Dala dipeptide towards de novo PG synthesis.[20,26] Several enzymes are involved in producing the UDP-MurNAc-tripeptide, which is a precursor that is ligated to D-ala-D-ala to the afford UDP-MurNAc-pepntapeptide. This monomer is in turn modified with undecaprenol phosphate within the cytoplasmic face of the inner membrane to form Lipid I (Figure 1.2).[20,26] Lipid II is the product of adding UDP-GlcNAc to the Lipid I intermediate. The disaccharide lipid subunits (Lipid II) are flipped to the periplasm for assembly into PG strands. Enzymes involved in transglycosylation and transpeptidation (including penicillin-binding proteins, PBPs) modify new PG and crosslink incorporated subunits into the existing meshwork (Figure 1.2).[20,26]

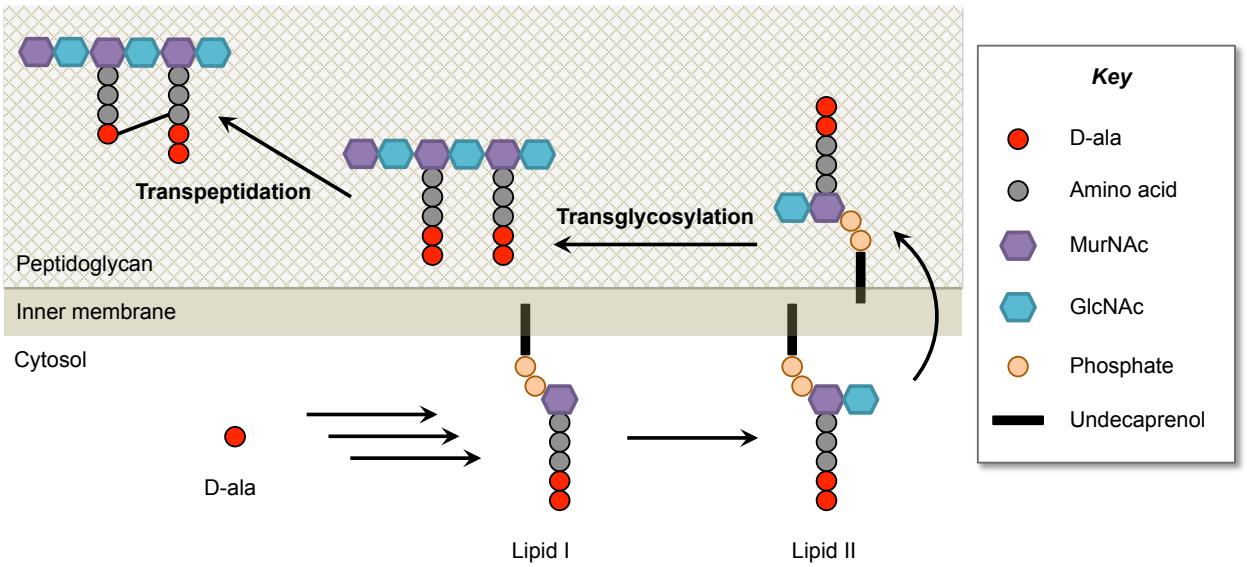

Figure 1.2 Peptidoglycan biosynthesis takes place in both cytosolic and perisplasmic compartments of the cell

In efforts to find new antibacterials, several antibiotics that target peptidoglycan have been identified to date. For example, vancomycin, a cyclic glycosylated antibiotic, inhibits nascent PG biosynthesis by binding D-alanine-D-alanine motif within the stem peptide from uncrosslinked strands. Installation of fluorophores on this antibiotic has found widespread use to visualize PG biosynthesis in live cells. A vancomycin-fluorescein (Van-Fl, Figure 1.3) conjugate revealed strong septal labeling and a helical pattern of the sidewall when incubated with live *B. subtilis*.[27] Walker and coworkers expanded upon this work and surveyed fluorescent derivatives of vancomycin and ramoplanin to visualize nascent PG in *B subtilis*, revealing the characteristic helical labeling pattern of the sidewall.[28] Ramoplanin binds lipid II extracellularly, therefore preventing incorporation of disaccharide-pentapeptide precursors into growing PG strands by transglycosylases.[29–32] Both vancomycin and ramoplanin derivatives (Ramo-Fl, Figure 1.3) induced perturbations in PG synthesis as denoted by dose-dependence studies, but ramoplanin conjugates provided a more robust signal at lower concentrations than MIC.[28] These studies highlighted how fluorescent antibiotics could inform on nascent PG synthesis and correlated with cytoskeletal elements, such as MbI-dependent colocalization.[33] Fluorescent antibiotics have also yielded high resolution imaging of PG labeling by super resolution techniques.[34] For extended imaging applications, a nitrone-modified version of vancomycin was reported to label Gram-positive *Lactococcus lactis* after ligation of a cyclooctyne-fluorophore conjugate.[35]

These powerful molecular tools are visualizable inhibitors that suffer from limited accessibility to their targets due to the permeability barriers in the cell wall, as exemplified by their widespread in Gram-positive organisms. Mycobacteria, which are highly impermeable to hydrophilic and hydrophobic small molecules,[36,4,37] necessitate at least 2 h incubation period to afford a robust signal from Van-Fl.[38,39] A long incubation requirement could obscure dynamics occurring in the order of minutes during cell envelope biosynthesis. In addition, their intrinsic toxicity limits fluorescence imaging to end-point experiments, which are only static snapshots of bacterial surface dynamics. Along a similar vein of fluorescent antibiotics, the design of new

molecular probes could include introduction of targocil[40,41] conjugates as the first visualizable inhibitor of wall teichoic acid biosynthesis,[3] which are covalently anchored to PG (Figure 1.1).

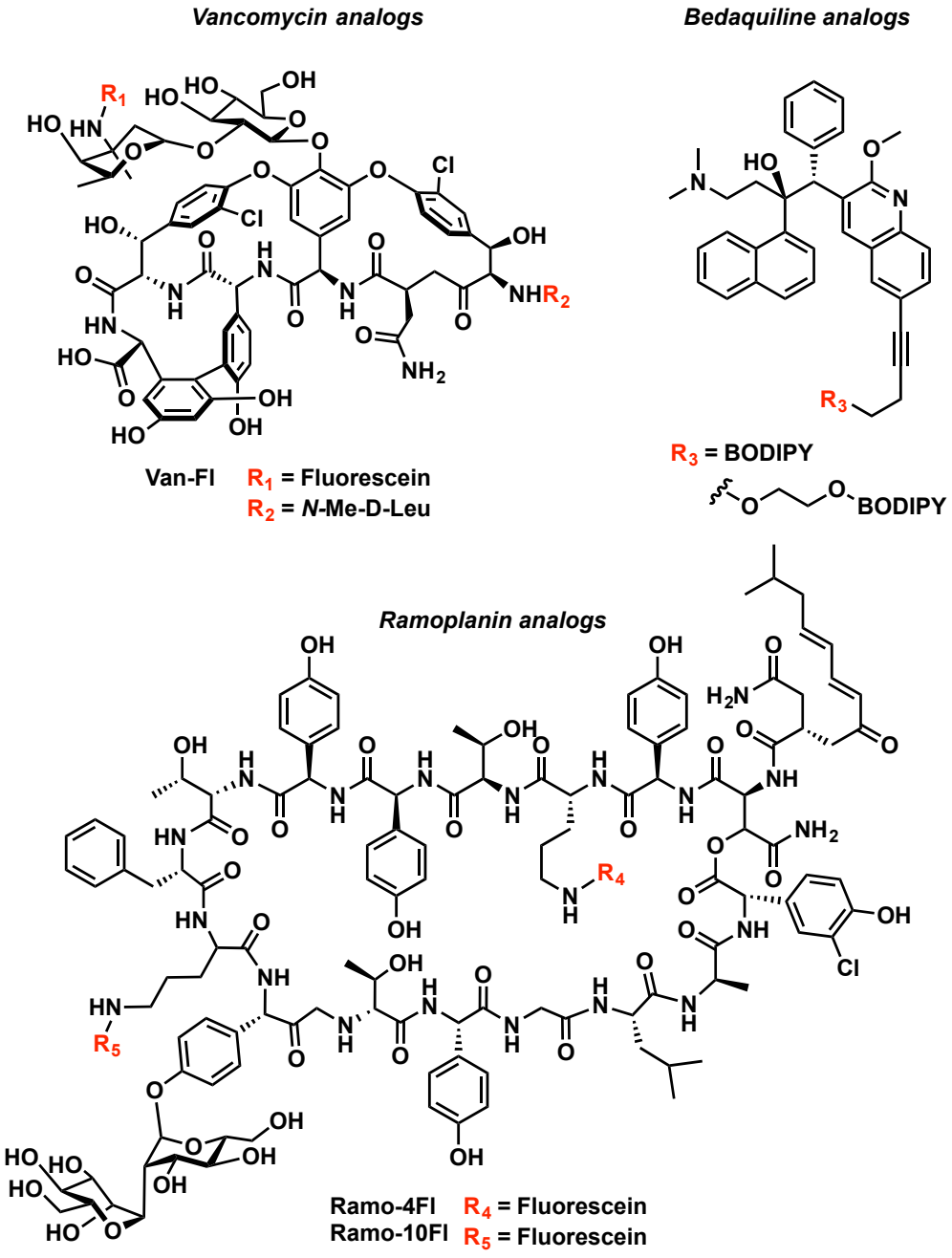

Figure 1.3 Drug-inspired fluorophore conjugates to image the bacterial cell envelope. Chemical structures for vancomycin, ramoplanin and bedaquiline molecular probes are illustrated.

Another example of drug-inspired probes involved the modification of bedaquiline with BODIPY fluorophore (Figure 1.3).[42] Bedaquiline emerged as a clinically approved drug to treat multi-drug resistant tuberculosis.[43,44] Its mechanism of action relies on the strong interaction with membrane-exposed ion-binding sites of the c-ring of F_1F_o-ATP synthase, therefore stopping ATP synthesis in mycobacteria.[45] Careful inspection of the linker length between bedaquiline and fluorophore afforded synthetic conjugates with 70-fold higher MIC than the parent drug.[42] These compounds could find broad applications in understanding diarylquinoline interactions with target protein and efflux pumps for biochemical or fluorescence imaging experiments. Additional examples of enzyme-targeted labeling with antibiotic conjugates have been reported for PBPs[46] and were recently reviewed elsewhere.[47]

Sortase-mediated ligation to label peptidoglycan

Bacterial sortases are endowed with the capacity to covalently link proteins to the PG layer in Gram-positive organisms (Figure 1.4).[48,49] Sortase A (SrtA) from *Staphylococcus aureus* requires recognition of the conserved LPXTG pentapeptide motif at the C-terminus of secreted proteins.[50,51] Several groups have exploited the selectivity of this motif to anchor pentapeptides modified with different payloads to PG.[52–54] Spiegel and coworkers demonstrated covalent modification of *S. aureus* cell wall with synthetic peptides carrying diverse functional handles, including bulkier substrates fluorescein and biotin.[52] More recent work has focused on improving sortase-tagging efficiency by optimizing the conserved recognition motif.[54] However, these efforts to modify PG layer within the cell envelope have been limited to Gram-positive organisms so far. Peptide substrates could be inaccessible to sortase-like enzymes by the higher impermeability presented by Gram-negative and mycobacterial species.

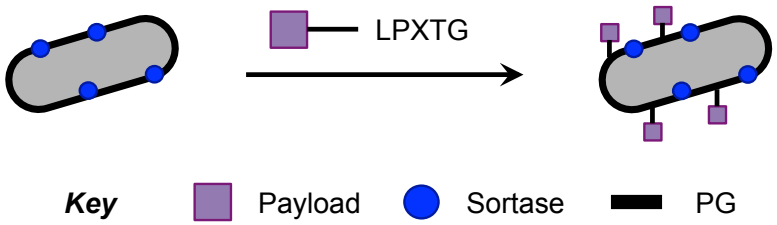

Figure 1.4 Sortase-mediated ligation of small molecules to the bacterial cell envelope

Taking inspiration from bacteria, the sortase-mediated ligation has found useful applications for bioconjugation strategies including new engineered variants.[55–58] In addition to sortases, other bacterial proteases that recognize VLK-peptide substrates have recently emerged as new candidates for PG-specific modification of Gram-positive bacteria.[59]

Biomolecule-specific covalent modification with synthetic metabolic reporters

Biochemical characterization of cell wall biosynthetic pathways has paved the way for understanding substrates, enzymes and products involved in such processes. Such knowledge has also highlighted diversification of enzymes among bacterial species. Notably, the first example of metabolic labeling falls within radiolabeling experiments, where radioactive metabolic

precursors are introduced to track cell metabolites. These experiments require dedicated equipment and generate toxic waste that can easily become cost-prohibitive. Nonetheless, it is widely accepted that the endogenous biosynthetic machinery of the cell can metabolize small synthetic reporters.[60] This approach has been demonstrated in both bacterial[6,61] and mammalian[60] systems. A metabolic reporter can hijack the biosynthetic pathways, where the promiscuity of such enzymes is exploited for installation of a visualizable handle onto the biomolecule of interest. Furthermore, metabolic labeling can take advantage of either cytosolic or extracellular incorporation of unnatural precursors (Figure 1.5).

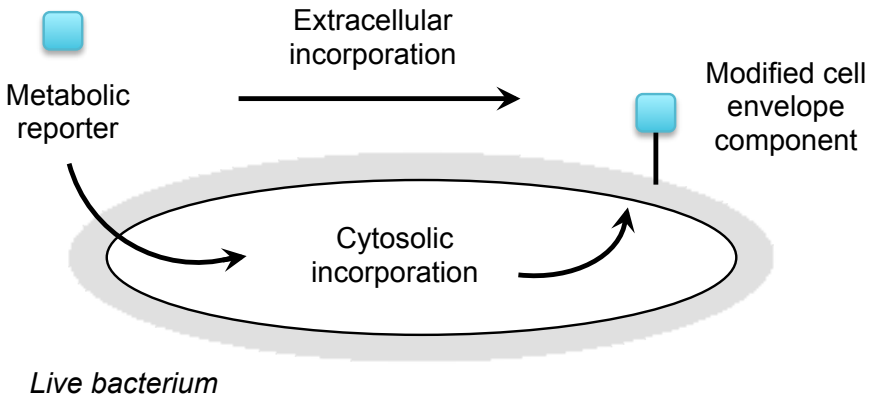

Figure 1.5 Metabolic labeling of the bacterial cell envelope via cytosolic and extracellular incorporation routes

Installation of a visualizable handle on the biomolecule of interest can be achieved in different ways. For example, introduction of a small functional group such as azides or alkynes on the reporter, which are agnostic to functionalities found in the biological milieu, can be covalently ligated with fluorophores by bioorthogonal chemistry.[62–64] If biosynthetic enzymes are promiscuous, larger functional groups directly installed on the reporter (i.e. fluorophores) can be visualized with a one-step labeling strategy. Metabolic labeling of the bacterial surface has been reviewed comprehensively by several groups.[60,6,61,65–69]

D-amino acid-derived molecular probes to label peptidoglycan

Bacteria accommodate several unnatural D-amino acids into the PG architecture, which are integral components for stem peptide crosslinking (Figure 1.2). de Pedro *et al.* first recognized this phenomenon by characterization of D-cysteine incorporation by *E. coli*. [70] Upon covalent ligation with thiol-reactive labels for fluorescence and electron microscopy, polar murein caps were found to be essentially inert in this organism. Although a powerful tool that revealed new PG biology, thiol reactions are not suited for two-step labeling methods during non-disruptive live cell imaging. Future work in this area spanned the installation of visualizable handles that had desirable properties for incorporation by live cells under physiological conditions. The first wave of such efforts involved appending small molecule fluorophores on D-alanine or D-lysine analogs such as coumarin, fluorescein, and tetramethylrhodamine.[71,72] Fluorescent D-amino acids (FDAA) have unveiled structural information with super resolution microscopy as well as *in vitro* growth and cell division dynamics in bacterial species.[71,73–77] In

addition, FDAAs have successfully identified a PG layer within the *Chlamydiae* cell envelope *in vitro* and in infected amoeba cells.[78] Collectively, these reports have highlighted important insights into PG synthesis, but fail to capture de novo PG biosynthesis occurring in the cytosol.

Smaller bioorthogonal reporters installed on D-amino acids are better suited to gain access into the cytosolic compartment of bacteria. A two-step labeling strategy to visualize PG dynamics *in vitro* and during infection was developed in our group by exploiting the minimal perturbation of azide and alkyne-D-alanine derivatives.[79] Additional, these click-chemistry armed derivatives have facilitated the impressive visualization PG dynamics of *Listeria monocytogenes* within infected macrophages[80] and sporulation of *Clostridium difficile*.[81] Even though small D-amino acids are efficiently metabolized by bacteria, delivery of secondary labeling reagents can suffer from poor accessibility and increased background arising from non-specific interactions. Due to these limitations, two-step labeling experiments might only capture end-point phenomena and afford a limited temporal resolution. To address this, several groups have focused on developing fluorogenic alternatives, where fluorophores have been rationally designed to only turn-on after reacting.[82–84] Our group has demonstrated PG labeling in bacteria with cyclooctyne D-amino acids that can be selectively visualized with azide-fluorogenic probes in live cells without any washing steps.[85] The Pires group has also developed reporters harboring alkenes that can be detected with tetrazine probes,[86] which are good candidates for a fluorogenic strategy.[87]

D-amino acids have also been envisioned as a means to target bacterial infections by installing motifs that could be recognized by the immune system.[69,88] Fura *et al.* elegantly demonstrated that the surface of Gram-positive bacteria could be labeled with dinitrophenyl-D-amino acid (DNP) derivatives that are recognized by anti-DNP antibodies.[89] This approach facilitated accelerated phagocytosis after chemically-inducing opsonization of *B. subtilis* by murine macrophages.[89] In particular, this approach could find clinical applications to treat bacterial infections as recently demonstrated for intracellular *S. aureus* during *in vivo* infection.[90] With the discovery that PG biosynthetic machinery is rather promiscuous and the advancement of bioorthogonal chemistry, diverse functionalities have been installed on D-amino acid analogs that are metabolically incorporated by bacteria (Figure 1.6). The current repertoire includes bioorthogonal handles from azides to cyclooctynes, fluorophores, biotin,[91] and dinitrophenol groups for antibody recognition.

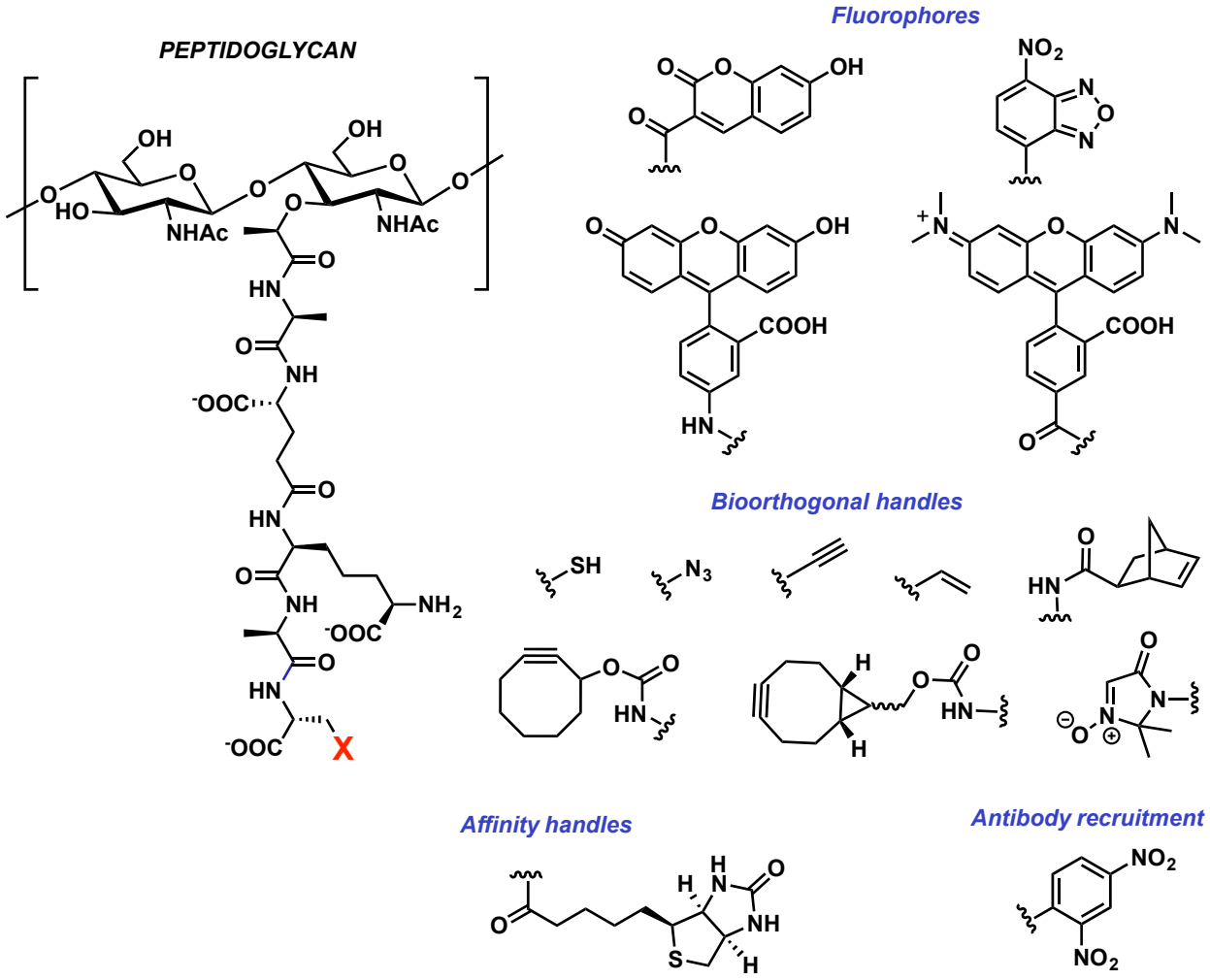

Figure 1.6 Functionalities installed on D-amino acid probes to metabolically label the bacterial cell envelope. Promiscuous PG biosynthetic machinery tolerates a range of functional groups including a variety of fluorophores, bioorthogonal handles, and affinity handles. The chemical structure of PG monomer is also depicted (left).

Bacteria can incorporate exogenous D-amino acids into peptidoglycan through both intracellular and extracellular pathways that can operate in different species. The former depends on the cytoplasmic addition of a new D-amino acid at the fifth position of the stem peptide by the action of D-alanine-D-alanine ligase (Ddl). The second pathway requires transpeptidases that install the new residue at either the fourth or the fifth position on the stem peptide. The preference over these incorporation routes has remained unclear since there is biochemical evidence that supports both alternatives.[92,93] Our two-step metabolic labeling strategy coupled with correlative light and electron microscopy[94,95] provided the resolution to discriminate between labeled surface PG strands and cytosolic PG intermediates bound to the inner membrane.[96] This work provided the first direct evidence of alkyne-D-alanine being primarily incorporated by a cytosolic route in *L. monocytogenes*.

More recent efforts have successfully modified the C-terminus of D-amino acid reporters. D-amino carboxamide probes have emerged as next generation reporters that dramatically increase incorporation efficiency into *B. subtilis* PG.[97] However, these reagents were not processed by L,D-transpeptidases or PBPs from *E. coli*, highlighting species-specific selectivity for processing unnatural reporters.[97] Pires and coworkers expanded upon this work by diversifying the modification at the C-terminus as means to profile bacterial species.[98] Notably they found that cell stiffness was substantially reduced after labeling, which indicates more prominent perturbations to PG acrchitecure.[98] D-amino carboxamide probes have also been used for antibody recruitment to the bacterial cell surface.[99]

A different variant of PG-inspired reporters takes advantage of endogenous recycling of PG fragments. Dipeptides harboring azides or alkynes are incorporated by the cell's biosynthetic machinery and can be visualized after delivery of a fluorescent handle[100] or attachment of haptens for antibody recruitment.[101] This dipeptide labeling strategy was used to prove the existence of PG in *Chlamydia trachomatis* and effectively dismiss the "chlamydial anomaly" by Liechti *et al*.[100] Fluorophore-tripeptide conjugates are also hypothesized to follow a cytosolic incorporation route.[102] In comparison, fluorescent stem peptide mimics have been developed to serve as donors during transpeptidation reactions by transferring a fluorophore to monitor activity of PBPs.[103] Finally, earlier work by Liu *et al.* and Sadamoto *et al.* showed that UDP-MurNAc-pentapeptide derivatives can metabolically label PG as well.[104–107] Collectively, PG reporters are incorporated by highly promiscuous biosynthetic machinery among bacteria and have provided significant insights into cell growth and division.

Carbohydrate-derived molecular probes to label polysaccharides and glycolipids

Metabolic oligosaccharide engineering was first described in mammalian systems, but has been widely adopted for bacterial systems in the last decade.[108] Similar to PG labeling strategies, the promiscuity of cell envelope biosynthetic enzymes can be exploited to introduce unnatural monosaccharides. Incorporation can vary from cytosolic to extracellular routes depending on the biosynthetic pathway of interest. Bertozzi and coworkers demonstrated for the first time the incorporation of metabolic reporters into lipooligosaccharides (LOS) of *Haemophilus ducreyi*.[109,110] Unnatural sialic acids with varying alkyl chain lengths on the N-acyl position were metabolized by an extracellular scavenging pathway (Figure 1.7A).[110] This strategy required arduous validation and quantification of incorporation efficiency by radioactive experiments and mass spectrometry. With the advent of the bioorthogonal chemistry toolbox, polysaccharides from *E. coli* have been visualized with two-step metabolic labeling strategy.[111] Utilizing fucose-derived analogs, Yi *et al.* performed metabolic engineering of a promiscuous sugar nucleotide biosynthetic pathway to afford chemically-defined bacterial lipopolysaccharides (LPS) (Figure 1.7B). Using a similar strategy, Dukan, Vauzeilles and coworkers identified 3-deoxy-D-manno-octulosonic acid (KDO) within the inner core of LPS as a potential candidate for metabolic labeling.[112] Installation of an azide on KDO (KDO-N_3) allowed visualization of LPS in live Gram-negative bacteria by fluorescence imaging[112] (Figure 1.7C). Future work from these groups encompassed developing reporters to label the O-antigen portion of LPS with legioaminic acid (Leg) precursors (highlighted in green, Figure 1.7C). Mas Pons *et al.* utilized these metabolic reporters for easy and specific detection of living *Legionella pneumophila*.[113] These approaches take advantage of species-specific building blocks, which are crucial for organism detection.

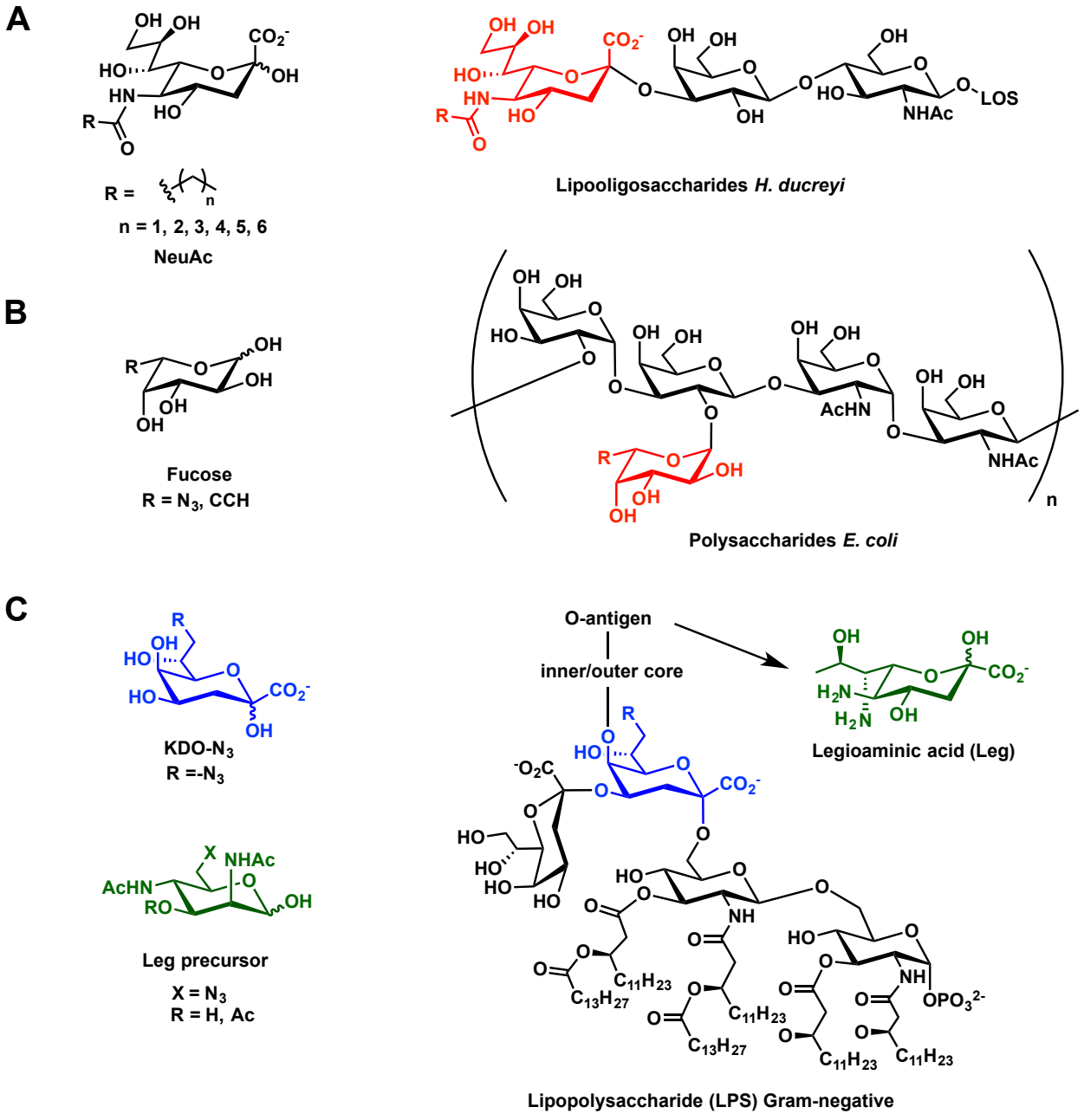

Figure 1.7 Glycan-derived probes to metabolically label diverse polysaccharides in bacteria. Strategies to metabolically label bacterial glycan conjugates include LOS (a) and capsular polysaccharides such as LPS (b, c) with NeuAc, fucose, and KDO/Leg precursors, respectively, are illustrated. *N*-acetylneuraminic acid (NeuAc), Lipooligosaccharides (LOS), 3-deoxy-D-manno-octulosonic acid (KDO), legioaminic acid (Leg)

In addition to glycan metabolic labeling of Gram-negative bacteria, important contributions have been made towards elucidating roles of unique glycolipids in mycobacteria. The mycomembrane supports a wide variety of non-covalently associated glycolipids, of which trehalose monomycolate (TMM) and dimycolate (TDM) are the most abundant species (Figure 1.8A).[5,114] Both of these glycolipids have been the subject of metabolic labeling efforts as interrogation of dynamics by biochemical or genetic approaches have not been successful. Barry, Davis and coworkers discovered that bulky modifications on the trehalose scaffold were tolerated for labeling live mycobacteria.[115] Impressively, a fluorescein-trehalose conjugate (FITC-Tre) in Figure 1.8B was metabolized to form trehalose mycolates by the antigen 85 complex (Ag85), a family of mycolyltransferases that convert 2 TMM units to TDM and free trehalose. This work highlighted for the first time how synthetic trehalose reporters could be utilized to visualize trehalose mycolate dynamics in mycobacteria by fluorescence imaging.

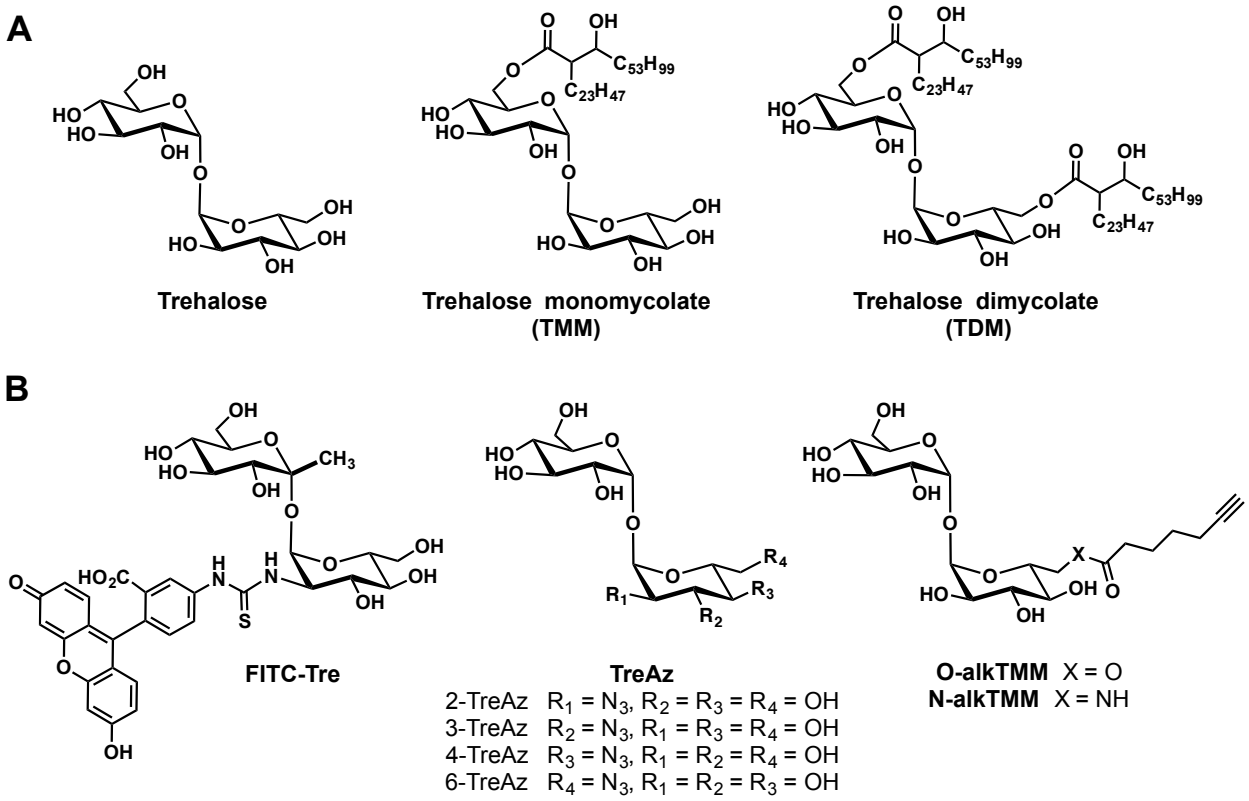

Figure 1.8 Trehalose reporters to metabolically label trehalose glycolipids. A) Chemical structures for trehalose and trehalose mycolates. B) Chemical structures of unnatural trehalose reporters to visualize trehalose mycolates by fluorescence imaging.

Late-stage incorporation by an extracellular route limited the ability to observe de novo biosynthesis of trehalose mycolates. Thus, Swarts *et al.* developed azide-trehalose (TreAz, Figure 1.8B) reporters that were taken up by live by mycobacteria and were visualized with cyclooctyne-fluorophore conjugates.[116] The site of modification determined whether these probes gained access to the cytosol through the trehalose transporter SugABC-Lpqy.[117] TreAz probes can also by accessed chemo-enzymatically[118] to perform mycobacterial labeling. Swarts and coworkers elegantly described the application of trehalose reporters that serve as TMM donors to

modify both trehalose mycolates and arabinogalactan (alkTMM, Figure 1.8B).[119] Besides fluorescence imaging, trehalose reporters have been proposed to serve as radiotracers[120] to follow tuberculosis human infection, as trehalose is completely absent in mammalian organisms. Collectively, trehalose reporters have been adopted for fluorescent labeling of the mycobacterial cell envelope with potential applications for clinical imaging as well as early diagnosis of tuberculosis disease.

SUMMARY AND OUTLOOK

The bacterial cell surface harbors many non-genetically encoded products that are integral components for cell envelope structure and dynamics. Recognizing orthogonal metabolites to the host or species-specific building blocks are both successful strategies to selectively visualize bacterial cell envelope components. D-amino acids and bacterial-derived glycan reporters serve this purpose, but fewer alternatives can label the bacterial cell envelope in a species-specific manner. With the development of super resolution techniques and application to bacterial imaging,[121,122] the visualization of metabolically labeled components should be around the corner. The molecular view of individual components could reveal important structural insights on cell envelope architecture as well as subcellular resolution of biomolecule dynamics. New technological advances such as imaging by stimulated Raman-scattering,[123] could harness an unperturbed view of biomolecule dynamics as heavy isotopes of metabolic reporters can be traced without interference from biological signatures.

Besides technological advances, the rational design of new visualizable handles to be installed on metabolic probes could immediately report on biophysical properties of the local environment. For example, solvatochromic probes are good candidates for reporting on local hydrophobicity[124] or pH changes.[125] Environment-sensitive probes[124–127] in combination with metabolic reporters could yield powerful point-of-care diagnostics that are bacterial species specific. In addition, chemical approaches to label the bacterial cell envelope are well-suited to deliver cargoes for photodynamic therapy (PDT).[128–131] Installation of small molecule PDT tracers[132,133] could be explored as a new avenue for treatment of bacterial infections.

Chemical approaches to engineer the bacterial cell surface can provide fine-tuned control required to understand molecular processes in biology. Rational design of antibiotic or cell envelope fragment reporters will continue to be powerful tools in microbiology.

REFERENCES

1. Walsh, C. *Antibiotics*. (American Society of Microbiology, 2003).
2. Kohanski, M. A., Dwyer, D. J. & Collins, J. J. How antibiotics kill bacteria: from targets to networks. *Nat. Rev. Microbiol.* **8,** 423–435 (2010).
3. Silhavy, T. J., Kahne, D. & Walker, S. The Bacterial Cell Envelope. *Cold Spring Harb. Perspect. Biol.* **2,** a000414 (2010).
4. Brennan, P. J. & Nikaido, H. The Envelope of Mycobacteria. *Annu. Rev. Biochem.* **64,** 29–63 (1995).
5. Jankute, M., Cox, J. A. G., Harrison, J. & Besra, G. S. Assembly of the Mycobacterial Cell Wall. *Annu. Rev. Microbiol.* **69,** 405–423 (2015).

6. N. Tra, V. & H. Dube, D. Glycans in pathogenic bacteria – potential for targeted covalent therapeutics and imaging agents. *Chem. Commun.* **50,** 4659–4673 (2014).
7. Christensen, H., Garton, N. J., Horobin, R. W., Minnikin, D. E. & Barer, M. R. Lipid domains of mycobacteria studied with fluorescent molecular probes. *Mol. Microbiol.* **31,** 1561–1572 (1999).
8. Maloney, E. A. *et al.* Alterations in phospholipid catabolism in Mycobacterium tuberculosis lysX mutant. *Cell. Infect. Microbiol. - Closed Sect.* **2,** 19 (2011).
9. Barák, I., Muchová, K., Wilkinson, A. J., O'Toole, P. J. & Pavlendová, N. Lipid spirals in Bacillus subtilis and their role in cell division. *Mol. Microbiol.* **68,** 1315–1327 (2008).
10. Pedro, M. A. de, Grünfelder, C. G. & Schwarz, H. Restricted Mobility of Cell Surface Proteins in the Polar Regions of Escherichia coli. *J. Bacteriol.* **186,** 2594–2602 (2004).
11. Ghosh, A. S. & Young, K. D. Helical Disposition of Proteins and Lipopolysaccharide in the Outer Membrane of Escherichia coli. *J. Bacteriol.* **187,** 1913–1922 (2005).
12. Rafelski, S. M. & Theriot, J. A. Mechanism of polarization of Listeria monocytogenes surface protein ActA. *Mol. Microbiol.* **59,** 1262–1279 (2006).
13. Aldridge, B. B. *et al.* Asymmetry and Aging of Mycobacterial Cells Lead to Variable Growth and Antibiotic Susceptibility. *Science* **335,** 100–104 (2012).
14. Nilsson, J. *et al.* Enrichment of glycopeptides for glycan structure and attachment site identification. *Nat. Methods* **6,** 809–811 (2009).
15. Zeng, Y., Ramya, T. N. C., Dirksen, A., Dawson, P. E. & Paulson, J. C. High-efficiency labeling of sialylated glycoproteins on living cells. *Nat. Methods* **6,** 207–209 (2009).
16. Beatty, W. L. *et al.* Trafficking and Release of Mycobacterial Lipids from Infected Macrophages. *Traffic* **1,** 235–247 (2000).
17. Beatty, W. L., Ullrich, H.-J. & Russell, D. G. Mycobacterial surface moieties are released from infected macrophages by a constitutive exocytic event. *Eur. J. Cell Biol.* **80,** 31–40 (2001).
18. Schleifer, K. H. & Kandler, O. Peptidoglycan types of bacterial cell walls and their taxonomic implications. *Bacteriol. Rev.* **36,** 407–477 (1972).
19. Typas, A., Banzhaf, M., Gross, C. A. & Vollmer, W. From the regulation of peptidoglycan synthesis to bacterial growth and morphology. *Nat. Rev. Microbiol.* **10,** 123–136 (2012).
20. Lovering, A. L., Safadi, S. S. & Strynadka, N. C. J. Structural Perspective of Peptidoglycan Biosynthesis and Assembly. *Annu. Rev. Biochem.* **81,** 451–478 (2012).
21. Scheffers, D.-J. & Pinho, M. G. Bacterial Cell Wall Synthesis: New Insights from Localization Studies. *Microbiol. Mol. Biol. Rev.* **69,** 585–607 (2005).
22. Vollmer, W., Blanot, D. & Pedro, M. A. D. Peptidoglycan structure and architecture. *FEMS Microbiol. Rev.* **32,** 149–167 (2008).
23. Vollmer, W. Structural variation in the glycan strands of bacterial peptidoglycan. *FEMS Microbiol. Rev.* **32,** 287–306 (2008).
24. Vollmer, W. & Seligman, S. J. Architecture of peptidoglycan: more data and more models. *Trends Microbiol.* **18,** 59–66 (2010).
25. Pinho, M. G., Kjos, M. & Veening, J.-W. How to get (a)round: mechanisms controlling growth and division of coccoid bacteria. *Nat. Rev. Microbiol.* **11,** 601–614 (2013).
26. Vollmer, W., Blanot, D. & Pedro, M. A. D. Peptidoglycan structure and architecture. *FEMS Microbiol. Rev.* **32,** 149–167 (2008).
27. Daniel, R. A. & Errington, J. Control of Cell Morphogenesis in Bacteria: Two Distinct Ways to Make a Rod-Shaped Cell. *Cell* **113,** 767–776 (2003).

28. Tiyanont, K. *et al.* Imaging peptidoglycan biosynthesis in Bacillus subtilis with fluorescent antibiotics. *Proc. Natl. Acad. Sci.* **103,** 11033–11038 (2006).
29. Hu, Y., Helm, J. S., Chen, L., Ye, X.-Y. & Walker, S. Ramoplanin Inhibits Bacterial Transglycosylases by Binding as a Dimer to Lipid II. *J. Am. Chem. Soc.* **125,** 8736–8737 (2003).
30. Hamburger, J. B. *et al.* A crystal structure of a dimer of the antibiotic ramoplanin illustrates membrane positioning and a potential Lipid II docking interface. *Proc. Natl. Acad. Sci.* **106,** 13759–13764 (2009).
31. Fang, X. *et al.* The mechanism of action of ramoplanin and enduracidin. *Mol. BioSyst.* **2,** 69–76 (2006).
32. Walker, S. *et al.* Chemistry and Biology of Ramoplanin: A Lipoglycodepsipeptide with Potent Antibiotic Activity. *Chem. Rev.* **105,** 449–476 (2005).
33. Cabeen, M. T. & Jacobs-Wagner, C. Bacterial cell shape. *Nat. Rev. Microbiol.* **3,** 601–610 (2005).
34. Wheeler, R., Mesnage, S., Boneca, I. G., Hobbs, J. K. & Foster, S. J. Super-resolution microscopy reveals cell wall dynamics and peptidoglycan architecture in ovococcal bacteria. *Mol. Microbiol.* **82,** 1096–1109 (2011).
35. A. MacKenzie, D., R. Sherratt, A., Chigrinova, M., J. Kell, A. & Paul Pezacki, J. Bioorthogonal labelling of living bacteria using unnatural amino acids containing nitrones and a nitrone derivative of vancomycin. *Chem. Commun.* **51,** 12501–12504 (2015).
36. Jarlier, V. & Nikaido, H. Mycobacterial cell wall: Structure and role in natural resistance to antibiotics. *FEMS Microbiol. Lett.* **123,** 11–18 (1994).
37. Li, X.-Z., Zhang, L. & Nikaido, H. Efflux Pump-Mediated Intrinsic Drug Resistance in Mycobacterium smegmatis. *Antimicrob. Agents Chemother.* **48,** 2415–2423 (2004).
38. Kang, C.-M., Nyayapathy, S., Lee, J.-Y., Suh, J.-W. & Husson, R. N. Wag31, a homologue of the cell division protein DivIVA, regulates growth, morphology and polar cell wall synthesis in mycobacteria. *Microbiology* **154,** 725–735 (2008).
39. Thanky, N. R., Young, D. B. & Robertson, B. D. Unusual features of the cell cycle in mycobacteria: Polar-restricted growth and the snapping-model of cell division. *Tuberculosis* **87,** 231–236 (2007).
40. Swoboda, J. G. *et al.* Discovery of a Small Molecule that Blocks Wall Teichoic Acid Biosynthesis in Staphylococcus aureus. *ACS Chem. Biol.* **4,** 875–883 (2009).
41. Lee, K., Campbell, J., Swoboda, J. G., Cuny, G. D. & Walker, S. Development of improved inhibitors of wall teichoic acid biosynthesis with potent activity against Staphylococcus aureus. *Bioorg. Med. Chem. Lett.* **20,** 1767–1770 (2010).
42. Rombouts, J. A. *et al.* Synthesis, Characterization and Biological Activity of Fluorescently Labeled Bedaquiline Analogues. *RSC Adv.* (2016). doi:10.1039/C6RA22693K
43. Zumla, A., Nahid, P. & Cole, S. T. Advances in the development of new tuberculosis drugs and treatment regimens. *Nat. Rev. Drug Discov.* **12,** 388–404 (2013).
44. Cole, S. T. Inhibiting Mycobacterium tuberculosis within and without. *Phil Trans R Soc B* **371,** 20150506 (2016).
45. Preiss, L. *et al.* Structure of the mycobacterial ATP synthase Fo rotor ring in complex with the anti-TB drug bedaquiline. *Sci. Adv.* **1,** e1500106 (2015).
46. Kocaoglu, O. *et al.* Selective Penicillin-Binding Protein Imaging Probes Reveal Substructure in Bacterial Cell Division. *ACS Chem. Biol.* **7,** 1746–1753 (2012).

47. Kocaoglu, O. & Carlson, E. E. Progress and prospects for small-molecule probes of bacterial imaging. *Nat. Chem. Biol.* **12,** 472–478 (2016).
48. Schneewind, O., Model, P. & Fischetti, V. A. Sorting of protein a to the staphylococcal cell wall. *Cell* **70,** 267–281 (1992).
49. Schneewind, O., Fowler, A. & Faull, K. F. Structure of the cell wall anchor of surface proteins in Staphylococcus aureus. *Science* **268,** 103–106 (1995).
50. Mazmanian, S. K., Liu, G., Ton-That, H. & Schneewind, O. Staphylococcus aureus Sortase, an Enzyme that Anchors Surface Proteins to the Cell Wall. *Science* **285,** 760–763 (1999).
51. Maresso, A. W. & Schneewind, O. Sortase as a Target of Anti-Infective Therapy. *Pharmacol. Rev.* **60,** 128–141 (2008).
52. Nelson, J. W. *et al.* A Biosynthetic Strategy for Re-engineering the Staphylococcus aureus Cell Wall with Non-native Small Molecules. *ACS Chem. Biol.* **5,** 1147–1155 (2010).
53. Maňásková, S. H. *et al.* Synthetic LPETG-Containing Peptide Incorporation in the Staphylococcus aureus Cell-Wall in a Sortase A- and Growth Phase-Dependent Manner. *PLOS ONE* **9,** e89260 (2014).
54. Maňásková, S. H. *et al.* Staphylococcus aureus Sortase A-Mediated Incorporation of Peptides: Effect of Peptide Modification on Incorporation. *PLOS ONE* **11,** e0147401 (2016).
55. Popp, M. W.-L., Antos, J. M. & Ploegh, H. L. in *Current Protocols in Protein Science* (John Wiley & Sons, Inc., 2001).
56. Tsukiji, S. & Nagamune, T. Sortase-Mediated Ligation: A Gift from Gram-Positive Bacteria to Protein Engineering. *ChemBioChem* **10,** 787–798 (2009).
57. Schmohl, L. & Schwarzer, D. Sortase-mediated ligations for the site-specific modification of proteins. *Curr. Opin. Chem. Biol.* **22,** 122–128 (2014).
58. Glasgow, J. E., Salit, M. L. & Cochran, J. R. In Vivo Site-Specific Protein Tagging with Diverse Amines Using an Engineered Sortase Variant. *J. Am. Chem. Soc.* (2016). doi:10.1021/jacs.6b03836
59. Hansenová Maňásková, S. *et al.* Incorporation of a Valine–Leucine–Lysine-Containing Substrate in the Bacterial Cell Wall. *Bioconjug. Chem.* **27,** 2418–2423 (2016).
60. Grammel, M. & Hang, H. C. Chemical reporters for biological discovery. *Nat. Chem. Biol.* **9,** 475–484 (2013).
61. Siegrist, M. S., Swarts, B. M., Fox, D. M., Lim, S. A. & Bertozzi, C. R. Illumination of growth, division and secretion by metabolic labeling of the bacterial cell surface. *FEMS Microbiol. Rev.* **39,** 184–202 (2015).
62. Prescher, J. A. & Bertozzi, C. R. Chemistry in living systems. *Nat. Chem. Biol.* **1,** 13–21 (2005).
63. Sletten, E. M. & Bertozzi, C. R. Bioorthogonal Chemistry: Fishing for Selectivity in a Sea of Functionality. *Angew. Chem. Int. Ed.* **48,** 6974–6998 (2009).
64. Patterson, D. M., Nazarova, L. A. & Prescher, J. A. Finding the Right (Bioorthogonal) Chemistry. *ACS Chem. Biol.* **9,** 592–605 (2014).
65. van Dam, V., Olrichs, N. & Breukink, E. Specific Labeling of Peptidoglycan Precursors as a Tool for Bacterial Cell Wall Studies. *ChemBioChem* **10,** 617–624 (2009).
66. Dube, D. H., Champasa, K. & Wang, B. Chemical tools to discover and target bacterial glycoproteins. *Chem. Commun.* **47,** 87–101 (2010).
67. Foss, M. H., Eun, Y.-J. & Weibel, D. B. Chemical–Biological Studies of Subcellular Organization in Bacteria. *Biochemistry (Mosc.)* **50,** 7719–7734 (2011).

68. Bunschoten, A., Welling, M. M., Termaat, M. F., Sathekge, M. & van Leeuwen, F. W. B. Development and Prospects of Dedicated Tracers for the Molecular Imaging of Bacterial Infections. *Bioconjug. Chem.* **24,** 1971–1989 (2013).
69. Gautam, S., Gniadek, T. J., Kim, T. & Spiegel, D. A. Exterior design: strategies for redecorating the bacterial surface with small molecules. *Trends Biotechnol.* **31,** 258–267 (2013).
70. Pedro, M. A. de, Quintela, J. C., Höltje, J. V. & Schwarz, H. Murein segregation in Escherichia coli. *J. Bacteriol.* **179,** 2823–2834 (1997).
71. Kuru, E. *et al.* In Situ Probing of Newly Synthesized Peptidoglycan in Live Bacteria with Fluorescent D-Amino Acids. *Angew. Chem. Int. Ed.* **51,** 12519–12523 (2012).
72. Kuru, E., Tekkam, S., Hall, E., Brun, Y. V. & Van Nieuwenhze, M. S. Synthesis of fluorescent D-amino acids and their use for probing peptidoglycan synthesis and bacterial growth in situ. *Nat. Protoc.* **10,** 33–52 (2015).
73. Eun, Y.-J. *et al.* Divin: A Small Molecule Inhibitor of Bacterial Divisome Assembly. *J. Am. Chem. Soc.* **135,** 9768–9776 (2013).
74. Tocheva, E. I. *et al.* Peptidoglycan transformations during Bacillus subtilis sporulation. *Mol. Microbiol.* **88,** 673–686 (2013).
75. Schirner, K. *et al.* Lipid-linked cell wall precursors regulate membrane association of bacterial actin MreB. *Nat. Chem. Biol.* **11,** 38–45 (2015).
76. Monteiro, J. M. *et al.* Cell shape dynamics during the staphylococcal cell cycle. *Nat. Commun.* **6,** 8055 (2015).
77. Tsui, H.-C. T. *et al.* Pbp2x localizes separately from Pbp2b and other peptidoglycan synthesis proteins during later stages of cell division of Streptococcus pneumoniae D39. *Mol. Microbiol.* **94,** 21–40 (2014).
78. Pilhofer, M. *et al.* Discovery of chlamydial peptidoglycan reveals bacteria with murein sacculi but without FtsZ. *Nat. Commun.* **4,** 2856 (2013).
79. Siegrist, M. S. *et al.* d-Amino Acid Chemical Reporters Reveal Peptidoglycan Dynamics of an Intracellular Pathogen. *ACS Chem. Biol.* **8,** 500–505 (2013).
80. Siegrist, M. S. *et al.* Host Actin Polymerization Tunes the Cell Division Cycle of an Intracellular Pathogen. *Cell Rep.* **11,** 499–507 (2015).
81. Fimlaid, K. A., Jensen, O., Donnelly, M. L., Siegrist, M. S. & Shen, A. Regulation of Clostridium difficile Spore Formation by the SpoIIQ and SpoIIIA Proteins. *PLOS Genet.* **11,** e1005562 (2015).
82. Shieh, P., Hangauer, M. J. & Bertozzi, C. R. Fluorogenic Azidofluoresceins for Biological Imaging. *J. Am. Chem. Soc.* **134,** 17428–17431 (2012).
83. Shieh, P. & Bertozzi, C. R. Design strategies for bioorthogonal smart probes. *Org. Biomol. Chem.* **12,** 9307–9320 (2014).
84. Shieh, P. *et al.* CalFluors: A Universal Motif for Fluorogenic Azide Probes across the Visible Spectrum. *J. Am. Chem. Soc.* **137,** 7145–7151 (2015).
85. Shieh, P., Siegrist, M. S., Cullen, A. J. & Bertozzi, C. R. Imaging bacterial peptidoglycan with near-infrared fluorogenic azide probes. *Proc. Natl. Acad. Sci.* **111,** 5456–5461 (2014).
86. Pidgeon, S. E. & Pires, M. M. Metabolic remodeling of bacterial surfaces via tetrazine ligations. *Chem. Commun.* **51,** 10330–10333 (2015).
87. Wu, H., Yang, J., Šečkutė, J. & Devaraj, N. K. In Situ Synthesis of Alkenyl Tetrazines for Highly Fluorogenic Bioorthogonal Live-Cell Imaging Probes. *Angew. Chem.* **126,** 5915–5919 (2014).

88. Kaewsapsak, P., Esonu, O. & Dube, D. H. Recruiting the Host's Immune System to Target Helicobacter pylori's Surface Glycans. *ChemBioChem* **14,** 721–726 (2013).
89. Fura, J. M., Sabulski, M. J. & Pires, M. M. d-Amino Acid Mediated Recruitment of Endogenous Antibodies to Bacterial Surfaces. *ACS Chem. Biol.* **9,** 1480–1489 (2014).
90. Lehar, S. M. *et al.* Novel antibody–antibiotic conjugate eliminates intracellular S. aureus. *Nature* **527,** 323–328 (2015).
91. Qiao, Y. *et al.* Detection of Lipid-Linked Peptidoglycan Precursors by Exploiting an Unexpected Transpeptidase Reaction. *J. Am. Chem. Soc.* **136,** 14678–14681 (2014).
92. Lupoli, T. J. *et al.* Transpeptidase-Mediated Incorporation of d-Amino Acids into Bacterial Peptidoglycan. *J. Am. Chem. Soc.* **133,** 10748–10751 (2011).
93. Cava, F., Pedro, M. A. de, Lam, H., Davis, B. M. & Waldor, M. K. Distinct pathways for modification of the bacterial cell wall by non - canonical d - amino acids. *EMBO J.* **30,** 3442–3453 (2011).
94. Sjollema, K. A., Schnell, U., Kuipers, J., Kalicharan, R. & Giepmans, B. N. G. in *Methods in Cell Biology* (ed. Verkade, T. M.-R. and P.) **111,** 157–173 (Academic Press, 2012).
95. de Boer, P., Hoogenboom, J. P. & Giepmans, B. N. G. Correlated light and electron microscopy: ultrastructure lights up! *Nat. Methods* **12,** 503–513 (2015).
96. Ngo, J. T. *et al.* Click-EM for imaging metabolically tagged nonprotein biomolecules. *Nat. Chem. Biol.* **12,** 459–465 (2016).
97. Lebar, M. D. *et al.* Reconstitution of Peptidoglycan Cross-Linking Leads to Improved Fluorescent Probes of Cell Wall Synthesis. *J. Am. Chem. Soc.* **136,** 10874–10877 (2014).
98. Pidgeon, S. E. *et al.* Metabolic Profiling of Bacteria by Unnatural C-terminated D-Amino Acids. *Angew. Chem. Int. Ed.* **54,** 6158–6162 (2015).
99. Fura, J. M. & Pires, M. M. d-amino carboxamide-based recruitment of dinitrophenol antibodies to bacterial surfaces via peptidoglycan remodeling. *Pept. Sci.* **104,** 351–359 (2015).
100. Liechti, G. W. *et al.* A new metabolic cell-wall labelling method reveals peptidoglycan in Chlamydia trachomatis. *Nature* **506,** 507–510 (2014).
101. Fura, J. M., Pidgeon, S. E., Birabaharan, M. & Pires, M. M. Dipeptide-Based Metabolic Labeling of Bacterial Cells for Endogenous Antibody Recruitment. *ACS Infect. Dis.* **2,** 302–309 (2016).
102. Olrichs, N. K. *et al.* A Novel in vivo Cell-Wall Labeling Approach Sheds New Light on Peptidoglycan Synthesis in Escherichia coli. *ChemBioChem* **12,** 1124–1133 (2011).
103. Gautam, S. *et al.* An Activity-Based Probe for Studying Crosslinking in Live Bacteria. *Angew. Chem.* **127,** 10638–10642 (2015).
104. Liu, H., Sadamoto, R., Sears, P. S. & Wong, C.-H. An Efficient Chemoenzymatic Strategy for the Synthesis of Wild-Type and Vancomycin-Resistant Bacterial Cell-Wall Precursors: UDP-N-acetylmuramyl-peptides. *J. Am. Chem. Soc.* **123,** 9916–9917 (2001).
105. Sadamoto, R. *et al.* Cell-Wall Engineering of Living Bacteria. *J. Am. Chem. Soc.* **124,** 9018–9019 (2002).
106. Sadamoto, R., Niikura, K., Monde, K. & Nishimura, S.-I. in (ed. Enzymology, B.-M. in) **362,** 273–286 (Academic Press, 2003).
107. Sadamoto, R. *et al.* Control of Bacteria Adhesion by Cell-Wall Engineering. *J. Am. Chem. Soc.* **126,** 3755–3761 (2004).
108. Sminia, T. J., Zuilhof, H. & Wennekes, T. Getting a grip on glycans: A current overview of the metabolic oligosaccharide engineering toolbox. *Carbohydr. Res.* **435,** 121–141 (2016).

109. Schilling, B. *et al.* Biosynthesis of Sialylated Lipooligosaccharides in Haemophilus ducreyi Is Dependent on Exogenous Sialic Acid and Not Mannosamine. Incorporation Studies Using N-Acylmannosamine Analogues, N-Glycolylneuraminic Acid, and 13C-Labeled N-Acetylneuraminic Acid. *Biochemistry (Mosc.)* **40,** 12666–12677 (2001).
110. Goon, S., Schilling, B., Tullius, M. V., Gibson, B. W. & Bertozzi, C. R. Metabolic incorporation of unnatural sialic acids into Haemophilus ducreyi lipooligosaccharides. *Proc. Natl. Acad. Sci.* **100,** 3089–3094 (2003).
111. Yi, W. *et al.* Remodeling bacterial polysaccharides by metabolic pathway engineering. *Proc. Natl. Acad. Sci.* **106,** 4207–4212 (2009).
112. Dumont, A., Malleron, A., Awwad, M., Dukan, S. & Vauzeilles, B. Click-Mediated Labeling of Bacterial Membranes through Metabolic Modification of the Lipopolysaccharide Inner Core. *Angew. Chem. Int. Ed.* **51,** 3143–3146 (2012).
113. Mas Pons, J. *et al.* Identification of Living Legionella pneumophila Using Species-Specific Metabolic Lipopolysaccharide Labeling. *Angew. Chem. Int. Ed.* **53,** 1275–1278 (2014).
114. Marrakchi, H., Lanéelle, M.-A. & Daffé, M. Mycolic Acids: Structures, Biosynthesis, and Beyond. *Chem. Biol.* **21,** 67–85 (2014).
115. Backus, K. M. *et al.* Uptake of unnatural trehalose analogs as a reporter for Mycobacterium tuberculosis. *Nat. Chem. Biol.* **7,** 228–235 (2011).
116. Swarts, B. M. *et al.* Probing the Mycobacterial Trehalome with Bioorthogonal Chemistry. *J. Am. Chem. Soc.* **134,** 16123–16126 (2012).
117. Kalscheuer, R., Weinrick, B., Veeraraghavan, U., Besra, G. S. & Jacobs, W. R. Trehalose-recycling ABC transporter LpqY-SugA-SugB-SugC is essential for virulence of Mycobacterium tuberculosis. *Proc. Natl. Acad. Sci.* **107,** 21761–21766 (2010).
118. Urbanek, B. L. *et al.* Chemoenzymatic Synthesis of Trehalose Analogues: Rapid Access to Chemical Probes for Investigating Mycobacteria. *ChemBioChem* **15,** 2066–2070 (2014).
119. Foley, H. N., Stewart, J. A., Kavunja, H. W., Rundell, S. R. & Swarts, B. M. Bioorthogonal Chemical Reporters for Selective In Situ Probing of Mycomembrane Components in Mycobacteria. *Angew. Chem. Int. Ed.* **55,** 2053–2057 (2016).
120. Rundell, S. R. *et al.* Deoxyfluoro-D-trehalose (FDTre) analogues as potential PET probes for imaging mycobacterial infection. *Org. Biomol. Chem.* **14,** 8598–8609 (2016).
121. Coltharp, C. & Xiao, J. Superresolution microscopy for microbiology. *Cell. Microbiol.* **14,** 1808–1818 (2012).
122. Gahlmann, A. & Moerner, W. E. Exploring bacterial cell biology with single-molecule tracking and super-resolution imaging. *Nat. Rev. Microbiol.* **12,** 9–22 (2014).
123. Wei, L. *et al.* Live-cell imaging of alkyne-tagged small biomolecules by stimulated Raman scattering. *Nat. Methods* **11,** 410–412 (2014).
124. Krueger, A. T. & Imperiali, B. Fluorescent Amino Acids: Modular Building Blocks for the Assembly of New Tools for Chemical Biology. *ChemBioChem* **14,** 788–799 (2013).
125. Yang, M. *et al.* Converting a Solvatochromic Fluorophore into a Protein-Based pH Indicator for Extreme Acidity. *Angew. Chem. Int. Ed.* **51,** 7674–7679 (2012).
126. Prifti, E. *et al.* A Fluorogenic Probe for SNAP-Tagged Plasma Membrane Proteins Based on the Solvatochromic Molecule Nile Red. *ACS Chem. Biol.* **9,** 606–612 (2014).
127. Kucherak, O. A., Richert, L., Mély, Y. & Klymchenko, A. S. Dipolar 3-methoxychromones as bright and highly solvatochromic fluorescent dyes. *Phys. Chem. Chem. Phys.* **14,** 2292 (2012).

128. Kharkwal, G. B., Sharma, S. K., Huang, Y.-Y., Dai, T. & Hamblin, M. R. Photodynamic therapy for infections: Clinical applications. *Lasers Surg. Med.* **43,** 755–767 (2011).
129. F. Sperandio, F., Huang, Y.-Y. & R. Hamblin, M. Antimicrobial Photodynamic Therapy to Kill Gram-negative Bacteria. *Recent Patents Anti-Infect. Drug Disc.* **8,** 108–120 (2013).
130. Wardlaw, J. L., Sullivan, T. J., Lux, C. N. & Austin, F. W. Photodynamic therapy against common bacteria causing wound and skin infections. *Vet. J.* **192,** 374–377 (2012).
131. Rice, D. R., Gan, H. & Smith, B. D. Bacterial imaging and photodynamic inactivation using zinc(II)-dipicolylamine BODIPY conjugates. *Photochem. Photobiol. Sci.* **14,** 1271–1281 (2015).
132. Jose, J. & Burgess, K. Benzophenoxazine-based fluorescent dyes for labeling biomolecules. *Tetrahedron* **62,** 11021–11037 (2006).
133. Kamkaew, A. *et al.* BODIPY dyes in photodynamic therapy. *Chem. Soc. Rev.* **42,** 77–88 (2013).

Chapter 2

Visualization of Mycobacterial Membrane Dynamics in Live Cells

This work was adapted in part from Rodriguez-Rivera, F. P.; Zhou, X.; Theriot, J. A.; Bertozzi, C. R. Visualization of mycombrane dynamics in live cells.

Chapter 2. Visualization of Mycobacterial Membrane Dynamics in Live Cells

INTRODUCTION

Tuberculosis (TB), the leading cause of death worldwide from a single infectious agent, *Mycobacterium tuberculosis* (Mtb), took 1.5 million lives in 2014 and remains a global public health emergency.[1] Mtb infects host macrophages and its survival within that hostile environment depends on an impermeable cell envelope that protects bacilli from biological stresses.[2,3] Furthermore, the cell envelope has proven to be a formidable physical barrier against many antibiotics that might otherwise be efficacious against Mtb.[4,5] For this reason, TB must be treated with drug combinations that include at least one compound that compromises cell envelope integrity.[6]

The mycobacterial cell envelope comprises inner membrane and peptidoglycan layers that are similar to those of common Gram-negative and –positive organisms, but then diverges considerably in the molecular composition of its outer layers (Figure 1A). Most prominent are mycolic acids that are covalently anchored to arabinogalactan chains.[7] Up to an impressive 90 carbons in length,[8] these lipids constitute the inner leaflet of the mycomembrane and form an interface with an outer leaflet composed of non-covalently associated glycolipids, the most abundant being trehalose monomycolate (TMM) and dimycolate (TDM) (Figure 1B). The result is a functional outer membrane that is unique to Mtb and other members of the suborder Corynebacterineae.

Given its importance in protecting Mtb from drug action, the cell envelope has been the focus of considerable structural work centered on isolating and identifying its various components and visualizing individual layers by electron microscopy (EM).[7] CryoEM studies have added information about the highly organized vertical architecture of the cell envelope at high resolution in a native state.[9,10] Far less is known, however, about the dynamics of the cell envelope components and very few studies have focused on the mycomembrane, the major contributor to the barrier function of the cell envelope. This deficit likely reflects a lack of tools for probing cell envelope metabolites in live cells with subcellular resolution, a problem that chemists have tackled in recent years with the development of new imaging methods.[11] For example, early work using lipophilic fluorophore conjugates that nonspecifically intercalate into the mycomembrane suggested a heterogeneous cell surface landscape.[12,13] Progress toward defining the dynamic properties of Mtb's cell envelope, however, requires more refined methods for imaging its specific components.

Recently, metabolic labeling has proven to be an effective strategy to image trehalose glycolipids in the mycomembrane of live mycobacteria.[14-17] The approach exploits the promiscuity of the antigen 85 complex (Ag85), a family of mycolyltransferases that converts two molecules of TMM to TDM and free trehalose (Figure 1A). In a screen of dozens of trehalose analogs, Backus *et al*. found that the backward reaction can be used to deliver unnatural trehalose derivatives into Mtb's mycomembrane, including a fluorescein conjugate (FITC-Tre, Figure 2A).[14] This observation suggests a means by which mycomembrane dynamics could be directly interrogated by molecular imaging.

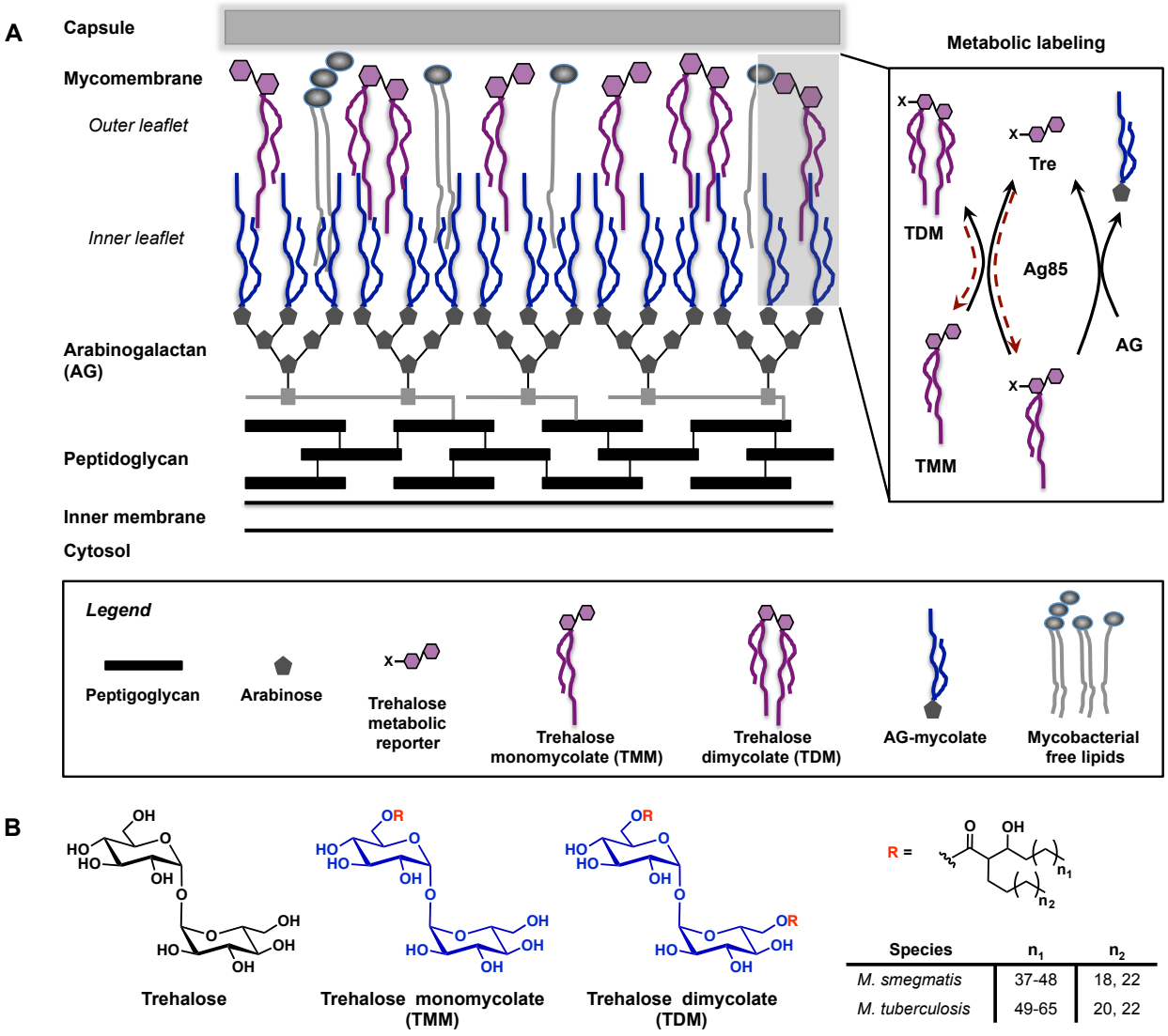

Figure 2.1 Mycobacterial cell envelope and structures of trehalose mycolates. A) Mycobacterial cell envelope components include inner membrane, peptidoglycan, arabinogalactan, mycomembrane, and capsule. Antigen 85 mediates mycolylation of arabinogalactan from TMM donor. Two molecules of TMM are used to generate TDM, thereby releasing one molecule of trehalose. Antigen 85 is predicted to be active in the mycomembrane. Red dashed line depicts metabolic incorporation route for unnatural trehalose reporters. B) Chemical structures for trehalose, trehalose monomycolate and trehalose dimycolate. Number of carbons (n_1, n_2) strictly in linear chains of mycolates are shown for *M. smegmatis* and *M. tuberculosis*. Trehalose monomycolate (TMM), trehalose dimycolate (TDM), trehalose (Tre), Antigen 85 (Ag85), arabinogalactan (AG).

In this chapter, a one-step metabolic labeling strategy was used to track the dynamics of non-covalently associated glycolipids within the mycomembrane. We identified fluorescein-trehalose analogs that are recognized by mycolyltransferases of diverse actinobacterial species,

including members of the *Mycobacteria*, *Corynebacteria*, *Nocardia* and *Rhodococcus* genera. The new probes were utilized to determine the subcellular distribution and dynamics of trehalose mycolates within the mycomembrane of live cells. Using fluorescence recovery after photobleaching (FRAP) experiments, we found a striking disparity in mycomembrane mobilities across species, which partially correlated with mycolic acid structure. Finally, this strategy allowed us to probe the effects of the front-line TB drug ethambutol on mycomembrane dynamics in live *M. smegmatis* cells. Our results highlight that drugs targeting the Mtb cell envelope influence mycomembrane fluidity and this parameter might therefore be considered when evaluating new drug combinations.

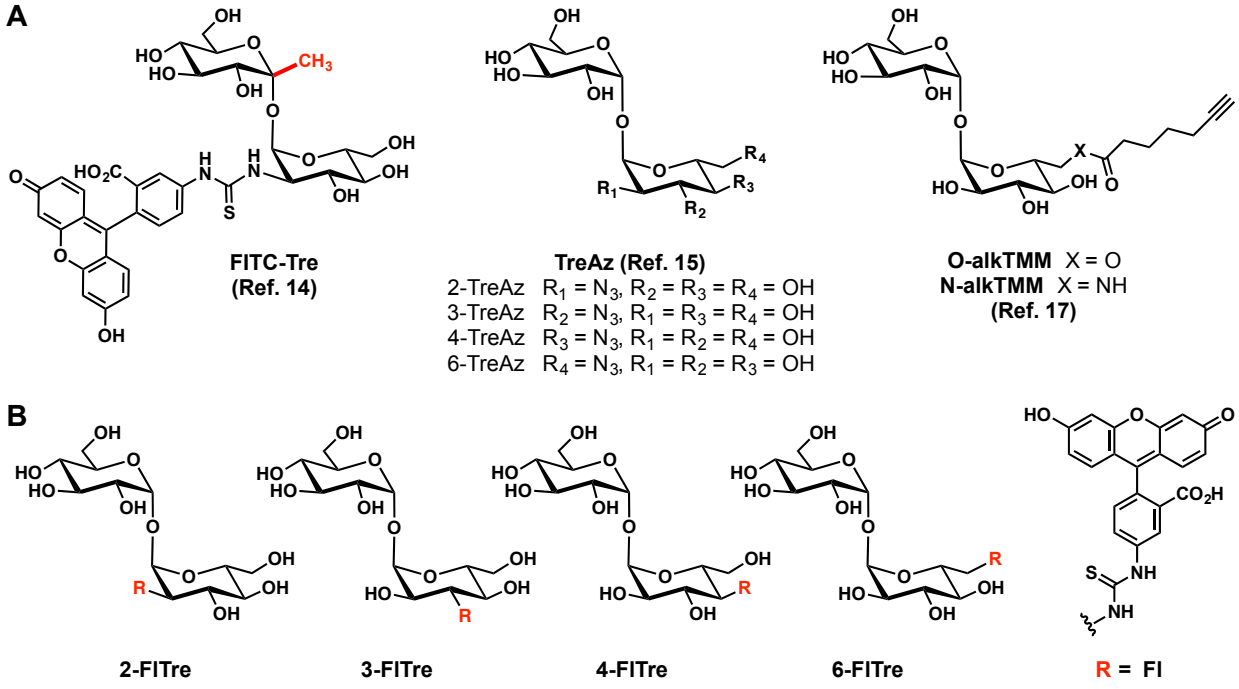

Figure 2.2 Metabolic labeling of trehalose glycolipids with unnatural trehalose reporters. A) Previously reported unnatural trehalose reporters including FITC-Tre, TreAz analogs and alkTMM analogs. B) Library of fluorescein-trehalose analogs (this work). Fluorescein isothiocyanate (FITC), azido-trehalose (TreAz), fluorescein-trehalose (FlTre).

RESULTS AND DISCUSSION

Design and synthesis of new fluorescein-trehalose conjugates

Our first goal was to develop a fluorescent trehalose reagent that efficiently labels trehalose mycolates across many actinobacterial species. A survey of previously reported trehalose analogs revealed them to be unsuitable for various reasons. We found that FITC-Tre (Figure 2A) labeled *Mycobacteria* and *Nocardia* species with poor efficiency, and did not label glycolipids of *Corynebacteria* at a detectable level (*vide infra*). We speculated that the anomeric methyl group (highlighted in red, Figure 2A), a directing group used by Backus *et al.* to form the

α,α-1,1-glycosidic linkage, may compromise the processing of FITC-Tre by the Ag85 complex.

Alternatively, we considered our own previously reported azido-trehalose derivatives (TreAz, Figure 2A), which are metabolically incorporated into trehalose glycolipids by several mycobacterial species and through both cytosolic and extracellular pathways.[15] However, these analogs get transformed to additional classes of trehalose metabolites beyond TMM and TDM, which complicates data interpretation. Moreover, the secondary reagents used to attach fluorescent probes (e.g. cyclooctyne-fluorophore conjugates) have limited access to the mycomembrane and engage in non-specific interactions. Recently, Swarts and coworkers elegantly introduced alkyne-functionalized trehalose analogs (alkTMM, Figure 2A) into the mycomembrane.[17] This approach also requires the use of secondary labeling reagents as well as Cu catalysis that may be cytotoxic.

In light of these issues, we returned to the notion of one-step labeling with a trehalose-fluorophore conjugate and focused on developing reagents with improved metabolic efficiency compared to FITC-Tre. Accordingly, we synthesized the panel of regioisomeric fluorescein-trehalose conjugates (FlTre, shown in Figure 2B), which all possess a native trehalose core structure. The compounds were prepared from the corresponding TreAz analogs by reduction to the amines followed by reaction with fluorescein isothiocyanate (FITC) (Scheme 2.1). Notably, 2-, 3- and 4-FlTre could, if recognized by Ag85, label both TMM and TDM, whereas 6-FlTre can only be metabolized to TMM.

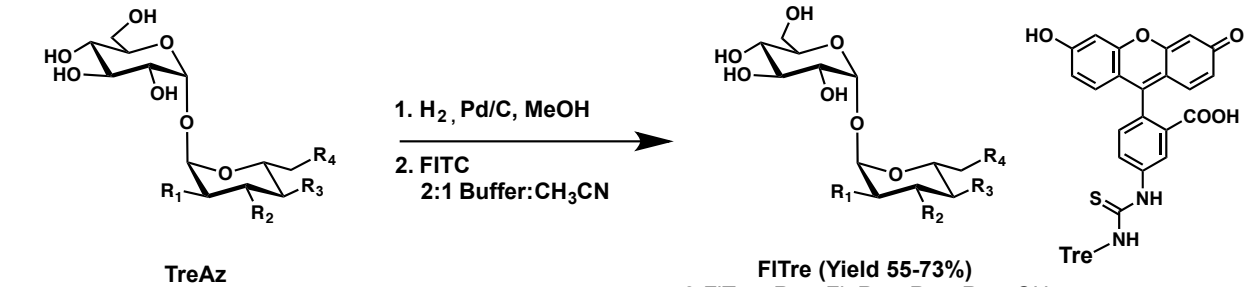

TreAz

2-TreAz $R_1 = N_3$, $R_2 = R_3 = R_4 = OH$
3-TreAz $R_2 = N_3$, $R_1 = R_3 = R_4 = OH$
4-TreAz $R_3 = N_3$, $R_1 = R_2 = R_4 = OH$
6-TreAz $R_4 = N_3$, $R_1 = R_2 = R_3 = OH$

FlTre (Yield 55-73%)

2-FlTre $R_1 = Fl$, $R_2 = R_3 = R_4 = OH$
3-FlTre $R_2 = Fl$, $R_1 = R_3 = R_4 = OH$
4-FlTre $R_3 = Fl$, $R_1 = R_2 = R_4 = OH$
6-FlTre $R_4 = Fl$, $R_1 = R_2 = R_3 = OH$

Scheme 2.1. Synthesis of FlTre library from corresponding TreAz analogs.

Fluorescein-trehalose analogs selectively label trehalose mycolates

We tested the labeling activity of the FlTre analogs as well as FITC-Tre using live cultures of *Mycobacterium smegmatis* and *Corynebacterium glutamicum*, organisms whose cell envelope composition and structure are similar to Mtb's.[18] All FlTre analogs outperformed FITC-Tre in both species as evaluated by flow cytometry (Figure 3A and B). Surprisingly, FITC-Tre was not metabolized at a detectable level by *C. glutamicum*, while 2-FlTre, which only differs from FITC-Tre by lacking an anomeric methyl group, labeled strongly (Figure 3B). This observation illustrates that small perturbations to probe structure can alter, or in this case, completely ablate labeling. The brightest labeling was observed with 6-FlTre, while 2-, 3- and 4-FlTre showed lower labeling in both species.

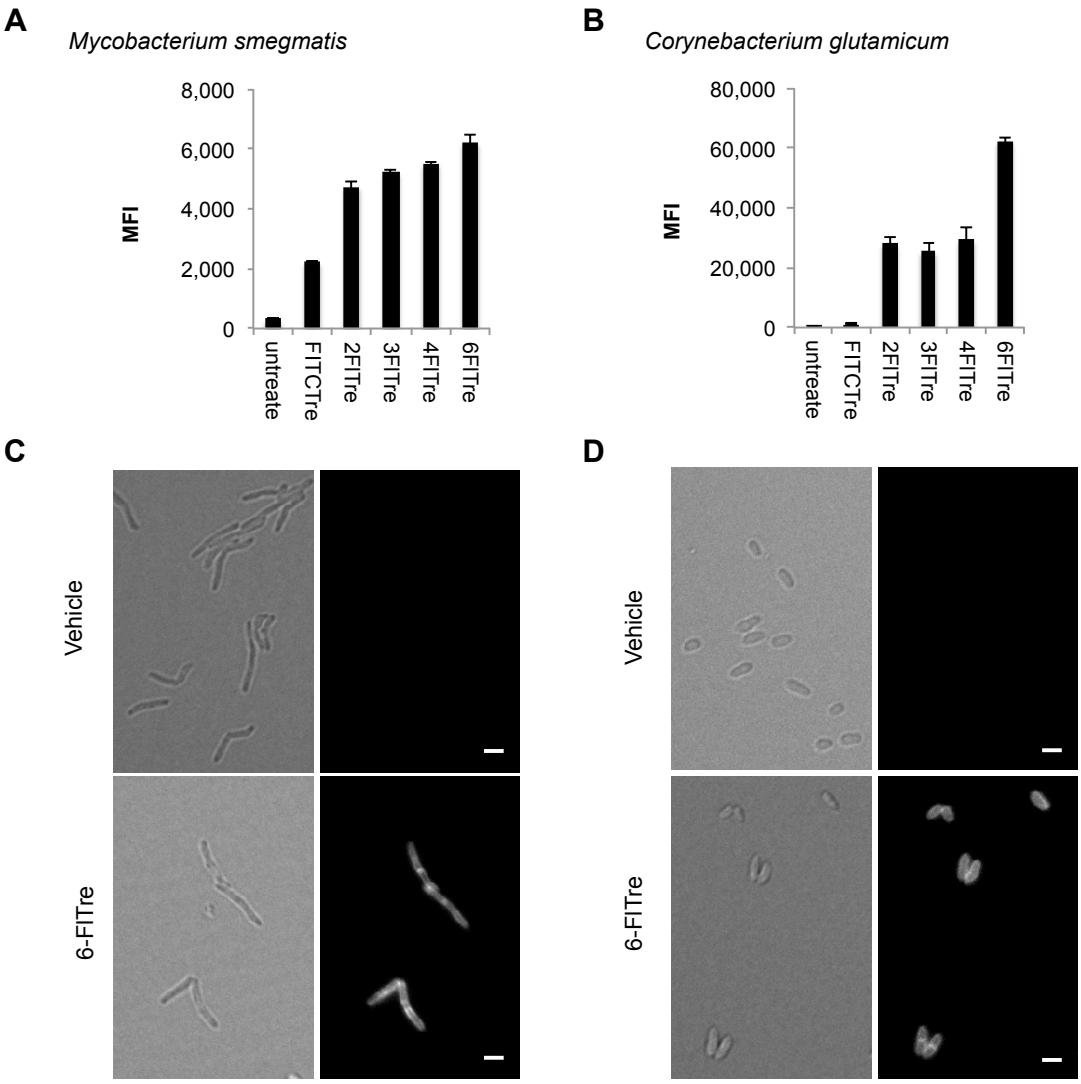

Figure 2.3 Metabolic labeling of actinobacteria with FlTre analogs. Labeling profile of FlTre analogs compared to FITC-Tre with *M. smegmatis* (A) and *C. glutamicum* (B). Bacteria were labeled with 100 μM trehalose analogs or vehicle for several doubling times. Error bars depict standard deviation of three replicate experiments. Results are representative of at least two independent experiments. Mean fluorescence intensity (MFI). Fluorescence microscopy images of *M. smegmatis* (C) and *C. glutamicum* (D) labeled with vehicle or 6-FlTre. Scale bar, 2 μm

In addition, we evaluated the spatial distribution of the fluorescence labeling by microscopy. Gratifyingly, cell envelope labeling was observed for both *M. smegmatis* and *C. glutamicum* after incubation with 100 μM 6-FlTre for several doubling times (Figure 3, C and D, respectively). No defects in cell growth or morphology were observed under these conditions. In particular, *M. smegmatis* showed polar labeling when treated for shorter incubations suggesting incorporation into newly synthesized cell envelope, where biosynthetic enzymes reside (Figure 4A).[19,20] Treatment of bacteria that lack trehalose mycolates, such as canonical

Gram-negative *Escherichia coli* and Gram-positive *Bacillus subtilis*, with 6-FlTre afforded no detectable labeling (Figure 4B and C).

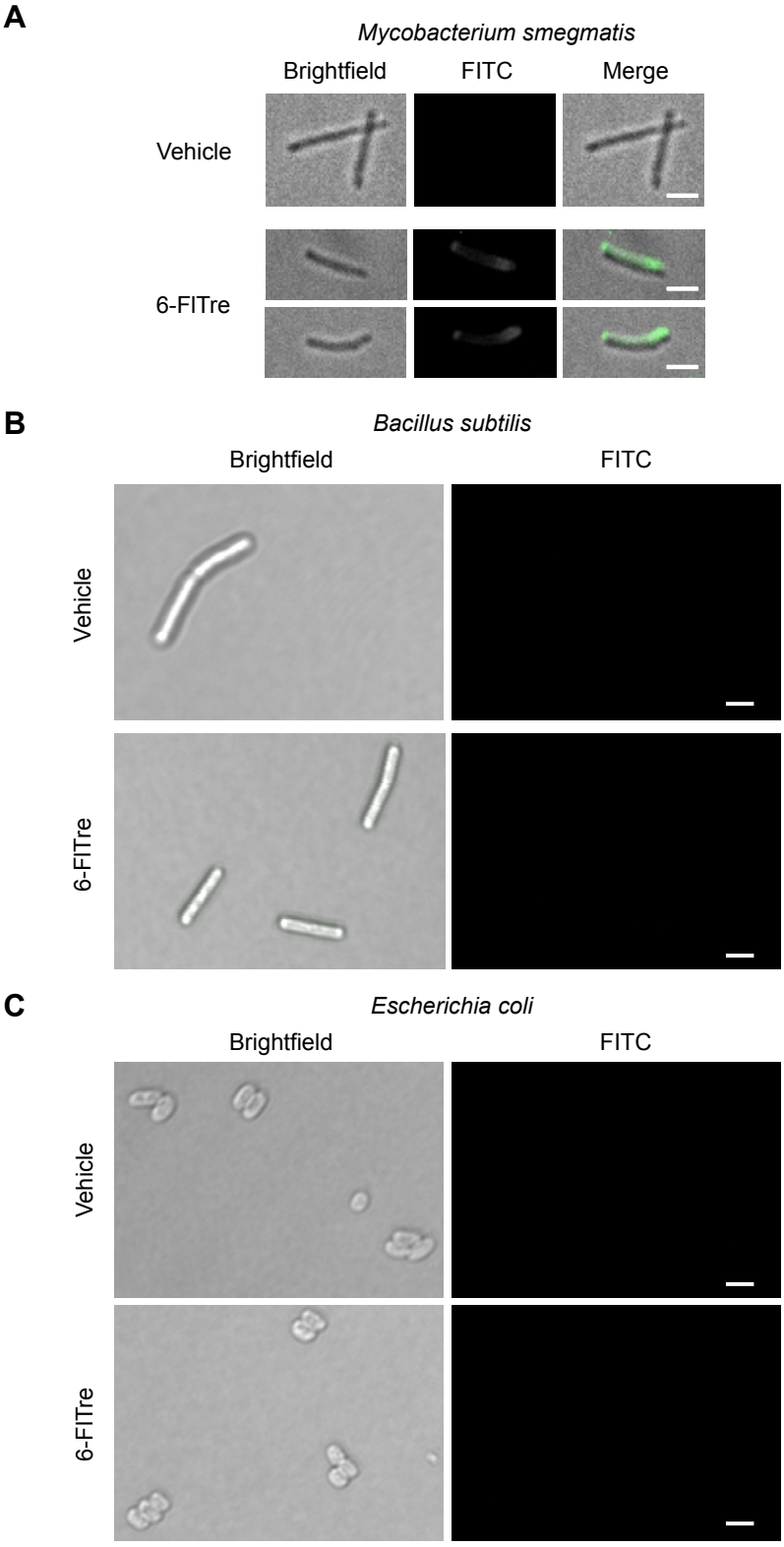

Figure 2.4 6-FlTre labels *M. smegmatis* selectively. A) 5h incubation of 6-FlTre with *M. smegmatis* cells reveals polar labeling. No labeling was observed for *B. subtilis* (B) or *E. coli*. (C) when treated with 6-FlTre for 2 h. Scale bar, 2 μm

To confirm that the FlTre isomers are biosynthetically converted to trehalose mycolates, we assessed whether exogenous trehalose, a native substrate for mycolyltransferases, could compete with reporter labeling. Bacterial cells that were coincubated with 2-, 3-, 4- or 6-FlTre (100 μM) and trehalose (0, 0.5, 5 mM) showed a dose-dependent decrease in metabolic labeling (Figure 5). In addition, we found that ebselen, an inhibitor of Ag85 activity in mycobacteria,[21,22] decreased 2-, 3-, 4- and 6-FlTre labeling in both *M. smegmatis* and *C. glutamicum* (Figure 5). Furthermore, partially purified trehalose glycolipids from 2- or 6-FlTre-labeled *C. glutamicum* were analyzed by mass spectrometry. For both analogs, we observed ions corresponding to the expected fluorescein-conjugated TMM analogs (Figure 6). Finally, total lipids extracted from 6-FlTre labeled *M. smegmatis* cells showed a single fluorescent band by thin layer chromatography (TLC) (Figure 6). Collectively, these data demonstrate that FlTre analogs are biosynthetically converted to trehalose mycolates in live bacterial cells.

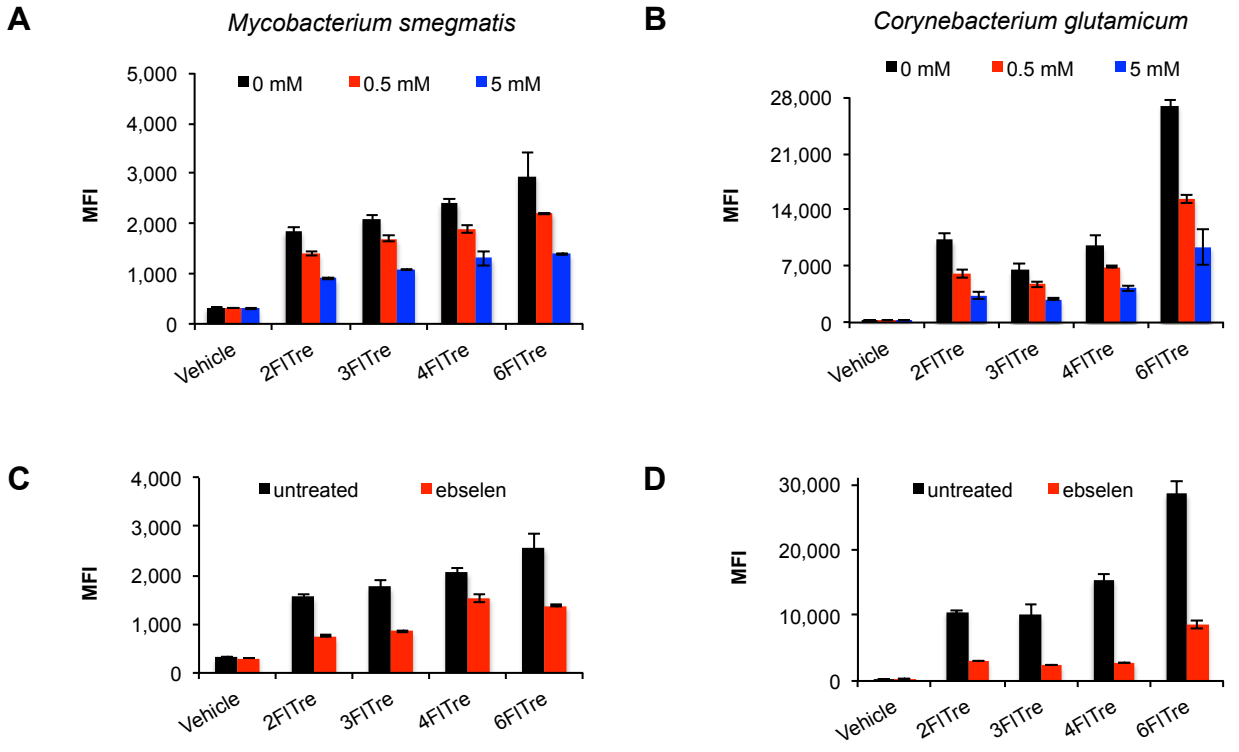

Figure 2.5 FlTre analogs are incorporated via a trehalose and Ag85-mediated pathway. Increasing concentrations of trehalose (0, 0.5, 5.0 mM) outcompetes FlTre labeling in *M. smegmatis* (A) and *C. glutamicum* (B) during bacterial growth. Ebselen (Ag85 inhibitor) treatment prior to FlTre labeling decreases incorporation in *M. smegmatis* (C) and *C. glutamicum* (D). Error bars depict standard deviation of three replicate experiments. Results are representative of at least two independent experiments. Mean fluorescence intensity (MFI).

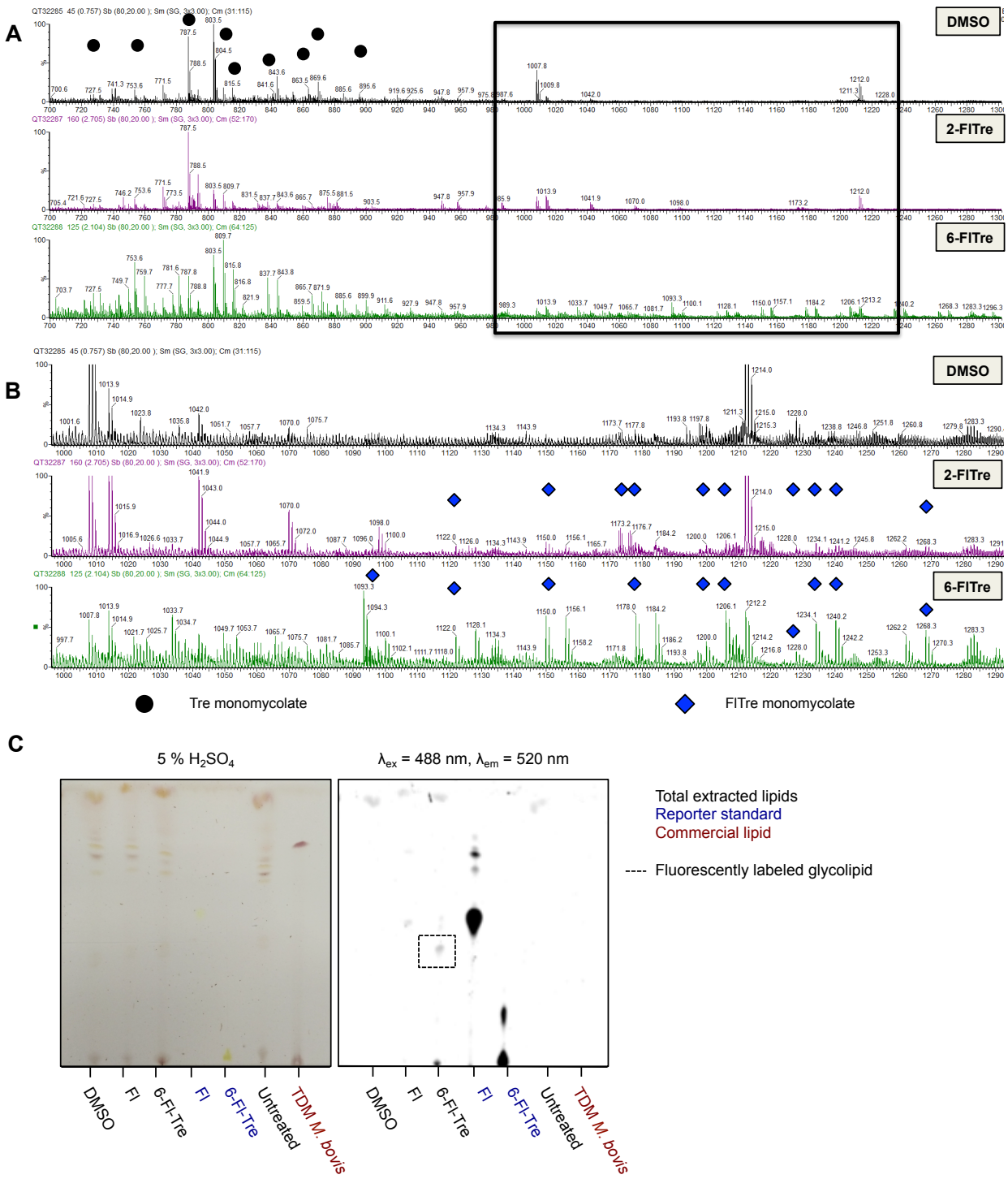

Figure 2.6. Validation of trehalose mycolate labeling in *C. glutamicum* and *M. smegmatis* with FlTre analogs by mass spectrometry and HPTLC. (A) Nano-ESI Q-TOF mass spectra depicting native and FlTre-labeled trehalose monomycolate species in *C. glutamicum*, plotting relative abundance (%) and m/z in *y* and *x*-axis, respectively. (B) Expansion of inset from spectra in A. Black circles and blue diamonds denote native TMM and Fl-TMM, respectively. C) HPTLC analysis of 6-FlTre-labled glycolipids in *M.* smegmatis. Total lipids were extracted from

cultures incubated with DMSO, Fl, and 6-FlTre. Dashed box indicates labeled glycolipid species. Labeled trehalose mycolates in *M. smegmatis* were not detected by mass spectrometry due to low abundance and poor ionization of these neutral lipids. Electrospray ionization (ESI), quadrupole time-of-flight (Q-TOF), high performance thin layer chromatography (HPTLC)

Fluorescein-trehalose analogs report on mycomembrane dynamics in live bacteria

We next sought to investigate the mobility of trehalose glycolipids in the mycomembrane during the course of cell growth. To that end, we performed two-color imaging experiments wherein cells were first labeled with 6-FlTre to visualize trehalose glycolipids, then later marked for newly formed cell wall with a peptidoglycan (PG) reporter, tetramethylrhodamine D-lysine (TDL), which replaces D-alanine residues in the stem peptides.[23] *M. smegmatis* was labeled with 6-FlTre for several generations, washed to remove excess reporter, and chased with TDL for 5 or 20 min (Figure 7A). Fluorescence microscopy revealed that labeled trehalose mycolates were excluded from newly biosynthesized cell wall at the poles during growth, as denoted by minimal overlap with polar labeling of PG. These results suggest that trehalose glycolipids in the mycomembrane remain rather immobile during growth in *M. smegmatis*. Conversely, *C. glutamicum* showed complete redistribution of labeled glycolipids after 6-FlTre had been removed from the growth media for the same time periods (Figure 7B). We were intrigued by the lack of fluidity in the mycomembrane of *M. smegmatis* that did not allow diffusion of labeled trehalose glycolipids to new cell wall regions. Indeed, low fluidity has been predicted based on extremely low permeability of the mycomembrane to lipophilic molecules[24] as well as differential scanning calorimetry (DSC) studies that revealed high temperature phase transitions in *Mycobacteria*.[25-27] Our results provide direct experimental confirmation of this prediction in live cells.

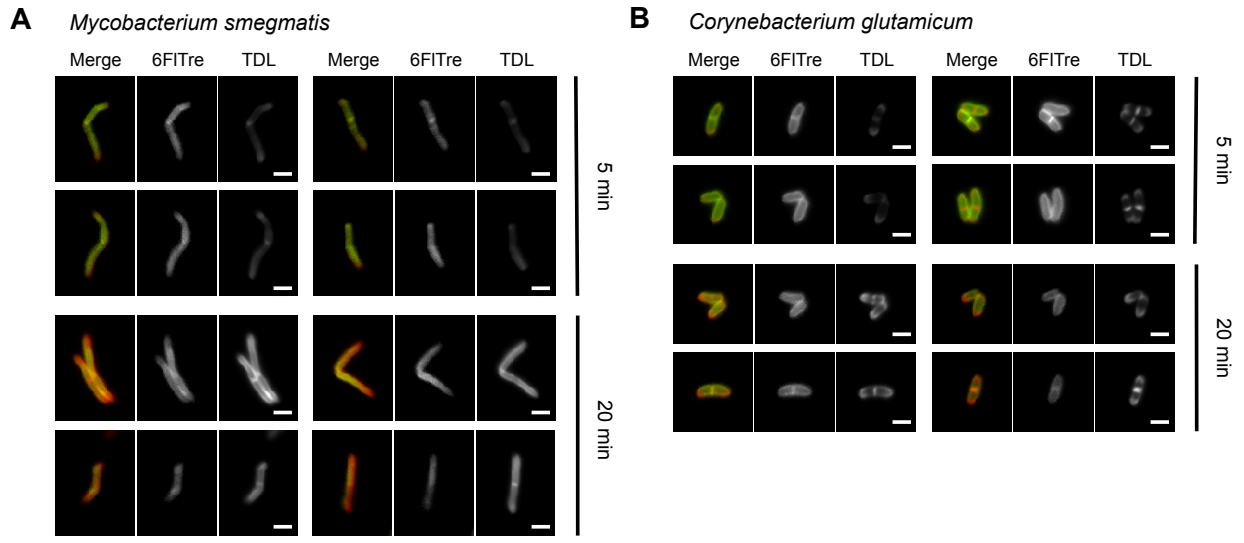

Figure 2.7 FlTre-labeled trehalose glycolipids show species-dependent mobility. A) Pre-labeled *M. smegmatis* glycolipids (6-FlTre, green) are excluded from the poles as depicted by peptidoglycan labeling (TDL, red). B) Pre-labeled *C. glutamicum* glycolipids are highly mobile and redistribute to the entire cell after 6-FlTre has been removed from the growth media. Scale bar, 2 μm

Mycolic acid-producing Actinobacteria have a wide range of mycomembrane fluidities that correlate with mycolic acid chain structure

Fluorescence recovery after photobleaching (FRAP)[28] experiments have been previously used to quantify diffusion dynamics and subcellular organization of membrane components in live bacteria with high temporal and spatial resolution.[29] We therefore applied the FRAP technique to directly elucidate the intrinsic mobility of labeled trehalose glycolipids in mycobacteria. Photobleaching of polar and mid-cellular regions of *M. smegmatis* pre-labeled with 6-FlTre revealed that trehalose glycolipids failed to move after irradiation (Figure 8A), even when monitored up to 10 min. However, under the same experimental conditions, *C. glutamicum* glycolipids diffused through the photobleached area in a few seconds (Figure 8B). The relatively high fluidity observed for the corynebacterial mycomembrane is consistent with previously reported lower temperature phase transitions as measured by DSC.[25] Quantification of fluorescence recovery traces and half-time measurements revealed similar recovery dynamics regardless of the photobleached area of the cell (pole or center) as shown in Figure 8C. Similar glycolipid mobility phenomena were also observed when cells were labeled with 2-FlTre (Figure 9) or trehalose reporters modified with different fluorophores at the same position (Figure 10, characterization of probes is shown in Figure 11), suggesting that the glycolipid dynamics we observed are not significantly altered by probe structure. In addition, for a control experiment, we performed FRAP analysis on cells that were metabolically labeled with D-amino acid reporters bearing the same fluorophores. As expected, the fluorophores integrated into PG were essentially immobile (Figure 12). It is noteworthy to mention that fluorescence recovery of D-ala-Fl labeled cells was similar to FlTre labeled cells. This suggests that the observed recovery might be a result of intrinsic green autofluorescence found in the cytosol of cells.

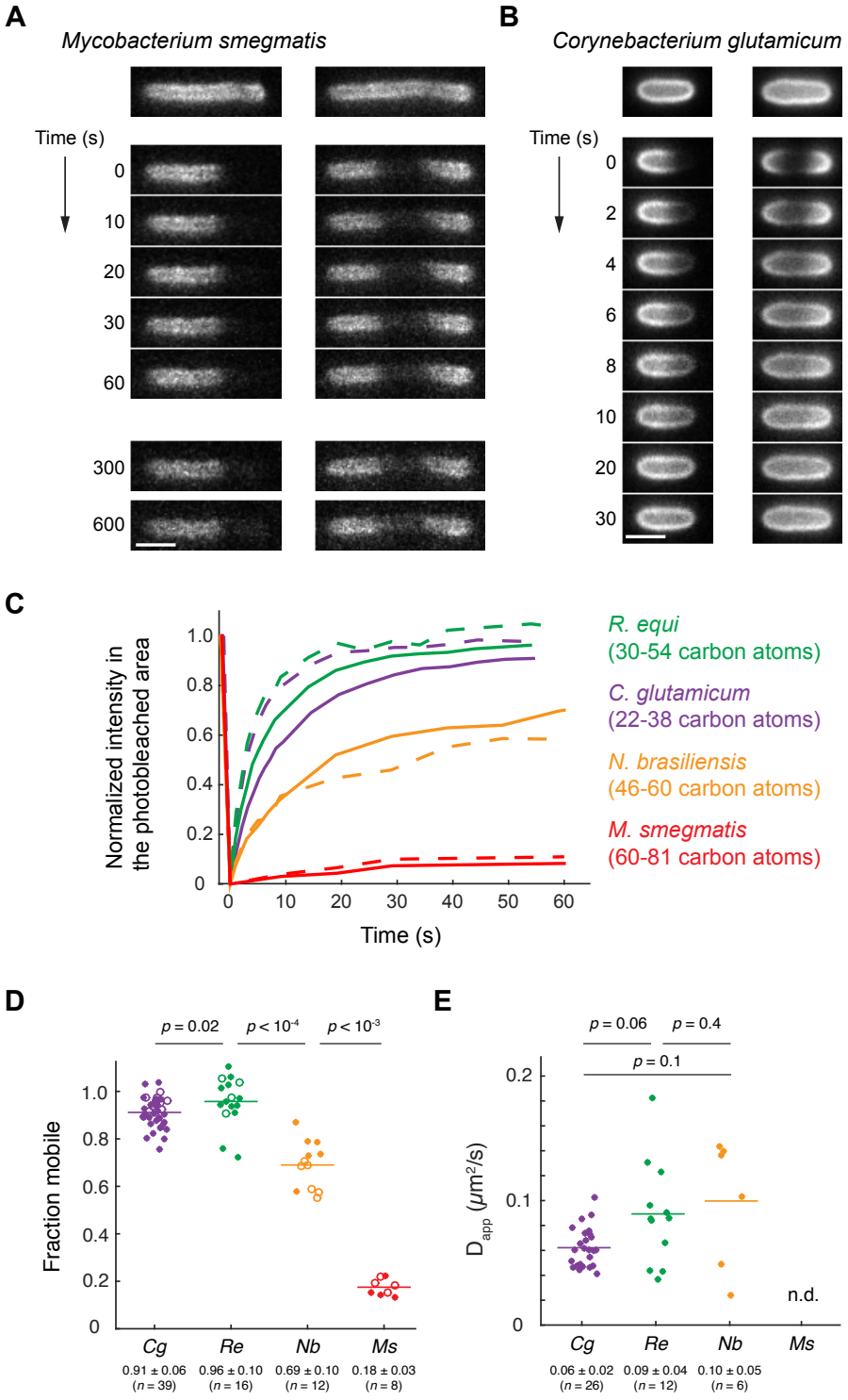

Figure 2.8 Mycobacterial trehalose glycolipids are relatively immobile. A) FRAP experiment of 6-FlTre labeled *M. smegmatis* (A) and *C. glutamicum* (B) after irradiation at the pole (left panel) and center (right panel). Scale bar, 2 μm. C) Fluorescence recovery curves after photobleaching for center and pole regions in 6-FlTre labeled cells across different bacterial species with the corresponding number of carbon atoms in mycolic acid chains. Lines represent

the averaged signal of n ≥ 6 cells, where solid and dotted lines correspond to pole and center regions, respectively. Comparison of fraction mobile (D) and apparent diffusion coefficient (E) extracted from fitting FRAP curves for different actinobacterial species. Filled and open circles correspond to pole and center regions, respectively. Number of cells evaluated and standard deviation are shown for every species. p-values between samples were calculated with a rank sum test. Fluorescence recovery after photobleaching (FRAP), *M. smegmatis* (*Ms*), *C. glutamicum* (*Cg*), *R. equi* (*Re*), *N. brasiliensis* (*Nb*), apparent diffusion coefficient (D_{app}), not determined (n.d.)

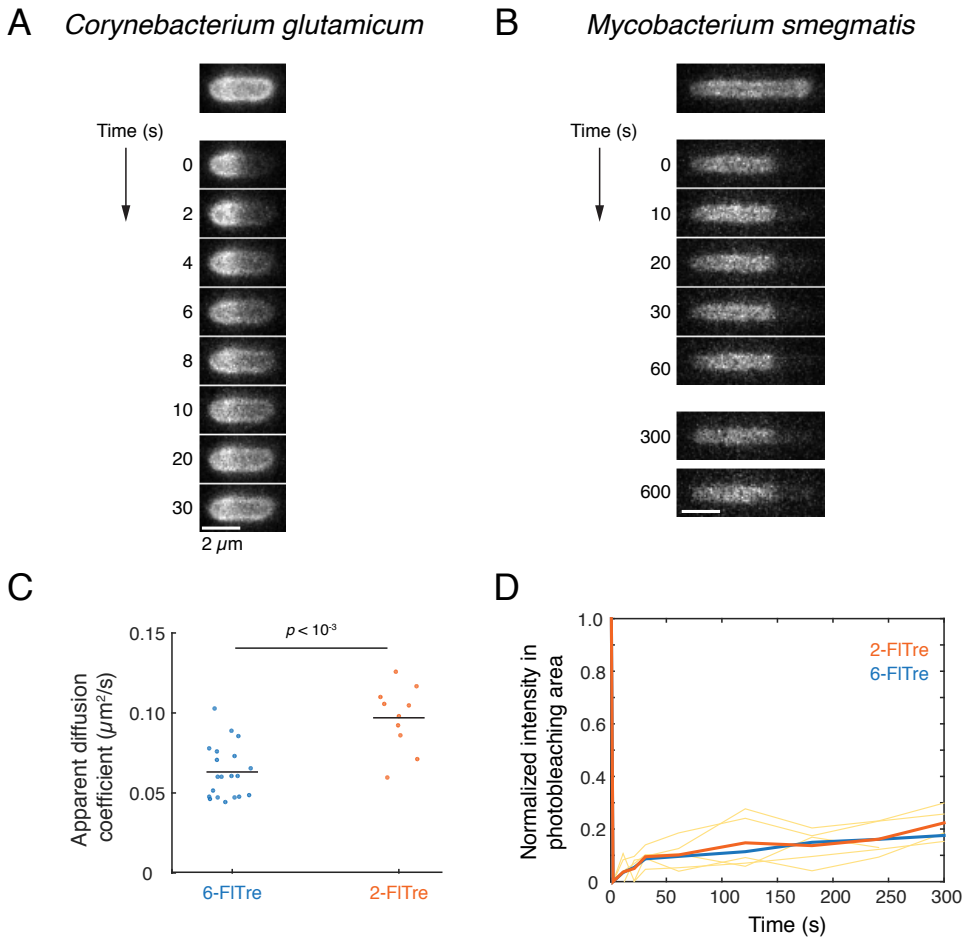

Figure 2.9 Trehalose glycolipids labeled with 2-FlTre show similar mobilities to 6-FlTre analog. Snapshots of FRAP experiments for *C. glutamicum* (A) and *M. smegmatis* (B) labeled with 2-FlTre. (C) Apparent diffusion coefficient of 6-FlTre labeled trehalose glycolipids (0.06 ± 0.02 μm^2/s, n = 20 cells) and 2-FlTre labeled trehalose glycolipids (0.10 ± 0.02 μm^2/s, n = 10 cells) in *C. glutamicum*. p-values between samples were calculated with a rank sum test. (D) Fluorescence recovery traces of the photobleached regions for 6-FlTre (blue, average of the traces in Fig. 5) and 2-FlTre (orange) labeled *M. smegmatis* cells. Thick lines represent the averaged signal. Scale bar, 2 μm

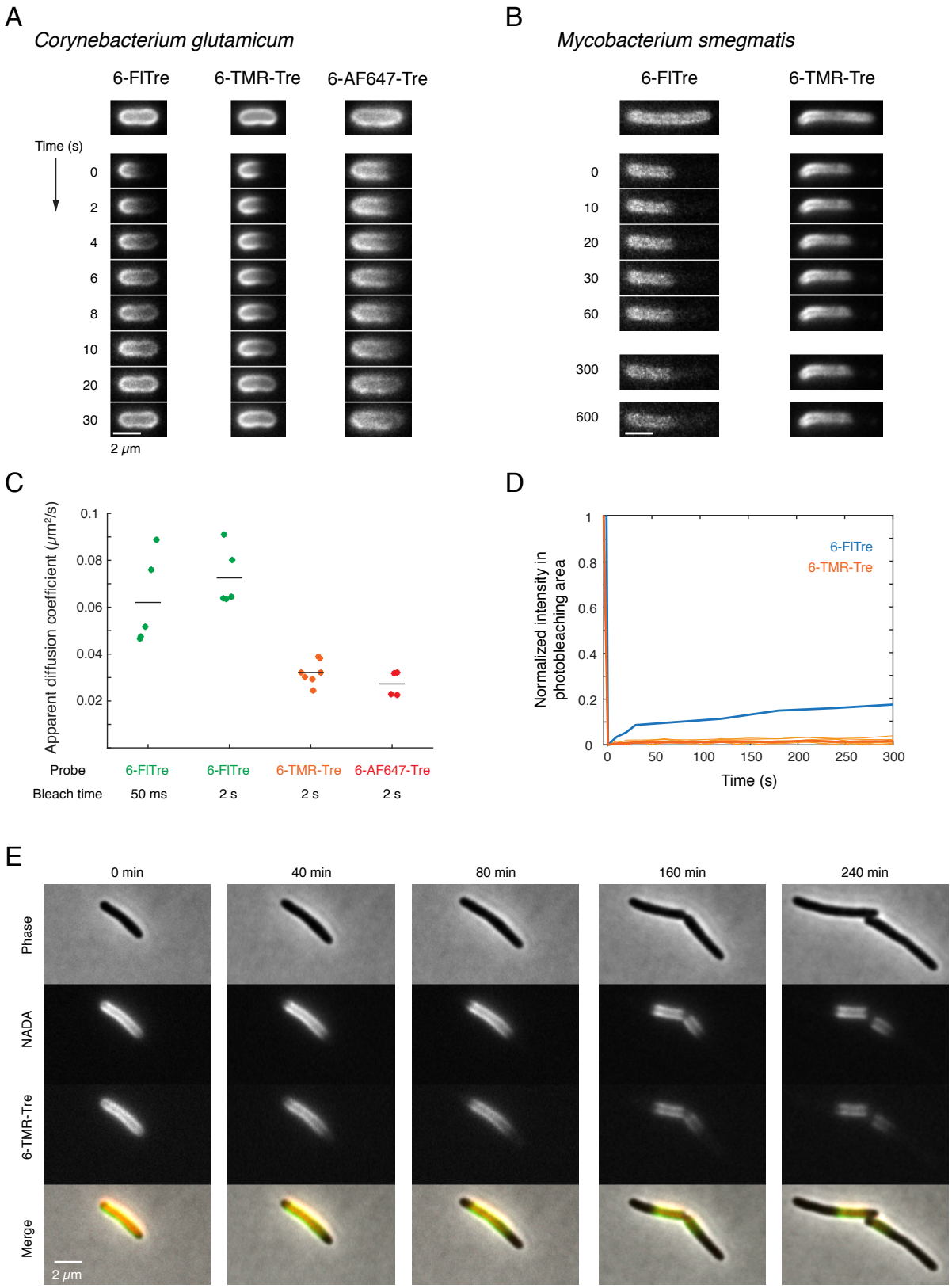
A
Corynebacterium glutamicum
6-FlTre
6-TMR-Tre
6-AF647-Tre
Time (s)
0
2
4
6
8
10
20
30
2 μm
B
Mycobacterium smegmatis
6-FlTre
6-TMR-Tre
0
10
20
30
60
300
600
C
Apparent diffusion coefficient (μm²/s)
0.1
0.08
0.06
0.04
0.02
Probe
6-FlTre
6-FlTre
6-TMR-Tre
6-AF647-Tre
Bleach time
50 ms
2 s
2 s
2 s
D
Normalized intensity in photobleaching area
1
0.8
0.6
0.4
0.2
0
6-FlTre
6-TMR-Tre
0
50
100
150
200
250
300
Time (s)
E
0 min
40 min
80 min
160 min
240 min
Phase
NADA
6-TMR-Tre
Merge
2 μm

Figure 2.10 Comparison of trehalose mycolate mobility when labeled with different fluorophores. Snapshots of FRAP experiments on *C. glutamicum* (A) and *M. smegmatis* (B) labeled with different trehalose probes. 2 s photobleaching with a 405 nm laser was used in all cases. The intensity was normalized in each frame to illustrate the fluorescence distribution pattern within the cell. Scale bars represent 2 μm. (C) Apparent diffusion coefficient of the trehalose glycolipids labeled with different probes in *C. glutamicum* cells. (D) Fluorescence recovery traces of the photobleaching regions for 6-FlTre (blue, average of the traces in Figure 5) and 6-TMR-Tre (orange) labeled *M. smegmatis* cells. Thick lines represent the averaged signal. (E) Time-lapse fluorescence microscopy of dual labeled *M. smegmatis* with NADA, a PG metabolic reporter, and 6-TMR-Tre monitoring growth over 4 h.

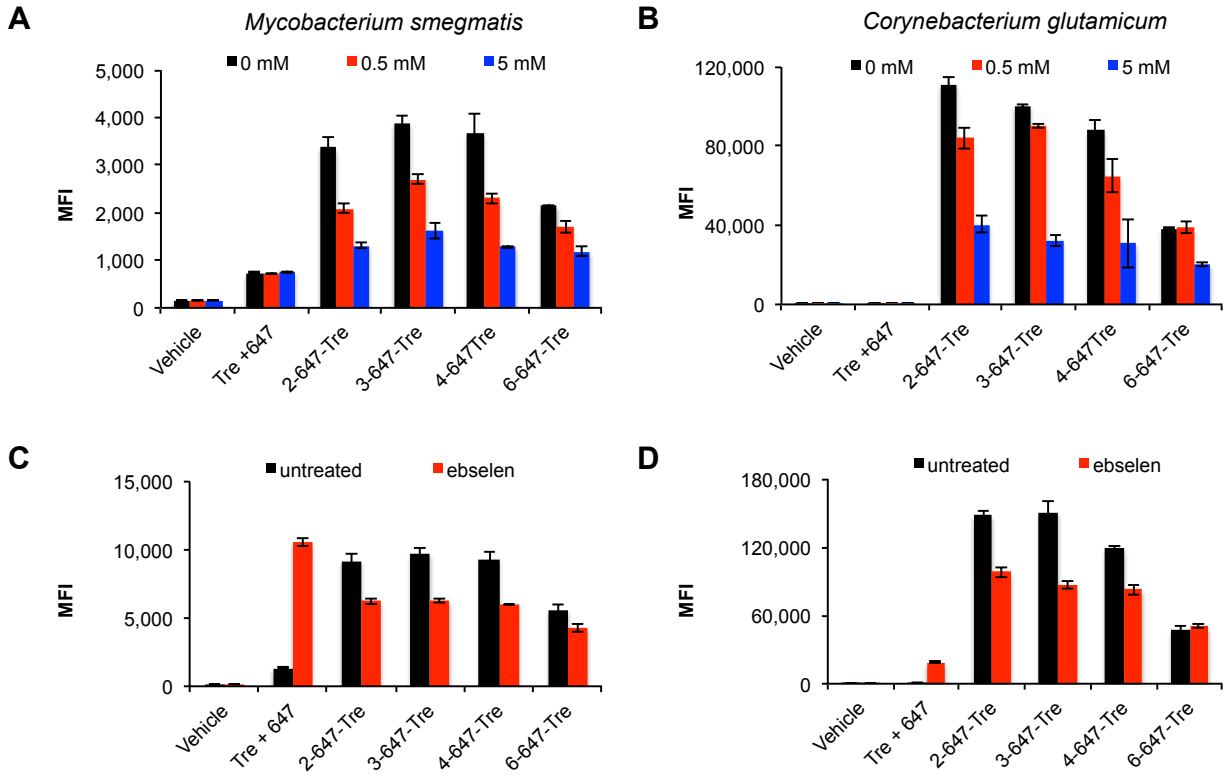

Figure 2.11 647-Tre analogs are incorporated through a mycolyltransferase mediated pathway. Increasing concentrations of trehalose (0, 0.5, 5.0 mM) can outcompete 647-Tre labeling in *M. smegmatis* (A) and *C. glutamicum* (B) during bacterial growth. Ebselen treatment prior to 647-Tre labeling decreases incorporation in *M. smegmatis* (C) and *C. glutamicum* (D). Ebselen compromises membrane integrity, thus allowing free 647 dye to result in higher background. Error bars depict standard deviation of three replicate experiments. Results are representative of at least two independent experiments. Mean fluorescence intensity (MFI)

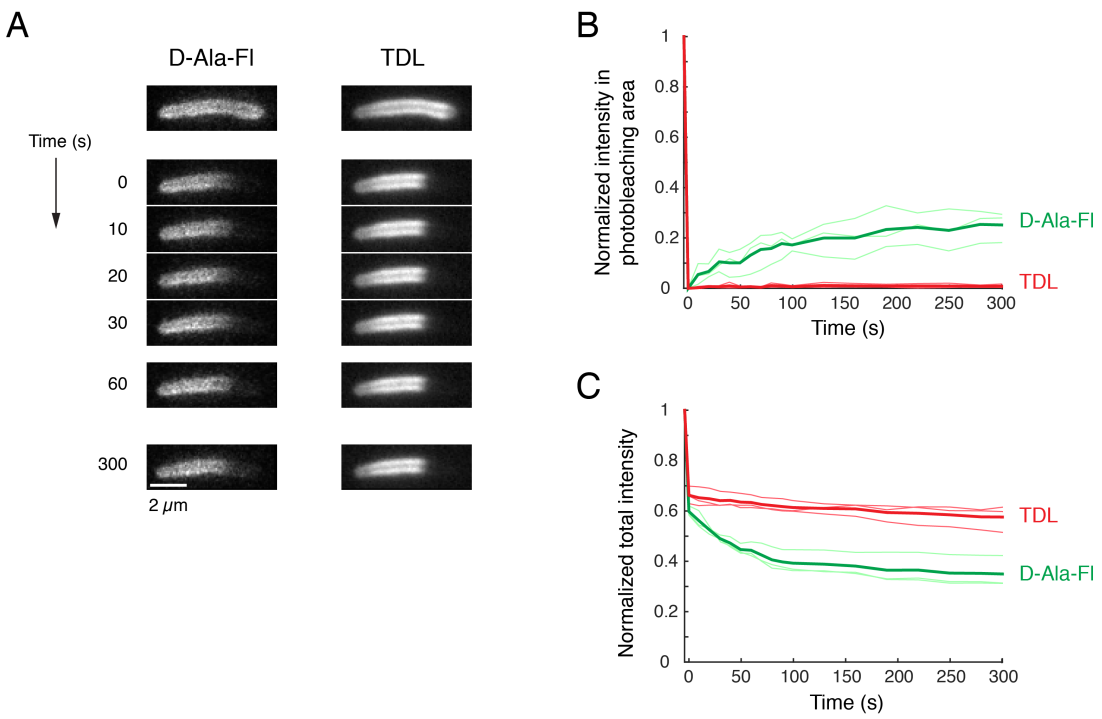

Figure 2.12 FRAP analysis of *M. smegmatis* labeled with fluorescent D-amino acids. (A) Snapshots of FRAP experiments on D-Ala-Fl (left) and TDL (right) labeled *M. smegmatis* cells. (B) Fluorescence recovery traces of the photobleached regions after the normalization. Thick lines represent the averaged signal. The recovery of D-Ala-Fl probe is likely a normalization artifact due to green cell autofluorescence as illustrated in C. (C) Total intensity of the photobleached cells over time highlights poor photostability of fluorescein.

In order to get a more quantitative understanding of observed diffusion phenomena, we modeled recovery data to calculate the apparent diffusion coefficients for labeled trehalose mycolates (Figure 13). A diffusion coefficient of 0.06 ± 0.02 $\mu m^2 s^{-1}$ (n = 20 cells) was obtained for 6-FlTre labeled glycolipids in *C. glutamicum*, while the lack of observable diffusion in *M. smegmatis* limited our ability to model fluorescence recovery. For comparison, lipopolysaccharide (LPS), an abundant glycolipid in the outer membrane of Gram-negative *E. coli*, diffuses slightly slower (0.020 ± 0.009 $\mu m^2 s^{-1}$) as determined by an exogenous rhodamine-LPS conjugate.[30] However, antibody binding of LPS to visualize glycolipid dynamics resulted in much slower diffusion dynamics (2.0 x 10^{-5} $\mu m^2 s^{-1}$),[31] suggesting potential perturbation by antibody detection and underscoring the benefits of directly visualizable glycolipids.

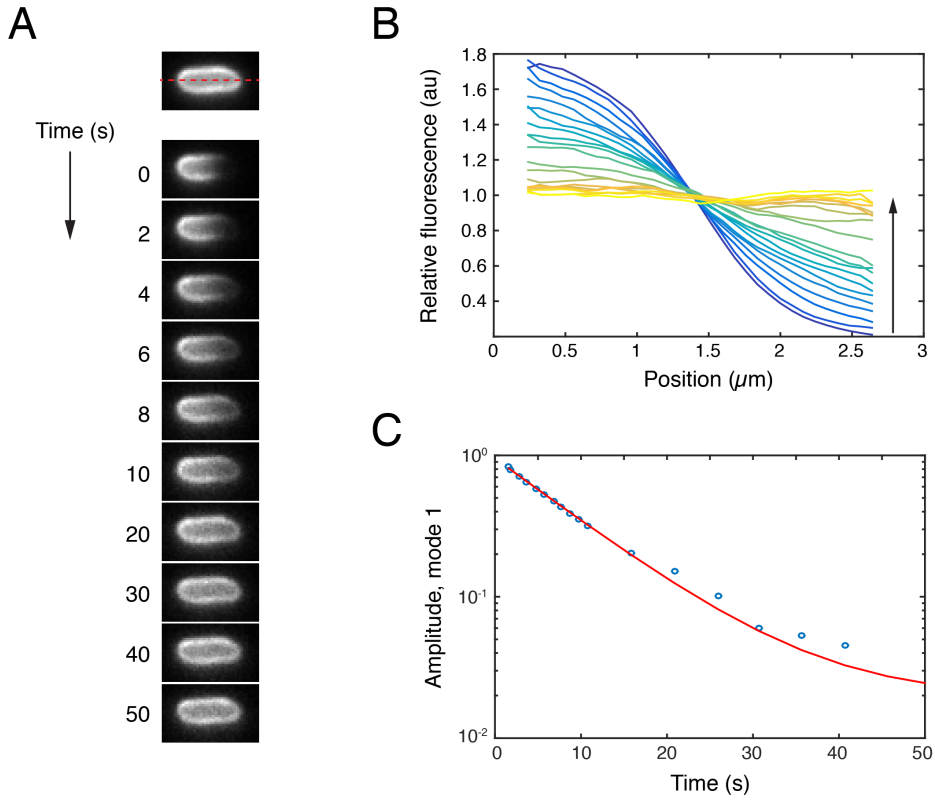

Figure 2.13 Analysis of FRAP experiments to estimate apparent diffusion coefficient. (A) Snapshots of a 6-FlTre labeled *C. glutamicum* cell before and after 50 ms of photobleaching. (B) Normalized fluorescence intensity profiles along the same cell at different times after photobleaching, as indicated by the red dotted line. Arrow indicates increase in time progression. (C) Temporal decay of the first Fourier amplitude with time. Circles correspond to data points while the red line is a fit to the exponential decay function for extraction of the apparent diffusion coefficient (see Methods).

Our results, consistent with DSC studies, suggest a potential correlation between trehalose mycolate structure and the empirically determined fluidity of the mycomembrane. Mycolic acid chain lengths vary significantly between *C. glutamicum* (22-38 carbon atoms)[32] and *M. smegmatis* (60-81 carbon atoms).[33] Fascinated by the dramatic differences in trehalose glycolipid mobility observed for *M. smegmatis* and *C. glutamicum*, we sought to test the correlation of mycomembrane fluidity and mycolic acid length by extending our analysis to other bacterial species. *Rhodococcus* and *Nocardia* species synthesize trehalose glycolipids with intermediate length mycolic acids, ranging from 30-54 and 46-60 carbon atoms, respectively.[34,35] We thus hypothesized that *Rhodococcus equi* and *Nocardia brasiliensis* would show intermediate glycolipid mobilities relative to *C. glutamicum* and *M. smegmatis*. FlTre analogs labeled both species as confirmed by flow cytometry and fluorescence microscopy (Figure 14). FRAP mobility studies revealed similar fluorescence recovery profiles for *R. equi*, and *C. glutamicum*, while *N. brasiliensis* displayed an intermediate recovery profile (Figure 8C and 15). These results were corroborated by evaluation of the relative fraction of mobile trehalose glycolipids, which showed significant differences between bacterial species (Figure 8D). Calculated apparent diffusion coefficients revealed small differences among species that were not statistically significant, suggesting subtle effects on diffusion from minor variations in

mycolic acid chain length. The diffusion coefficient for *M. smegmatis* was not calculated since recovery was not observed after 10 min (Figure 8A). These observations highlighted that mycolic acid chain length is not the only factor that determines mycomembrane fluidity. Indeed, functional groups such as ketones, methoxy, and cyclopropyl groups found in mycobacterial mycolic acids significantly influence membrane fluidity as determined by DSC studies.[25-27] Taken together, our results correlate real-time mycomembrane fluidity to mycolic acid structure across several actinobacteria.

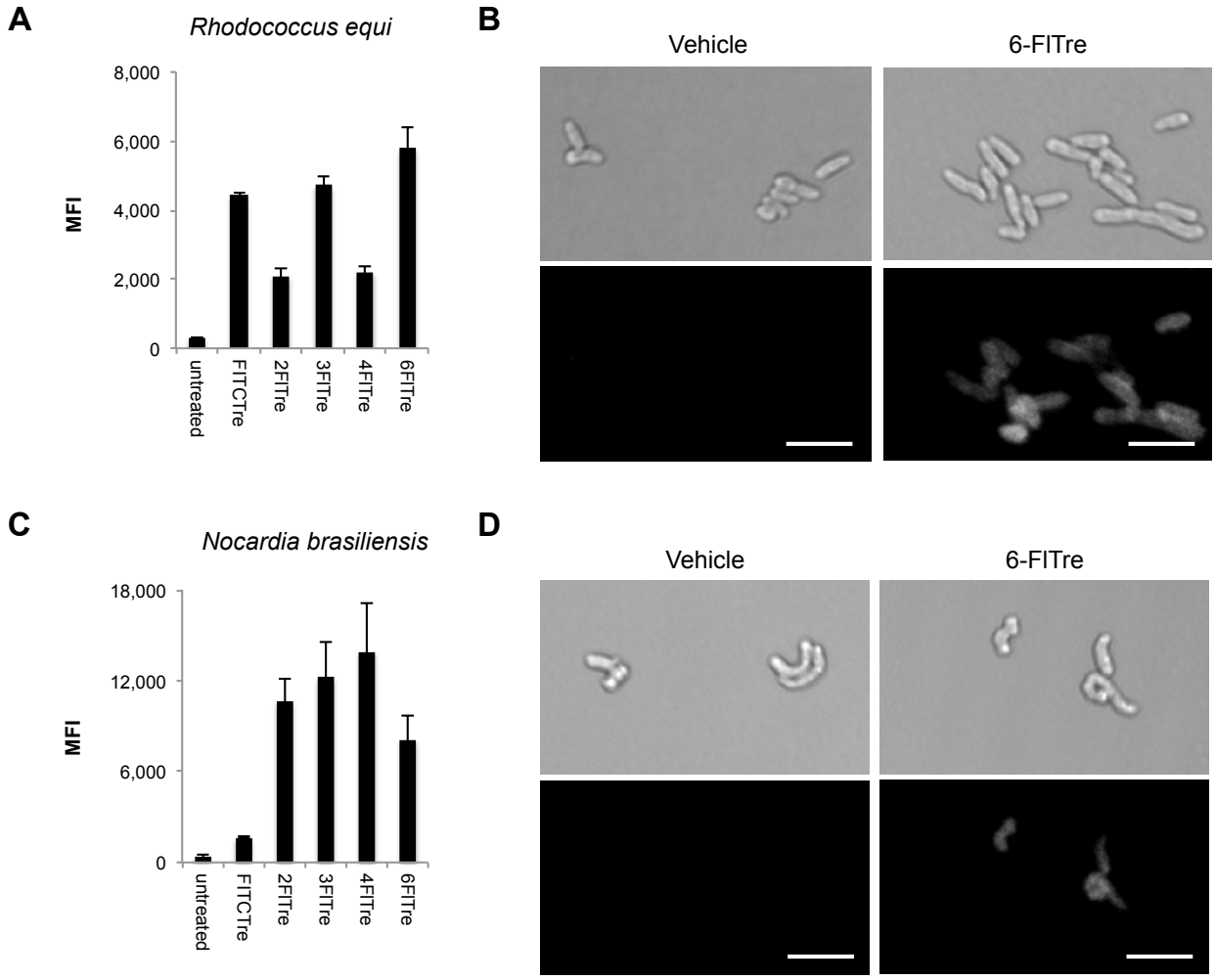

Figure 2.14 Characterization of FlTre-labeling in additional actinobacterial species. FlTre-labeling profile in *R. equi* (A) and *N. brasiliensis* (C) when labeled for several generations. *N. brasiliensis* grows in bacterial aggregates, which might affect labeling efficiency. Error bars depict standard deviation of three replicate experiments. Results are representative of at least two independent experiments. Mean fluorescence intensity (MFI). Spatial distribution for 6-FlTre in *R. equi* (B) and *N. brasiliensis* (D) was determined by fluorescence microscopy. Scale bar, 5 μm

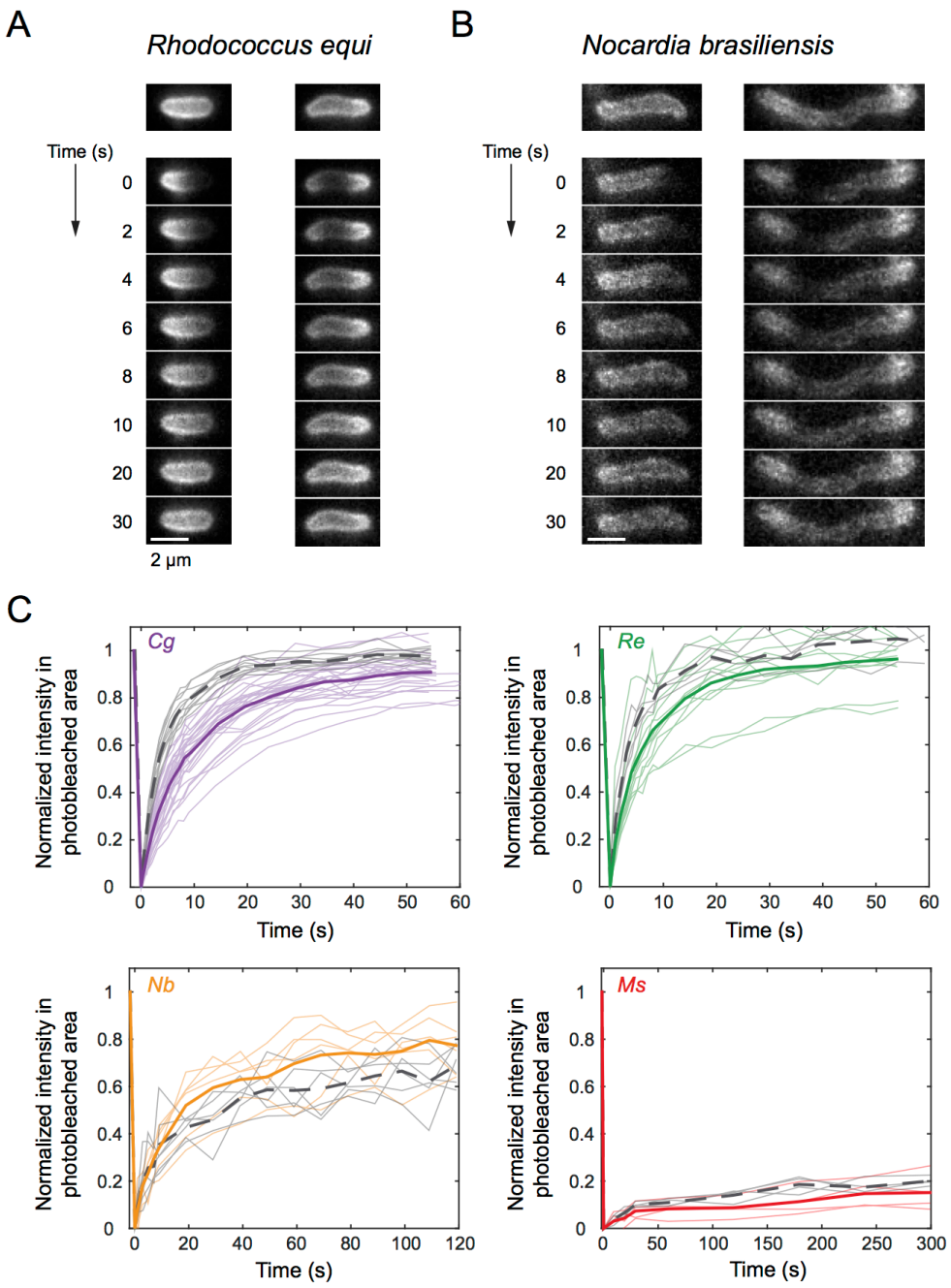

Figure 2.15 FRAP mobility analysis of actinobacterial species in this study. (A) FRAP experiment of 6-FlTre labeled *R. equi* (A) and *N. brasiliensis* (B) when irradiated at the pole (left panel) and center (right panel). Scale bar, 2 µm. C) Fluorescence recovery curves after photobleaching for center and pole regions in 6-FlTre labeled cells across different bacterial species. Thick lines represent the averaged signal of n ≥ 6 cells, where solid colored and gray dotted lines correspond to pole and center regions, respectively. Fluorescence recovery after photobleaching (FRAP), *M. smegmatis* (*Ms*), *C. glutamicum* (*Cg*), *R. equi* (*Re*), *N. brasiliensis* (*Nb*).

Ethambutol treatment alters mycomembrane dynamics

Impermeable membranes within the cell envelope can serve as static barriers against antibiotics and biological stresses. Genes involved in the biosynthesis of the bacterial cell envelope components are essential for growth and division and thus are important antibiotic targets.[7,36] Our imaging strategy could find broad applications in characterizing mycomembrane changes in live cells upon treatment with current front-line TB drugs. For example, ethambutol inhibits the arabinosyl transferase EmbB that installs arabinose residues to growing arabinogalactan chains,[36,37] which results in reduced sites for mycolylation of the inner leaflet of the mycomembrane. We hypothesized that the fluidity of the mycomembrane could be altered by treatment with ethambutol as a result of changing the membrane's physical properties.

We evaluated trehalose mycolate's mobility in 6-FlTre pre-labeled mycobacteria after ethambutol treatment. TDL labeling of peptidoglycan marked new cell wall biosynthesis and also reported on relative growth rates, an indicator of drug toxicity. *M. smegmatis* cells were pre-labeled with 6-FlTre over several generations and treated with different doses of ethambutol for 3 h in the presence of 6-FlTre. Cells were then chased with TDL for 20 min, washed, fixed and examined by fluorescence microscopy. As shown in Figure 16B, untreated cells showed exclusion of pre-labeled glycolipids from new cell wall regions. However, ethambutol treatment at doses as low as 0.5 μg/mL led to redistribution of labeled trehalose mycolates across the entire cell surface, with accumulation of signal at the poles (Figure 16B). *M. smegmatis* has been reported to upregulate trehalose mycolate biosynthesis after exposure to ethambutol,[38,39] which is consistent with higher metabolic labeling observed at the poles during drug treatment. Overall, these results indicate that ethambutol treatment could enhance mycomembrane fluidity. Notably, we observed increased diffusion for sub-minimal inhibitory concentration (MIC) doses (ethambutol's MIC = 1.0 μg/mL for *M. smegmatis*[40]). To confirm ethambutol's effects on mycomembrane dynamics, we examined ethambutol treated cells by FRAP analysis, which revealed increased fraction of mobile glycolipids in a drug dose-dependent manner (Figure 16 C and D, Figure 17). Our results demonstrate that mycomembrane fluidity can be altered with sub-lethal antibiotic concentrations, which could improve permeability and drug accessibility in the context of co-therapy. Modulation of mycomembrane integrity with sublethal concentrations of ethambutol has been previously shown to reverse Mtb resistance to clarithromycin,[41] suggesting reduction of the barrier effectiveness of the mycomembrane. Moreover, increased susceptibility to the beta-lactam cefepime has been observed during cotreatment with ethambutol.[42] Together, these reports provide precedent for potentiating approved therapeutics and repurposing high MIC drugs by co-treatment with low concentrations of ethambutol.[6] Understanding how the permeability of the mycomembrane can be modulated could facilitate the design or access of new therapeutic agents.

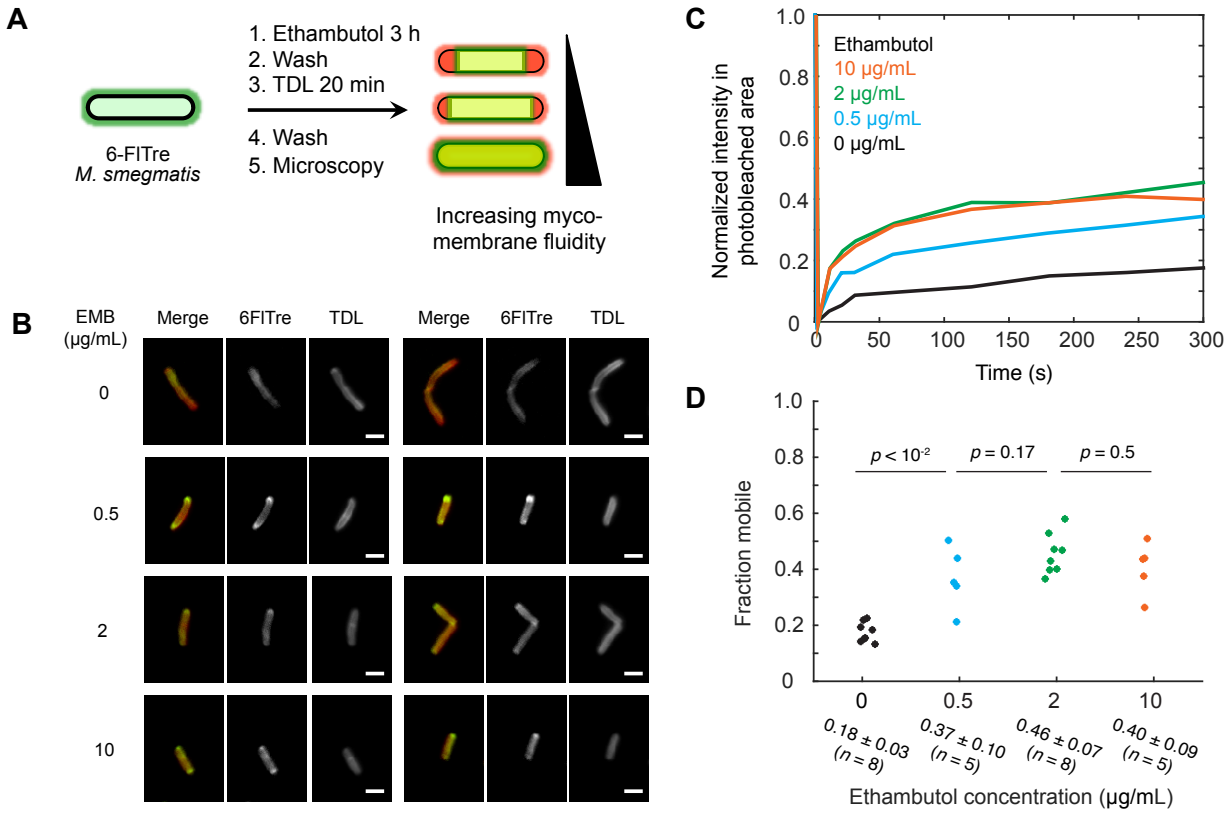

Figure 2.16 FlTre metabolic labeling reports on cell wall dynamics during ethambutol (EMB) treatment. A) Scheme depicting experimental workflow and labeling pattern expected for differential mycomembrane fluidity. *M. smegmatis* was pre-labeled with 6-FlTre, then treated with EMB at different concentrations for 3 h. Cells were washed to remove excess 6-FlTre and chased with TDL in the absence of drug for 20 min. Spatial distribution of labeled glycolipids was evaluated by fluorescence microscopy after fixation (B). Representative cells are shown in each panel. 6-FlTre and TDL signals are shown in green and red channels, respectively, for merged images (left panel). FRAP recovery traces (C) and fraction mobile (D) for cells treated with different concentrations of EMB. Recovery trace lines represent the averaged signal of n ≥ 5 cells. Scale bar, 2 μm

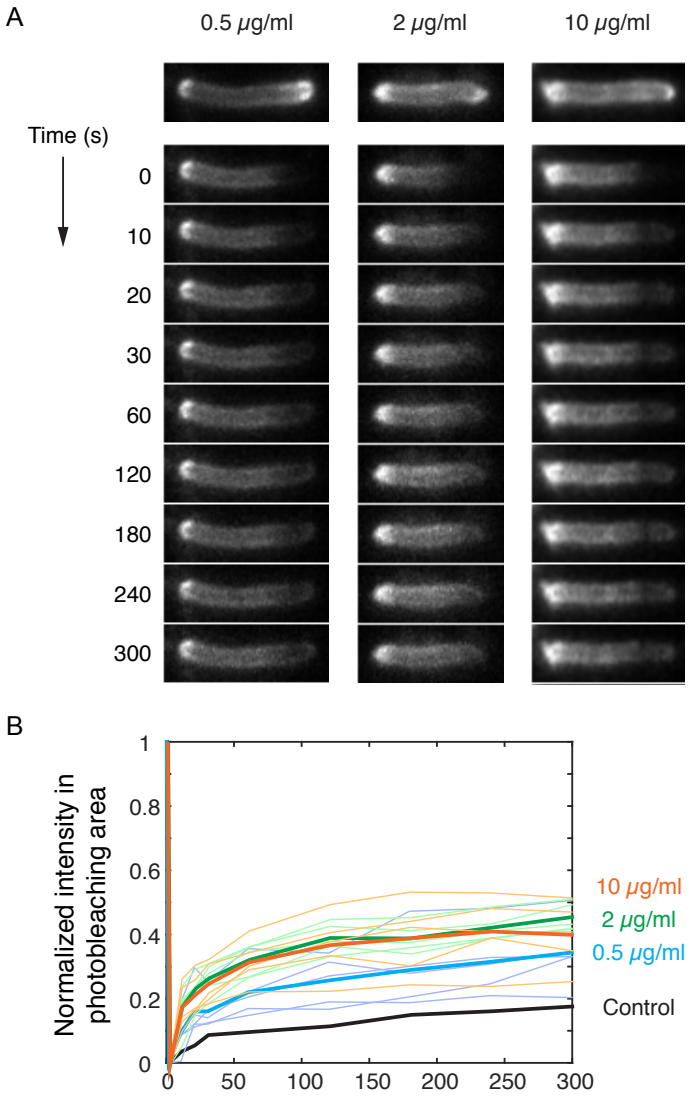

Figure 2.17 FRAP mobility studies of ethambutol treatment in *M. smegmatis*. (A) FRAP experiment of 6-FlTre labeled *M. smegmatis* after ethambutol treatment (0.5, 2, 10 μg/mL) when irradiated at the poles. B) Fluorescence recovery curves after photobleaching for pole regions in 6-FlTre labeled cells at different ethambutol concentrations. Thick lines represent the averaged signal of $n \geq 5$ cells.

CONCLUSION

The complex and unusual cell envelope of mycobacteria has captured the attention of biologists, chemists, and biophysicists alike for almost a century. Tightly packed mycolic acids in the mycomembrane were first predicted by Minnikin to explain the observed impermeability to lipophilic molecules.[24,43] Nikaido and coworkers validated the prediction of a quasi-crystalline arrangement of mycolic acids extending perpendicularly from the cell wall plane by X-ray absorption studies.[44] As well, they elegantly studied the mobility of spin-labeled fatty acids inserted into mycomembranes from *M. chelonae* cell walls.[45] Additionally, DSC studies provided an empirical foundation for our understanding of membrane fluidity in terms of phase transition temperatures across bacterial cell walls.[25] This pioneering series of studies provided insights into mycomembrane dynamics in the context of isolated cell walls preparations, but could not be extended to studies in live cells.

The targeted metabolic labeling strategy used herein enabled direct interrogation of trehalose glycolipids in live cells, in their native context, with minimal perturbation. With this approach, we quantitated trehalose glycolipid mobilities in the mycomembrane and found a relationship between diffusion kinetics and mycolic acid chain length. Notably, the trehalose glycolipids in *Mycobacteria*, which produces the most extravagant mycolic acids, are extremely immobile. We also discovered that ethambutol, a front-line TB drug, enhances mycomembrane fluidity of *M. smegmatis* at sub-lethal doses, an effect that may underlie its synergism with other TB drugs. Consistent with this postulate is a recent report that mycobacteriophage SWU1 gp39 affects *M. smegmatis'* cell envelope permeability and thereby potentiates the efficacy of multiple antibiotics.[46] These observations argue that more high-throughput screens against Mtb should be performed in the presence of a mycomembrane-compromising agent such as ethambutol.[42,47,48] Consequent insights could provide avenues for development of new drug combinations for the treatment of TB.

MATERIALS AND METHODS

General methods for synthesis

Materials and reagents were obtained from commercial sources without further purification unless otherwise noted. Anhydrous solvents were obtained either commercially or from an alumina column solvent purification system. All reactions were carried out in oven-dried glassware under nitrogen unless otherwise noted. Analytical TLC was performed on SiliCycle glass-backed silica gel 60 Å plates (thickness 250 μm) and detected by UV lamp or charring with 5% H_2SO_4 in MeOH. Column chromatography was performed using SiliCycle SiliaFlash P60 silica gel (40-63 μm). ^{1}H NMR spectra were recorded at 400, 500 or 600 MHz with chemical shifts in ppm referenced to solvent peaks. ^{13}C NMR spectra were recorded at 100 or 150 MHz with chemical shifts referenced to solvent peaks. NMR spectra were obtained on Bruker AVQ400, AVB-400, AV-500, or AV-600 instruments. Coupling constants (*J*) are reported in hertz (Hz). High-resolution electrospray ionization mass spectrometry (HR ESI MS) was performed at the UC Berkeley Mass Spectrometry Facility.

Reversed-phase HPLC was performed on a Varian Pro Star system with a Varian UV-Vis detector model 345 (210, 254 nm) on a Dynamax Microsorb C-18 preparative column (21.4 x 250 mm) at a flow rate of 20 mL/min or on an Agilent Eclipse XDB-C18 5μm semi-preparative column (9.4 x 250 mm) at a flow rate of 3 mL/min.

TreAz,[50] BTTAA,[51] TDL,[52] and NADA[52] were synthesized as previously reported.

General procedure for the synthesis of fluorescein-trehalose analogs

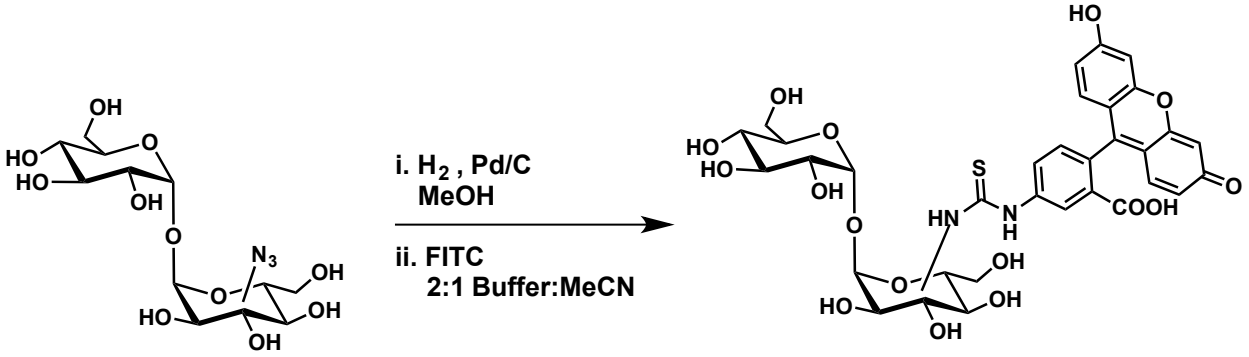

To a stirring solution of TreAz in anhydrous MeOH (at a final concentration of 20 mM) under argon atmosphere, 10% Pd/C was added to reaction mixture. A hydrogen-filled balloon was connected to the reaction flask to replace the argon atmosphere and stirred overnight at room temperature. The reaction mixture was filtered through celite and concentrated by rotary evaporation to afford the amine-trehalose product. Without further purification, amine-trehalose (1 equiv) was subjected to a reaction with fluorescein isothiocyanate (FITC) (1.1 equiv) after dissolving in a ratio of 2:1 75 mM $NaHCO_3$ (pH = 9):MeCN. Reaction mixture was heated to 65

°C and stirred for 3 hours, followed by cooling to room temperature. Reverse-phase HPLC purification using a 5-100% MeCN/H_2O + 0.1%TFA gradient afforded desired product.

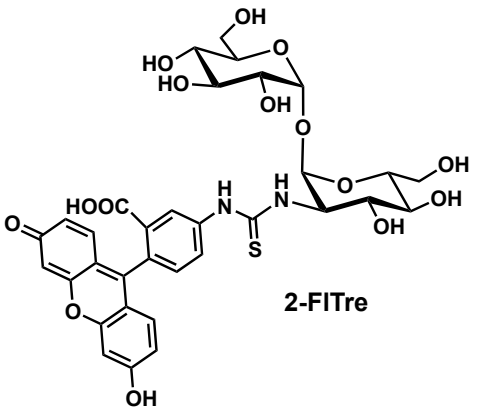

2-FITre

N-(fluorescein-5-yl)-thioureido-2-amino-2-deoxy-α,α-D-trehalose **(2-FITre, 2.1)** (16.5 mg, 61%) was obtained as a yellow-orange solid. R_f = 0.74 (1:2:2 H_2O:EtOAc:IPA, 5% H_2SO_4 in MeOH) ^{1}H NMR (500 MHz, d_6-DMSO): δ 10.16 (s, 1H), 8.09 (s, 1H), 7.65 (s, 1H), 7.00 (d, J = 8.3 Hz, 1H), 6.69 (d, 1H), 6.17 (d, J = 9.0 Hz, 1H), 6.08 (s, 1H), 4.96 (d, J = 3.4 Hz, 1H), 4.92 (s, 2H), 4.94 – 4.84 (m, 1H), 4.44 (s, 1H), 4.19 (s, 1H), 3.88 (s, 1H), 3.83 (s, 1H), 3.68 (d, J = 9.6 Hz, 1H), 3.57 (d, J = 12.7 Hz, 1H), 3.24 (s, 1H), 3.15 (t, J = 9.4 Hz, 1H). ^{13}C NMR (125 MHz, d_6-DMSO): δ 201.12, 181.47, 180.39, 169.82, 158.55, 157.56, 130.86, 110.38, 103.17, 93.78, 93.71, 73.78, 73.23, 72.75, 70.47, 61.35, 57.62. HRMS (ESI): Calculated for $C_{33}H_{35}N_2O_{15}S$ [M-H]$^+$ 731.1753, found 731.1737.

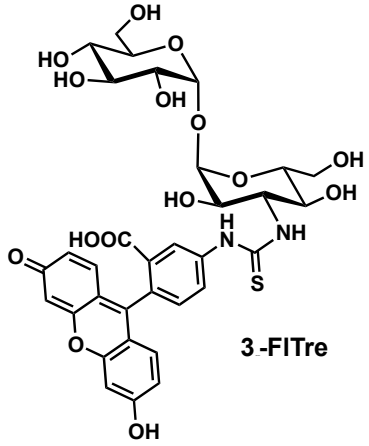

3-FITre

N-(fluorescein-5-yl)-thioureido-3-amino-3-deoxy-α,α-D-trehalose **(3-FITre,2.2)** (11.7 mg, 55%) was obtained as a yellow-orange solid. R_f = 0.71 (1:2:2 H_2O:EtOAc:IPA, 5% H_2SO_4 in MeOH) ^{1}H NMR (500 MHz, d_6-DMSO): δ 10.03 (s, 1H), 8.25 (d, J = 8.2 Hz, 1H), 7.74 (d, J = 8.0 Hz, 1H), 7.19 (d, J = 8.3 Hz, 1H), 6.68 (d, J = 2.3 Hz, 2H), 6.62 (d, J = 8.7 Hz, 2H), 6.57 (dd, J = 8.7, 2.3 Hz, 2H), 4.96 (d, J = 3.5 Hz, 1H), 4.94 (d, J = 3.7 Hz, 1H), 3.70 – 3.45 (m, 10H), 3.27 (s, 1H), 3.15 (t, J = 9.6 Hz, 1H). ^{13}C NMR (125 MHz, d_6-DMSO): δ 193.83, 169.21, 160.19, 152.55, 129.76, 113.29, 110.37, 102.93, 81.64, 73.42, 70.81, 70.47, 61.42, 60.91. HRMS (ESI): Calculated for $C_{33}H_{35}N_2O_{15}S$ [M-H]$^+$ 731.1753, found 731.1754.

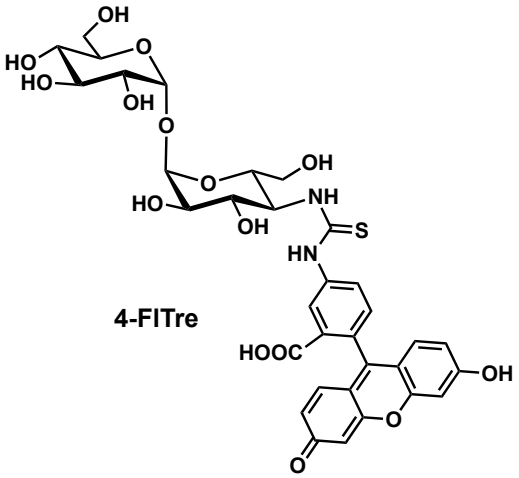

N-(fluorescein-5-yl)-thioureido-4-amino-4-deoxy-α,α-D-trehalose **(4-FITre, 2.3)** (3.5 mg, 73%) was obtained as a yellow-orange solid. R_f = 0.71 (1:2:2 H_2O:EtOAc:IPA, 5% H_2SO_4 in MeOH) ^{1}H NMR (500 MHz, *d*$_6$-DMSO): δ 3.14 – 3.20 (m, 1H), 3.27 (dt, *J* = 13.5, 6.4 Hz, 1H), 3.36 – 3.44 (m, 1H), 3.54 (m, 5H), 3.64 – 3.76 (m, 1H), 3.78 – 3.93 (m, 2H), 3.97 – 4.00 (m, 1H), 4.27 (q, *J* = 9.8 Hz, 1H), 4.89 – 5.00 (m, 2H), 6.56 – 6.67 (m, 5H), 6.70 (d, *J* = 2.1 Hz, 2H), 7.20 (dd, *J* = 14.2, 8.3 Hz, 1H), 7.80 (d, *J* = 8.4 Hz, 1H), 7.88 (d, *J* = 8.5 Hz, 1H), 8.00 (d, *J* = 8.7 Hz, 1H), 8.14 (d, *J* = 9.0 Hz, 1H), 8.23 (s, 1H), 9.76 (s, 1H), 10.04 (s, 1H). ^{13}C NMR (125 MHz, *d*$_6$-DMSO): δ 57.49, 57.63, 61.34, 61.99, 70.84, 71.04, 72.25, 72.42, 72.68, 72.87, 73.25, 73.79, 93.39, 93.59, 93.78, 94.21, 102.86, 103.04, 110.53, 112.37, 113.50, 113.83, 114.66, 116.96, 117.17, 119.26, 125.13, 126.98, 127.34, 129.88, 131.26, 142.06, 142.61, 147.52, 152.72, 158.70, 159.01, 159.31, 159.61, 160.49, 169.18, 180.95, 181.73. HRMS (ESI): Calculated for $C_{33}H_{35}N_2O_{15}S$ $[M-H]^+$ 731.1753, found 731.1769.

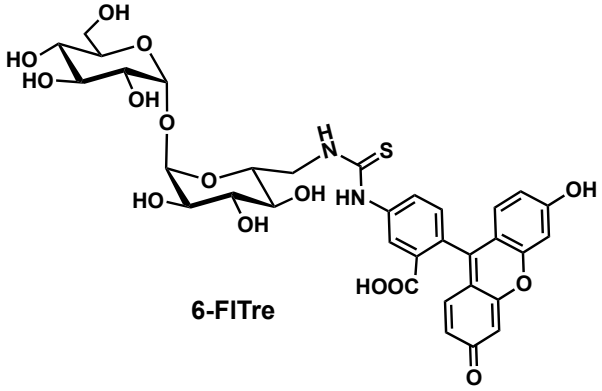

N-(fluorescein-5-yl)-thioureido-6-amino-6-deoxy-α,α-D-trehalose **(6-FITre, 2.4)** (11.7 mg, 70%) was obtained as a yellow-orange solid. R_f = 0.71 (1:2:2 H_2O:EtOAc:IPA, 5% H_2SO_4 in MeOH) ^{1}H NMR (500 MHz, *d*$_6$-DMSO): δ 10.20 (s, 1H), 8.42 (s, 1H), 7.84 – 7.70 (m, 2H), 7.18 (d, *J* = 8.3 Hz, 1H), 6.67 (t, *J* = 1.7 Hz, 2H), 6.62 – 6.54 (m, 4H), 4.97 (d, *J* = 3.5 Hz, 1H), 4.95 (d, *J* = 3.5 Hz, 1H), 3.96 – 3.89 (m, 2H), 3.70 – 3.66 (m, 1H), 3.57 (p, *J* = 8.9, 8.2 Hz, 4H), 3.51 – 3.46 (m, 2H), 3.33 (dd, *J* = 9.5, 3.7 Hz, 1H), 3.26 (dd, *J* = 9.6, 3.6 Hz, 1H), 3.14 (t, *J* = 9.4 Hz, 1H), 3.09 (t, *J* = 9.2 Hz, 1H). ^{13}C NMR (125 MHz, *d*$_6$-DMSO): δ 181.21, 169.26, 160.19, 152.56, 129.77, 127.12, 113.32, 110.41, 102.91, 94.27, 94.18, 73.50, 73.32, 73.20, 72.27, 72.17,

70.74, 70.47, 61.46. HRMS (ESI): Calculated for $C_{33}H_{35}N_2O_{15}S$ $[M-H]^+$ 731.1753, found 731.1745.

Bacterial strains, media, and reagents

Bacterial strains used in this work include *Corynebacterium glutamicum* 534 (ATCC 13032) and *Mycobacterium smegmatis* mc^2155 (ATCC 700084). *C. glutamicum* was cultured in brain heart infusion (BHI) media at 30 ^oC. *M. smegmatis* was cultured in Middlebrook 7H9 media supplemented with 10% ADC (albumin, dextrose, catalase), 0.5% glycerol, and 0.05% tween 80 at 37 ^oC. *Escherichia coli* K12 MG1655 and *Bacillus subtilis* 168 were cultured in Luria broth (LB) at 37 ^oC. *Rhodococcus equi* (ATCC 6939) was cultured at 37 ^oC in BHI. *Nocardia brasiliensis* (ATCC 19296) was cultured at 37 ^oC in 1% glucose, 0.5% yeast extract, 0.5% peptone, and 0.05% tween 80 to minimize bacterial aggregates. All strains were obtained from the American Type Culture Collection (ATCC).

Stock solutions of FlTre analogs were prepared at 10 mM in DMSO and stored at -20 ^oC. Cu-click trehalose-fluorophore analogs at 1.28 mM (see general synthetic procedures) were stored at -20 ^oC. Other reagent stocks include ethambutol (Sigma Aldrich, 4 mg/mL in H_2O, stored at 4 ^oC), ebselen (Cayman Chemical, 2 mg/mL in EtOH, stored at -20 ^oC), FITC-Tre (Kerafast, 10 mM in DMSO, stored at -20 ^oC), Fluorescein-N_3 (Lumiprobe, 10 mM in DMSO, stored at -20 ^oC), D-propargyl glycine or alkDala (Acros, 1 M in H_2O, stored at -20 ^oC). Stock solution of TDL was prepared at 25 mM in DMSO and stored at -20 ^oC.

General procedure for the preparation of AF647-trehalose and TAMRA-trehalose analogs

Cu-click reactions were performed as previously described.[53] TreAz analogs were dissolved at 25 mM in doubly distilled water and filtered through 0.2 μm membrane. Stock solutions of BTTAA and $CuSO_4$ at 50 mM, in DMSO and water, respectively, and 10 mM alkyne-AF647 or alkyne-TAMRA (Invitrogen) in DMSO were prepared and stored at -20 ^oC. A 100 mM sodium abscorbate was freshly prepared prior to CuCAAC reaction. Cu-click cocktail was prepared by mixing 0.5 μL 50 mM BTTAA, 3 μL 50 mM $CuSO_4$, 1 μL 25 mM TreAz analog, 12.5 μL 100 mM sodium abscorbate, and 2.5 μL 10 mM alkyne-AF647 or alkyne-TAMRA. Reaction was allowed to proceed at room temperature with rapid mixing for 30 min. Cu-clicked products at a final concentration of 1.28 mM were used immediately for cell labeling experiments or stored at -20 ^oC.

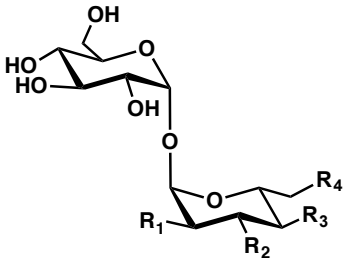

AF647-Tre

2-AF647-Tre R_1 = AF647, R_2 = R_3 = R_4 = OH
3-AF647-Tre R_2 = AF647, R_1 = R_3 = R_4 = OH
4-AF647-Tre R_3 = AF647, R_1 = R_2 = R_4 = OH
6-AF647-Tre R_4 = AF647, R_1 = R_2 = R_3 = OH

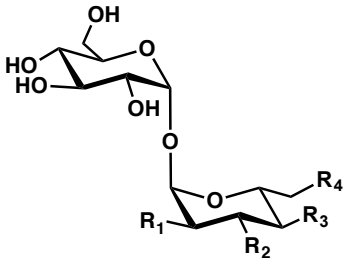

TAMRA-Tre

2-TAMRA-Tre R_1 = TAMRA, R_2 = R_3 = R_4 = OH
3-TAMRA-Tre R_2 = TAMRA, R_1 = R_3 = R_4 = OH
4-TAMRA-Tre R_3 = TAMRA, R_1 = R_2 = R_4 = OH
6-TAMRA-Tre R_4 = TAMRA, R_1 = R_2 = R_3 = OH

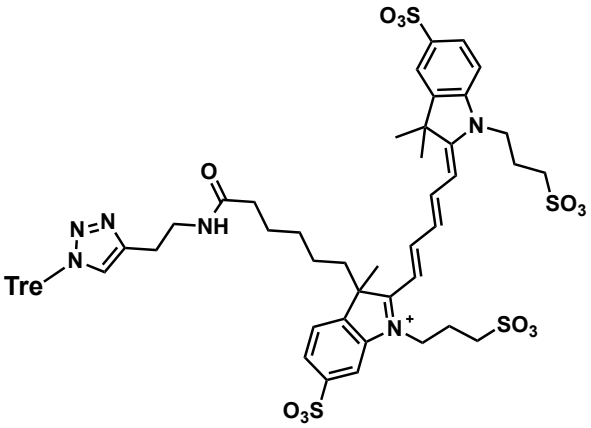

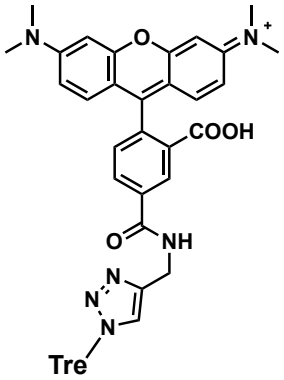

General procedure for the preparation of D-ala-Fl analog

Cu click reactions were performed as for fluorophore-trehalose analogs with the following modifications 2.5 µL 10 mM Fluorescein-N_3 and 0.5 µL alkDala, for the azide and alkyne reactive partners, respectively.

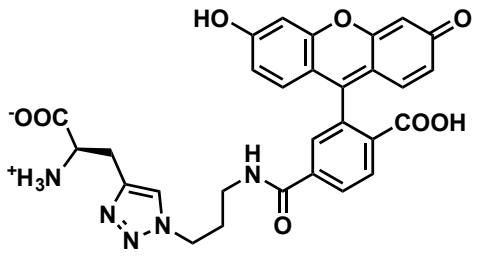

D-ala-Fl

Bacterial metabolic labeling conditions
Single colonies were used to start stationary phase cultures, which were used to innoculate experimental cultures for all bacterial strains. Cells were grown in aerated culture tubes or 96-well plates with shaking until the desired optical density was achieved. Bacterial cultures in exponential growth phase were incubated with trehalose probes until designated end-point of the experiment. Bacterial cells were fixed prior to flow cytometry or fluorescence microscopy unless otherwise noted.

For FlTre labeling profile, *C. glutamicum, M. smegmatis*, *R. equi* and *N. brasiliensis* were incubated with 100 μM FlTre for time periods encompassing several doubling times: 3 h, 18 h, 14 h, and 24 h, respectively. *B. subtilis* and E. *coli* were exposed to FlTre analogs for 2 h during exponential growth phase.

For *in vitro* pulse-chase experiments, bacteria were labeled with 100 μM FlTre or 50 μM 647-Tre reporters. Trehalose competition experiments included co-incubation of native trehalose at 0, 0.5 or 5.0 mM with designated trehalose reporter for *C. glutamicum* and *M. smegmatis*, for 2 and 3 hours respectively. Bacterial cells were co-treated with 20 or 50 μg/mL ebselen, for *C. glutamicum* (2 h) and *M. smegmatis* (3 h), respectively, as well as with trehalose reporters.

For mycomembrane mobility experiments, *C. glutamicum* and *M. smegmatis* were labeled with 100 μM 6-FlTre for several generations, washed to remove excess reporter and chased with TDL for different time periods from 5 to 30 min. TDL was used at a final concentration of 250 μM for pulse-chase labeling experiments.

For FRAP experiments, bacterial species were labeled with 20 μM D-ala-Fl, 100 μM TDL, or 100 μM FlTre for several generations overnight (~16 hours)

Antibiotic or drug treatment experiments involving *M. smegmatis* were conducted as follows: 1) inoculated cultures were labeled with 100 μM 6-FlTre for several generations; 2) treated with different concentrations of ethambutol during log phase; 3) washed excess reporter and drug with growth media; 4) incubated with 250 μM TDL for 20 min; 5) washed with growth media, fixed, and prepared samples for microscopy. This experiment was carried out in a 96-well plate to simultaneously evaluate ethambutol (0.5, 2, 10 μg/mL) and untreated cells.

Flow cytometry
Fluorescently labeled cells were analyzed in 96-well plate format in a BD Biosciences Accuri C6 flow cytometer equipped with a BD C-Sampler. Data was collected for 100,000 events at a rate of > 5,000 events/s for each sample. All flow cytometry experiments were performed in triplicate where results are representative of at least two independent experiments.

Fluorescence microscopy
Bacterial cultures (1-3 μL) were spotted on 1% agarose pads mounted on glass slides, installed coverslip, and sealed with nail polish. Fluorescence imaging was performed with a Nikon A1R resonant scanning confocal microscope using a CFI Plan Apo Lambda 60x oil objective. Images were captured with a Cool Snap HQ^2 (Photometrics) and processed with NIS Elements software. Acquisition and processing of images was performed identically for control and test samples.

Isolation and purification of free glycolipids
Bacterial cultures incubated with trehalose probes were washed two times with corresponding growth media to remove excess reporter. Wet cell pellets were subjected to organic extraction by adding 1 mL 2:1 $CHCl_3$:MeOH and stirring vigorously in conical glass tubes overnight. Resulting heterogeneous mixture was centrifuged for 10 min at 3700 x g, clarified organic layer supernatant was saved and cell pellet was re-extracted twice with the same protocol. Combined organic layers recovered after centrifugation were concentrated and analyzed by HPTLC (Uniplate HPTLC-GHL, 5 x 5 cm, 150 μm thickness) developed with 65:25:4 $CHCl_3$:MeOH:H_2O. Fluorescently labeled glycolipids developed in HPTLC plates were imaged with typhoon scanner (Amersham Biosciences, Typhoon 9410). Free lipids were partially purified by preparative TLC (Analtech, 20 x 20 cm, 1 mm thickness).

Mass spectrometry validation of FlTre-labeled glycolipids
C. glutamicum bacterial cultures (100 mL) were grown 5 μM trehalose, 2-FlTre, or 6-FlTre until early stationary phase. Trehalose glycolipis were isolated as described above. Partially purified glycolipids were dissolved in 100 μL 2:1 $CHCl_3$:MeOH (HPLC grade) and filtered through a 0.45 μm PVDF membrane. Mass spectra were acquired on a Waters Q-tof Premier quadrupole time-of-flight mass spectrometer equipped with a nanoelectrospray ionization (nanoESI) source. Ions were formed in the positive ion mode from pulled borosilicate glass nanoESI tips. Mass spectra were recorded over the range, mass-to-charge ratio (m/z) = 100 to 4000. Data acquisition was controlled using MassLynx software (version 4.1, Waters). This instrumentation is located in the QB3/Chemistry Mass Spectrometry Facility at the University of California, Berkeley. Detected ions were verified with previously reported mycolic acid characterization in *C. glutamicum* strain used.[54]

Fluorescence recovery after photobleaching (FRAP) experiments
FRAP experiments was performed on a Nikon Eclipse Ti inverted fluorescence microscope with a 100x (NA 1.49) oil-immersion Apo TIRF objective (Nikon Instruments), Andor iXon3 885 EMCCD camera and a Mosaic II patterned illumination system system (Andor) under the control of NIS-Elements. Photobleaching was performed with a 450 mW 405 nm laser for 50 ms to 2 s using a circular spot with a diameter of 1-2 μm and followed by a series of acquisitions with a 492 nm (for FlTre) / 561 nm (for 6-TMR-Tre) / 642 nm (for 6-AF647-Tre) laser at shallow angle TIRF and 50 ms exposure. Two segments with different acquisition interval (1 s and 5 s, respectively) were used to acquire the FRAP data for *C. glutamicum* and 10 s and 30 s intervals were used for *M. smegmatis*. Labeled cells were mounted on 1% agarose pad with either growth media or PBS.

A custom Matlab script was used to analyze the FRAP data to extract the fluorescence recovery kinetics. Briefly, the first image before photobleaching was used to generate a binary mask for the entire cell and a second mask was generated during experiment to mark the area of photobleaching. Total fluorescence intensities in both the whole cell area and the bleached area (overlap between the cell mask and photobleaching area mask) were extracted and normalized to correct for photobleaching of the dyes due to acquisition. The normalized fluorescence intensity of the bleached area (see Figures 2.8 and 2.13 for example traces) were then fitted to the equation below to extract the half-time and fraction of recovery:

$$Y = Y_{\max}\left(1 - e^{\left(\frac{-\ln 2}{t_{1/2}}\right)\left(t - t_0\right)}\right)$$

where Y_{max} is the plateau of the recovery curve (fraction recovered) and $t_{1/2}$ is the half-time for the recovery.

The apparent diffusion coefficients were calculated from the FRAP measurements as reported before by solving a one-dimensional continuous diffusion equation.[55] Briefly, a long axis was first identified in the cell based on the pre-photobleaching cell mask and the fluorescence intensity profile along this long axis was calculated by averaging the intensity of the stripe of pixels perpendicular to the long axis with the ends truncated for each frame. To correct for the intrinsic heterogeneity of the fluorescence intensity along the long axis as well as intensity loss due to acquisition, the fluorescence intensity profiles were first normalized to the pre-photobleaching image and then to the mean intensity in each frame. Only the first mode of Fourier series solution was considered and is calculated as

$$A_1\left(t\right) = \frac{2}{L}\int_0^L \cos\left(\frac{\pi}{L}x\right) I\left(x,t\right) dx$$

where L is the length of the cell and $I(x,t)$ is the fluorescence intensity at given position x and time t. The apparent diffusion coefficient D is then extracted by fitting A_1 to equation

$$A_1\left(t\right) = Be^{-\left(\frac{\pi}{L}\right)^2 Dt} + C$$

Statistics

p-values between samples were calculated with a rank sum test.

REFERENCES

1. World Health Organization, Global tuberculosis report 2015 **2015**
2. Russell, D. G. Mycobacterium tuberculosis: here today, and here tomorrow. *Nat. Rev. Mol. Cell Biol.* **2,** 569–586 (2001).
3. Philips, J. A. & Ernst, J. D. Tuberculosis Pathogenesis and Immunity. *Annu. Rev. Pathol. Mech. Dis.* **7,** 353–384 (2012).
4. Jarlier, V. & Nikaido, H. Mycobacterial cell wall: Structure and role in natural resistance to antibiotics. *FEMS Microbiol. Lett.* **123,** 11–18 (1994).
5. Zhang, Y. The Magic Bullets and Tuberculosis Drug Targets. *Annu. Rev. Pharmacol. Toxicol.* **45,** 529–564 (2005).
6. Zumla, A., Nahid, P. & Cole, S. T. Advances in the development of new tuberculosis drugs and treatment regimens. *Nat. Rev. Drug Discov.* **12,** 388–404 (2013).

7. Jankute, M., Cox, J. A. G., Harrison, J. & Besra, G. S. Assembly of the Mycobacterial Cell Wall. *Annu. Rev. Microbiol.* **69,** 405–423 (2015).
8. Marrakchi, H., Lanéelle, M.-A. & Daffé, M. Mycolic Acids: Structures, Biosynthesis, and Beyond. *Chem. Biol.* **21,** 67–85 (2014).
9. Hoffmann, C., Leis, A., Niederweis, M., Plitzko, J. M. & Engelhardt, H. Disclosure of the mycobacterial outer membrane: Cryo-electron tomography and vitreous sections reveal the lipid bilayer structure. *Proc. Natl. Acad. Sci.* **105,** 3963–3967 (2008).
10. Zuber, B. *et al.* Direct Visualization of the Outer Membrane of Mycobacteria and Corynebacteria in Their Native State. *J. Bacteriol.* **190,** 5672–5680 (2008).
11. Siegrist, M. S., Swarts, B. M., Fox, D. M., Lim, S. A. & Bertozzi, C. R. Illumination of growth, division and secretion by metabolic labeling of the bacterial cell surface. *FEMS Microbiol. Rev.* **39,** 184–202 (2015).
12. Christensen, H., Garton, N. J., Horobin, R. W., Minnikin, D. E. & Barer, M. R. Lipid domains of mycobacteria studied with fluorescent molecular probes. *Mol. Microbiol.* **31,** 1561–1572 (1999).
13. Maloney, E. A. *et al.* Alterations in phospholipid catabolism in Mycobacterium tuberculosis lysX mutant. *Cell. Infect. Microbiol. - Closed Sect.* **2,** 19 (2011).
14. Backus, K. M. *et al.* Uptake of unnatural trehalose analogs as a reporter for Mycobacterium tuberculosis. *Nat. Chem. Biol.* **7,** 228–235 (2011).
15. Swarts, B. M. *et al.* Probing the Mycobacterial Trehalome with Bioorthogonal Chemistry. *J. Am. Chem. Soc.* **134,** 16123–16126 (2012).
16. Urbanek, B. L. *et al.* Chemoenzymatic Synthesis of Trehalose Analogues: Rapid Access to Chemical Probes for Investigating Mycobacteria. *ChemBioChem* **15,** 2066–2070 (2014).
17. Foley, H. N., Stewart, J. A., Kavunja, H. W., Rundell, S. R. & Swarts, B. M. Bioorthogonal Chemical Reporters for Selective In Situ Probing of Mycomembrane Components in Mycobacteria. *Angew. Chem. Int. Ed.* **55,** 2053–2057 (2016).
18. Dover, L. G., Cerdeño-Tárraga, A. M., Pallen, M. J., Parkhill, J. & Besra, G. S. Comparative cell wall core biosynthesis in the mycolated pathogens, Mycobacterium tuberculosis and Corynebacterium diphtheriae. *FEMS Microbiol. Rev.* **28,** 225–250 (2004).
19. Carel, C. *et al.* Mycobacterium tuberculosis Proteins Involved in Mycolic Acid Synthesis and Transport Localize Dynamically to the Old Growing Pole and Septum. *PLOS ONE* **9,** e97148 (2014).
20. Meniche, X. *et al.* Subpolar addition of new cell wall is directed by DivIVA in mycobacteria. *Proc. Natl. Acad. Sci.* **111,** E3243–E3251 (2014).
21. Favrot, L. *et al.* Mechanism of inhibition of Mycobacterium tuberculosis antigen 85 by ebselen. *Nat. Commun.* **4,** 2748 (2013).
22. Favrot, L., Lajiness, D. H. & Ronning, D. R. Inactivation of the Mycobacterium tuberculosis Antigen 85 Complex by Covalent, Allosteric Inhibitors. *J. Biol. Chem.* **289,** 25031–25040 (2014).
23. Kuru, E. *et al.* In Situ Probing of Newly Synthesized Peptidoglycan in Live Bacteria with Fluorescent D-Amino Acids. *Angew. Chem. Int. Ed.* **51,** 12519–12523 (2012).
24. Brennan, P. J. & Nikaido, H. The Envelope of Mycobacteria. *Annu. Rev. Biochem.* **64,** 29–63 (1995).
25. Liu, J., Barry, C. E., Besra, G. S. & Nikaido, H. Mycolic Acid Structure Determines the Fluidity of the Mycobacterial Cell Wall. *J. Biol. Chem.* **271,** 29545–29551 (1996).

26. George, K. M., Yuan, Y., Sherman, D. R. & Barry, C. E. The biosynthesis of cyclopropanated mycolic acids in Mycobacterium tuberculosis. Identification and functional analysis of CMAS-2. *J. Biol. Chem.* **270,** 27292–27298 (1995).
27. Yuan, Y., Crane, D. C., Musser, J. M., Sreevatsan, S. & Barry, C. E. MMAS-1, the branch point between cis- and trans-cyclopropane-containing oxygenated mycolates in Mycobacterium tuberculosis. *J. Biol. Chem.* **272,** 10041–10049 (1997).
28. Ishikawa-Ankerhold, H. C., Ankerhold, R. & Drummen, G. P. C. Advanced Fluorescence Microscopy Techniques—FRAP, FLIP, FLAP, FRET and FLIM. *Molecules* **17,** 4047–4132 (2012).
29. Ghosh, A. S. & Young, K. D. Helical Disposition of Proteins and Lipopolysaccharide in the Outer Membrane of Escherichia coli. *J. Bacteriol.* **187,** 1913–1922 (2005).
30. Schindler, M., Osborn, M. J. & Koppel, D. E. Lateral diffusion of lipopolysaccharide in the outer membrane of Salmonella typhimurium. *Nature* **285,** 261–263 (1980).
37. Muhlradt, P.F., Menzel J., Golecki, J.R., Speth, V.Outer Membrane of Salmonella. Sites of export of newly synthesised lipopolysaccharide on the bacterial surface. \iEur. J. Biochem. \b35, 471–481 (1973).
32. Yang, Y., Shi, F., Tao, G. & Wang, X. Purification and structure analysis of mycolic acids in Corynebacterium glutamicum. *J. Microbiol.* **50,** 235–240 (2012).
33. Baba, T., Kaneda, K., Kusunose, E., Kusunose, M. & Yano, I. Molecular species of mycolic acid subclasses in eight strains ofMycobacterium smegmatis. *Lipids* **23,** 1132–1138 (1988).
34. Nishiuchi, Y., Baba, T. & Yano, I. Mycolic acids from Rhodococcus, Gordonia, and Dietzia. *J. Microbiol. Methods* **40,** 1–9 (2000).
35. Nishiuchi, Y., Baba, T., Hotta, H. H. & Yano, I. Mycolic acid analysis in Nocardia species: The mycolic acid compositions of Nocardia asteroides, N. farcinica, and N. nova. *J. Microbiol. Methods* **37,** 111–122 (1999).
36. Hett, E. C. & Rubin, E. J. Bacterial Growth and Cell Division: a Mycobacterial Perspective. *Microbiol. Mol. Biol. Rev.* **72,** 126–156 (2008).
37. Takayama, K., Armstrong, E. L., Kunugi, K. A. & Kilburn, J. O. Inhibition by Ethambutol of Mycolic Acid Transfer into the Cell Wall of Mycobacterium smegmatis. *Antimicrob. Agents Chemother.* **16,** 240–242 (1979).
38. Telenti, A. *et al.* The emb operon, a gene cluster of Mycobacterium tuberculosis involved in resistance to ethambutol. *Nat. Med.* **3,** 567–570 (1997).
39. Kilburn, J. O. & Takayama, K. Effects of ethambutol on accumulation and secretion of trehalose mycolates and free mycolic acid in Mycobacterium smegmatis. *Antimicrob. Agents Chemother.* **20,** 401–404 (1981).
40. Mikusová, K., Slayden, R. A., Besra, G. S. & Brennan, P. J. Biogenesis of the mycobacterial cell wall and the site of action of ethambutol. *Antimicrob. Agents Chemother.* **39,** 2484–2489 (1995).
41. Li, X.-Z., Zhang, L. & Nikaido, H. Efflux Pump-Mediated Intrinsic Drug Resistance in Mycobacterium smegmatis. *Antimicrob. Agents Chemother.* **48,** 2415–2423 (2004).
42. Bosne-David, S., Barros, V., Verde, S. C., Portugal, C. & David, H. L. Intrinsic resistance of Mycobacterium tuberculosis to clarithromycin is effectively reversed by subinhibitory concentrations of cell wall inhibitors. *J. Antimicrob. Chemother.* **46,** 391–395 (2000).
43. Abate, G. & Hoffner, S. E. Synergistic antimycobacterial activity between ethambutol and the beta-lactam drug cefepime. *Diagn. Microbiol. Infect. Dis.* **28,** 119–122 (1997).
44. Minnikin, D. E. Lipids: complex lipids, their chemistry, biosynthesis and roles. (1982).

45. Nikaido, H., Kim, S.-H. & Rosenberg, E. Y. Physical organization of lipids in the cell wall of Mycobacterium chelonae. *Mol. Microbiol.* **8,** 1025–1030 (1993).
46. Liu, J., Rosenberg, E. Y. & Nikaido, H. Fluidity of the lipid domain of cell wall from Mycobacterium chelonae. *Proc. Natl. Acad. Sci. U. S. A.* **92,** 11254–11258 (1995).
47. Li, Q. *et al.* Mycobacteriophage SWU1 gp39 can potentiate multiple antibiotics against Mycobacterium via altering the cell wall permeability. *Sci. Rep.* **6,** (2016).
48. Farha, M. A. & Brown, E. D. Unconventional screening approaches for antibiotic discovery. *Ann. N. Y. Acad. Sci.* **1354,** 54–66 (2015).
49. Ramón-García, S. *et al.* Synergistic Drug Combinations for Tuberculosis Therapy Identified by a Novel High-Throughput Screen. *Antimicrob. Agents Chemother.* **55,** 3861–3869 (2011).
50. Swarts, B. M. *et al.* Probing the Mycobacterial Trehalome with Bioorthogonal Chemistry. *J. Am. Chem. Soc.* **134,** 16123–16126 (2012).
51. Besanceney-Webler, C. *et al.* Increasing the Efficacy of Bioorthogonal Click Reactions for Bioconjugation: A Comparative Study. *Angew. Chem. Int. Ed.* **50,** 8051–8056 (2011).
52. Kuru, E. *et al.* In Situ Probing of Newly Synthesized Peptidoglycan in Live Bacteria with Fluorescent D-Amino Acids. *Angew. Chem. Int. Ed.* **51,** 12519–12523 (2012).
53. Shieh, P., Siegrist, M. S., Cullen, A. J. & Bertozzi, C. R. Imaging bacterial peptidoglycan with near-infrared fluorogenic azide probes. *Proc. Natl. Acad. Sci.* **111,** 5456–5461 (2014).
54. Yang, Y., Shi, F., Tao, G. & Wang, X. Purification and structure analysis of mycolic acids in Corynebacterium glutamicum. *J. Microbiol.* **50,** 235–240 (2012).
55. Elowitz, M. B., Surette, M. G., Wolf, P.-E., Stock, J. B. & Leibler, S. Protein Mobility in the Cytoplasm ofEscherichia coli. *J. Bacteriol.* **181,** 197–203 (1999).

Chapter 3

Front-line Tuberculosis Drugs Modulate Cell Wall Biogenesis in Mycobacteria

This work was adapted in part from Rodriguez-Rivera, F. P.; Zhou, X.; Theriot, J. A.; Bertozzi, C. R. Front-line tuberculosis drugs modulate cell wall biogenesis in mycobacteria.

Chapter 3. Front-line Tuberculosis Drugs Modulate Cell Wall Biogenesis in Mycobacteria

INTRODUCTION

Over a third of the population is thought to be infected with TB, which is caused by the single infectious agent *Mycobacterium tuberculosis* (Mtb).[1] Clinical treatment requires a cocktail of 4 drugs prescribed for at least a 6-month regimen. However, very recent reports highlight high degree of inflammation with potentially viable Mtb in the lungs of patients after this ineffective regimen.[2,3] Furthermore, failure to complete extensive drug treatments has led to increased drug resistance.[4,5] Some currently employed chemotherapies include ethambutol and isoniazid,[4] which target the biosynthesis of the cell wall, a formidable barrier to many host stresses and therapeutics.[6–9] Despite the identification of enzymatic drug targets, our current understanding of how existing drugs alter live cell physiology remains inadequate due to a lack of tools to monitor cell wall dynamics in real-time. In addition, increasing cellular phenotypic heterogeneity under drug treatment further complicates analysis of cell-to-cell variation.[10,11] Therefore, new molecular methods to address changes in cell wall physiology during the aforementioned stresses are sorely needed.

Mycobacterial peptidoglycan is covalently modified with arabinogalactan polymers, which in turn are elaborated with long lipid chains called mycolic acids.[12] These mycolic acids form the inner leaflet of the mycomembrane, which also includes an outer leaflet comprised of a variety of non-covalently associated lipids (Figure 3.1A). The most abundant glycolipids are trehalose monomycolate (TMM) and trehalose dimycolate (TDM) which comprise 40% of the dry weight of cell envelope lipids.[13] Decades of research have characterized the cell wall by means of bulk isolation and purification of individual components, a method that necessarily obscures important information about the native architecture and real-time dynamics of the mycobacterial cell wall.[12] Strategies enabling the imaging of these components would be highly advantageous since biochemical and genetic approaches are insufficient to study these non-genetically encoded products in live cells.

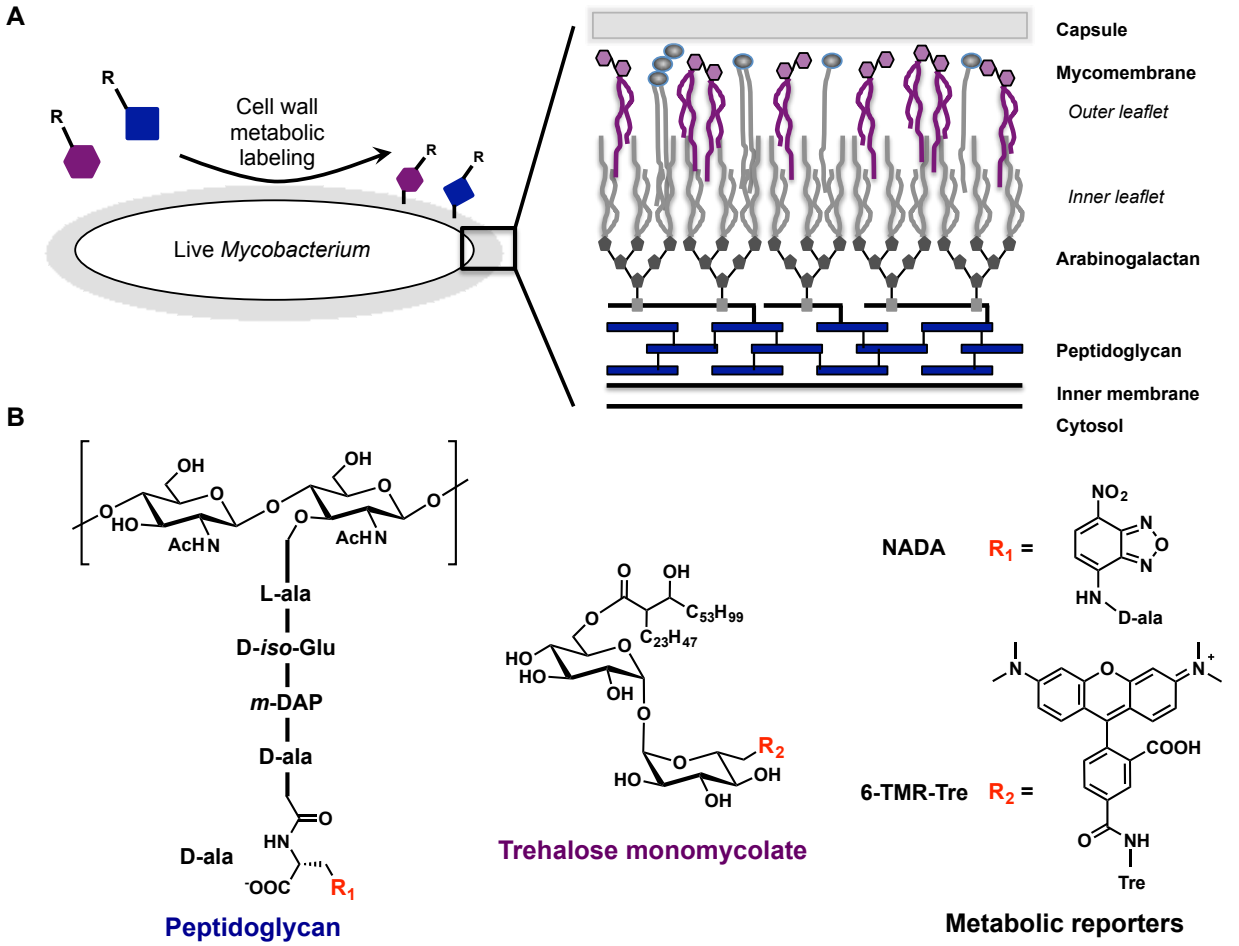

Figure 3.1 Metabolic labeling of the mycobacterial cell wall and structures of peptidoglycan and trehalose monomycolate. A) Mycobacterial cell wall components include inner membrane, peptidolycan, arabinogalactan, mycomembrane, and capsule. Individual layers can be metabolically labeled with unnatural reporters as depicted by blue squares (peptidoglycan, also in blue) and purple hexagons (trehalose mycolates, also in purple). B) Chemical structures for mycobacterial peptidoglycan and trehalose monomycolate with metabolic reporters NADA and 6-TMR-Tre. Nitrobenzofurazan (NADA)

In order to visualize unique mycobacterial cell wall components and to monitor them in live bacteria, the development of metabolic probes with unique functionalities is essential.[14] Metabolic labeling approaches have been used to label single components, peptidoglycan[15–18] and trehalose glycolipids[19–23], by exploiting enzyme promiscuities in biosynthetic pathways. However, these powerful tools have not yet been used in combination to provide a molecular view of how dynamics of both cell wall components are orchestrated during cell growth and biological stresses. Covalent tagging of the cell wall would allow visualization of single cells with high resolution to interrogate cell physiology, metabolic state and population dynamics. This strategy could capture cell heterogeneity with subcellular resolution, induced by pressures from front-line drug treatment and host defenses (or stresses).

Here, we developed a new trehalose-fluorophore conjugate to image trehalose monomycolate by super resolution microscopy in live mycobacteria. We utilized a dual metabolic labeling strategy to monitor cell wall dynamics of peptidoglycan and trehalose monomycolate in *Mycobacterium marinum*, a pathogenic species that is one of the closest genetic relatives to Mtb[24] (Figure 3.1B). With this dual metabolic labeling approach, we found that mycobacteria undergo a drastic shift in their cell wall biosynthesis program when cells are treated with mycomembrane-targeting front-line TB drugs ethambutol and isoniazid. Our work provides insight into the underlying molecular consequences in cell physiology during TB drug treatment.

RESULTS AND DISCUSSION

TAMRA-trehalose selectively labels trehalose mycolates

Seminal work from Barry, Davis and coworkers demonstrated that unnatural trehalose reporters are processed permissively by the antigen 85 complex (Ag85), a family of mycolyltransferases that resides in the cell wall and converts 2 molecules of TMM to form TDM and free trehalose.[19,25] Our work and others have shown that installation of a fluorescein dye at different positions in the trehalose scaffold is recognized by mycolyltrasnferases in live cells from mycolic-acid producing actinobacteria genera (see Chapter 2). However, the poor photostability of the fluorescein dye limited our ability to perform long-term fluorescence imaging and super resolution microscopy.

We envisioned that installing a tetramethylrhodamine (TAMRA) fluorophore on the trehalose core would afford the desired imaging properties. TAMRA is a common fluorophore choice for a wide range of super resolution methods in both bacteria and mammalian cells.[26–29] Our previous studies showed that the modification of the 6-position of trehalose with fluorescein (6-FlTre) yielded the highest incorporation efficiency by the biosynthetic machinery in *Mycobacterium smegmatis* (see Chapter 2), an established organism with a cell wall very similar to Mtb's. We installed TAMRA at this position to afford TAMRA-trehalose conjugate, 6-TMR-Tre in high yields from the parent 6-TreAz compound (see methods section). In liquid culture, short pulses of this probe revealed polar localization of fluorescence in live mycobacteria (Figure 3.2) in agreement with the known polar localization of cell wall biosynthetic enzymes during log phase growth.[30,31] Gratifyingly, 6-TMR-Tre was not metabolized by bacteria devoid of trehalose mycolates such as Gram-positive *Bacillus subtilis* or Gram-negative *Eschericia coli*, (Figure 3.3).

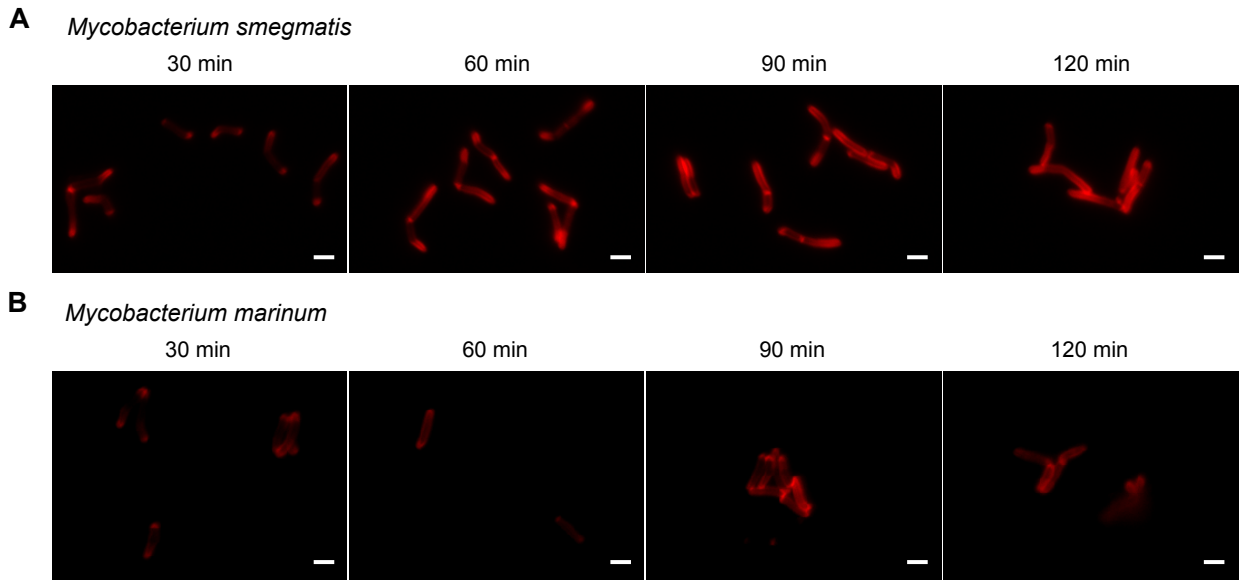

Figure 3.2 Short pulses of 6-TMR-Tre shows localization to the poles. Cells were incubated with 100 uM 6-TMRTre for the indicated times in *M. smegmatis* (A) and *M. marinum* (B). Scale bar, 2 μm

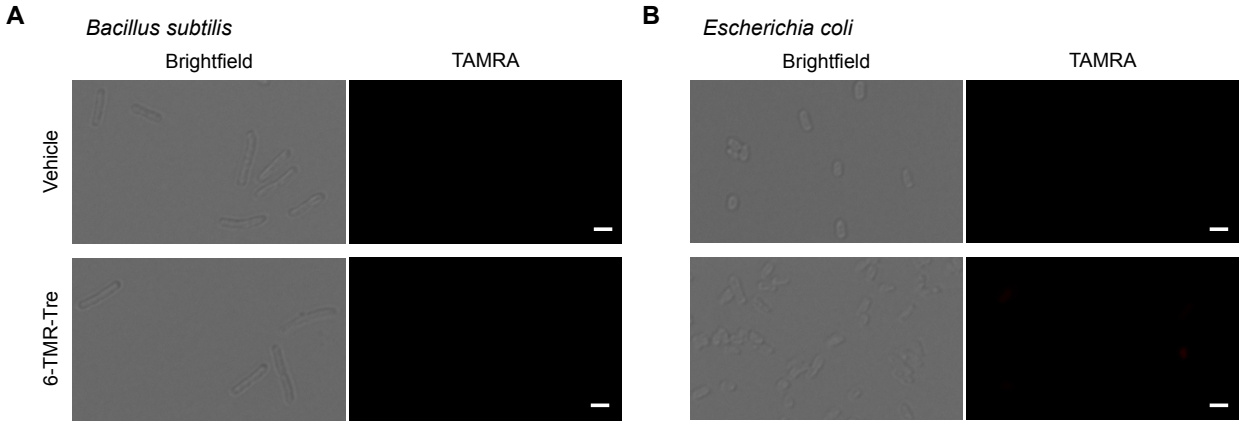

Figure 3.3 6-TMR-Tre does not label common Gram-positive and negative bacteria. Cells were incubated with 100 uM 6-TMRTre for 2 h for *B. subtilis* (A) and *E. coli* (B). Scale bar, 2 μm

Next, we sought to validate that 6-TMR-Tre was being processed by Ag85 to access trehalose monomycolates selectively. We asked whether exogenous trehalose could outcompete 6-TMR-Tre labeling in mycobacteria as trehalose is a native substrate for Ag85 activity. Increasing concentrations of trehalose produced a dose-dependence decrease in labeling for *M. smegmatis* and *M. marinum* during short incubation periods of 3 h and 4 h, respectively (Figure 3.4A). In addition we tested the effect of ebselen, a covalent Ag85 inhibitor,[32,33] on labeling efficiency. For the same incubation periods used in trehalose competition experiments, ebselen treatment significantly reduced metabolic incorporation of 6-TMR-Tre in both species (Figure 3.4B). Finally, we isolated the apolar total lipid fraction of prelabeled mycobacteria and analyzed

them by thin layer chromatography (TLC). Fluorescence scanning of TLC plates revealed a single fluorescent band corresponding to TMM labeled with 6-TMR-Tre in both *M. smegmatis* and *M. marinum* (Figure 3.5). These experiments were also carried out in parallel for *Corynebacterium glutamicum* cells to demonstrate selective labeling of trehalose monocorynemycolate by 6-TMR-Tre (Figure 3.6). Collectively, these results show that 6-TMR-Tre selectively labels TMM in trehalose mycolate producing species.

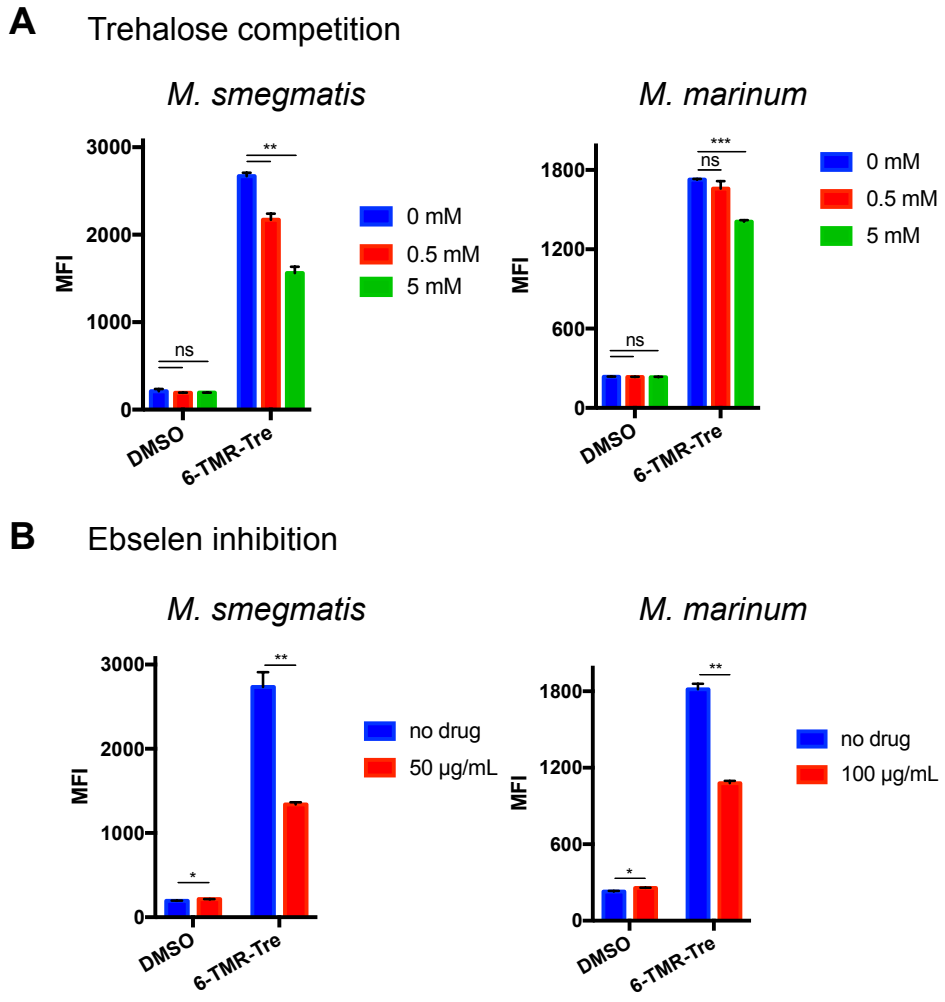

Figure 3.4 6-TMR-Tre is incorporated through an Ag85-mediated pathway. *M. smegmatis* and *M. marinum* were labeled with 100 µM 6-TMR-Tre for 3 and 4 h, respectively. A) Increasing concentrations of trehalose (0, 0.5, 5.0 mM) can outcompete 6-TMR-Tre labeling in both species during bacterial growth. B) Ebselen treatment during 6-TMR-Tre labeling decreases incorporation in both species. Error bars depict standard deviation of three replicate experiments. Results are representative of at least two independent experiments. Statistical significance is given by $*P < 0.05$, $**P < 0.01$, $***P < 0.001$. Mean fluorescence intensity (MFI)

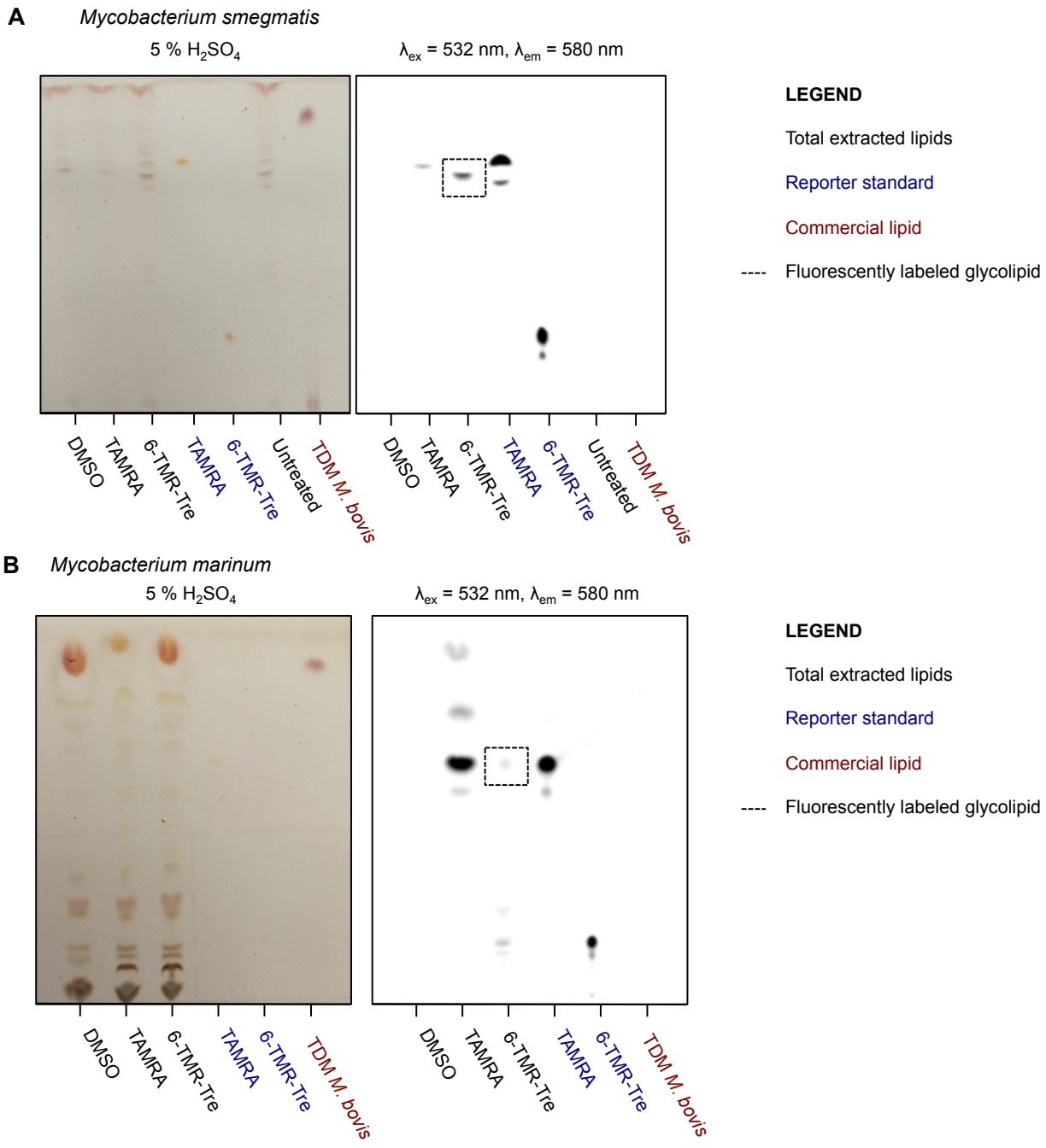

Figure 3.5 6-TMR-Tre selectively labels mycobacterial trehalose monomycolate. Cells were incubated with 100 μM 6-TMR-Tre or TAMRA for several doubling times in a 5 mL culture and then glycolipids were isolated by organic extraction. HPTLC analysis of labeled glycolipids is shown for *M. smegmatis* (A) and *M. marinum* (B). Glycolipids were visualized with 5 % H_2SO_4 and fluorescence scanning. High performance thin layer chromatography (HPTLC)

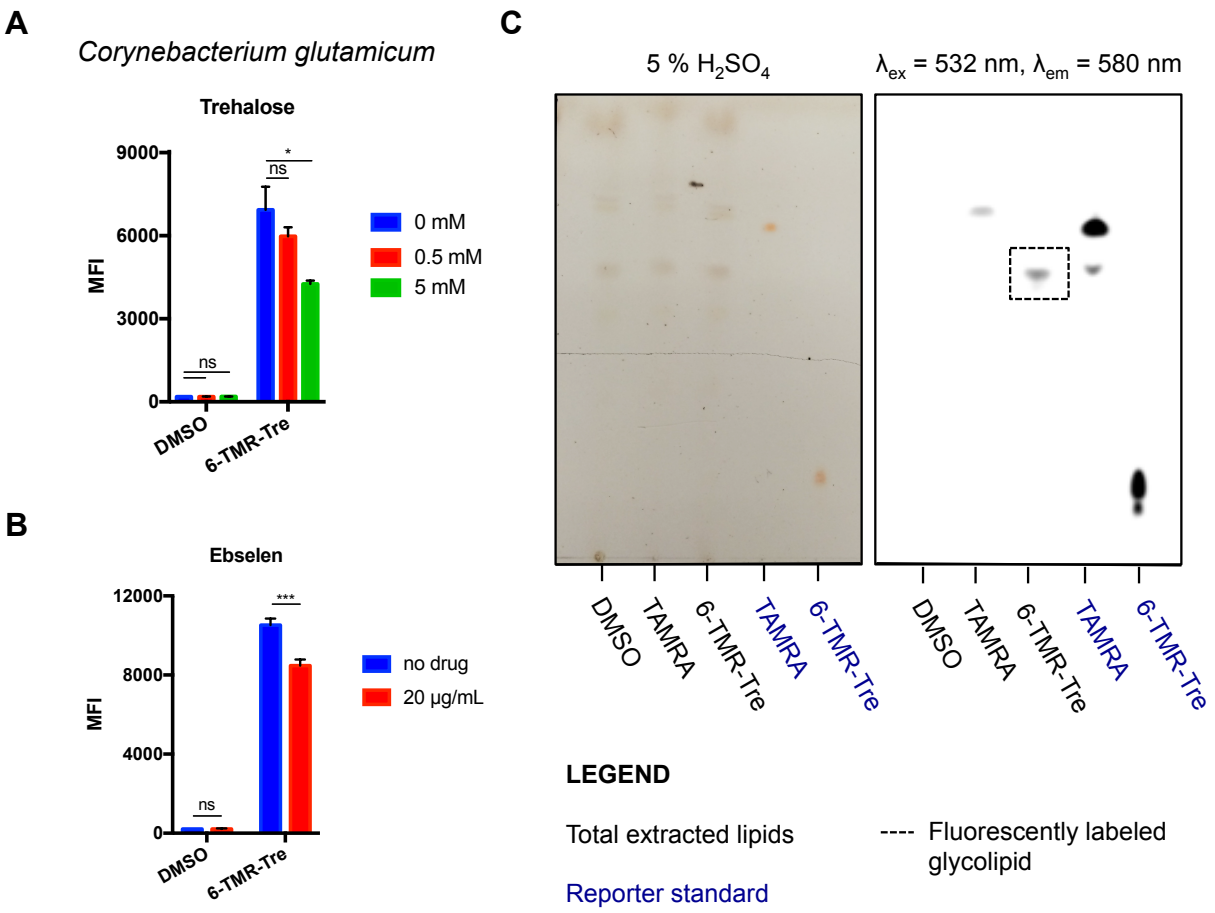

Figure 3.6 6-TMR-Tre is incorporated through a mycolyltransferase mediated pathway in *C. glutamicum*. Cells were labeled with 100 µM 6-TMR-Tre for 2 h in trehalose competition and ebselen experiments. A) Increasing concentrations of trehalose (0, 0.5, 5.0 mM) can outcompete 6-TMR-Tre labeling during bacterial growth. B) Ebselen treatment during to 6-TMR-Tre labeling decreases reporter incorporation. Error bars depict standard deviation of three replicate experiments. Results are representative of at least two independent experiments. Statistical significance is given by $*P < 0.05$, $**P < 0.01$, $***P < 0.001$. Mean fluorescence intensity (MFI) C) HPTLC analysis of labeled glycolipids is shown for 5 % H_2SO_4 and fluorescence scanning visualization. High performance thin layer chromatography (HPTLC)

Installation of TMR in the trehalose scaffold allowed us to visualize the subcellular organization of TMM by structure illumination microscopy (SIM). We pulsed *M. smegmatis* cells with short incubations of 6-TMR-Tre for 5, 15 or 30 min, washed, fixed and prepared for SIM. Longer incubation times afforded stronger labeling in the polar regions of the cells (Figure 3.7A). 6-TMR-Tre is localized to the very tip of the cell pole, in contrast to the subpolar addition of PG by *M. smegmatis* with alkyne-functionalized D-amino acids (alkDala),[31] which suggests different processing of trehalose-fluorophore conjugates by the cell's biosynthetic machinery. This might be a consequence of alkDala potentially being incorporated by a cytosolic route as observed in other bacteria.[34] We observed significant labeling along the cell length, which was more heterogeneous in nature, affording an uneven coat of the cell surface when *M. marinum* was incubated with 6-TMR-Tre for 45 min (Figure 3.7B). To our knowledge, this is the first example of super resolution microscopy of trehalose mycolates in mycobacteria.

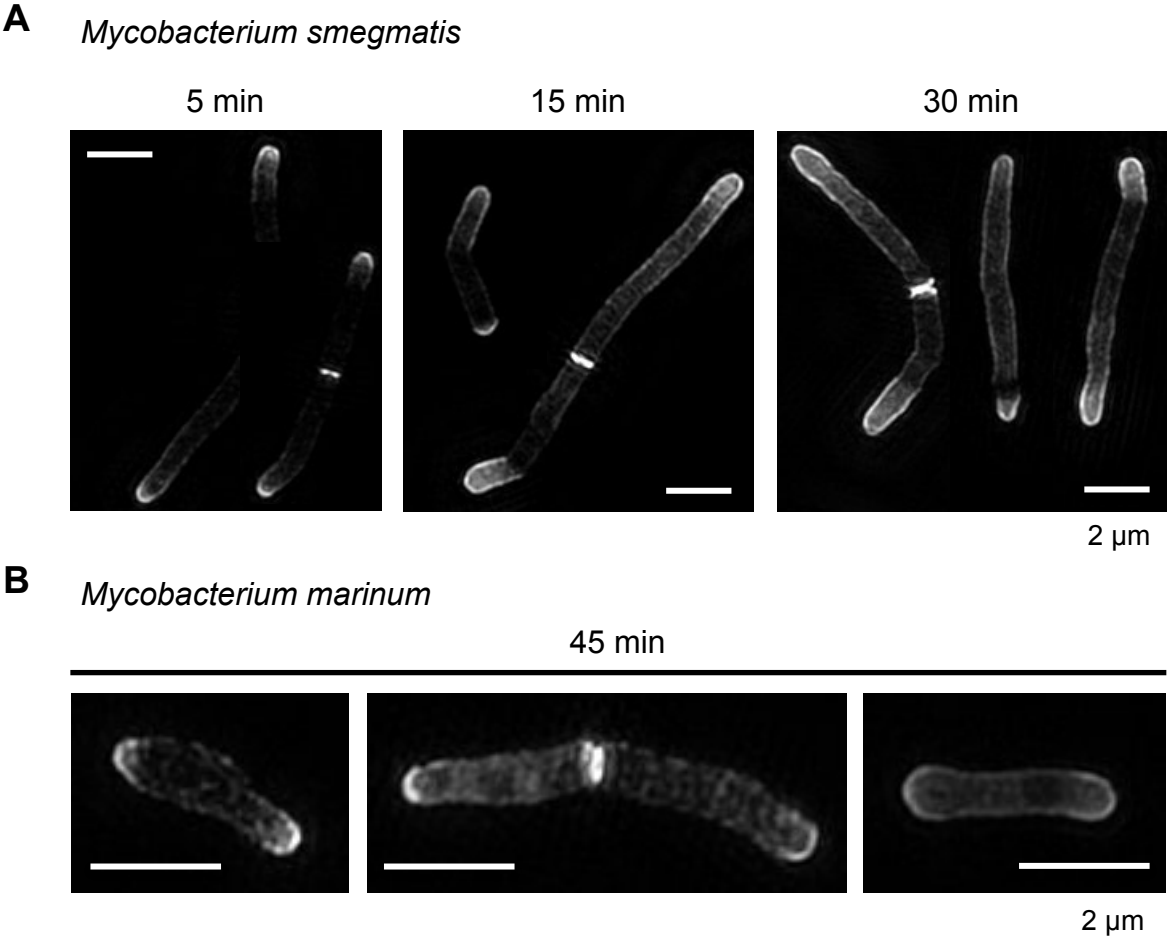

Figure 3.7 Structured illumination microscopy reveals polar addition 6-TMR-Tre in mycobacteria. Representative images are shown as maximum intensity z-projections. (A) *M. smegmatis* cells were incubated for 5, 15 or 30 min with 6-TMR-Tre prior to SIM visualization. (B) Short pulse of 45 min in *M. marinmum* reveals ultrastructural information on TMM mycomembrane organization. Scale bar, 2 µm

Dual metabolic labeling reveals cell wall dynamics during growth

We then sought to monitor real-time dynamics of TMM with our metabolic labeling strategy by imaging live mycobacteria. In order to confirm glycolipid immobility in the mycomembrane of *M. marinum*, cells were prelabeled with 6-TMR-Tre for several generations, washed, and marked with NADA, a fluorescent D-amino acid conjugate,[15] for different time periods prior to fluorescence imaging. 6-TMR-Tre labeled TMM was excluded from the poles in *M. smegmatis* after a 20 min NADA chase demonstrating a similar immobility to FlTre-labeled species (Figure 3.8A) (as shown in Chapter 2). *M. marinum* also showed negligible 6-TMR-Tre labeling at the poles after a similar chase (Figure 3.8B), suggesting that labeled TMM does not diffuse away from the original site of incorporation. Dual cell wall labeling with NADA and 6-TMR-Tre was an attractive strategy to simultaneously visualize cell wall biosynthesis of PG and TMM with a single labeling step. Thus, we proceeded to treat *M. marinum* with short pulses of both reporters to capture dynamics during cell growth in liquid culture. We found high colocalization of NADA and 6-TMR-Tre signal at the poles, where enzymes involved in new PG and TMM biosynthesis are primarily localized (Figure 3.9).[30,31] Interestingly, we observed increasing labeling of the side-wall of mycobacteria at longer incubations with both reporters, suggesting remodeling or maturation processes for the existing cell wall. These observations were also made for *M. smegmatis* cells that were labeled for 5, 15 or 30 min (Figure 3.9A). Taken together, our results demonstrate that dual cell wall labeling of live mycobacteria reveals real-time dynamics with subcellular resolution during cell growth.

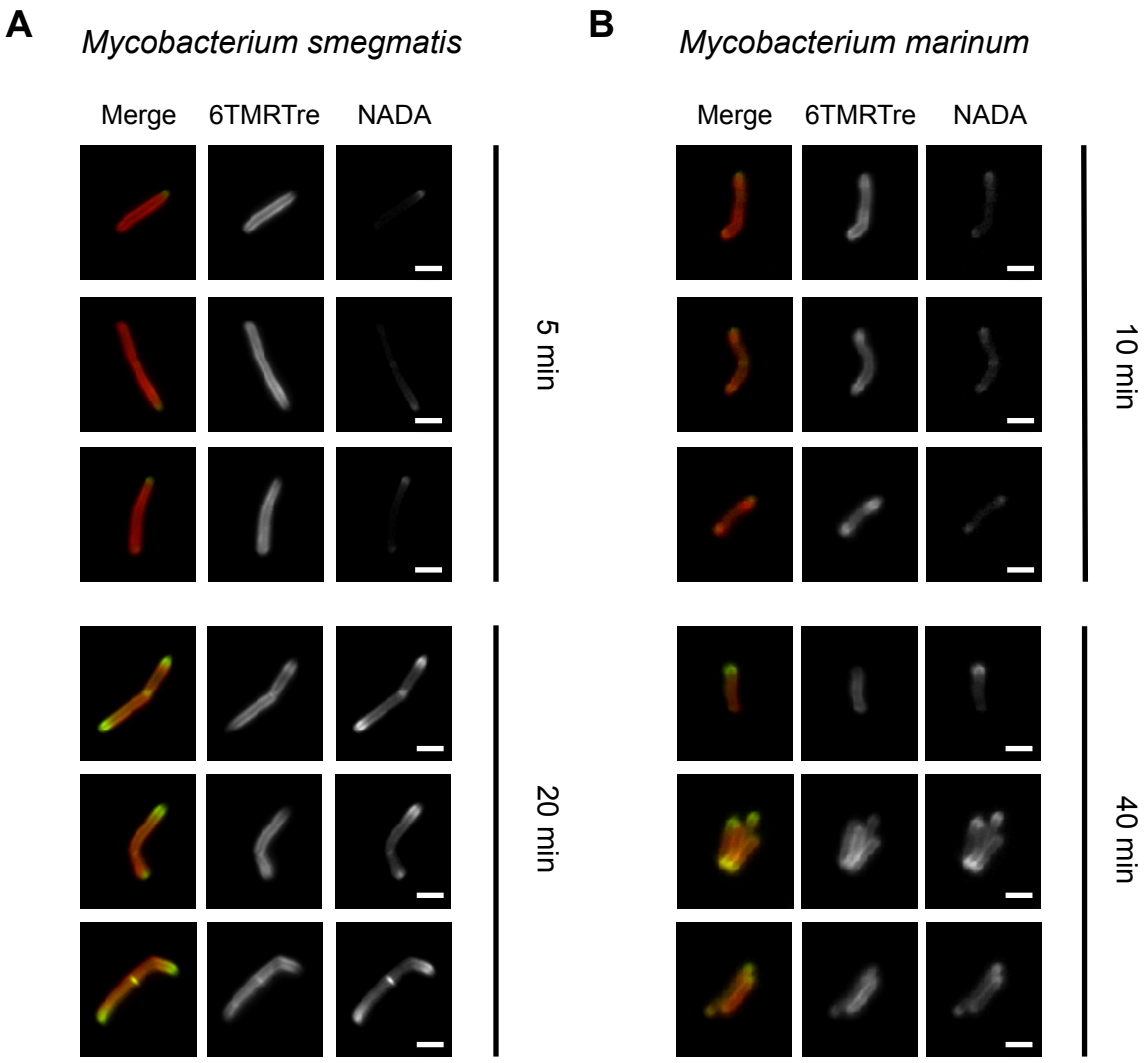

Figure 3.8. Mycomembrane mobility assay in mycobacteria. Cells were incubated with 100 uM 6-TMRTre for several doubling times, washed and chased with 1 mM NADA for the indicated time periods. Representative images are shown for *M. smegmatis* (A) and *M. marinum* (B). Scale bar, 2 μm

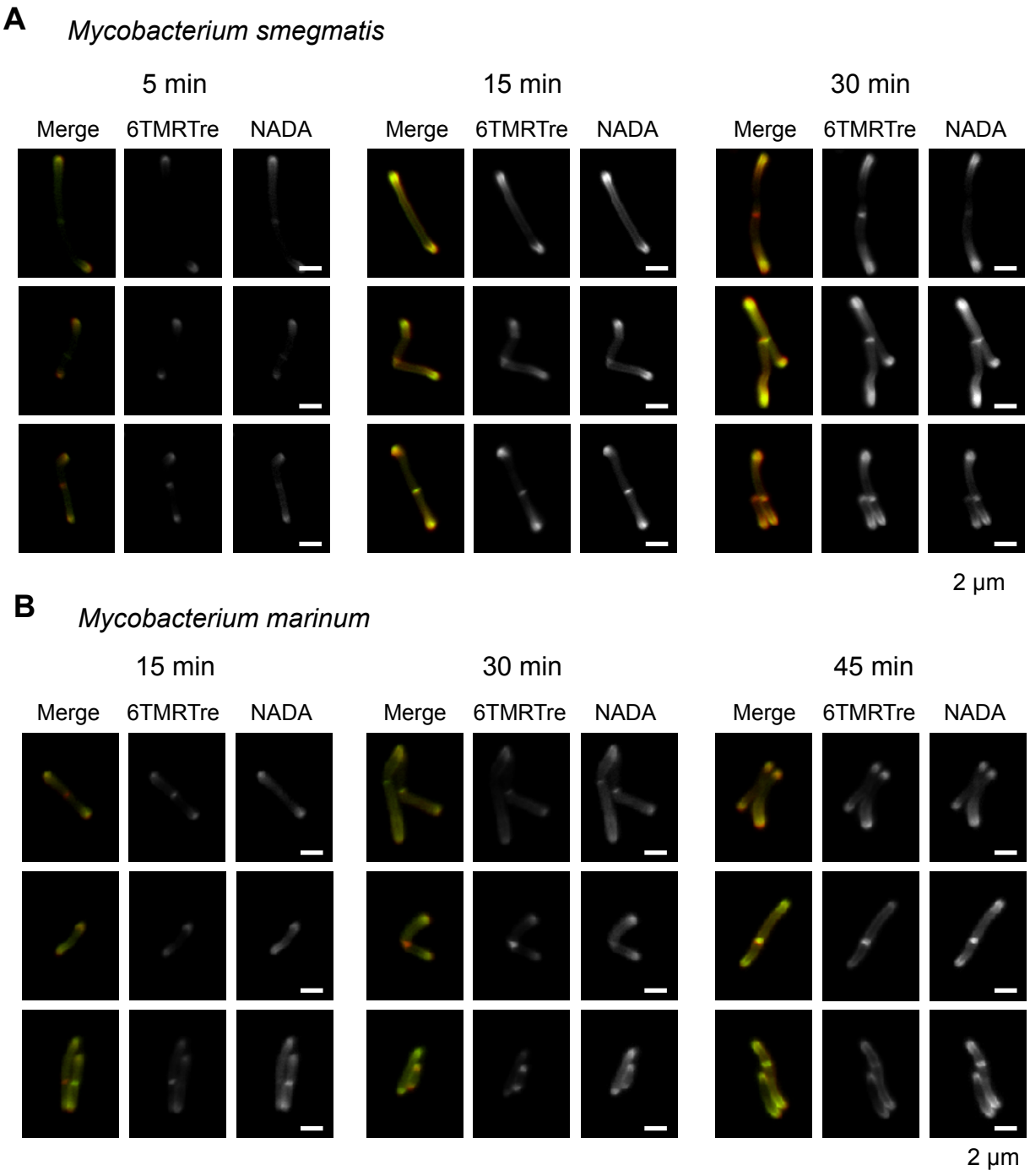

Figure 3.9 Short pulse dual cell wall labeling in mycobacteria reveals subcellular distribution of PG and TMM biosynthesis in mycobacteria. *M. smegmatis* (A) and *M. marinum* (B) cells were incubated with 100 uM 6-TMR-Tre and 1 mM NADA for the indicated times. Representative images are shown for widefield fluorescence microscopy. Scale bar, 2 μm

Mycomembrane-compromising drugs redirect cell wall biosynthesis

Current understanding of stress responses to cell wall-targeting drugs is limited to genetic readouts[35–39] or endpoint electron micrographs.[40] These methods are not amenable to real-time live cell imaging of targeted cell wall components. Our metabolic labeling platform would facilitate the investigation of the cell wall molecular consequences upon front-line TB drug treatment in live mycobacteria. In particular, we focused our efforts on visualizing the underlying changes that cells incur when treated with mycomembrane-compromising agents such as ethambutol (EB) and isoniazid (INH). EB inhibits EmbB, an arabinosyl transferase that installs arbaninose residues to arabinogalactan chains,[41,42] which results in reduced sites for mycolylation of the inner leaflet. INH is a prodrug that targets mycolic acid synthesis by generating an NADH adduct that inhibits the fatty acid synthase InhA when activated by the catalase-peroxidase enzyme KatG.[43] In addition to EB and INH treatments, we included SQ109 in this study to examine alterations produced by inhibition of MmpL3, a TMM-specific transporter.[40] Furthermore, we included rifampicin (RIF) in our studies, a front-line TB drug that targets RNA polymerase to inhibit transcription, which would serve as a negative control.[44] The chemical structures of these antibiotics are shown in Figure 3.10. Cell wall labeling of PG and TMM would report on cell physiology, including metabolic state and toxicity induced by these drugs. We also utilized a fluorescent vancomycin conjugate (Vanco-Fl) to label PG as an indicator for probe accessibility in the context of membrane integrity.

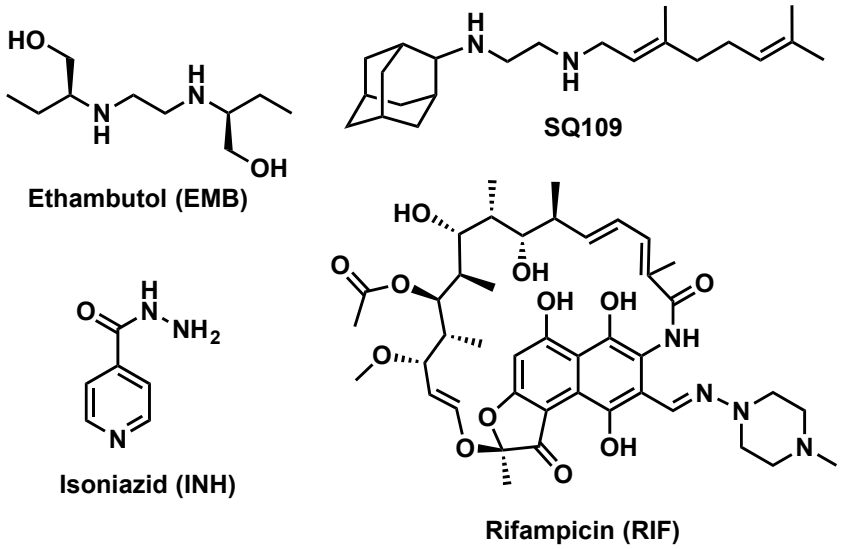

Figure 3.10 Chemical structures of front-line TB drugs used in the clinic and phase 2 clinical trial candidate SQ109

To this end, *M. marinum* cells were treated with a range of concentrations (below and above MIC) of EB, INH, SQ109, and RIF for 2 h, while NADA, 6-TMR-Tre, or Vanco-Fl reporters were also present in the growth media. Cells were washed, fixed and analyzed by flow cytometry to evaluate all conditions tested (Figure 3.11). Overall, NADA and 6-TMR-Tre labeling decreased with increasing concentrations of drugs, which suggests toxicity. Notably, EB treatment showed a significant dose-dependent increase in 6-TMR-Tre labeling after a 2 h

treatment. This is in agreement with previously reported upregulation of mycolic acids and trehalose mycolate biosynthesis after EB treatment.[42,45] Vanco-Fl staining showed a drastic increase in signal upon cell exposure to high SQ109 concentration, suggesting a compromised mycomembrane since NADA labeling did not increase. On the other hand, RIF inhibition of transcription resulted in minor changes in NADA, 6-TMR-Tre and Vanco-Fl labeling profiles as expected. Similar results were obtained when *M. smegmatis* was treated under the same experimental conditions (Figure 3.12). Together, these results pointed at different cell wall biosynthesis responses during the course of individual drug treatment for the averaged cell population.

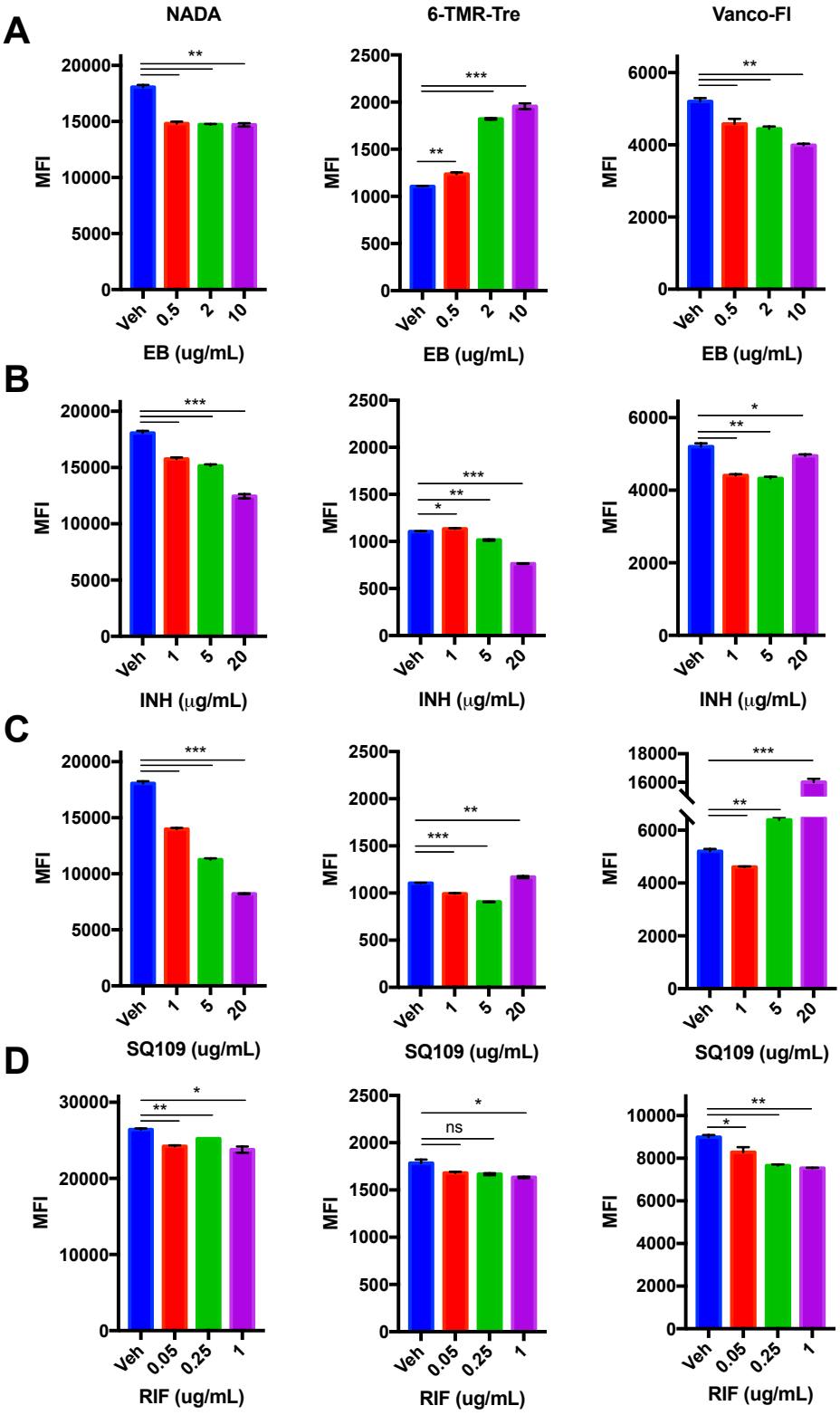

Figure 3.11 Effects of short drug treatment at different concentrations in *M. marinum*. Bacteria were treated for 2 h with EB (A), INH (B), SQ109 (C), RIF (D) and labeled with

NADA, 6-TMR-Tre or Vanco-Fl followed by flow cytometry analysis. Error bars depict standard deviation of three replicate experiments. Results are representative of at least two independent experiments. Statistical significance is given by $*P < 0.05$, $**P < 0.01$, $***P < 0.001$. Mean fluorescence intensity (MFI)

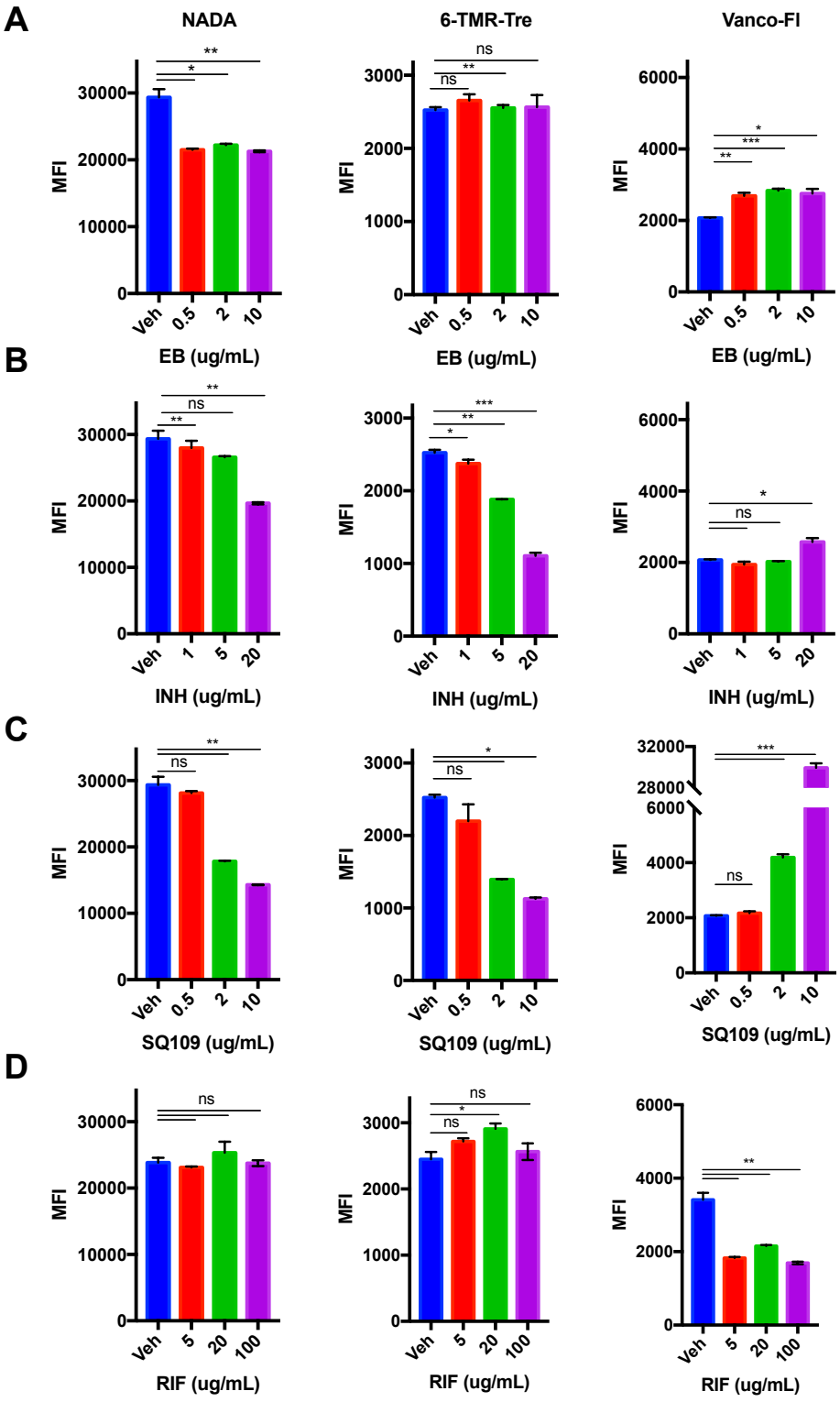

Figure 3.12 Effects of short drug treatment at different concentrations in *M. smegmatis*. Bacteria were treated for 2 h with EB (A), INH (B), SQ109 (C), RIF (D) and labeled with NADA, 6-TMR-Tre or Vanco-Fl followed by flow cytometry analysis. Error bars depict standard deviation of three replicate experiments. Results are representative of at least two independent experiments. Statistical significance is given by $*P < 0.05$, $**P < 0.01$, $***P < 0.001$. Mean fluorescence intensity (MFI)

However, the strength of our method relies on the visualization of the subcellular changes in cell wall labeling of single cells. Upon closer examination, fluorescence microscopy revealed drug-specific dual cell wall labeling patterns in live mycobacteria (Figures 3.13 and 3.14, for *M. marinum* and *M. smegmatis*, respectively). NADA showed polar incorporation for all drug treatments, where lower labeling correlated with higher drug doses. Similarly, 6-TMR-Tre labeling decreased with increasing drug concentration. Surprisingly, EB exposure showed a stronger side-wall labeling profile at all concentrations. Next, we pursued characterization and quantification of this phenomenon on a single cell basis. Fluorescence intensity for both NADA and 6-TMR-Tre labeling were plotted against the cell length to illustrate subcellular staining, where the brightest pole was oriented as position 0 μm in x-axis (Figure 3.15). We also calculated the polarity index to account for cell wall remodeling differences during treatment, defined as the intensity of the dimmest region divided by the intensity of the brightest pole. These measurements indicate that *M. marinum* redirects cell wall biosynthesis to different extents specific to drug treatment (Figure 3.16). EB is the strongest inducer of side-wall labeling of all conditions tested for both PG and TMM. Similar observations were made for *M. smegmatis* cells treated with the same drugs (Figure 3.17). Our results are consistent with the upregulation of cell wall remodeling enzymes after drug treatment as revealed by gene profiling.[35,37,38] Cell wall targeting drugs directly affect the *iniBAC* operon, which is involved in alleviating cell wall stress.[36,39] Notably, we did not observe *iniBAC* upregulation under our experimental conditions with a *M. marinum* reporter strain (Figure 3.18). Collectively, we have demonstrated that front-line TB drug pressures can alter cell wall remodeling before significant activation of the *iniBAC* operon, suggesting a faster response than genetic regulation of cell stress.

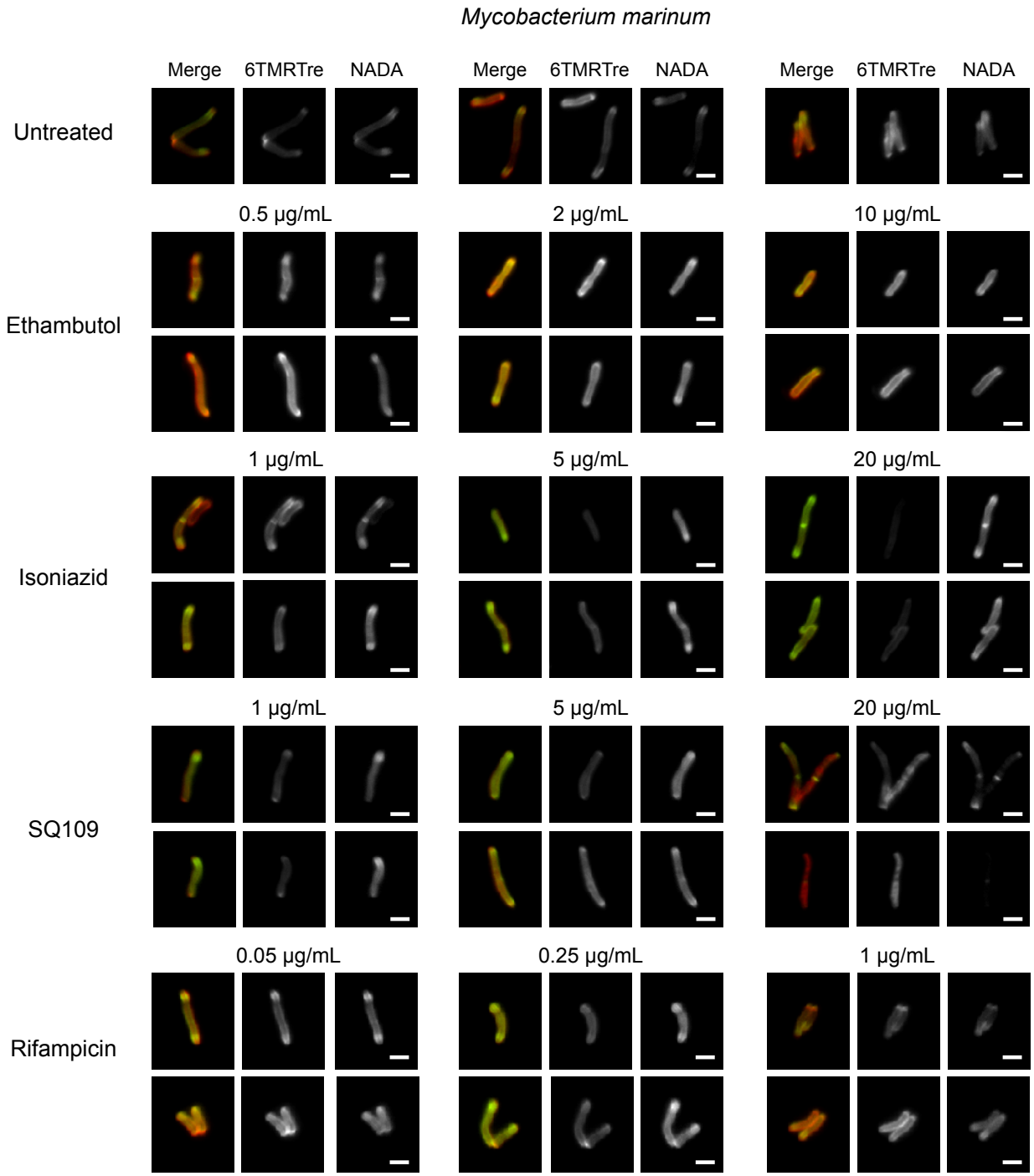

Figure 3.13 Effects of mycomembrane-compromising agents in *M. marinum*. Cells were incubated with 100 uM 6-TMRTre and 1 mM NADA in the presence of the following drugs: EB, INH, SQ109, and RIF at different concentrations for a 2 h period. Representative images are shown for *M. marinum* cells. Scale bar, 2 µm

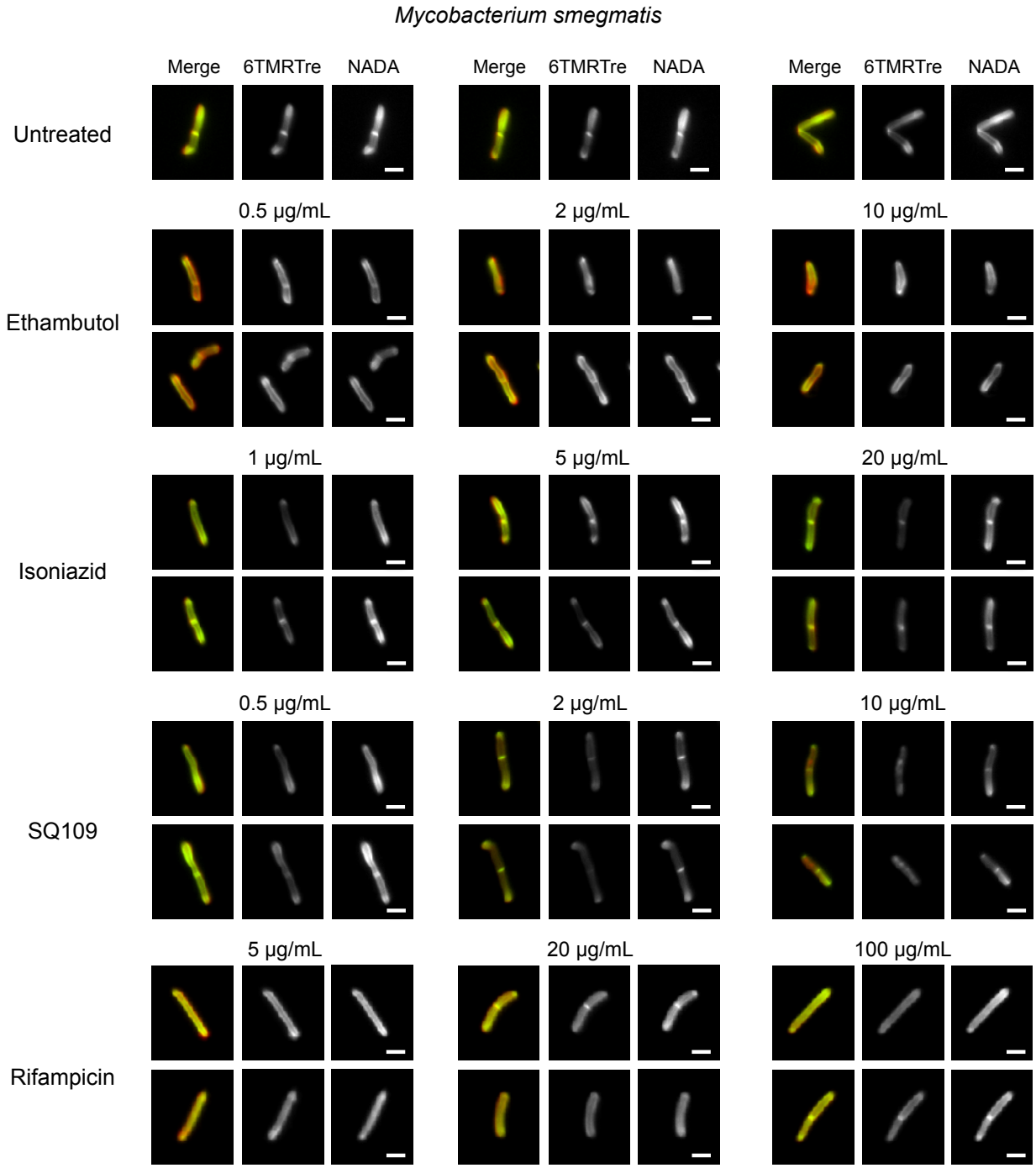

Figure 3.14 Effects of mycomembrane-compromising agents in *M. smegmatis*. Cells were incubated with 100 uM 6-TMRTre and 1 mM NADA in the presence of the following drugs: EB, INH, SQ109, and RIF at different concentrations for a 2 h period. Representative images are shown for *M. smegmatis* cells. Scale bar, 2 µm

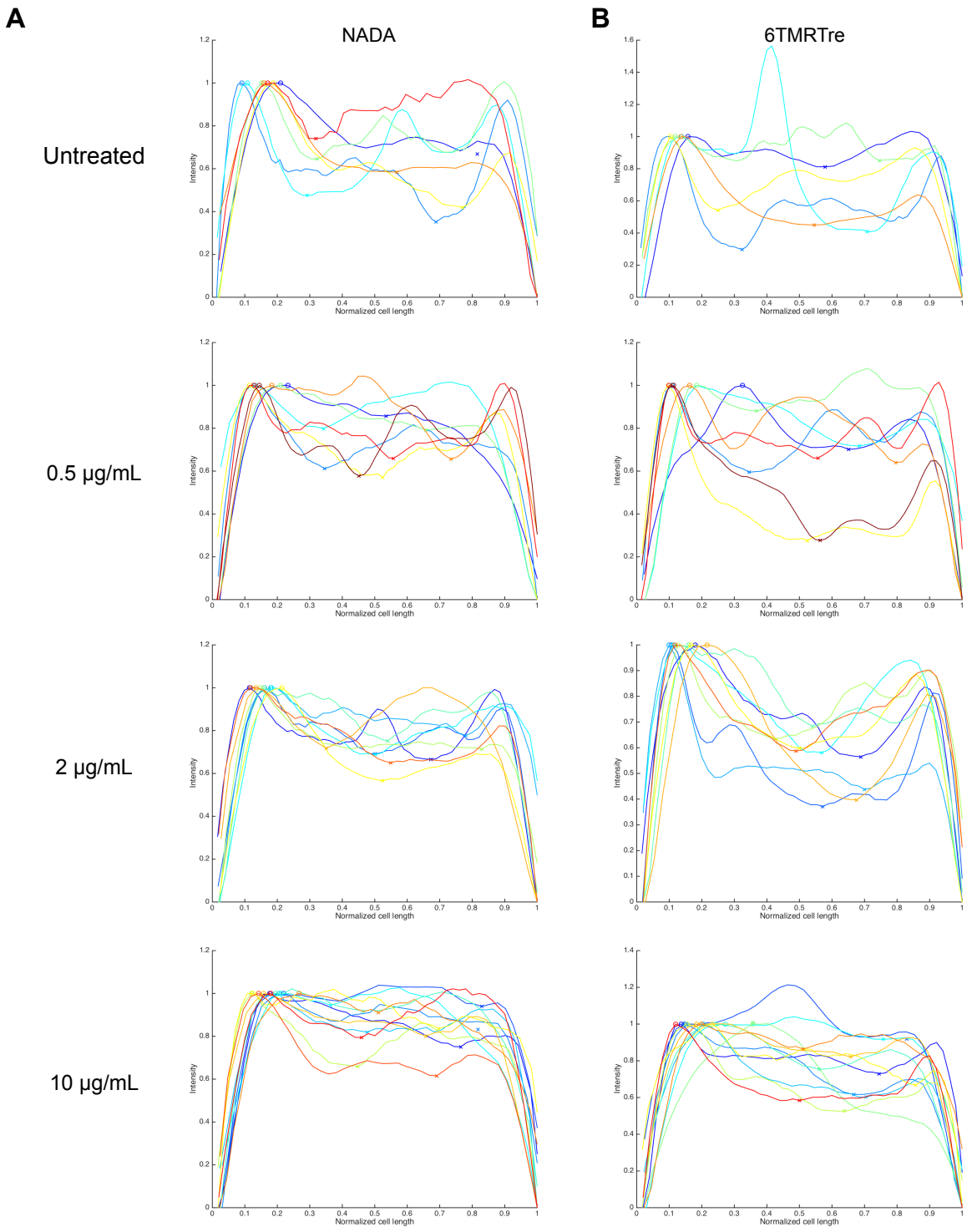

Figure 3.15 Cell length fluorescence traces for *M. marinum* cells labeled with metabolic reporters during EB treatment. Cells were aligned with brightest pole at the origin of the graph and normalized fluorescence intensity was plotted on the y-axis. Empty circles represent highest fluorescent intensity residing at the pole, while crosses lowest fluorescence intensity used

to calculated polarity index. These measurements were applied to both NADA (A) and 6-TMR-Tre (B) labeling profiles.

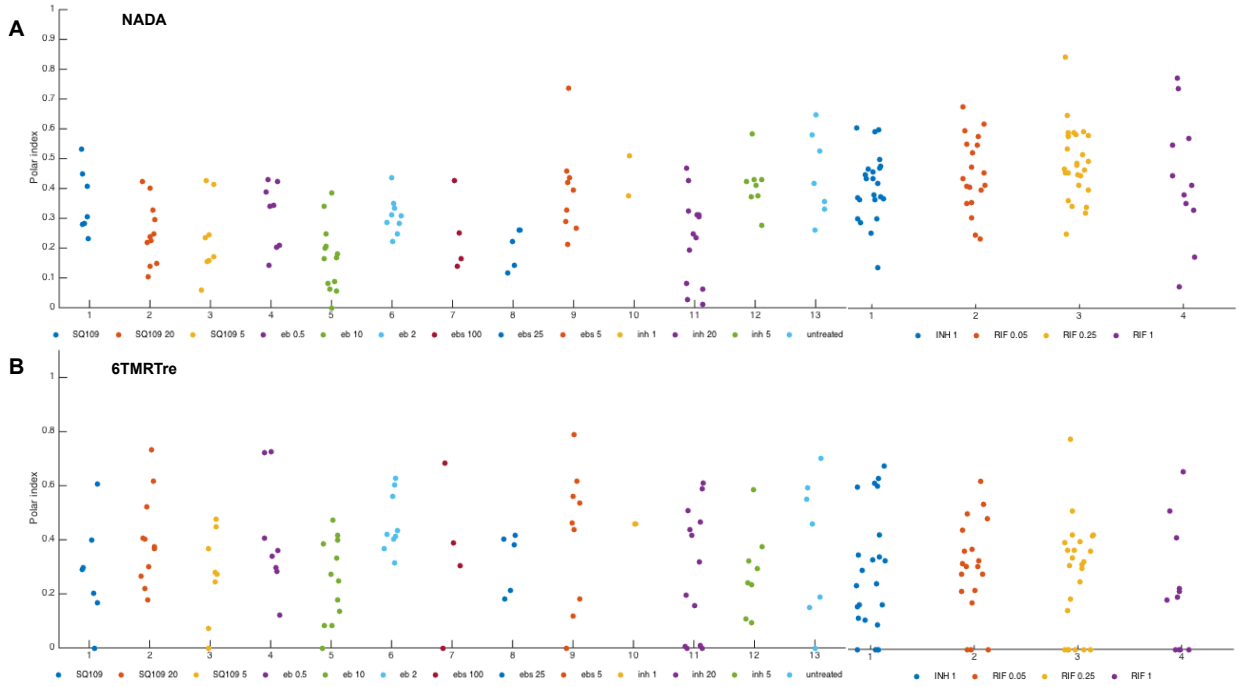

Figure 3.16 Front-line TB drugs alter cell wall metabolic labeling profile in *M. marinum*. Cells were incubated with NADA and 6-TMR-Tre reporters during short 2h drug treatment with EB, INH, SQ109, and rifampicin. Cell length fluorescence traces were obtained to measure spatial distribution of labeling intensity. Polarity index was calculated by dividing lowest intensity along the cell length by the highest intensity localized to the pole for NADA (A) and 6-TMR-Tre (B) channels.

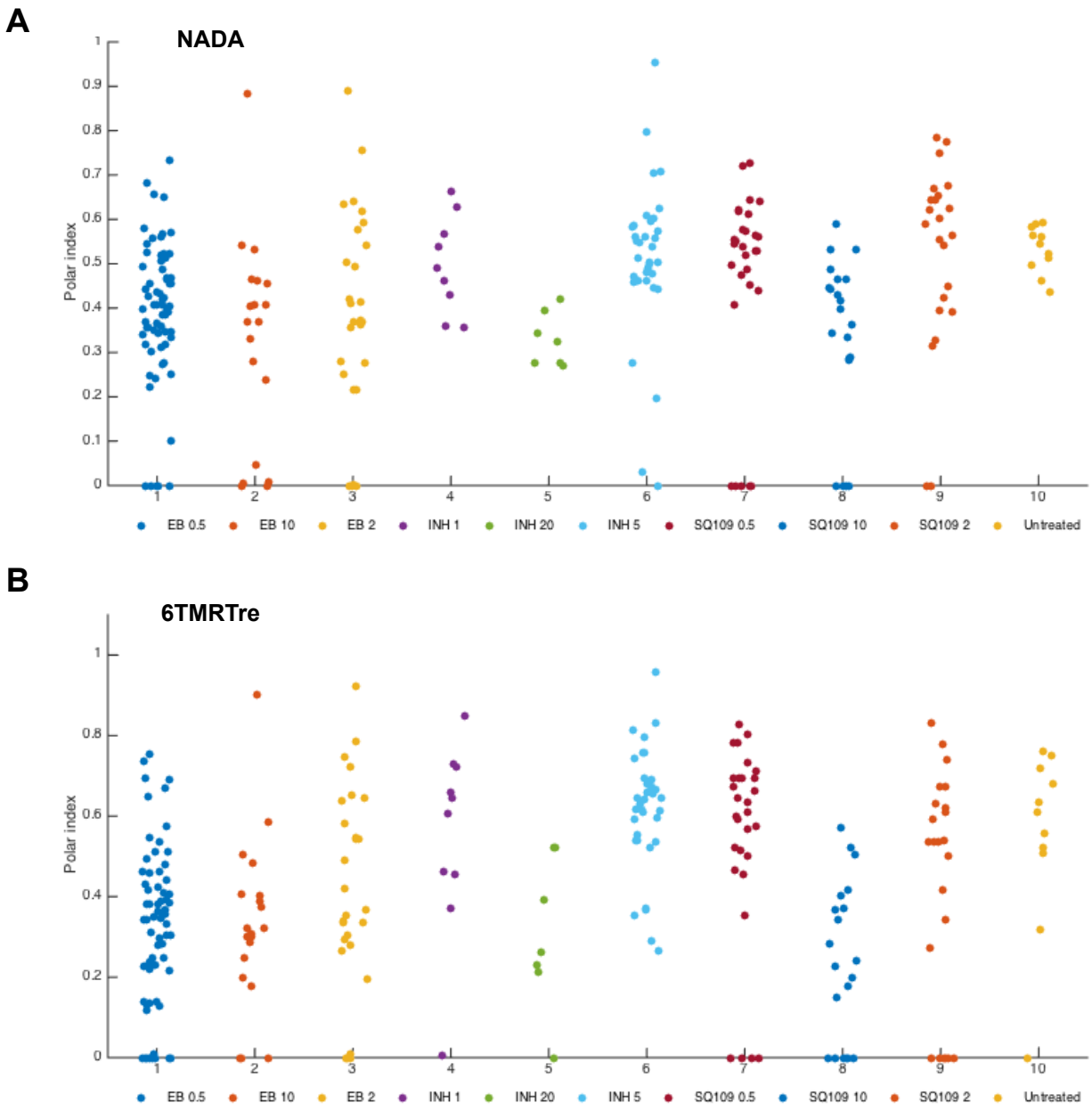

Figure 3.17 Front-line TB drugs alter cell wall metabolic labeling profile in *M. smegmatis*. Cells were incubated with NADA and 6-TMR-Tre reporters during short 2h drug treatment with EB, INH, SQ109, and rifampicin. Cell length fluorescence traces were obtained to measure spatial distribution of labeling intensity. Polarity index was calculated by dividing lowest intensity along the cell length by the highest intensity localized to the pole for NADA (A) and 6-TMR-Tre (B) channels.

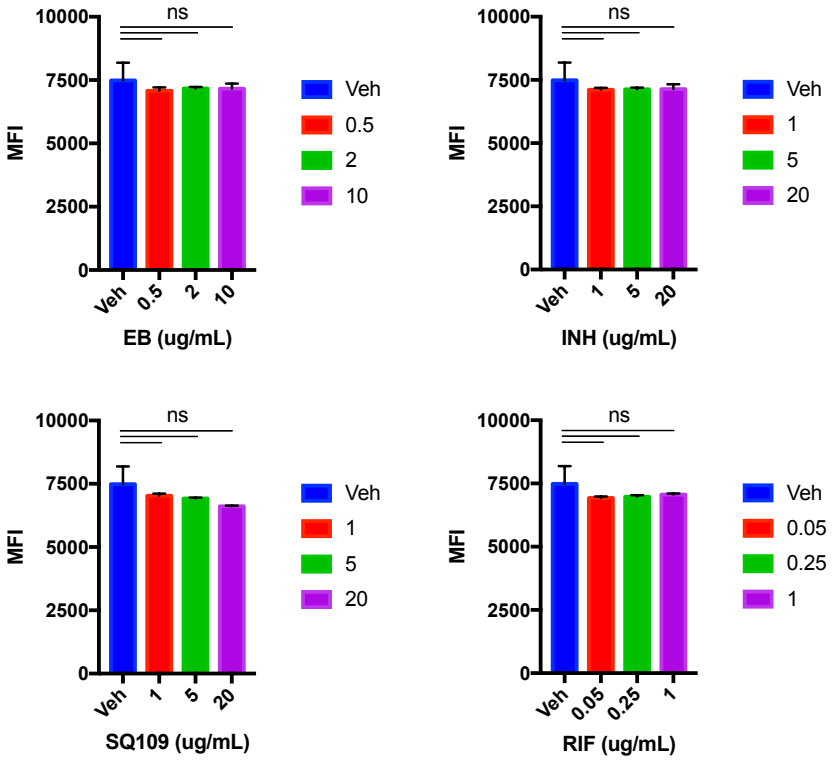

Figure 3.18 *iniBAC* regulon is not activated during short drug treatment in *M. marinum* reporter strain. Error bars depict standard deviation of three replicate experiments. Results are representative of at least two independent experiments. Statistical significance is given by $*P < 0.05$, $**P < 0.01$, $***P < 0.001$. Mean fluorescence intensity (MFI)

CONCLUSION

The TB field has been frustrated with the lack of new therapeutic alternatives to treat patients. Ever-increasing drug resistance threatens our ability to control disease dissemination. It has become more clear that understanding the mechanism of drug action is essential to tease apart the underlying changes occurring at the metabolic[46,47] and epigenetic levels.[48] However, far less is known about the native state of the cell wall, which constitutes the first barrier to develop therapeutics and is primarily composed of non-genetically encoded products. Current knowledge encompasses morphological changes observed by electron microscopy,[40] cell wall signatures by surface-enhanced Raman scattering detection,[49] and genetic reprograming[35–39] after drug exposure, forming an incomplete and static view of cell wall physiology.

In this chapter, we developed metabolic reporters to study mycobacterial cell wall architecture by super resolution microscopy, including pathogenic *M. marinum*. Our results suggests that mycobacteria undergo cell wall maturation or remodeling during growth in rich media as observed by incorporation of 6-TMR-Tre in the side-wall of cells. Combination of this metabolic reporter with NADA allowed the real-time dual visualization of PG and TMM dynamics, highlighting analysis of single cell heterogeneity in the population. We extended our studies to front-line TB drug treatment and discovered drug-specific metabolic labeling profiles.

Notably, ethambutol treatment, regardless of the concentration tested, resulted in a redirection of the cell wall remodeling program from a polar to a side-wall phenotype. Even though the polar region of mycobacteria was proposed to be the Achilles heel of mycobacteria,[30] our work argues that cell wall biosynthesis or remodeling enzymes can be localized to the side-wall during drug treatment. In addition, we were able to capture cell wall dynamics as early as 2 h during drug treatment, which can be challenging to identify by genetic approaches.

Our approach is well suited for direct translation into *in vivo* model of tuberculosis pathogenesis in zebrafish.[50–53] Interrogation of cell wall dynamics during *in vivo* infection by fluorescence microscopy could shed light into highly relevant host-pathogen interactions. Importantly, addressing how drug tolerance is achieved as a result of host pressures[54] in the context of the mycobacterial cell wall is key to eliminating the discordance in drug efficacy from *in vitro* studies to clinical therapy of patients.

MATERIALS AND METHODS

General methods for synthesis

Materials and reagents were obtained from commercial sources without further purification unless otherwise noted. Anhydrous solvents were obtained either commercially or from an alumina column solvent purification system. All reactions were carried out in oven-dried glassware under nitrogen unless otherwise noted. Analytical TLC was performed on SiliCycle glass-backed silica gel 60 Å plates (thickness 250 μm) and detected by UV lamp or charring with 5% H_2SO_4 in MeOH. Column chromatography was performed using SiliCycle SiliaFlash P60 silica gel (40-63 μm). ^{1}H NMR spectra were recorded at 500 MHz with chemical shifts in ppm referenced to solvent peaks. ^{13}C NMR spectra were recorded at 125 MHz with chemical shifts referenced to solvent peaks. NMR spectra were obtained on Varian AV-500 instrument. Coupling constants (*J*) are reported in hertz (Hz). High-resolution electrospray ionization mass spectrometry (HR ESI MS) was performed at the Stanford University Mass Spectrometry Facility.

Reversed-phase HPLC was performed on a Varian Pro Star system with a Varian UV-Vis detector model 345 (210, 254 nm) on a Dynamax Microsorb C-18 preparative column (21.4 x 250 mm) at a flow rate of 20 mL/min or on an Agilent Eclipse XDB-C18 5μm semi-preparative column (9.4 x 250 mm) at a flow rate of 3 mL/min.

6-TreAz,[20] NADA [15], and 6-FlTre were synthesized as previously reported.

Synthesis of 6-TMR-Tre

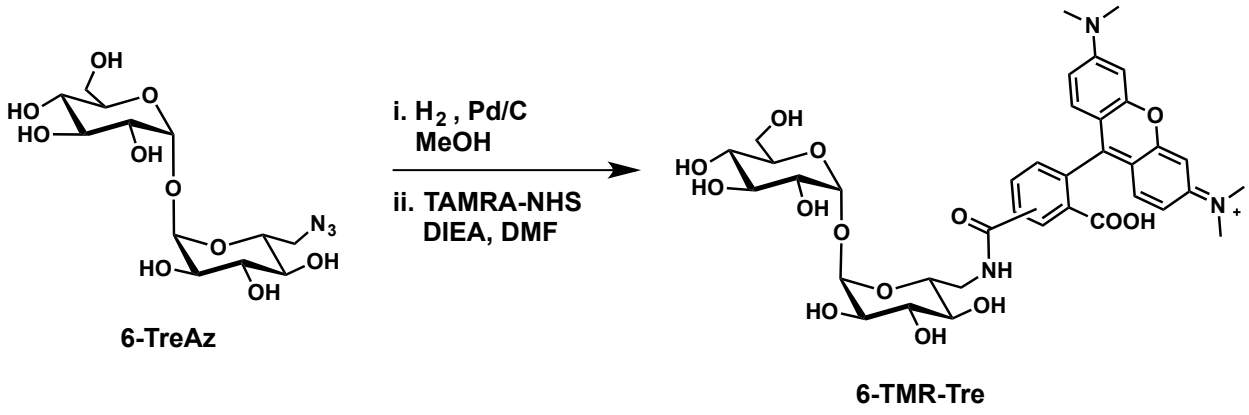

***(TAMRA-5-yl)-6-amido-6-deoxy-α,α-D-trehalose* (6-TMR-Tre, 3.1)**

To a stirring solution of 6-TreAz in anhydrous MeOH (at a final concentration of 20 mM) under argon atmosphere, 10% Pd/C was added to the reaction mixture. A hydrogen-filled balloon was connected to the reaction flask to replace the argon atmosphere and stirred overnight at room temperature. The reaction mixture was filtered through celite and concentrated by rotary evaporation to afford the amine-trehalose product. Without further purification, 6-amino-trehalose (5.1 mg, 0.015 mmol, 1.0 eq) was subjected to a reaction with TAMRA-NHS (7.7 mg, 0.015 mmol, 1.0 eq) after dissolving in anhydrous DMF and treated with DIPEA (6 μL, 0.034 mmol, 2.2 eq). Reaction mixture was stirred for 5 h at room temperature and concentrated.

Desired product was purified by reverse-phase HPLC using a 5-100% MeCN/H_2O + 0.1%TFA gradient.

6-TMR-Tre (9.0 mg, 80% yield) was obtained as a purple solid. R_f = 0.08 (1:2:2 H_2O:EtOAc:IPA, visualized with 5% H_2SO_4 in MeOH) ^{1}H NMR (500 MHz, d_6-DMSO): δ 3.07 (t, J = 9.3 Hz, 1H), 3.12 (t, J = 9.3 Hz, 1H), 3.30 (dd, J = 9.5, 3.7 Hz, 1H), 3.45 – 3.55 (m, 5H), 3.56 – 3.61 (m, 3H), 3.64 – 3.69 (m, 4H), 3.93 (td, J = 6.9, 3.3 Hz, 2H), 4.92 (d, J = 3.6 Hz, 2H), 6.96 (s, 2H), 7.06 (q, J = 9.9, 9.4 Hz, 4H), 7.58 (d, J = 7.9 Hz, 1H), 8.28 (dd, J = 7.9, 1.7 Hz, 1H), 8.67 (d, J = 1.7 Hz, 1H), 8.75 (t, J = 5.8 Hz, 1H). ^{13}C NMR (125 MHz, d_6-DMSO): δ 41.24, 41.52, 61.35, 70.68, 71.26, 72.30, 72.34, 72.52, 73.18, 73.27, 73.53, 94.09, 94.20, 96.96, 131.31, 136.72, 157.28, 157.38, 157.46, 157.53, 157.53, 158.52, 158.78, 166.15, 166.63. HRMS (ESI): Calculated for $C_{33}H_{35}N_2O_{15}S$ $[M\text{-}Na]^+$ 777.2637, found 777.2645.

Bacterial strains, media, and reagents

Bacterial strains used in this work include *Corynebacterium glutamicum* 534, *Mycobacterium smegmatis* mc^{2}155 and *Mycobacterium marinum* M. *C. glutamicum* was cultured in brain heart infusion (BHI) media at 30 ^{o}C. *M. smegmatis* was cultured in Middlebrook 7H9 media supplemented with 10% ADC (albumin, dextrose, catalase), 0.5% glycerol, and 0.05% tween 80 at 37 ^{o}C. *M. marinum* was cultured in Middlebrook 7H9 media supplemented with 10% OADC (oleic acid, albumin, dextrose, catalase), 0.5% glycerol, and 0.05% tween 80 at 33 ^{o}C. *Escherichia coli* K12 MG1655 and *Bacillus subtilis* 168 were cultured in Luria broth (LB) at 37 ^{o}C. All strains were obtained from the American Type Culture Collection (ATCC).

Stock solutions of 6-TMR-Tre and NADA were prepared at 10 mM and 100 mM in DMSO, respectively, and stored at -20 ^{o}C. Other reagent stocks include ethambutol (Sigma Aldrich, 4 mg/mL in H_2O, stored at 4 ^{o}C), ebselen (Cayman Chemical, 2 mg/mL in EtOH, stored at -20 ^{o}C), isoniazid (Sigma Aldrich, 2 mg/mL in H_2O, stored at 4 ^{o}C), SQ109 (Sigma Aldrich, 10 mM in DMSO, stored at -20 ^{o}C), and rifampicin (Sigma Aldrich, 3 mg/mL in DMSO, stored at -20 ^{o}C). Stock solutions of TDL and 6-FlTre were prepared at 25 mM and 10 mM, respectively, in DMSO and stored at -20 ^{o}C.

Bacterial metabolic labeling conditions

Single colonies were used to start stationary phase cultures, which were used to innoculate experimental cultures for all bacterial strains. Cells were grown in aerated culture tubes or 96-well plates with shaking until the desired optical density was achieved. Bacterial cultures in exponential growth phase were incubated with trehalose probes until designated end-point of the experiment. Bacterial cells were fixed prior to flow cytometry or fluorescence microscopy unless otherwise noted.

For 6-TMR-Tre labeling, *C. glutamicum, M. smegmatis*, and *M. marinum* were incubated with 100 μM trehalose reporter for time periods encompassing several doubling times unless otherwise noted. *B. subtilis* and E. *coli* were exposed to 6-TMR-Tre analogs for 2 h during exponential growth phase.

For *in vitro* pulse-chase experiments, bacteria were labeled with 100 μM 6-TMR-Tre reporter. Trehalose competition experiments included co-incubation of native trehalose at 0, 0.5 or 5.0

mM and trehalose reporter in *C. glutamicum, M. smegmatis*, and *M. marinum* cultures, for 2, 3, and 4 hours respectively. Bacterial cells were incubated with 100 μM 6-TMR-Tre and treated with 20, 50, or 100 μg/mL ebselen, in *C. glutamicum* (2 h), *M. smegmatis* (3 h), and *M. marinum* (4 h) respectively.

For mycomembrane mobility experiments, *C. glutamicum* and *M. smegmatis* were labeled with 100 μM 6-FlTre for several generations, washed to remove excess reporter and chased with TDL for different 5 – 30 min. TDL was used at a final concentration of 250 μM for pulse-chase labeling experiments.

Antibiotic or drug treatment experiments involving *M. smegmatis* and *M. marinum* were conducted as follows: 1) inoculated cultures were labeled with 100 μM 6-TMR-Tre for several generations; 2) treated with different concentrations of drugs during log phase; 3) washed excess reporter and drug with growth media; 4) incubated with 1 mM NADA for 20 min; 5) washed with growth media, fixed, and prepared samples for microscopy. This experiment was carried out in a 96-well plate to simultaneously evaluate ebselen, ethambutol, isoniazid and SQ109. The same experiments were carried out with 100 μM 6-FlTre and 25 μM TDL reporter pair.

Drug treatment	***M. smegmatis*** (μg/mL)	***M. marinum*** (μg/mL)
Ebselen	2 10 50	5 20 100
Ethambutol	0.5 2 10	0.5 2 10
Isoniazid	1 5 10	1 5 20
SQ109	0.5 2 10	1 5 20
Rifampicin	5 20 100	0.05 0.25 1

In a similar fashion, new cell wall biosynthesis was evaluated in *M. smegmatis* and *M. marinum* with 100 μM 6-TMR-Tre and 1 mM NADA during a 2 h antibiotic treatment (see table above).

Evaluation of elongation rate and growth during antibiotic treatment (see table above) are described below. Cells were washed with PBS + 0.05% tween 80 (PBST) and labeled with 0.05 mg/mL AF488 NHS for 30 min at room temperature. Cell were then washed with PBST and resuspended in growth media. Treatment with antibiotics (2 h) was carried out at the concentrations listed above for ebselen, ethambutol, isoniazid and SQ109. Cells were fixed immediately and prepared for fluorescence microscopy.

Flow cytometry
Fluorescently labeled cells were analyzed in 96-well plate format in a BD Biosciences Accuri C6 flow cytometer equipped with a BD C-Sampler. Data was collected for 100,000 events at a rate of > 5,000 events/s for each sample. All flow cytometry experiments were performed in triplicate where results are representative of at least two independent experiments.

Widefield fluorescence microscopy
Bacterial cultures (1-3 μL) were spotted on 1% agarose pads mounted on glass slides, installed coverslip, and sealed with nail polish. Fluorescence imaging was performed with a Nikon A1R resonant scanning confocal microscope using a CFI Plan Apo Lambda 60x oil objective. Images were captured and processed with NIS Elements software. Acquisition and processing of images was performed identically for control and test samples.

Structured illumination microscopy (SIM)
Samples were mounted on agarose pads with Vectashield using high performance coverslips #1.5 (18 mm x 18 mm, Zeiss) and sealed with nail polish. Fluorescence images were acquired with OMX Blaze 3-D structure illumination microscope (Applied Precision, Inc.) fitted with a U-PLANAPO 100X SIM objective (NA = 1.4). Acquisition parameters included 15 images per z-section, where each plane was separated by 125 nm, with DeltaVision OMX software. Raw data was processed with softWoRx software to generate SI image reconstruction.

Single-cell fluorescence microscopy analysis
Raw images were analyzed with in-house Matlab algorithm.

Isolation and purification of free glycolipids
Bacterial cultures incubated with trehalose probes were washed two times with corresponding growth media to remove excess reporter. Wet cell pellets were subjected to organic extraction by adding 1 mL 2:1 $CHCl_3$:MeOH and stirring vigorously in conical glass tubes overnight. Resulting heterogeneous mixture was centrifuged for 10 min at 3700 x g, clarified organic layer supernatant was saved and cell pellet was re-extracted twice with the same protocol. Combined organic layers recovered after centrifugation were concentrated and analyzed by HPTLC (Uniplate HPTLC-GHL, 5 x 5 cm, 150 μm thickness) developed with 65:25:4 $CHCl_3$:MeOH:H_2O. Fluorescently labeled glycolipids developed in HPTLC plates were imaged with typhoon scanner (Amersham Biosciences, Typhoon 9410). Free lipids were partially purified by preparative TLC (Analtech, 20 x 20 cm, 1 mm thickness).

In addition, partially purified fluorescent glycolipids were dissolved in 1 mL 2:1 $CHCl_3$:MeOH. Labeling efficiency of free glycolipids was assessed by fluorimetry. Fluorescence spectra were recorded on a Photon Technology International Quanta Master 4 L-format scanning spectrofluorometer equipped with an LPS-220B 75-W xenon lamp and power supply, A-1010B lamp housing with an integrated igniter, switchable 814 photon counting/analog photomultiplier detection unit, and MD5020 motor driver. Measurements were made in 1 cm x 0.4 cm quartz cuvettes with a total sample volume of 1 mL.

Statistics
p-values between samples were calculated with student paired t-tests.

REFERENCES

1. WHO | Global tuberculosis report 2015. *WHO* Available at: http://www.who.int/tb/publications/global_report/en/. (Accessed: 2nd May 2016)
2. Malherbe, S. T. *et al.* Persisting positron emission tomography lesion activity and Mycobacterium tuberculosis mRNA after tuberculosis cure. *Nat. Med.* **advance online publication,** (2016).
3. Esmail, H. *et al.* Characterization of progressive HIV-associated tuberculosis using 2-deoxy-2-[18F]fluoro-D-glucose positron emission and computed tomography. *Nat. Med.* **22,** 1090–1093 (2016).
4. Zumla, A., Nahid, P. & Cole, S. T. Advances in the development of new tuberculosis drugs and treatment regimens. *Nat. Rev. Drug Discov.* **12,** 388–404 (2013).
5. Cole, S. T. Inhibiting Mycobacterium tuberculosis within and without. *Phil Trans R Soc B* **371,** 20150506 (2016).
6. Russell, D. G. Mycobacterium tuberculosis: here today, and here tomorrow. *Nat. Rev. Mol. Cell Biol.* **2,** 569–586 (2001).
7. Philips, J. A. & Ernst, J. D. Tuberculosis Pathogenesis and Immunity. *Annu. Rev. Pathol. Mech. Dis.* **7,** 353–384 (2012).
8. Jarlier, V. & Nikaido, H. Mycobacterial cell wall: Structure and role in natural resistance to antibiotics. *FEMS Microbiol. Lett.* **123,** 11–18 (1994).
9. Zhang, Y. The Magic Bullets and Tuberculosis Drug Targets. *Annu. Rev. Pharmacol. Toxicol.* **45,** 529–564 (2005).
10. Manina, G., Dhar, N. & McKinney, J. D. Stress and Host Immunity Amplify Mycobacterium tuberculosis Phenotypic Heterogeneity and Induce Nongrowing Metabolically Active Forms. *Cell Host Microbe* **17,** 32–46 (2015).
11. Richardson, K. *et al.* Temporal and intrinsic factors of rifampicin tolerance in mycobacteria. *Proc. Natl. Acad. Sci.* 201600372 (2016). doi:10.1073/pnas.1600372113
12. Jankute, M., Cox, J. A. G., Harrison, J. & Besra, G. S. Assembly of the Mycobacterial Cell Wall. *Annu. Rev. Microbiol.* **69,** 405–423 (2015).
13. Marrakchi, H., Lanéelle, M.-A. & Daffé, M. Mycolic Acids: Structures, Biosynthesis, and Beyond. *Chem. Biol.* **21,** 67–85 (2014).
14. Siegrist, M. S., Swarts, B. M., Fox, D. M., Lim, S. A. & Bertozzi, C. R. Illumination of growth, division and secretion by metabolic labeling of the bacterial cell surface. *FEMS Microbiol. Rev.* **39,** 184–202 (2015).
15. Kuru, E. *et al.* In Situ Probing of Newly Synthesized Peptidoglycan in Live Bacteria with Fluorescent D-Amino Acids. *Angew. Chem. Int. Ed.* **51,** 12519–12523 (2012).
16. Siegrist, M. S. *et al.* d-Amino Acid Chemical Reporters Reveal Peptidoglycan Dynamics of an Intracellular Pathogen. *ACS Chem. Biol.* **8,** 500–505 (2013).
17. Shieh, P., Siegrist, M. S., Cullen, A. J. & Bertozzi, C. R. Imaging bacterial peptidoglycan with near-infrared fluorogenic azide probes. *Proc. Natl. Acad. Sci.* **111,** 5456–5461 (2014).
18. Kuru, E., Tekkam, S., Hall, E., Brun, Y. V. & Van Nieuwenhze, M. S. Synthesis of fluorescent D-amino acids and their use for probing peptidoglycan synthesis and bacterial growth in situ. *Nat. Protoc.* **10,** 33–52 (2015).
19. Backus, K. M. *et al.* Uptake of unnatural trehalose analogs as a reporter for Mycobacterium tuberculosis. *Nat. Chem. Biol.* **7,** 228–235 (2011).

20. Swarts, B. M. *et al.* Probing the Mycobacterial Trehalome with Bioorthogonal Chemistry. *J. Am. Chem. Soc.* **134,** 16123–16126 (2012).
21. Urbanek, B. L. *et al.* Chemoenzymatic Synthesis of Trehalose Analogues: Rapid Access to Chemical Probes for Investigating Mycobacteria. *ChemBioChem* **15,** 2066–2070 (2014).
22. Foley, H. N., Stewart, J. A., Kavunja, H. W., Rundell, S. R. & Swarts, B. M. Bioorthogonal Chemical Reporters for Selective In Situ Probing of Mycomembrane Components in Mycobacteria. *Angew. Chem. Int. Ed.* **55,** 2053–2057 (2016).
23. Rundell, S. R. *et al.* Deoxyfluoro-D-trehalose (FDTre) analogues as potential PET probes for imaging mycobacterial infection. *Org. Biomol. Chem.* **14,** 8598–8609 (2016).
24. Stinear, T. P. *et al.* Insights from the complete genome sequence of Mycobacterium marinum on the evolution of Mycobacterium tuberculosis. *Genome Res.* **18,** 729–741 (2008).
25. Backus, K. M. *et al.* The Three Mycobacterium tuberculosis Antigen 85 Isoforms Have Unique Substrates and Activities Determined by Non-active Site Regions. *J. Biol. Chem.* **289,** 25041–25053 (2014).
26. Fernández-Suárez, M. & Ting, A. Y. Fluorescent probes for super-resolution imaging in living cells. *Nat. Rev. Mol. Cell Biol.* **9,** 929–943 (2008).
27. Dempsey, G. T., Vaughan, J. C., Chen, K. H., Bates, M. & Zhuang, X. Evaluation of fluorophores for optimal performance in localization-based super-resolution imaging. *Nat. Methods* **8,** 1027–1036 (2011).
28. Lee, M. K., Rai, P., Williams, J., Twieg, R. J. & Moerner, W. E. Small-Molecule Labeling of Live Cell Surfaces for Three-Dimensional Super-Resolution Microscopy. *J. Am. Chem. Soc.* **136,** 14003–14006 (2014).
29. Erdmann, R. S. *et al.* Super-Resolution Imaging of the Golgi in Live Cells with a Bioorthogonal Ceramide Probe. *Angew. Chem. Int. Ed.* **53,** 10242–10246 (2014).
30. Carel, C. *et al.* Mycobacterium tuberculosis Proteins Involved in Mycolic Acid Synthesis and Transport Localize Dynamically to the Old Growing Pole and Septum. *PLOS ONE* **9,** e97148 (2014).
31. Meniche, X. *et al.* Subpolar addition of new cell wall is directed by DivIVA in mycobacteria. *Proc. Natl. Acad. Sci.* **111,** E3243–E3251 (2014).
32. Favrot, L. *et al.* Mechanism of inhibition of Mycobacterium tuberculosis antigen 85 by ebselen. *Nat. Commun.* **4,** 2748 (2013).
33. Favrot, L., Lajiness, D. H. & Ronning, D. R. Inactivation of the Mycobacterium tuberculosis Antigen 85 Complex by Covalent, Allosteric Inhibitors. *J. Biol. Chem.* **289,** 25031–25040 (2014).
34. Ngo, J. T. *et al.* Click-EM for imaging metabolically tagged nonprotein biomolecules. *Nat. Chem. Biol.* **12,** 459–465 (2016).
35. Wilson, M. *et al.* Exploring drug-induced alterations in gene expression in Mycobacterium tuberculosis by microarray hybridization. *Proc. Natl. Acad. Sci.* **96,** 12833–12838 (1999).
36. Alland, D., Steyn, A. J., Weisbrod, T., Aldrich, K. & Jacobs, W. R. Characterization of the Mycobacterium tuberculosis iniBAC Promoter, a Promoter That Responds to Cell Wall Biosynthesis Inhibition. *J. Bacteriol.* **182,** 1802–1811 (2000).
37. Betts, J. C. *et al.* Signature Gene Expression Profiles Discriminate between Isoniazid-, Thiolactomycin-, and Triclosan-Treated Mycobacterium tuberculosis. *Antimicrob. Agents Chemother.* **47,** 2903–2913 (2003).

38. Boshoff, H. I. M. *et al.* The Transcriptional Responses of Mycobacterium tuberculosis to Inhibitors of Metabolism NOVEL INSIGHTS INTO DRUG MECHANISMS OF ACTION. *J. Biol. Chem.* **279,** 40174–40184 (2004).
39. Boot, M. *et al.* iniBAC Induction is Vitamin B12 and MutAB-dependent in Mycobacterium marinum. *J. Biol. Chem.* jbc.M116.724088 (2016). doi:10.1074/jbc.M116.724088
40. Tahlan, K. *et al.* SQ109 Targets MmpL3, a Membrane Transporter of Trehalose Monomycolate Involved in Mycolic Acid Donation to the Cell Wall Core of Mycobacterium tuberculosis. *Antimicrob. Agents Chemother.* **56,** 1797–1809 (2012).
41. Takayama, K., Armstrong, E. L., Kunugi, K. A. & Kilburn, J. O. Inhibition by Ethambutol of Mycolic Acid Transfer into the Cell Wall of Mycobacterium smegmatis. *Antimicrob. Agents Chemother.* **16,** 240–242 (1979).
42. Telenti, A. *et al.* The emb operon, a gene cluster of Mycobacterium tuberculosis involved in resistance to ethambutol. *Nat. Med.* **3,** 567–570 (1997).
43. Johnsson, K. & Schultz, P. G. Mechanistic Studies of the Oxidation of Isoniazid by the Catalase Peroxidase from Mycobacterium tuberculosis. *J. Am. Chem. Soc.* **116,** 7425–7426 (1994).
44. Campbell, E. A. *et al.* Structural Mechanism for Rifampicin Inhibition of Bacterial RNA Polymerase. *Cell* **104,** 901–912 (2001).
45. Kilburn, J. O. & Takayama, K. Effects of ethambutol on accumulation and secretion of trehalose mycolates and free mycolic acid in Mycobacterium smegmatis. *Antimicrob. Agents Chemother.* **20,** 401–404 (1981).
46. Gomez, J. E. & McKinney, J. D. M. tuberculosis persistence, latency, and drug tolerance. *Tuberculosis* **84,** 29–44 (2004).
47. Baek, S.-H., Li, A. H. & Sassetti, C. M. Metabolic Regulation of Mycobacterial Growth and Antibiotic Sensitivity. *PLOS Biol* **9,** e1001065 (2011).
48. Adams, K. N. *et al.* Drug Tolerance in Replicating Mycobacteria Mediated by a Macrophage-Induced Efflux Mechanism. *Cell* **145,** 39–53 (2011).
49. Liu, T.-T. *et al.* A High Speed Detection Platform Based on Surface-Enhanced Raman Scattering for Monitoring Antibiotic-Induced Chemical Changes in Bacteria Cell Wall. *PLOS ONE* **4,** e5470 (2009).
50. Tobin, D. M. & Ramakrishnan, L. Comparative pathogenesis of Mycobacterium marinum and Mycobacterium tuberculosis. *Cell. Microbiol.* **10,** 1027–1039 (2008).
51. Ramakrishnan, L. Revisiting the role of the granuloma in tuberculosis. *Nat. Rev. Immunol.* **12,** 352–366 (2012).
52. Cronan, M. R. & Tobin, D. M. Fit for consumption: zebrafish as a model for tuberculosis. *Dis. Model. Mech.* **7,** 777–784 (2014).
53. Takaki, K., Davis, J. M., Winglee, K. & Ramakrishnan, L. Evaluation of the pathogenesis and treatment of Mycobacterium marinum infection in zebrafish. *Nat. Protoc.* **8,** 1114–1124 (2013).
54. Liu, Y. *et al.* Immune activation of the host cell induces drug tolerance in Mycobacterium tuberculosis both in vitro and in vivo. *J. Exp. Med.* **213,** 809–825 (2016).

Chapter 4

Mapping Cell Wall Biosynthesis During Cell Growth and Division in Actinobacteria

This work was adapted in part from Rodriguez-Rivera, F. P.*; Zhou, X.*; Theriot, J. A.; Bertozzi, C. R. Mapping cell wall biosynthesis during cell growth and division in Actinobacteria. Rodriguez-Rivera, F. P. and Zhou, X. contributed equally to this work.

Chapter 4. Mapping Cell Wall Biosynthesis During Cell Growth and Division in Actinobacteria

INTRODUCTION

Actinomycetes include species from *Corynebacteria*, *Mycobacteria*, *Nocardia*, and *Rhodoccocus* families. Beyond highly studied mycobacterial pathogens, well-characterized members among corynebacteria include *C. glutamicum*[1] and human pathogen *C. diphtheriae*.[2] In addition, both *N. asteroides* and *N. brasiliensis* have also been identified as human pathogens involved in lung infections.[3,4] The aforementioned actinobacterial species share high similarities in the composition and structure of the bacterial cell wall.[5,6] In particular, many efforts have been devoted to the structural characterization of cell wall components in both corynebacterial and mycobacterial species,[7–9] as well as visualization by electron microscopy methods.[10,11] The complexity in their cell wall arises from elaboration of the mycolyl-arabinogalactan-peptidoglycan (mAGP) covalent polymer, whose inner leaflet of the mycomembrane also supports non-covalently associated glycolipids.[5] Significant deviation between species arises from the core structure of mycolic acids, as mycobacteria can generate mycolic acids up to 90 carbon atoms in length,[6] while corynebacteria harbor shorter versions (22-34 carbon atoms).[12]

Many successful antibiotics target bacterial cell wall biosynthesis to disrupt essential processes during growth and division. Rod-shaped bacteria have been subjected to intensive study to discover key steps as well as enzymes involved during cell division, but efforts have not been focused on actinobacterial species. For example, Gram-negative *Escherichia coli* and Gram-positive *Bacillus subtilis* undergo gradual (in the order of minutes) symmetric daughter cell separation driven by enzymatic remodeling.[13,14] A millisecond daughter cell separation by a mechanical crack propagation in the peripheral ring has been recently described for Gram-positive *Staphylococcus aureus*.[15] In comparison, only a set of positive and negative regulators of cytokinesis are known for corynebacteria[16] while more efforts have focused on mycobacteria.[17] Actinobacteria divide by a process called "V-snapping", where daughter cells remained joined until rapid snapping to form the characteristic V-shape (Figure 4.1).[18–21] However, the exact cell wall layer that undergoes rupture during V-snapping and the temporal landscape for this process remains unclear.

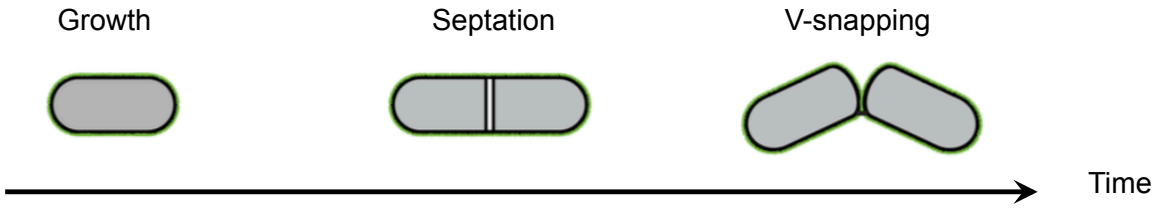

Figure 4.1 Cell growth and division in actinobacteria

Assembly of cell wall components in daughter cells is tightly regulated, but the orchestration of these events is poorly understood for actinobacterial species. Molecular chemical tools have emerged as a useful strategy to visualize cell wall dynamics in live cells.[22] For instance, peptidoglycan biosynthesis occurs at the subpolar region in *M. smegmatis* cells as revealed with unnatural D-amino acid reporters and super resolution microscopy.[23] Additionally,

several groups have directed efforts towards visualizing dynamics of trehalose glycolipids with metabolic trehalose reporters.[24–28] Nonetheless, these methods have not been used in combination to directly interrogate cell wall assembly in actinobacteria during cell growth and division.

In this chapter, we describe a metabolic labeling strategy to simultaneously probe three independent components of the cell wall during bacterial cell division, mainly, peptidoglycan, arabinogalactan, and trehalose mycolates. We utilized unnatural cell wall reporters, amenable to ligation of fluorophores by bioorthogonal chemistry, to visualize how cell wall organization is coordinated in *Corynebacteria* and *Mycobacteria*. This strategy allowed us to map cell wall assembly at the septum, which is built vertically outward. Dynamics of the cell wall reveal that new peptidoglycan and arabinogalactan are actively biosynthesized during septation, but non-covalently membrane-bound glycolipids are only mobilized to the septum right before V-snapping occurs in corynebacteria. We correlated the delayed mobilization of the labeled glycolipids before V-snapping with septal perforations in the peripheral ring. In addition, daughter cell separation was independent of mycolic acids or S-layer, but is driven by turgor pressure. Our data suggests that peptidoglycan is the layer that undergoes mechanical rupture prior to V-snapping and daughter cell separation.

RESULTS AND DISCUSSION

Vertical nature of cell wall assembly at the septum in corynebacteria and mycobacteria

Structurally diverse non-genetically encoded biomolecules make up the majority of the actinobacterial cell wall. Our knowledge base has been focused on understanding enzymatic pathways as well as visualizing dynamics of biosynthetic enzymes during bacterial division, but less so in understanding the very dynamic nature of independent cell wall layers. Gratifyingly, biosynthetic enzymes are permissive to a wide range of site perturbations and can incorporate modified substrates into cell wall components. For example, unnatural D-amino acids are well tolerated by the peptidoglycan biosynthesis machinery and are inserted into the stem peptide, where a D-alanine residue would normally reside.[29–32] At high resolution by electron microscopy, alkyne-D-alanine has allowed visualization of peptidoglycan intermediates residing in the cytoplasmic side of the inner cell membrane.[33] However, secondary labeling reagents can suffer from poor penetrance and non-specific interactions for live-cell imaging purposes. For this reason, we chose to pursue our studies with tetramethylrhodamine-D-lysine (TDL)[29,32] to visualize peptidoglycan dynamics with one-step labeling (Figure 4.2).

Similar to peptidoglycan, trehalose mycolate biosynthesis can be hijacked by unnatural trehalose reporters. Barry, Davis and coworkers probed the promiscuity of Antigen 85 (Ag85) complex with trehalose reporters bearing different functional groups.[24] This enzyme takes two molecules of trehalose monomycolate (TMM) and converts them into trehalose dimycolate (TDM) and free trehalose. The reverse reaction is also possible and is currently hypothesized to mediate unnatural trehalose reporter incorporation. Recently, Swarts and coworkers showed that a short unnatural trehalose ester can serve as a TMM donor, where the short acyl chain can be transesterified onto arabinogalactan.[27] We chose to modify the alkyne version of this reporter (O-alkTMM) with a fluorophore to take advantage of the operational simplicity of one-step labeling. Cu-click reaction of O-alkTMM with azide-AlexaFluor647 afforded O-TMM-647 conjugate(see

Methods section), which could report on arabinogalactan dynamics (Figure 4.2). Finally, 6-FlTre (see synthesis and characterization in Chapter 2), also metabolized by Ag85 activity, was selected to label TMM, an integral component of the mycomembrane (Figure 4.2). O-TMM-647 and 6-FlTre would report on both inner and outer leaflet of the mycomembrane, respectively.

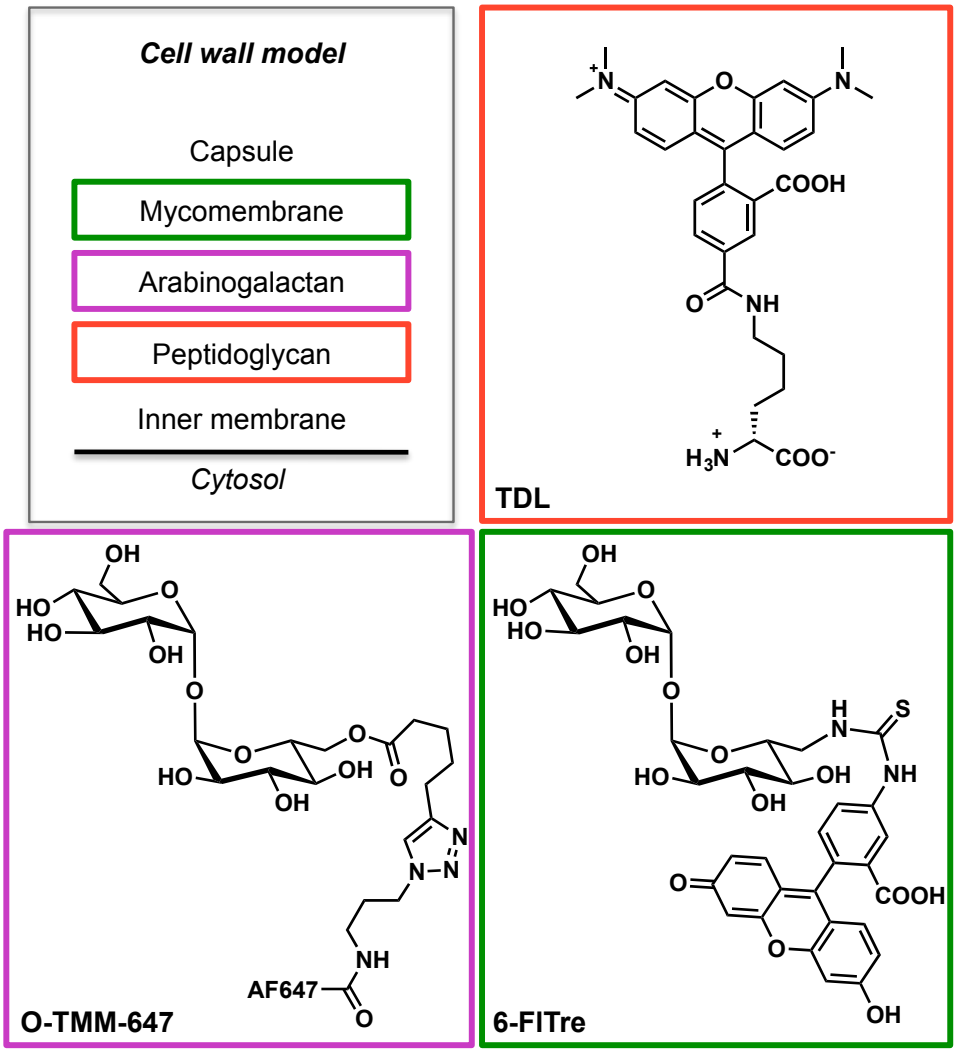

Figure 4.2 Cell wall metabolic labeling strategy in actinobacteria to simultaneously visualize peptidoglycan, arabinogalactan and trehalose mycolate biosynthesis. Reporters TDL, O-TMM-647 and 6-FlTre were used to selectively label peptidoglycan, arabinogalactan and TMM, respectively. Colors of outlined boxes represent cell wall layer as assigned in the cell wall model (upper left corner).

To obtain a better understanding of cell wall dynamics, we selected well-studied *C. glutamicum* and *M. smegmatis* species to perform live cell imaging of metabolically labeled cells. Both of these species share similar structure and composition of individual cell wall components.[5] We proceeded to label cells with 100 μM TDL, 40 μM O-TMM-647 and 100 μM 6-FITre for several doubling times. Cells at various stages of the cell cycle were selected and arranged from left (early) to right (late) according to their fluorescence labeling profile (Figure 4.3). Full coverage of the cell by metabolic staining was expected for this incubation period, but clear differences were observed at the septum. *C. glutamicum* cells showed peptidoglycan staining as the first step toward cell wall biosynthesis at the septum (Figure 4.3A). Arabinogalactan shortly followed as observed by O-TMM-647 labeling. Finally, we observed 6-FlTre labeling corresponding to TMM to be localized to the septum before the cells would undergo V-snapping, after which we still observed fluorescence signal at the septum (far right). Visualization of cell wall biosynthesis at the septum with these metabolic reporters suggested a vertical direction towards building this region of the cell, where the peptidoglycan layer was synthesized first, followed by arabinogalactan, and then trehalose mycolates. Furthermore, labeling of *M. smegmatis* cells demonstrated a very similar metabolic labeling pattern with the observed vertical nature as for *C. glutamicum* (Figure 4.3B). However, short-pulse (5 min) labeling experiments with 6-TMR-Tre (TAMRA installed at the 6-position, see Chapter 3) revealed strong septal signal exclusively for *M. smegmatis*, which suggested de novo TMM biosynthesis at the septum (see results in Chapter 3). This strategy allowed us to define the order of cell wall biosynthesis at the septum of growing *C. glutamicum* and *M. smegmatis* cells. Our results support the high conservation of cell wall architecture among bacteria, but also reveal subtle differences that warrant further investigation.

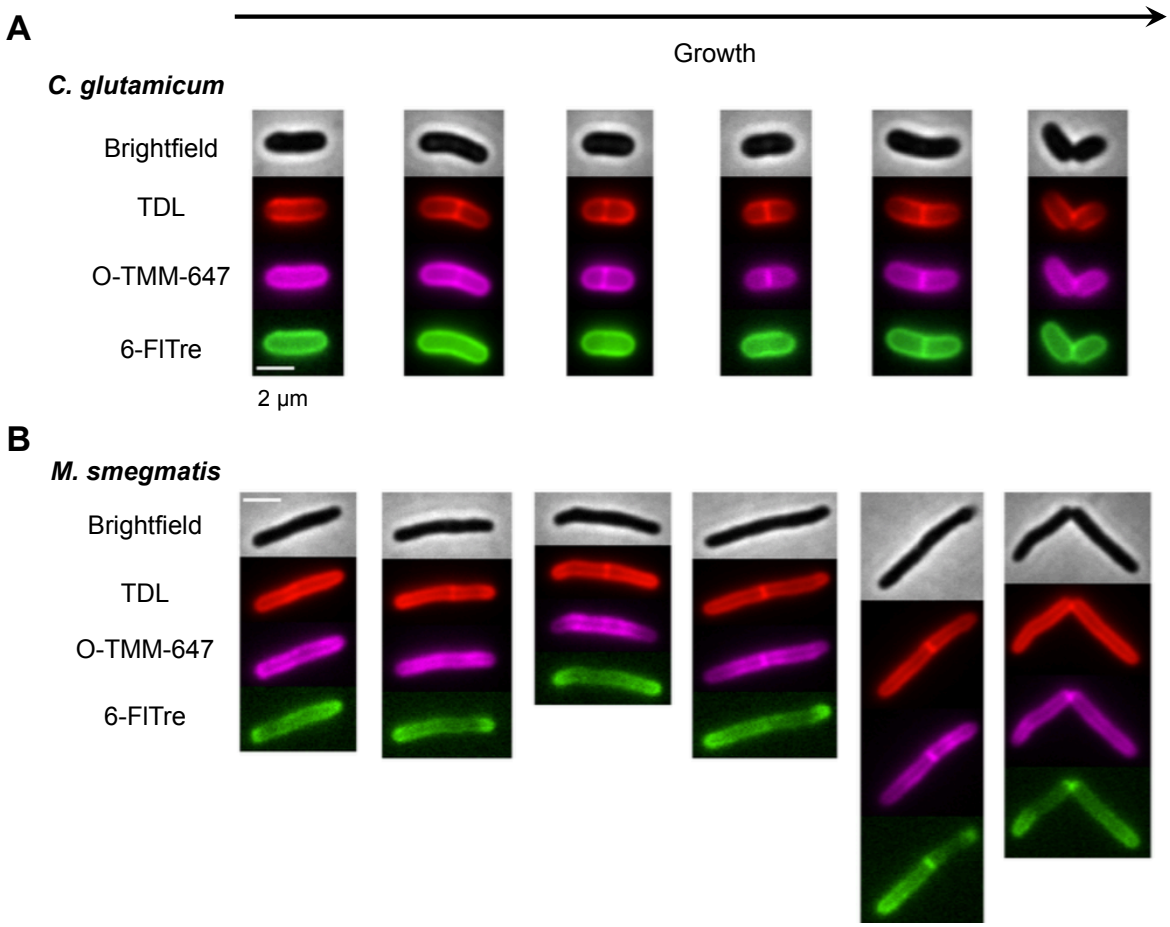

Figure 4.3 Cell wall metabolic labeling in live *C. glutamicum* and *M. smegmatis*. Representative images for triple metabolic labeling of cells grown with TDL (100 µM), O-TMM-647 (40 µM) and 6-FITre (100 µM) for several doubling times are shown forn *C. glutamicum* (A) and *M. smegmatis* (B). Scale, 2 µm

Trehalose mycolates are mobilized to the septum before V-snapping

Next, we wanted to discriminate between active TMM biosynthesis at the septum versus diffusion of labeled glycolipids into this region during growth. The latter hypothesis is supported by mycomembrane fluidity studies in live cells described in Chapter 2 that correlate this phenomenon to mycolic acid structure. We found that *C. glutamicum* FlTre-labeled glycolipids are highly mobile within the native mycomembrane of live cells. To differentiate between these two hypotheses, we examined dynamics of 6-FlTre labeling in live cells within a microfluidic device that would provide temporal control of reporter exposure. To this end, *C. glutamicum* cells were subjected to 5 min labeling periods followed by 1 min washing periods and image capture. We included a non-specific fluorescent membrane dye FM-4-64 (FM) to delineate the cell wall in this experiment. With this platform, FlTre-labeled glycolipids were evenly distributed within the cell surface for the majority of the growth cycle, but only minutes before V-snapping, they were mobilized to the septum (Figure 4.4, indicated by white arrowheads). The

migration of FlTre-labeled trehalose mycolates occurred in the order of minutes, even though FM staining reveal early signal at the septum (second frame from the left). Therefore, the hypothesis of TMM biosynthesis at the septum was ruled out as no labeling was observed in the first ~35 min of the cell cycle.

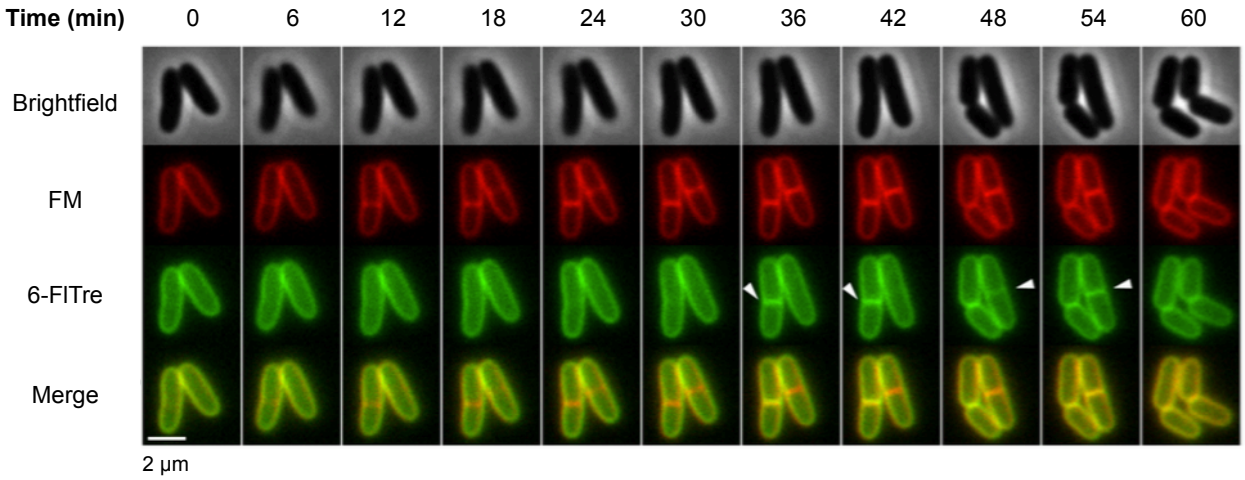

Figure 4.4 FlTre-labeled glycolipids mobilize to the septum right before V-snapping. *C. glutamicum* were subjected to short labeling periods of 6-FlTre and FM dye for 5 min prior to washes and image capture. White arrowheads depict the mobilization of FlTre-labeled glycolipids to the septum prior to V-snapping. Scale 2 µm

To better understand the local environment of the septum, we envisioned installing the solvatochromic fluorophore N,N-dimethylaminonaphthalimide (DMN)[34] on cell wall reporters. This tool could provide information on the delayed mobilization of 6-FlTre labeled glycolipids prior to V-snapping. We hypothesized that mycolylation of arabinogalactan was a prerequisite for FlTre-labeled species to diffuse into the septum. To probe septum hydrophobicity, we installed DMN on the O-TMM reporter by click chemistry to afford O-TMM-DMN (see Methods section). Dual labeling with O-TMM-DMN and -647 reported on both septation progress as well as degree of mycolylation by fluorescence signal stemming from DMN fluorophore (Figure 4.5). We observed good correlation for both reporters at the septum, indicative of mycolyltransferases being present at the septum and engaging in arabinogalactan biosynthesis, while the environment was hydrophobic enough for DMN to fluoresce (Figure 4.5).

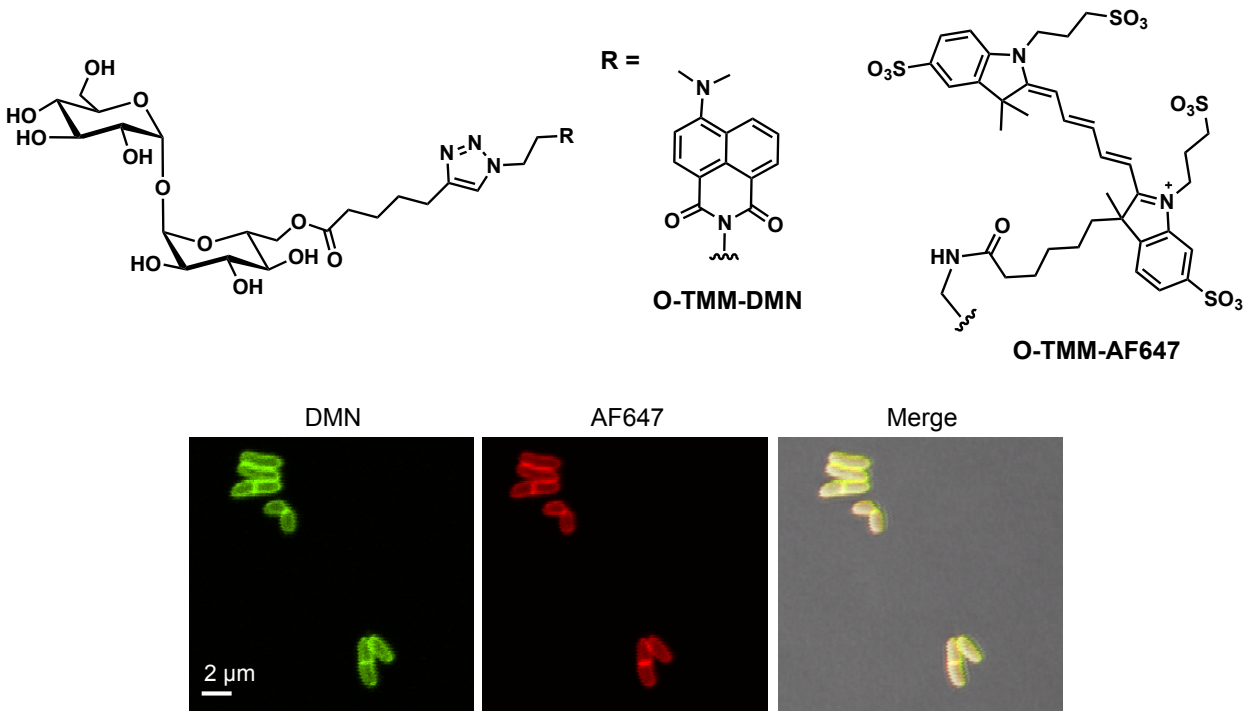

Figure 4.5 Arabinogalactan biosynthesis and mycolylation occurs at the septum as revealed by O-TMM reporter incorporation. Chemical structures of O-TMM-probes with DMN and AF647 fluorophores (top) and representative images of dual labeling of *C. glutamicum* to probe septum hydrophobicity during cell growth are shown. Scale, 2 µm

In order to validate the septal dynamics of O-TMM labeling, we next characterized the incorporation site of these reporters in *C. glutamicum*. We set out to prelabel cells for several generations with different reporters and the appropriate negative and positive controls followed by isolation of mAGPG polymer and extractable lipids. If O-TMM reporters were donating the acyl chain to arabinogalactan, we would hypothesize that most of the fluorescent signal would remain covalently associated with mAGPG polymer. Fluorescence of isolated cell wall components was measured with a fluorimeter after samples were resuspended in toluene for cells labeled with O-TMM-DMN or O-TMM-647 (Figure 4.6). Negative controls such as untreated cells or trehalose and azide-AF647 showed negligible fluorescence under these conditions. Surprisingly, free DMN was found to be tightly associated with mAGPG (Figure 4.6A), presumably due to strong hydrophobic interactions with the corynemycolic acids attached to arabinogalactan. Evaluation of D-ala-DMN indicated exclusive incorporation into mAGPG (fluorescence measurement of this sample in water showed negligible fluorescence, data not shown), which supported selective labeling of peptidoglycan. In turn, O-TMM-DMN was found in both mAGPG core and extractable lipids suggesting that mycolyltransferase activity partially tranesterifies this analog onto arabinogalactan (Figure 4.6A). On the other hand, O-TMM-647 showed a similar profile with incorporation into both isolated fractions (Figure 4.6B). In addition, 6-TreAz modified with AlexaFluor647 by Cu-click was found to exclusively reside in the extractable lipid fraction. Collectively, these results show that O-TMM analogs are partially transferred onto mAGPG, which correlates with observed mobilization of O-TMM species into the septum before V-snapping (highlighted by yellow arrows in Figure 4.7).

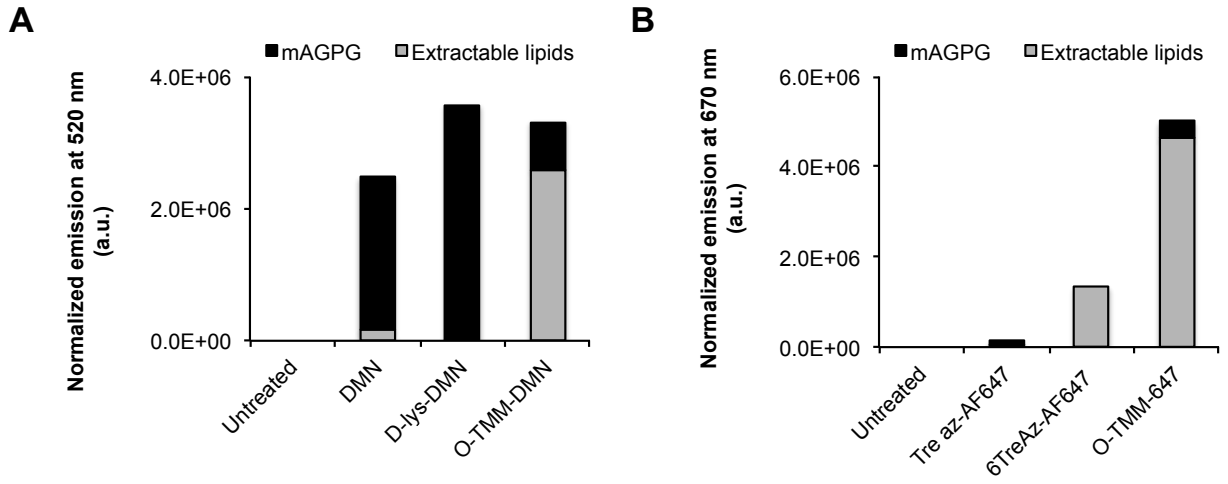

Figure 4.6 O-TMM-fluorophore probes reports on both leaflets of the mycomembrane. Probe destination was characterized in *C. glutamicum* cells when treated with (A) O-TMM-DMN and (B) O-TMM-AF647 in isolated mAGPG and exractable lipids by fluorimetry measurements. Fluorescence signal was normalized to untreated cells in both (A) and (B).

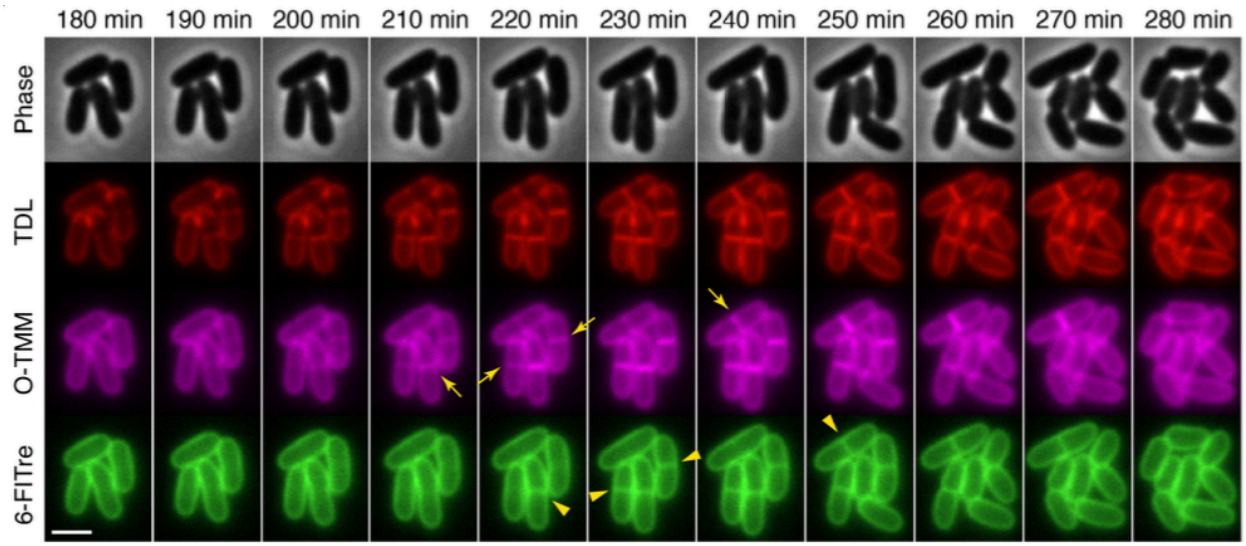

Figure 4.7 O-TMM-647 probe stains arabinogalactan in septum and diffusing species move to the septum prior to V-snapping. Representative images of *C. glutamicum* cells during triple metabolic labeling of cells grown with TDL (100 μM), O-TMM-647 (40 μM) and 6-FITre (100 μM) in microfluidic chamber. Arrows indicate septal incorporation of O-TMM-647 during septation and prior to the increase in septal 6-FITre signal, and arrowheads denote the first appearance of septal labeling with 6-FITre, at which point O-TMM-647 signal also increases at the septum. Scale bar, 2 μm

At this point, our data suggested FlTre-labeling glycolipids are prevented from diffusing into the septum right before V-snapping. However, characterization of O-TMM reporter labeling indicated that the local environment of the septum is hydrophobic enough to fluoresce, which supported that mycolylation of arabinogalactan precedes glycolipid mobilization. We hypothesized that inhibiting arabinogalactan synthesis would negatively impact septum mobilization and daughter cell separation. Thus, we chose to treat cells with ethambutol, which directly inhibits installation of the distal arabinose residue on arabinogalactan, therefore decreasing the number of mycolylated sites.[35,36] Cells were labeled with 6-FlTre and FM dye in the presence of 50 μg/mL ethambutol for 2 h prior to fluorescence imaging (Figure 4.8). 6-FlTre labeled glycolipids failed to migrate to the septum and the new poles after cells had undergone V-snapping (Figure 4.8A). Furthermore, this high ethambutol concentration delayed daughter separation as most cells presented several septa (Figure 4.8B). Taken together, these results support a more mechanistic understanding of mobilization of FlTre-labeled species during cell division, which is crucial for daughter cell separation.

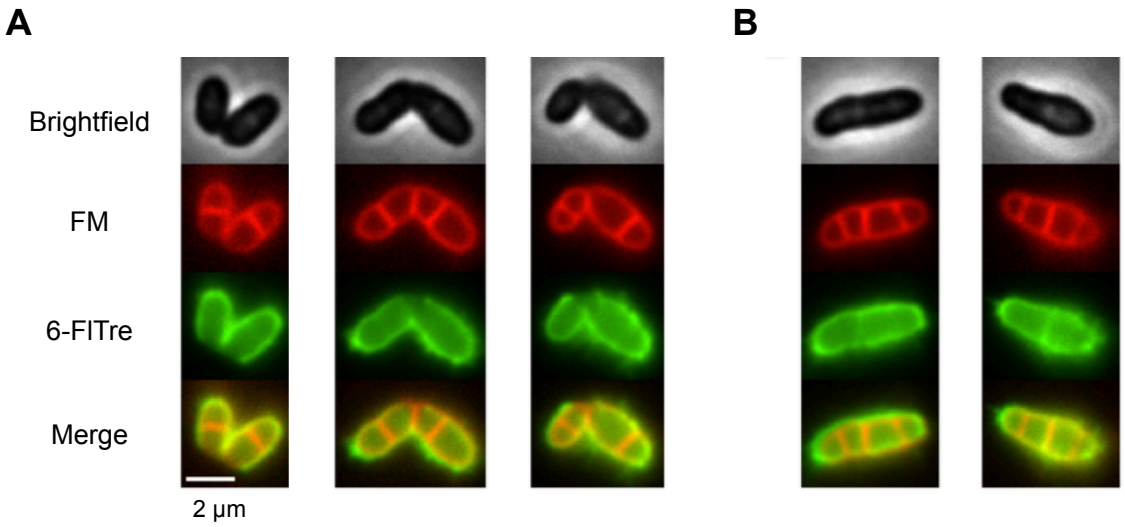

Figure 4.8 Ethambutol treatment prevents mobilization of FlTre-labeled glycolipids and delays daughter cell separation. Cells were grown with 50 μg/ml ethambutol for two hours am incubated with 1 μg/ml FM 4-64 and 100 μM 6-FITre. (A) Representative cells with the septum and new poles devoid of 6-FITre label are shown. (B) Delayed daughter cell separation was also observed, as evaluated by the presence of multiple septa in a single cell. Scale, 2 μm

Septal 6-FlTre-labeling correlates with perforations in the peripheral ring

With the current information in hand, we propose that FlTre-labeled glycolipids reside mostly in the peripheral wall with negligible presence at the septum during septation. These glycolipids can then populate the septal region prior to V-snapping, but only after a physical diffusion barrier has been dissolved, therefore facilitating this process. We hypothesized that the delayed mobilization of FlTre-labeled species was a consequence of septal perforations in the peripheral ring of *C. glutamicum*. To test this hypothesis, we performed correlative light and scanning electron microscopy of cells that had been labeled with 6-FlTre and FM dye (Figure

4.9). Cells (n = 154 cells) were binned according to their labeling profile where septal FM was assigned as the earliest stage detected during septation (Figure 4.9B) to the last stage where cells had undergone V-snapping (Figure 4.9D). Only 46 of the examined cells showed septal 6-FlTre labeling, where 70% (n = 32 cells) showed clear and evenly-spaced septal perforations in the peripheral ring (Figure 4.9C). We propose that the remaining 30% of FlTre-labeled septums have perforations large enough to allow diffusion, but small enough to not be detected by scanning electron microscopy. These results suggest a good correlation between delayed FlTre-labeling and septal perforations, both required for V-snapping to occur.

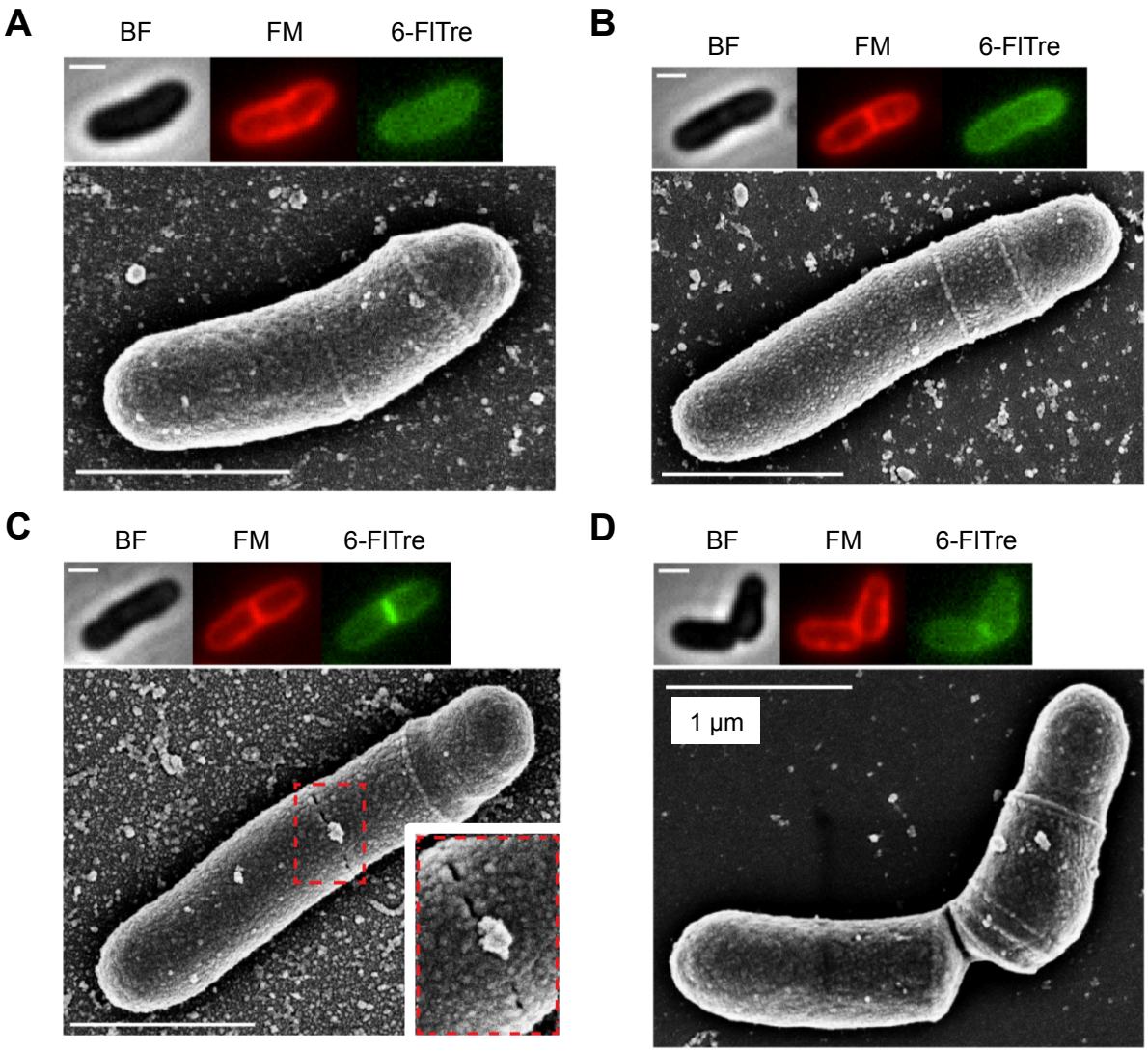

Figure 4.9 FlTre-labeled TMM migration correlates with septal perforations. Cells were labeled with 6-FlTre and FM dye for several generations, placed on imaging grid, fixed and visualized by correlative microscopy. Cells were classified on stages of the cell cycle based on the fluorescence dual labeling pattern of the septum (A-D). Scale, 1 µm

Millisecond V-snapping in Corynebacteria is independent of mycolic acids and driven by turgor pressure

We previously demonstrated that daughter cell separation (V-snapping) in *C. glutamicum* occurs within 10 ms.[21] Improved temporal resolution allowed us to determine that V-snapping of *C. glutamicum* can be completed within 1 ms (Figure 4.10A). To test whether V-snapping is driven by turgor pressure, cells were grown in medium with oscillatory changes in osmolarity. V-snapping events were recorded as a function of the phase of the changes in osmolarity (Figure 4.10B). Indeed, the frequency of snapping highly depends on the phase of the osmotic shock similar to *S. aureus*.[15] However, the specific response profile is different: the frequencies of snapping in low osmolarity medium, rather than just the interval when the medium osmolarity is being lowered, are generally higher than in high osmolarity medium. It appears that *C. glutamicum* responds to the absolute osmolarity of the medium and *S. aureus* responds to the rate of changing in medium osmolarity. One possibility is that *S. aureus* actively regulates its turgor pressure at a higher rate and extent than *C. glutamicum*. Nonetheless, the millisecond daughter cell separation (V-snapping) of *C. glutamicum* is driven by turgor pressure and cell wall stress.

Given the complex cell wall composition of *Corynebacterium*, we next wondered which layer(s) can undergo mechanical rupture during the V-snapping and still links both daughter cells. It has been suggested in the literature that the mycolic acid or the S-layer might act as the linking material to join the two daughter cells after snapping and gives rise to the V-shaped arrangement.[37,38] Interestingly, the *C. glutamicum* strain we used (ATCC 13032) happens to be deficient in S-layer production due to the absence of the S-layer promoter PS2,[39] yet still undergoes V-snapping, which ruled out the S-layer requirement. To evaluate the contribution of mycolic acids to the ultrafast V-snapping, we utilized a natural isolate of *C. amycolatum* that is devoid of mycolic acids.[40] We found that *C. amycolatum* snaps just like *C. glutamicum* and occurs within 10 ms (Figure 4.10C). Therefore, we conclude that V-snapping in *Corynebacterium* is independent of mycolic acids or S-layer.

We propose that peptidoglycan provides the mechanical strength to hold the daughter cells together against the turgor pressure prior to V-snapping and undergoes the mechanical rupture. Transmission electron microscopy (TEM) on thin sections of *Corynebacterium* showed a similar organization of the septal wall as in *S. aureus* where the septal peptidoglycan appeared as two separate plates that are connected by a peripheral ring of peptidoglycan.[41,42] V-snapping likely results from the resolution of this peripheral ring through a turgor pressure-driven mechanical crack propagation, initiated at one location in the ring (perhaps from one of the perforations shown in Figure 4.10D). Disruption of NlpC/P60 like cell wall hydrolase, which digests peptidoglycan in *Corynebacterium*, has been shown to delay daughter cell separation and leads to elongated cells with multiple septa,[42] supporting the hypothesis that peptidoglycan holds the two daughters together. We also suggest that a similar mechanism applies to *Mycobacterium*, since a mutant devoid of mycolic acid production displayed V-shaped arrangement of daughter cells.[43] In addition, TEM thin section of *Mycobacterium* revealed similar septal wall geometry as *Corynebacterium*.[44] Finally, several reports support the activity of RipA, a peptidoglycan hydrolase, to be essential for daughter cell separation in mycobacteria.[45–47]

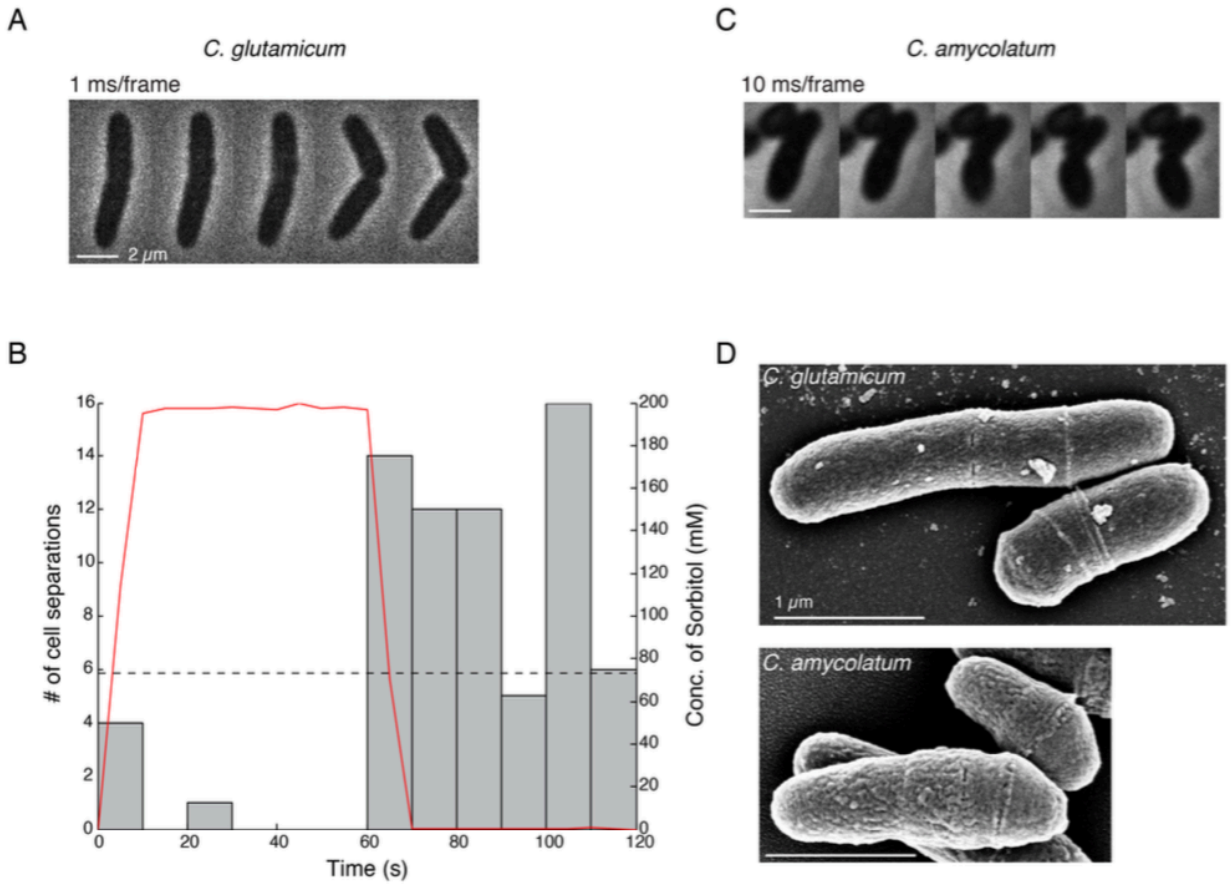

Figure 4.10. V-snapping in *Corynebacterium* occurs within milliseconds and is driven by turgor pressure. (A) Daughter cell separation (V-snapping) of *C. glutamicum* was captured with phase contrast microscopy at 1 ms per frame. Scale, 2 μm (B) Occurrence of V-snapping at different phases of the oscillatory osmotic shock period is shown. Red line denotes the concentration of sorbitol in the medium (n = 81 events). (C) Daughter cell separation (V-snapping) of *C. amycolatum* was captured with phase contrast microscopy at 10 ms per frame. Scale, 2 μm (D) Scanning electron micrographs of both *C. glutamicum* (top) and *C. amycolatum* (bottm) show septal perforations in the peripheral ring. Scale, 1 μm

Model for cell wall assembly in C. glutamicum

Based on our studies, *C. glutamicum* spends a significant period of time during the cell cycle building a functional septum that efficiently separates two daughter cells. Metabolic reporters allowed us to map cell wall assembly at the septum during cell growth and division. We propose a new model for cell wall biosynthesis during septation and V-snapping of *C. glutamicum* (Figure 4.11), where the green outline represents our results afforded by 6-FlTre metabolic labeling. First, cells elongate from the poles during growth, at which point an evenly coated surface of FlTre-labeled glycolipids is observed. Next, the septation process involves a bottom-up cell wall layer biosynthesis, where peptidoglycan labeling was observed before arabinogalactan incorporation. This observation is supported by O-TMM probe incorporation as

well as environment-sensitive fluorophores that report on the local hydrophobicity of the septum. Even though the cell has completed its septum and we observe robust peptidoglycan and arabinogalactan labeling, the cell is still not ready to undergo bacterial cytokinesis. At this stage, FlTre-labeled glycolipids are rapidly mobilized (in the order of minutes) to the septum before V-snapping occurs. Our results support the hypothesis of a diffusion barrier being removed to allow FlTre-glycolipid migration into the septum, which is facilitated by septal perforations of the peripheral ring as observed by SEM. Once the future new poles have a robust mycomembrane with low permeability, the cells undergo ultrafast V-snapping to afford two daughter cells that remain joined by the hinge region. We also propose that peptidoglycan is the cell wall layer that undergoes mechanical rupture after hydrolase activity has created weak points along the peripheral ring, presumably originating from the septal perforations observed by SEM. Finally, our turgor pressure data reveals that mechanical rupture is independent from both mycolic acids and S-layer, which further supports our hypothesis that peptidoglycan sustains the described cell wall stress during V-snapping.

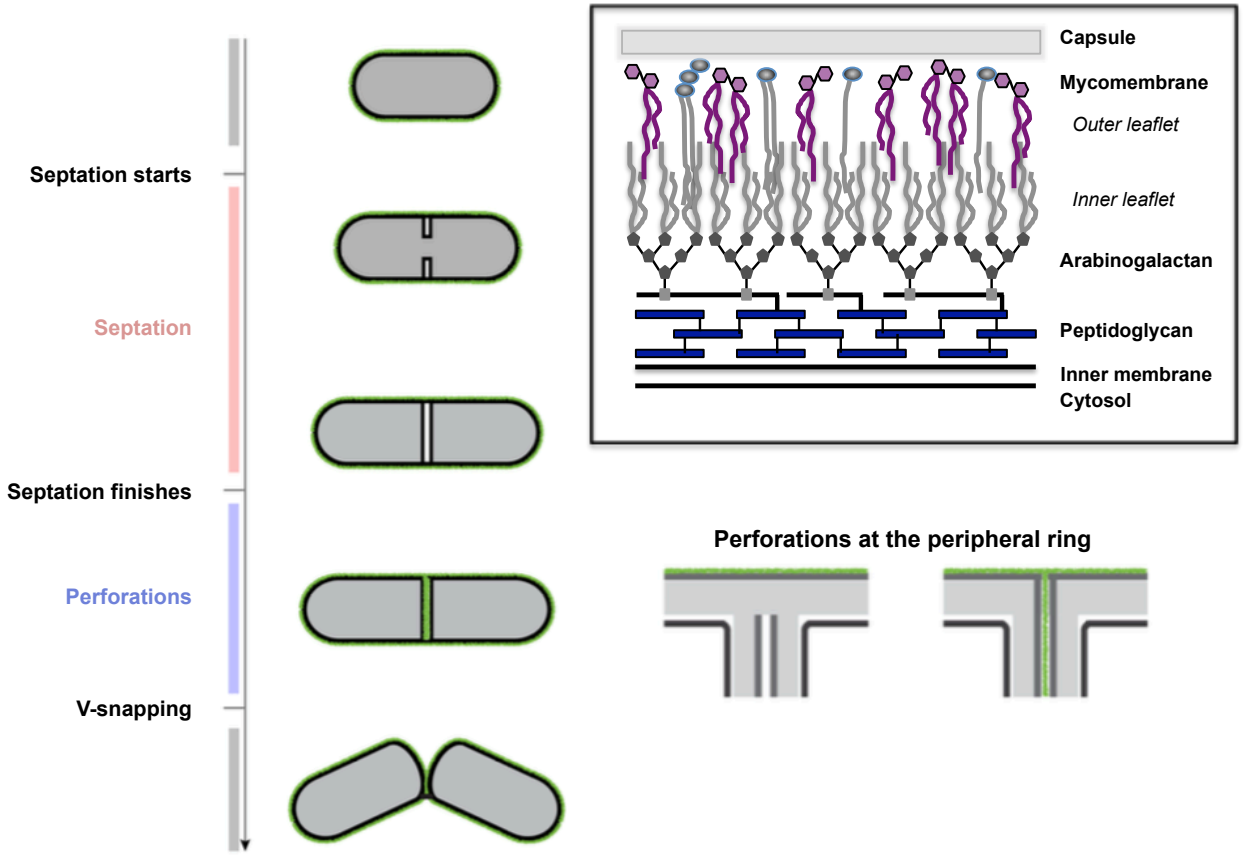

Figure 4.11 Actinobacterial cell wall assembly model during cell growth and division. At the growing pole, new mycolic acids are exported and transferred to both the arabinogalactan layer and free TMM to build both leaflets of the mycomembrane; the free trehalose mycolates diffuse rapidly to the entire cell surface (FlTre, depicted in green), but not to the new septum due to the peripheral peptdigoglycan ring (barrier); at the growing septum, there is no considerable amount of trehalose mycolates during septation, likely due to limited mycolic acids exported that are preferentially transferred to the arabinogalactan layer; prior to V-snapping, septal perforations

are formed at the peripheral ring which resolve the diffusion barrier for trehalose mycolates to migrate from the cell periphery into the septum to form the "outer leaflet" layer of the mycomembrane and prepare the new poles for exposure to the environment; when one perforation reaches the critical length, it will mechanically rupture the peripheral ring driven by turgor pressure and separates the two daughter cells into the established V-shaped arrangement.

CONCLUSION

Dynamics of individual cell wall components are notoriously challenging to study by both biochemical and genetic methods. We utilized unnatural cell wall reporters, amenable to ligation of fluorophores by bioorthogonal chemistry, to visualize how cell wall organization is orchestrated in *C. glutamicum* and *M. smegmatis*. We harnessed the spatiotemporal resolution of a triple metabolic labeling strategy to molecularly map cell wall assembly during cell growth and division in both species. Visualization of the cell wall revealed that new peptidoglycan and arabinogalactan are actively biosynthesized during septation, but non-covalently membrane-bound glycolipids are only mobilized to the septum before V-snapping occurs in *C. glutamicum*. Utilization of additional chemical tools such as environment-sensitive reporters allowed local hydrophobicity probing of the septum. We propose that mobilization of trehalose mycolates to the septum is facilitated by septal perforations of the peripheral ring, which is a crucial step for V-snapping and subsequent daughter cell separation. Our results also support that V-snapping is independent of mycolic acids and is driven by turgor pressure. Identification of peptidoglycan hydrolase mutants that lack FlTre-glycolipid mobilization to the septum might be an interesting avenue to identify putative enzymes involved in the mechanical rupture preceding V-snapping.

MATERIALS AND METHODS

General methods for synthesis

Materials and reagents were obtained from commercial sources without further purification unless otherwise noted. Anhydrous solvents were obtained either commercially or from an alumina column solvent purification system. All reactions were carried out in oven-dried glassware under nitrogen unless otherwise noted. Analytical TLC was performed on SiliCycle glass-backed silica gel 60 Å plates (thickness 250 μm) and detected by UV lamp or charring with 5% H_2SO_4 in MeOH. Column chromatography was performed using SiliCycle SiliaFlash P60 silica gel (40-63 μm). ^{1}H NMR spectra were recorded at 400, 500 or 600 MHz with chemical shifts in ppm referenced to solvent peaks. ^{13}C NMR spectra were recorded at 100 or 150 MHz with chemical shifts referenced to solvent peaks. NMR spectra were obtained on Bruker AVQ400, AVB-400, AV-500, or AV-600 instruments. Coupling constants (*J*) are reported in hertz (Hz). High-resolution electrospray ionization mass spectrometry (HR ESI MS) was performed at the UC Berkeley Mass Spectrometry Facility.

Reversed-phase HPLC was performed on a Varian Pro Star system with a Varian UV-Vis detector model 345 (210, 254 nm) on a Dynamax Microsorb C-18 preparative column (21.4 x 250 mm) at a flow rate of 20 mL/min or on an Agilent Eclipse XDB-C18 5μm semi-preparative column (9.4 x 250 mm) at a flow rate of 3 mL/min.

TreAz,[25] O-alkTMM,[27] TDL,[29] BTTAA,[48] azide-DMN,[34] and FlTre (Chapter 2) were synthesized as previously reported.

General procedure for the preparation of trehalose-AF647 analogs

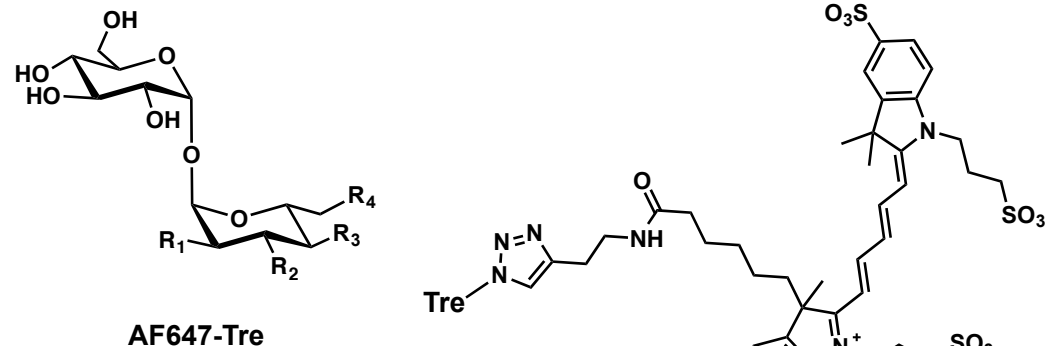

AF647-Tre

2-AF647-Tre R_1 = AF647, R_2 = R_3 = R_4 = OH
3-AF647-Tre R_2 = AF647, R_1 = R_3 = R_4 = OH
4-AF647-Tre R_3 = AF647, R_1 = R_2 = R_4 = OH
6-AF647-Tre R_4 = AF647, R_1 = R_2 = R_3 = OH

TreAz analogs were dissolved at 25 mM in doubly distilled water and filtered through 0.2 μm membrane. Stock solutions of BTTAA and $CuSO_4$ at 50 mM, in DMSO and water, respectively, and 10 mM alkyne-AF647 (Invitrogen) in DMSO were prepared and stored at -20 ^{o}C. A 100 mM sodium ascorbate was freshly prepared prior to CuCAAC reaction. Cu-click cocktail was prepared by mixing 0.5 μL 50 mM BTTAA, 3 μL 50 mM $CuSO_4$, 1 μL 25 mM TreAz analog, 12.5 μL 100 mM sodium ascorbate, and 10 mM alkyne-AF647. Reaction was allowed to proceed

at room temperature with rapid mixing for 30 min. Cu-clicked products at a final concentration of 1.28 mM were used immediately for cell labeling experiments or stored at -20 ^{o}C.

Synthesis of D-ala-DMN

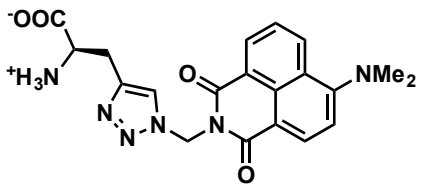

D-ala-DMN

alkDala was dissolved at 1 M in doubly distilled water and filtered through 0.2 μm membrane. Stock solutions were prepared as described above. Cu-click cocktail was prepared by mixing 0.5 μL 50 mM BTTAA, 3 μL 50 mM $CuSO_4$, 10 mM azide-DMN, 12.5 μL 100 mM sodium abscorbate, and 0.5 μL 1 M alkDala. Reaction was allowed to proceed at room temperature with rapid mixing for 30 min. Cu-clicked products at a final concentration of 1.28 mM were used immediately for cell labeling experiments or stored at -20 ^{o}C.

General procedure for the preparation of O-alkTMM-fluorophore analogs

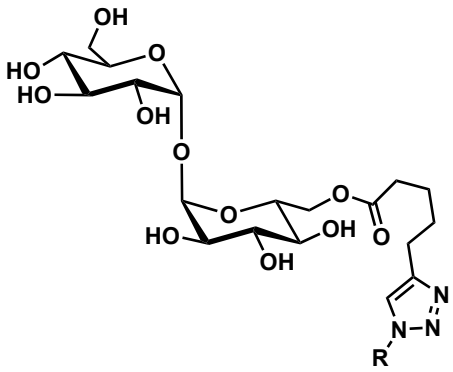

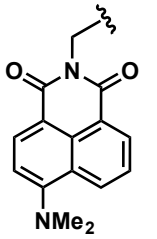

O-TMM-DMN

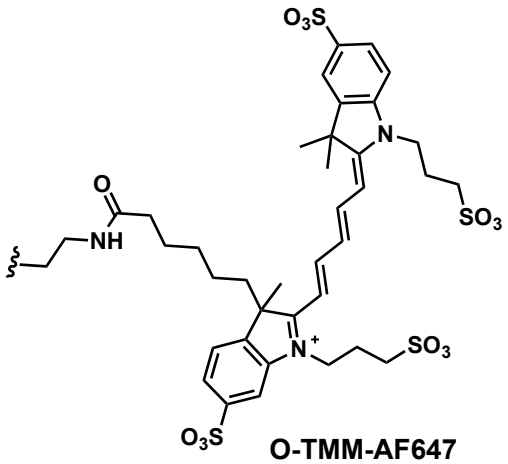

O-TMM-AF647

O-alkTMM was dissolved at 25 mM in doubly distilled water and filtered through 0.2 μm membrane. Stock solutions were prepared as described above. Cu-click cocktail was prepared by mixing 0.5 μL 50 mM BTTAA, 3 μL 50 mM $CuSO_4$, 10 mM azide-fluorophore, 12.5 μL 100 mM sodium abscorbate, and 1 μL 25 mM O-alkTMM. Reaction was allowed to proceed at room temperature with rapid mixing for 30 min. Cu-clicked products at a final concentration of 1.28 mM were used immediately for cell labeling experiments or stored at -20 ^{o}C.

Bacterial strains, media, and reagents
Bacterial strains used in this work include *Corynebacterium glutamicum* 534 and *Mycobacterium smegmatis* mc^2155. *C. glutamicum* was cultured in brain heart infusion (BHI) media at 30 ^oC. *M. smegmatis* was cultured in 7H9 media supplemented with 10% ADC (albumin, dextrose, catalase), 0.5% glycerol, and 0.05% tween 80 at 37 ^oC.

Stock solutions of FlTre analogs were prepared at 10 mM in DMSO and stored at -20 ^oC. Cu-click trehalose-fluorophore analogs at 1.28 mM (see general synthetic procedures) were stored at -20 ^oC. Other reagent stocks include nile red (Sigma Aldrich, 100 μg/mL in MeOH, stored at -20 ^oC), ethambutol (Sigma Aldrich, 50 mg/mL in H_2O, stored at 4 ^oC), ebselen (Cayman Chemical, 2 mg/mL in EtOH, stored at -20 ^oC).

Bacterial metabolic labeling conditions
Single colonies were used to start stationary phase cultures, which were used to innoculate experimental cultures for both *C. glutamicum* and *M. smegmatis*. Cells were grown in aerated culture tubes or 96-well plates with shaking until the desired optical density was achieved, unless otherwise noted. Bacterial cultures were incubated with trehalose probes until designated end-point of the experiment. Bacterial cells were fixed prior to flow cytometry or fluorescence microscopy unless otherwise noted

Flow cytometry
Fluorescently labeled cells were analyzed in 96-well plate format in a BD Biosciences Accuri C6 flow cytometer equipped with a BD C-Sampler. Data was collected for 100,000 events at a rate of > 5,000 events/s for each sample. All flow cytometry experiments were performed in triplicate where results are representative of at least two independent experiments.

Confocal microscopy
Bacterial cultures (1-3 μL) were spotted on 1% agarose pads mounted on glass slides, installed coverslip, and sealed with nail polish. Fluorescence imaging was performed with a Nikon A1R resonant scanning confocal microscope using a CFI Plan Apo Lambda 60x oil objective. Images were captured and processed with NIS Elements software. Acquisition and processing of images was performed identically for control and test samples.

Microfluidic platform
For the in situ labeling, log phase cultures were loaded into the ONIX microfluidic perfusion platform (CellASIC) with CellASIC B04A plate (EMD Millipore, Inc.) and fresh medium with different combinations of fluorescent probes was pressurized to the chamber. 30s before the image acquisition, fresh medium without fluorescent probes was switched in to wash away the excess reporters.

Light microscopy of live cells
2D time-lapse imaging was performed on a Nikon Eclipse Ti inverted fluorescence microscope with a 100x (NA 1.40) oil-immersion objective (Nikon Instruments) and MicroManager v1.4. Cells grown on agarose pad were maintained at targeted temperature during imaging with an active-control environmental chamber (HaisonTech). An iXon3 888 EMCCD camera (Andor) was used for fluorescent time-lapse microscopy experiments and a Zyla 5.5 sCMOS camera

(Andor) was used for millisecond phase imaging of cell separation.

Oscillatory osmotic shock

A microfluidic flow cell (CellASIC, EMD Millipore) was used to exchange media with different osmolarities.[15] Mid-exponential phase cells were diluted 200-fold into fresh medium and loaded into a CellASIC B04A plate and incubated at 30 °C in the microscope environmental chamber. The osmolarity of the medium in the chamber was switched between growth medium (medium A) and growth medium plus 0 to 200 mM sorbitol (medium B) with the ONIX microfluidic perfusion platform (CellASIC) every minute. To monitor medium osmolarity during the osmotic shock, 0.5 μg/mL deactivated AlexaFluor-647 carboxylic acid succinimidyl ester dye (Life Technologies) was included with medium B as a tracer dye. Cell were imaged every 10 s with phase contrast to record division events and Cy5 excitation to monitor the dye intensity (medium osmolarity).

Correlative light and scanning electron microscopy

μ-Dish 35 mm, high Glass Bottom Grid-50 (ibidi) imaging dishes were used to localize cells for the correlative SEM. 6-Tre labeled and FM 4-64FX (Life Technologies) stained cells were pelleted and resuspended in cold PBS, and settled onto poly-L-lysine (Sigma- Aldrich) treated correlative imaging dishes for 2 min on ice. After three washes with cold PBS, the absorbed cells were fixed with 2% glutaraldehyde and 4% paraformaldehyde in 0.1 M sodium cacodylate buffer (pH 7.3) on the coverslip at 4 °C overnight. The fixed cells on the imaging dish were washed with PBS and were imaged with light microscopy first where epifluorescence and phase contrast images were collected and the locations of cells on the grids were recorded for later correlation. Imaged cells were post-fixed with 1% OsO4 at 4 °C for 1 h (after this step the coverslips with the immobilized cells were cut out from the dish with a diamond knife), dehydrated in a series of increasing concentrations of ethanol (50%, 70%, 95%, and 100%), and inserted into an Autosamdri®-815 Series A Critical Point Dryer (Tousimis) to remove residual ethanol with carbon dioxide. The dehydrated samples were then sputter-coated with gold-palladium to ~65 Å-thickness and visualized with a Sigma series field emission scanning electron microscope (Zeiss).

Isolation and purification of free glycolipids

Bacterial cultures incubated with trehalose probes were washed two times with corresponding growth media to remove excess reporter. Wet cell pellets were subjected to organic extraction by adding 1 mL 2:1 $CHCl_3$:MeOH and stirring vigorously in conical glass tubes overnight. Resulting heterogeneous mixture was centrifuged for 10 min at 3,700xg, organic layer supernatant was saved and cell pellet was re-extracted twice. Combined organic layers were concentrated and analyzed by HPTLC (Uniplate HPTLC-GHL, 5 x 5 cm, 150 μm thickness) developed with 65:25:4 $CHCl_3$:MeOH:H_2O. Fluorescently labeled glycolipids developed in HPTLC plates were imaged with typhoon scanner (Amersham Biosciences, Typhoon 9410). Free lipids were partially purified by preparative TLC (Analtech, 20 x 20 cm, 1 mm thickness).

Analysis of O-alkTMM labeling distribution in cell wall components

After extracting free lipids, residual cell pellet containing mycolyl-arabinogalactan peptidoglycan (mAGPG) polymer was sonicated in 1 mL 2:1 $CHCl_3$:MeOH. Partially purified fluorescent glycolipids were dissolved in 1 mL 2:1 $CHCl_3$:MeOH. Labeling efficiency of free glycolipids and mAGPG was assessed by fluorimetry. Fluorescence spectra were recorded on a Photon Technology International Quanta Master 4 L-format scanning spectrofluorometer equipped with an LPS-220B 75-W xenon lamp and power supply, A-1010B lamp housing with an integrated igniter, switchable 814 photon counting/analog photomultiplier detection unit, and MD5020 motor driver. Measurements were made in 1 cm x 0.4 cm quartz cuvettes with a total sample volume of 1 mL in toluene.

FM-4-64 staining

To a bacterial culture (100 µL), 1 µL of 100 µg/mL FM-4-64 solution were added and incubated for 15 min at room temperature. Excess dye was removed with 3 PBS washes.

REFERENCES

1. Ikeda, M. & Takeno, S. in *Corynebacterium glutamicum* (eds. Yukawa, H. & Inui, M.) 107–147 (Springer Berlin Heidelberg, 2013).
2. Hadfield, T. L., McEvoy, P., Polotsky, Y., Tzinserling, V. A. & Yakovlev, A. A. The Pathology of Diphtheria. *J. Infect. Dis.* **181,** S116–S120 (2000).
3. Schaal, K. P. & Lee, H.-J. Actinomycete infections in humans — a review. *Gene* **115,** 201–211 (1992).
4. Beaman, B. L., Burnside, J., Edwards, B. & Causey, W. Nocardial Infections in the United States, 1972–1974. *J. Infect. Dis.* **134,** 286–289 (1976).
5. Dover, L. G., Cerdeño-Tárraga, A. M., Pallen, M. J., Parkhill, J. & Besra, G. S. Comparative cell wall core biosynthesis in the mycolated pathogens, Mycobacterium tuberculosis and Corynebacterium diphtheriae. *FEMS Microbiol. Rev.* **28,** 225–250 (2004).
6. Marrakchi, H., Lanéelle, M.-A. & Daffé, M. Mycolic Acids: Structures, Biosynthesis, and Beyond. *Chem. Biol.* **21,** 67–85 (2014).
7. Puech, V. *et al.* Structure of the cell envelope of corynebacteria: importance of the non-covalently bound lipids in the formation of the cell wall permeability barrier and fracture plane. *Microbiology* **147,** 1365–1382 (2001).
8. Jankute, M., Cox, J. A. G., Harrison, J. & Besra, G. S. Assembly of the Mycobacterial Cell Wall. *Annu. Rev. Microbiol.* **69,** 405–423 (2015).
9. Grzegorzewicz, A. E. *et al.* Assembling of the Mycobacterium tuberculosis Cell Wall Core. *J. Biol. Chem.* jbc.M116.739227 (2016). doi:10.1074/jbc.M116.739227
10. Zuber, B. *et al.* Direct Visualization of the Outer Membrane of Mycobacteria and Corynebacteria in Their Native State. *J. Bacteriol.* **190,** 5672–5680 (2008).
11. Hoffmann, C., Leis, A., Niederweis, M., Plitzko, J. M. & Engelhardt, H. Disclosure of the mycobacterial outer membrane: Cryo-electron tomography and vitreous sections reveal the lipid bilayer structure. *Proc. Natl. Acad. Sci.* **105,** 3963–3967 (2008).
12. Yang, Y., Shi, F., Tao, G. & Wang, X. Purification and structure analysis of mycolic acids in Corynebacterium glutamicum. *J. Microbiol.* **50,** 235–240 (2012).

13. Gray, A. N. *et al.* Coordination of peptidoglycan synthesis and outer membrane constriction during Escherichia coli cell division. *eLife* **4,** e07118 (2015).
14. Chai, Y., Norman, T., Kolter, R. & Losick, R. An epigenetic switch governing daughter cell separation in Bacillus subtilis. *Genes Dev.* **24,** 754–765 (2010).
15. Zhou, X. *et al.* Mechanical crack propagation drives millisecond daughter cell separation in Staphylococcus aureus. *Science* **348,** 574–578 (2015).
16. Donovan, C. & Bramkamp, M. Cell division in Corynebacterineae. *Microb. Physiol. Metab.* **5,** 132 (2014).
17. Hett, E. C. & Rubin, E. J. Bacterial Growth and Cell Division: a Mycobacterial Perspective. *Microbiol. Mol. Biol. Rev.* **72,** 126–156 (2008).
18. Letek, M. *et al.* Cell growth and cell division in the rod-shaped actinomycete Corynebacterium glutamicum. *Antonie Van Leeuwenhoek* **94,** 99–109 (2008).
19. Sguros, P. L. NEW APPROACH TO THE MODE OF FORMATION OF CLASSICAL MORPHOLOGICAL CONFIGURATIONS BY CERTAIN CORYNEFORM BACTERIA. *J. Bacteriol.* **74,** 707–709 (1957).
20. Dahl, J. L. Electron microscopy analysis of Mycobacterium tuberculosis cell division. *FEMS Microbiol. Lett.* **240,** 15–20 (2004).
21. Zhou, X., Halladin, D. K. & Theriot, J. A. Fast Mechanically Driven Daughter Cell Separation Is Widespread in Actinobacteria. *mBio* **7,** e00952–16 (2016).
22. Siegrist, M. S., Swarts, B. M., Fox, D. M., Lim, S. A. & Bertozzi, C. R. Illumination of growth, division and secretion by metabolic labeling of the bacterial cell surface. *FEMS Microbiol. Rev.* **39,** 184–202 (2015).
23. Meniche, X. *et al.* Subpolar addition of new cell wall is directed by DivIVA in mycobacteria. *Proc. Natl. Acad. Sci.* **111,** E3243–E3251 (2014).
24. Backus, K. M. *et al.* Uptake of unnatural trehalose analogs as a reporter for Mycobacterium tuberculosis. *Nat. Chem. Biol.* **7,** 228–235 (2011).
25. Swarts, B. M. *et al.* Probing the Mycobacterial Trehalome with Bioorthogonal Chemistry. *J. Am. Chem. Soc.* **134,** 16123–16126 (2012).
26. Urbanek, B. L. *et al.* Chemoenzymatic Synthesis of Trehalose Analogues: Rapid Access to Chemical Probes for Investigating Mycobacteria. *ChemBioChem* **15,** 2066–2070 (2014).
27. Foley, H. N., Stewart, J. A., Kavunja, H. W., Rundell, S. R. & Swarts, B. M. Bioorthogonal Chemical Reporters for Selective In Situ Probing of Mycomembrane Components in Mycobacteria. *Angew. Chem. Int. Ed.* **55,** 2053–2057 (2016).
28. Rundell, S. R. *et al.* Deoxyfluoro-D-trehalose (FDTre) analogues as potential PET probes for imaging mycobacterial infection. *Org. Biomol. Chem.* **14,** 8598–8609 (2016).
29. Kuru, E. *et al.* In Situ Probing of Newly Synthesized Peptidoglycan in Live Bacteria with Fluorescent D-Amino Acids. *Angew. Chem. Int. Ed.* **51,** 12519–12523 (2012).
30. Siegrist, M. S. *et al.* d-Amino Acid Chemical Reporters Reveal Peptidoglycan Dynamics of an Intracellular Pathogen. *ACS Chem. Biol.* **8,** 500–505 (2013).
31. Shieh, P., Siegrist, M. S., Cullen, A. J. & Bertozzi, C. R. Imaging bacterial peptidoglycan with near-infrared fluorogenic azide probes. *Proc. Natl. Acad. Sci.* **111,** 5456–5461 (2014).
32. Kuru, E., Tekkam, S., Hall, E., Brun, Y. V. & Van Nieuwenhze, M. S. Synthesis of fluorescent D-amino acids and their use for probing peptidoglycan synthesis and bacterial growth in situ. *Nat. Protoc.* **10,** 33–52 (2015).
33. Ngo, J. T. *et al.* Click-EM for imaging metabolically tagged nonprotein biomolecules. *Nat. Chem. Biol.* **12,** 459–465 (2016).

34. Krueger, A. T. & Imperiali, B. Fluorescent Amino Acids: Modular Building Blocks for the Assembly of New Tools for Chemical Biology. *ChemBioChem* **14,** 788–799 (2013).
35. Takayama, K., Armstrong, E. L., Kunugi, K. A. & Kilburn, J. O. Inhibition by Ethambutol of Mycolic Acid Transfer into the Cell Wall of Mycobacterium smegmatis. *Antimicrob. Agents Chemother.* **16,** 240–242 (1979).
36. Mikusová, K., Slayden, R. A., Besra, G. S. & Brennan, P. J. Biogenesis of the mycobacterial cell wall and the site of action of ethambutol. *Antimicrob. Agents Chemother.* **39,** 2484–2489 (1995).
37. Peyret, J. L. *et al.* Characterization of the cspB gene encoding PS2, an ordered surface-layer protein in Corynebacterium glutamicum. *Mol. Microbiol.* **9,** 97–109 (1993).
38. Hansmeier, N. *et al.* Classification of hyper-variable Corynebacterium glutamicum surface-layer proteins by sequence analyses and atomic force microscopy. *J. Biotechnol.* **112,** 177–193 (2004).
39. Hansmeier, N. *et al.* The surface (S)-layer gene cspB of Corynebacterium glutamicum is transcriptionally activated by a LuxR-type regulator and located on a 6 kb genomic island absent from the type strain ATCC 13032. *Microbiology* **152,** 923–935 (2006).
40. Barreau, C., Bimet, F., Kiredjian, M., Rouillon, N. & Bizet, C. Comparative chemotaxonomic studies of mycolic acid-free coryneform bacteria of human origin. *J. Clin. Microbiol.* **31,** 2085–2090 (1993).
41. Umeda, A. & Amako, K. Growth of the Surface of Corynebacterium diphtheriae. *Microbiol. Immunol.* **27,** 663–671 (1983).
42. Tsuge, Y., Ogino, H., Teramoto, H., Inui, M. & Yukawa, H. Deletion of cgR_1596 and cgR_2070, Encoding NlpC/P60 Proteins, Causes a Defect in Cell Separation in Corynebacterium glutamicum R. *J. Bacteriol.* **190,** 8204–8214 (2008).
43. Portevin, D. *et al.* A polyketide synthase catalyzes the last condensation step of mycolic acid biosynthesis in mycobacteria and related organisms. *Proc. Natl. Acad. Sci.* **101,** 314–319 (2004).
44. Vijay, S., Anand, D. & Ajitkumar, P. Unveiling Unusual Features of Formation of Septal Partition and Constriction in Mycobacteria—an Ultrastructural Study. *J. Bacteriol.* **194,** 702–707 (2012).
45. Hett, E. C., Chao, M. C. & Rubin, E. J. Interaction and Modulation of Two Antagonistic Cell Wall Enzymes of Mycobacteria. *PLOS Pathog.* **6,** e1001020 (2010).
46. Ruggiero, A. *et al.* Structure and Functional Regulation of RipA, a Mycobacterial Enzyme Essential for Daughter Cell Separation. *Structure* **18,** 1184–1190 (2010).
47. Böth, D., Schneider, G. & Schnell, R. Peptidoglycan Remodeling in Mycobacterium tuberculosis: Comparison of Structures and Catalytic Activities of RipA and RipB. *J. Mol. Biol.* **413,** 247–260 (2011).
48. Besanceney-Webler, C. *et al.* Increasing the Efficacy of Bioorthogonal Click Reactions for Bioconjugation: A Comparative Study. *Angew. Chem. Int. Ed.* **50,** 8051–8056 (2011).

Chapter 5

Investigating the Role of Trehalose Mycolates during *in vivo* Infection in the *Mycobacterium marinum*-Zebrafish Model

Joshua Yoon and Prof. William E. Moerner provided instruments and technical assistance for this work.

Chapter 5. Investigating the Role of Trehalose Mycolates during *in vivo* Infection in the *Mycobacterium marinum*-Zebrafish Model

INTRODUCTION

Clinical management of tuberculosis (TB) necessitates patients to endure a 6-month regimen of a four drug cocktail. Extensive treatment is efficacious for patients with drug-susceptible TB, but deviations can give rise to drug resistance. Survival of *Mycobacterium tuberculosis* (Mtb) within the hostile environment of the host macrophage largely depends on an impermeable cell wall that protects bacilli from biological stresses.[1,2] Furthermore, its cell wall serves as an intrinsic static barrier to many antibiotics and therapeutics, resulting in challenging and ineffective treatment alternatives.[3,4] Mycobacteria elaborate their peptidoglycan with arabinogalactan chains, from which mycolic acids are covalently installed at the distal arabinose residues in the cell wall.[5] Mycobacterial mycolic acids, up to 90 carbons in length,[6] serve as the inner leaflet of the mycomembrane that supports non-covalently associated glycolipids (Figure 5.1). Different classes of free glycolipids in the outer leaflet have attracted significant attention in the host-pathogen community and are proposed to have important immunogenic roles.[2,7–10] Earlier work by Russell and coworkers has provided insights into how mycobacterial cell wall components are trafficked during infection of macrophages by non-specific oxidation of surface components followed by labeling with hydrazide-functionalized fluorophores. This approach is unable to discriminate between different classes of labeled species.[11] Strategies enabling the selective imaging of these glycolipids would be highly advantageous since biochemical and genetic approaches are insufficient to study these non-genetically encoded products.

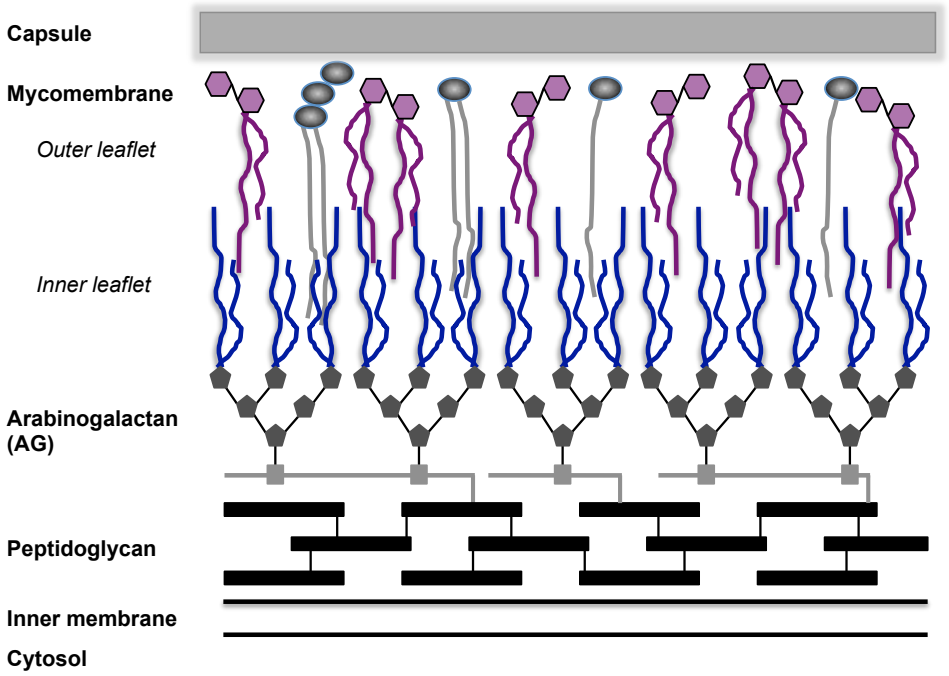

Figure 5.1 Mycobacterial cell wall

More than 40 % of the dry weight of the cell envelope is comprised of lipids,[6] where trehalose monomycolate and dimycolate, TMM and TDM, respectively, are the most abundant glycolipids in the Mtb cell wall (Figure 5.2).[12] Decades of research have led to characterization from bulk isolation and purification of several trehalose glycolipids including the trehalose mycolates (Figure 5.2), but these methods fail to recapitulate the native architecture of the mycobacterial cell wall.[5] Selective visualization of defined classes of mycobacterial glycolipids in live cells without altering cell wall composition through genetic approaches remains an unmet need, impeding advances towards unraveling their structural roles and virulence properties. In order to visualize trehalose glycolipids, the development of unnatural trehalose analogs with unique functionalities that will report on their dynamics in live bacteria is essential.[13]

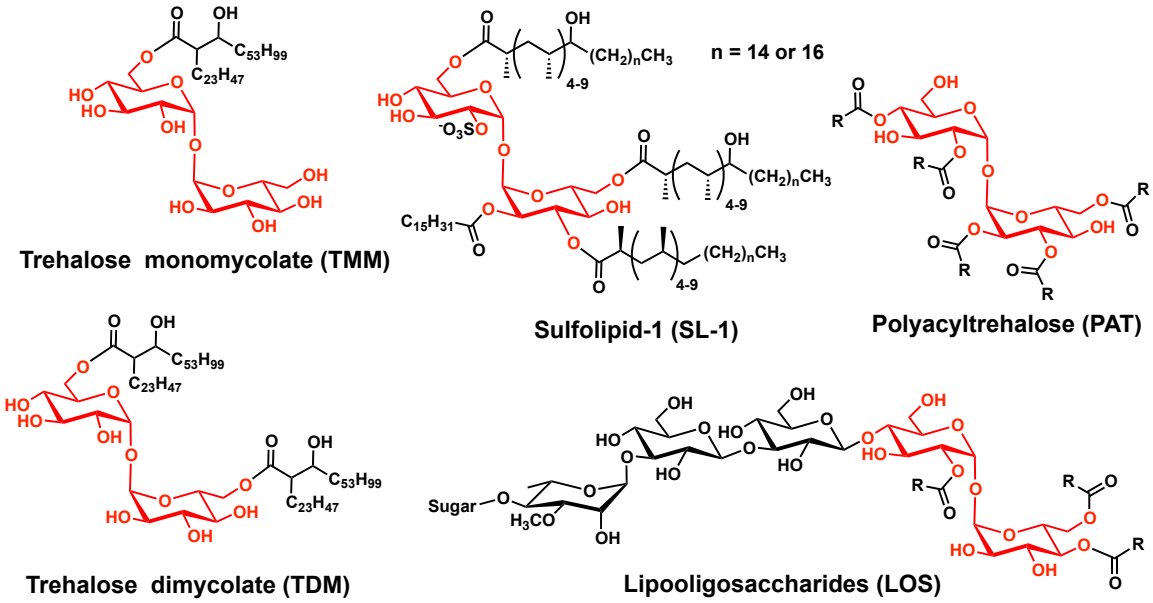

Figure 5.2 Chemical structures trehalose glycolipids in mycobacteria. Trehalose dissacharide is highlighted in red.

Significant progress has been achieved by metabolically labeling trehalose glycolipids in mycobacteria. Chemical biology approaches take advantage of the cell's biosynthetic machinery and harness enzyme promiscuities during cell wall biosynthesis to metabolize unnatural trehalose reporters.[14–18] Larger functional groups on trehalose reporters can be accommodated by the antigen 85 complex (Ag85), a family of mycolyltransferases that convert two molecules of TMM to TDM and free trehalose, as first shown in Mtb by Davis, Barry and coworkers.[14] We were particularly attracted to the operational simplicity afforded by the metabolic labeling of trehalose-fluorophore conjugates from our work and others.[14] We envisioned using a metabolic labeling strategy to monitor trehalose mycolates dynamics during infection, which still remain largely undefined.

Trehalose mycolates are essential for mycobacterial cell viability.[8,19] In addition, full virulence of pathogenic mycobacteria in model organisms requires production of TMM and TDM.[19–21] Even though their precise roles in pathogenesis remain poorly understood, it has been proposed to include functions such as modulating phagocytosis and bacilli survival in macrophages,[22] as well as resistance to environmental stresses.[20,21,23,24] However, the diversity of

host-pathogen interactions choreographed during TB disease cannot be recapitulated with infection studies in tissue-cultured cells. For this reason, TB pathogenesis research relies heavily on animal infection models, most prominent the murine model, which can diverge considerably from human disease.[25,26] In the last decade, significant insight has been provided by the macaque tuberculosis model with particular focus on latency and wide spectrum of heterogeneous TB lesions.[27–29] Due to their opacity, both of these models are not amenable to non-invasive fluorescence imaging during infection.

An attractive alternative is the zebrafish animal model,[30–32] which is naturally infected by pathogenic *Mycobacterium marinum* (Mm). Mm is the closest genetic relative of Mtb and shares a significant number of major virulence factors.[33] Pathogenesis of Mm infection in zebrafish is remarkably similar to TB disease in humans,[34,35] even more so than Mtb infection in mice. Notably, Mm macrophage infection results in halting phago-lysosome fusion[36,37] and granuloma formation,[38,39] as well as achievement of latency.[30,31] Mtb and Mm utilize similar exploitation schemes to subvert the host immune response,[10,40] including innate and adaptive immunity mechanisms.[34] The cell wall of Mm includes trehalose glycolipids TMM and TDM,[41,42] which share similar structure to those of Mtb. Furthermore, the zebrafish-Mm model provides several practical advantages such as genetic tractability and optical translucency, which facilitate the molecular view of host-pathogen interactions with *in vivo* fluorescence imaging.[38,40,43,44]

Previous methods interrogating roles of mycobacterial cell wall components during pathogenesis have been unable to deconvolute contributions from individual glycolipid species without genetic manipulation. This is consistent with the dearth of tools to monitor species such as trehalose mycolates in real-time, specifically in dynamics involving host-pathogen interactions. Here, the application of a metabolic labeling strategy with unnatural trehalose reporters to visualize trehalose mycolates in the context of infection is described. We developed a new class of trehalose-conjugates that includes a bicyclononyne functionality, which are amenable to *in vivo* imaging. Incorporation of unnatural trehalose reporters into trehalose mycolates was validated for Mm. We show that trehalose mycolates can be selectively visualized in infected murine macrophages as well as live zebrafish. Importantly, vertebrates neither biosynthesize trehalose nor use this disaccharide as a building block. Thus, exogenous trehalose should selectively label Mm glycolipids within the infected host. Our studies reveal active trafficking of labeled trehalose mycolates and incorporation into mycobacterial outer membrane vesicles. This metabolic labeling strategy allowed visualization of unprecedented glycolipid dynamics that point at the importance of microvesicle composition during tuberculosis pathogenesis.

RESULTS AND DISCUSSION

Validation of FlTre labeling in M. marinum

In order to spatio-temporally resolve glycolipid dynamics, we envisioned that the installation of a fluorophore (i.e., fluorescein) on the trehalose scaffold would allow comprehensive probing of mycolyltransferase promiscuity in live cells, while bypassing the additional labeling step of secondary reagents. Our designed library would comprise of analogs that share the native stereochemistry and unaltered core of trehalose, where we can evaluate a panel of regioisomers for optimal labeling (Figure 5.3). Fluorescein-trehalose analogs (FlTre)

can be easily accessed with a two-step procedure by reduction of the azide group and subsequent reaction with fluorescein isothiocyanate (FITC) as described in Chapter 2. This strategy allowed synthesis of four analogs 2-, 3-, 4-, and 6-FlTre in good yields. We hypothesized that selective installation of fluorescein at different positions would inform on the enzyme tolerance for site perturbations along the modified glucose ring.

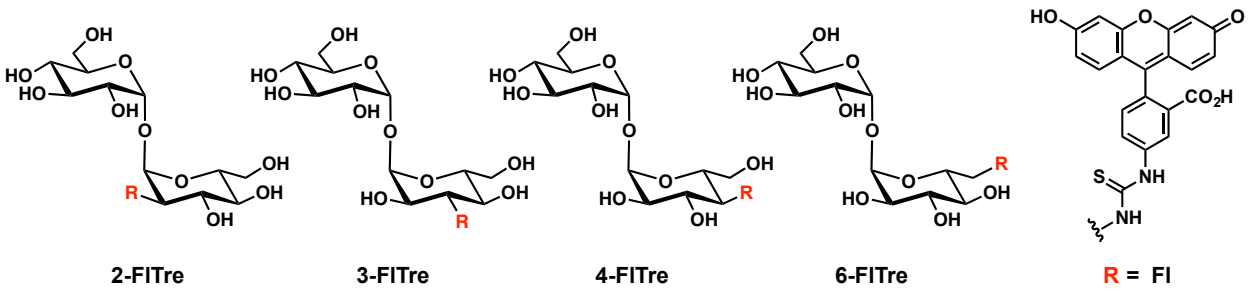

Figure 5.3 FlTre reporter library used in this study

With FlTre analogs in hand, we set out to probe incorporation efficiency by live bacterial cells in liquid culture. In order to benchmark our metabolic reporters, we compared our library to previously reported FITC-Tre[14] in *M. marinum* (Figure 5.4A), which shares high similarity in composition and structure to the Mtb cell wall.[45] All FlTre analogs outperformed FITC-Tre as evaluated by flow cytometry, except 6-FlTre. Highest incorporation efficiency was observed for 2-FlTre, while 3-, 4-, and 6-FlTre showed similar labeling.

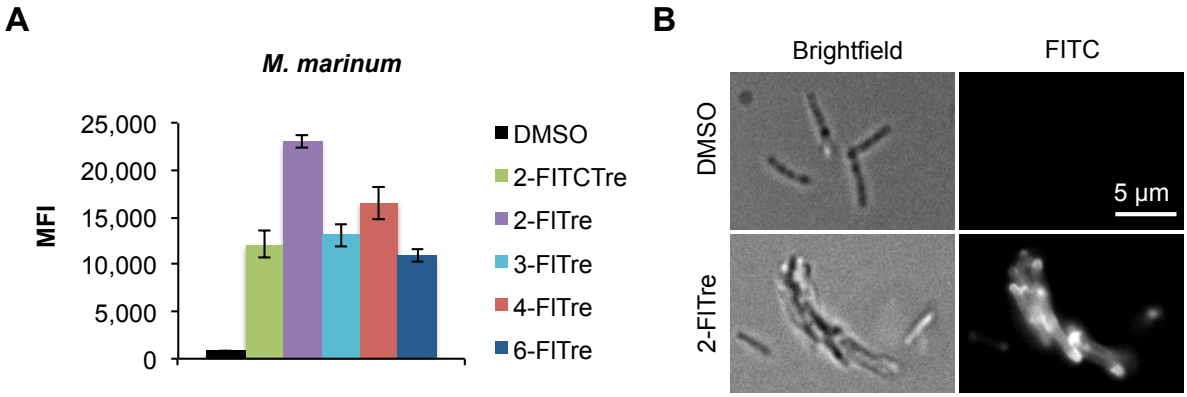

Figure 5.4 Metabolic labeling of *M. marinum* with FlTre reporters. Labeling profile of FlTre analogs compared to FITC-Tre in Mm (A). Bacteria were labeled with 100 µM trehalose analogs or vehicle for several doubling times. Error bars depict standard deviation of three replicate experiments. Results are representative of at least two independent experiments. Mean fluorescence intensity (MFI). (B) Fluorescence microscopy images of Mm cells labeled with vehicle or 2-FlTre. Scale bar, 5 µm

In addition, we evaluated spatial distribution of labeled trehalose glycolipids by fluorescence microscopy. Gratifyingly, cell wall labeling was observed for Mm after incubation of FlTre reporters at 100 μM for several doubling times, which did not show any cell growth or morphology defects (Figure 5.4B). To further investigate the specificity for FlTre incorporation, we assessed if increasing concentrations of trehalose, as native substrate for mycolyltransferases, could outcompete reporter labeling. Bacterial cells that were coincubated with 100 μM of FlTre reporters and trehalose (0, 0.5, 5 mM) showed a decrease in metabolic labeling as trehalose concentration was increased for Mm (Figure 5.5A). Trehalose concentrations as high as 5 mM were required, as this disaccharide is actively scavenged by SugABC-LpqY, a specific trehalose transporter in mycobacteria.[46] In parallel, ebselen, a selenium-based inhibitor that selectively inhibits Ag85 activity in mycobacteria,[47,48] can decrease FlTre labeling in both species (Figure 5.5B). For the final corroboration step, partially purified fluorescent trehalose glycolipids were analyzed by TLC and mass spectrometry to confirm selective modification of trehalose mycolates with FlTre analogs in *M. marinum* (Figure S1 and S2). Species corresponding to FlTre-labeled TMM were identified for all analogs, while Fl-Tre-TDM was only identified for 2-, 3-, and 4-FlTre. This result was expected as 6-FlTre effectively blocks the second acylation at the 6-position of trehalose by Ag85 activity. Collectively, validation by trehalose competition experiments, ebselen inhibition studies and mass spectrometry of glycolipids demonstrates FlTre's exquisite selectivity towards labeling trehalose mycolates in live bacterial cells. This chemical biology strategy bypasses arduous synthetic challenges to obtain chemically-defined trehalose mycolates[20] or exogenously added fluorophore-glycolipid probes that might not report on native membrane organization.

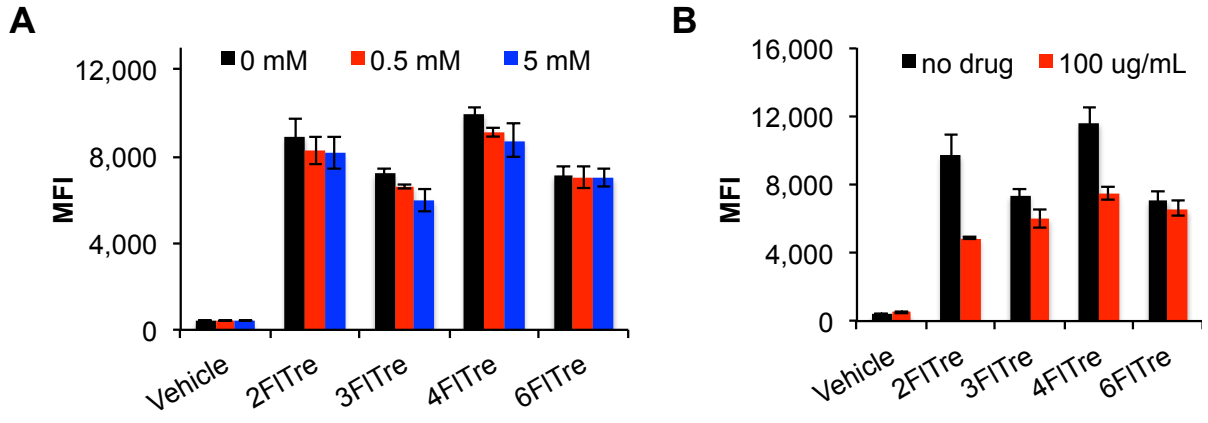

Figure 5.5 Validation of FlTre metabolic labeling of trehalose mycolates in *M. marinum*. Cells were labeled with 100 μM FlTre for 4 h in trehalose competition and ebselen experiments. A) Increasing concentrations of trehalose (0, 0.5, 5.0 mM) can outcompete FlTre labeling during bacterial growth. B) Ebselen treatment during FlTre labeling decreases reporter incorporation. Error bars depict standard deviation of three replicate experiments. Results are representative of at least two independent experiments. Mean fluorescence intensity (MFI).

Development of BCN-Tre analogs for in vivo imaging

We were attracted to the possibility of expanding the current trehalose reporter library to include bicyclononynes (BCN) that would be desirable for *in vivo* imaging. Incorporation of these analogs could be assessed with turn-on probes, which only become fluorescent after the bioorthogonal reaction has occurred, and have been used previously for visualizing systemic glycans in zebrafish.[49] This approach would take advantage of tetrazine[50] and azide fluorogen-conjugates,[51] and would provide another dimension of temporal control during imaging of *in cellulo* and *in vivo* infection models.

We chose to synthesize our analogs from TreAz probes as the essential α,α-1,1-glycosidic linkage is preserved. Bicyclononyne-trehalose analogs (BCN-Tre) can be easily accessed with a two-step procedure by reduction of the azide group to an amine and subsequent reaction with BCN-p-nitrophenol. This strategy allowed synthesis of four analogs 2-, 3-, 4-, and 6-endoBCNTre in good yields. We hypothesized that selective installation of BCN at different positions would report on enzyme promiscuity towards perturbations along the modified glucose ring.

TreAz

2-TreAz $R_1 = N_3$, $R_2 = R_3 = R_4 = OH$
3-TreAz $R_2 = N_3$, $R_1 = R_3 = R_4 = OH$
4-TreAz $R_3 = N_3$, $R_1 = R_2 = R_4 = OH$
6-TreAz $R_4 = N_3$, $R_1 = R_2 = R_3 = OH$

BCNTre (Yield 72-92%)

2-BCNTre $R_1 = BCN$, $R_2 = R_3 = R_4 = OH$
3-BCNTre $R_2 = BCN$, $R_1 = R_3 = R_4 = OH$
4-BCNTre $R_3 = BCN$, $R_1 = R_2 = R_4 = OH$
6-BCNTre $R_4 = BCN$, $R_1 = R_2 = R_3 = OH$

Scheme 5.1 Synthesis of BCNTre library from corresponding TreAz analogs

Next, we screened the library of BCN-Tre analogs to evaluate incorporation efficiency by *M. marinum* in liquid culture. To assess metabolic labeling, cells were incubated with 100 μM trehalose analogs or vehicle for several doubling times. Cells were then washed, fixed and labeled with tetrazine-Cy5 prior to analysis. All analogs demonstrated significant signal over background when compared to the vehicle control by flow cytometry (Figure 5.6A). We hypothesize that the secondary labeling reagent might contribute to determining the extent of labeling under these conditions since differences in labeling between analogs was less pronounced than for the FlTre library. Fluorescence microscopy revealed cell wall localization of BCN-Tre analogs with polar patterns in some cells (Figure 5.6B). Small amounts of these analogs limited our ability to conduct validation of trehalose mycolate incorporation by TLC and mass spectrometry methods.

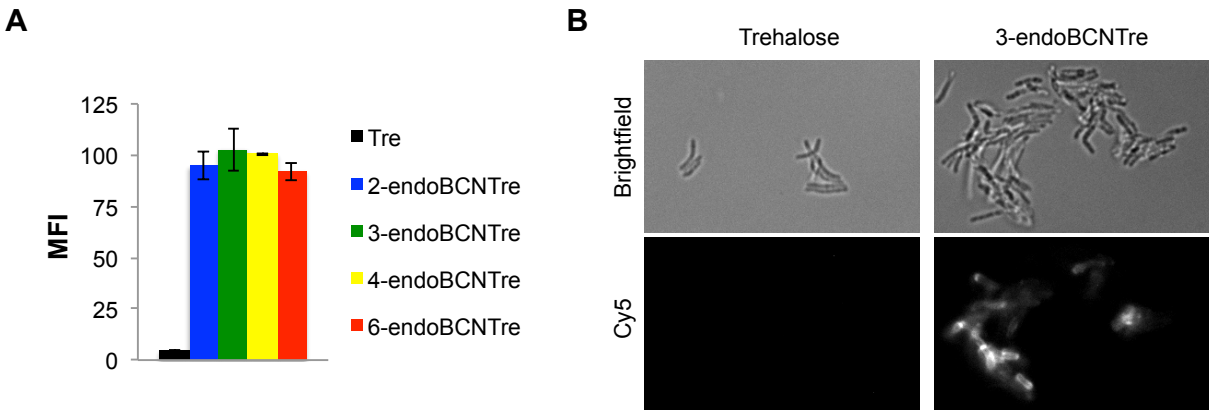

Figure 5.6 Metabolic labeling of *M. marinum* with BCNTre reporters. Labeling profile of BCNTre analogs for Mm is shown (A). Bacteria were incubated with 100 μM trehalose analogs or vehicle for several doubling times. Cells were washed, fixed and labeled with tetrazine-Cy5 prior to analysis. Error bars depict standard deviation of three replicate experiments. Results are representative of at least two independent experiments. Mean fluorescence intensity (MFI). (B) Fluorescence microscopy images of Mm cells labeled with vehicle or 3-endoBCNTre.

In vitro trehalose mycolate dynamics

After validating metabolic incorporation of trehalose reporters into trehalose mycolates, we proceeded to interrogate dynamics of prelabeled glycolipids. Our work from pulse-chase labeling experiments shows that trehalose mycolates are rather immobile in mycobacteria, where pre-labeled glycolipids are unable to diffuse into new areas of growth. These results were further validated by quantification of diffusion dynamics with a fluorescence recovery after phobleaching, or FRAP, strategy (Chapter 2). We also wanted to address whether turnover of trehalose mycolates is actively occurring in the mycobacterial cell wall. To this end, Mm cells were prelabeled with FlTre analogs for several generations, washed and chased with vehicle for different time periods (see experimental scheme in Figure 5.7A). We found that prelabeled cells labeling intensity decreased with time for all analogs in live cells (Figure 5.7B). Conversely, heat-killed cells did not change labeling intensity over the course of 3 h. These results suggested that shedding of labeled glycolipids is an active process, where living cells are required. Release of labeled trehalose mycolates was more pronounced at the 5 h timepoint, noting that Mm divides every 6 hours. At this timepoint, 6-FlTre-labeled glycolipids were released into the extracellular milieu faster than the 2-FlTre counterparts (Figure 5.7C). We have observed that this decrease in metabolic labeling intensity was a result of an accumulation of fluorescence in the growth media (*a priori*). Taken together, our results point at active dynamics of trehalose mycolates in liquid culture, where the extent of glycolipid shedding is dependent on the FlTre analog used and incubation time after labeling.

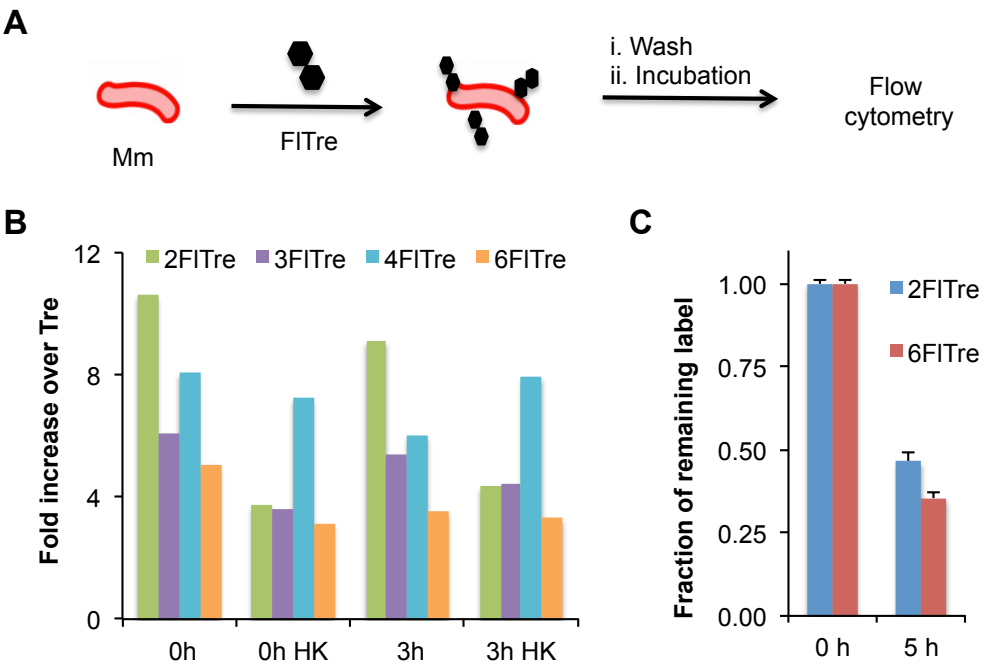

Figure 5.7 Dynamics of trehalose mycolates in *M. marinum in vitro*. A) Experimental set up to evaluate prelabeled glycolipid turn over in mycobacterial cells. Cells were labeled with FlTre reporters for several generations, washed and incubated for desired vehicle chase times, and later evaluated for remaining label by flow cytometry. B) Labeled trehalose mycolates are actively release by live Mm cells in liquid culture, but not by heat-killed (HK) cells. C) 6-FlTre glycolipids are released faster into the growth media than 2-FlTre at the 5 h timepoint.

In parallel, visualization of prelabeled Mm cells with FlTre analogs revealed labeling intensities or puncta, when cells were imaged with 0.2 µm z-slices in a confocal microscope (Figure 5.8). The photostability of the fluorophore conjugate limited our ability to perform long-term as well as super resolution microscopy.

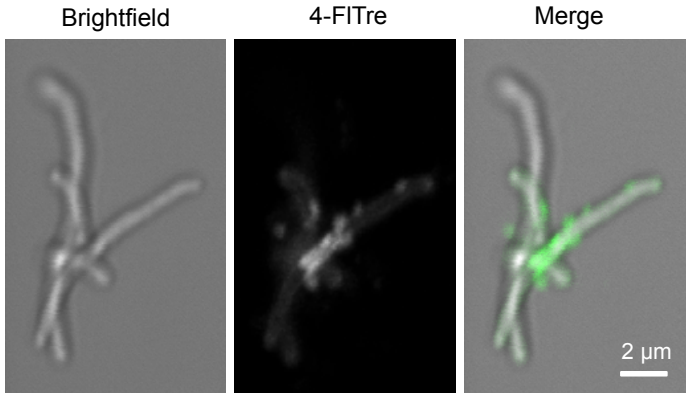

Figure 5.8 Widefield confocal microscopy of FlTre labeled *M. marinum*. Cells were labeled with FlTre for several doubling times and imaged by confocal microscopy with z-sectioning of 0.2 µm slices, only one z-slice is shown. Scale bar, 2 µm

To address these limitations, we next sought to modify the trehalose scaffold with a fluorophore amenable to super resolution microscopy, which would afford a more defined picture of trehalose mycolate ultrastructure within the cell wall. Thus, we installed an AlexaFluor 647 on the 6-position of trehalose (6-AF647-Tre), a photostable fluorophore commonly used in super resolution microscopy.[52–54] This trehalose analog was obtained in good yield after HPLC purification by reacting 6-amino trehalose with AF647-NHS. This analog was well tolerated by the Mm cell wall biosynthetic machinery (data not shown).

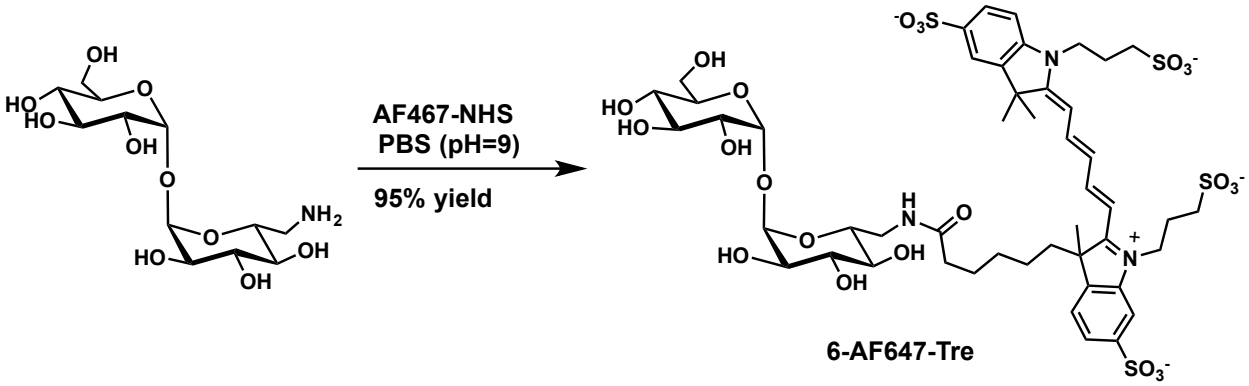

Scheme 5.2 Synthesis of 6-AF647-Tre analog for super resolution microscopy

We envisioned using advanced imaging techniques to further characterize the nature of the heterogeneous coat of labeled glycolipids, in particular the areas of concentrated reporter. The question remained whether these concentrations of signal were a result of cell wall biosynthesis centers or accumulations of prelabeled species due to the native architecture of the cell wall that would also support our glycolipid shedding hypothesis (Figure 5.9A). Single-particle tracking and super resolution imaging have shed light on previously unobservable biological processes in bacterial cell biology.[53] For example, single-molecule imaging of the transmembrane Smoothened protein that resides in the ever-fluctuating plasma membrane of primary cilia revealed molecular interactions with binding partners.[54] To this end, Mm cells were labeled with 100 μm 6-AF647-Tre for several generations, washed, fixed and mounted on agar pads for single-particle tracking data acquisition. Single-molecule tracks revealed some fluorophores were diffusing along the cell wall freely (orange line), while more molecules seemed to be restricted to a particular radius (Figure 5.9B). These results indicated different behaviors for the fluorophores observed by single-molecule tracking methods. We next pursued the visualization of prelabeled Mm cells by a three-dimensional super resolution microscopy approach with a resolution of 20 and 30 nm in x-y and z planes, respectively. Visualization of labeled trehalose mycolates in Mm revealed an uneven coat in the cell wall (Figure 5.9C), as previously observed by widefield microscopy with FlTre reporters. However, the concentration of labeling spots were distributed along the entire cell and varied in size, suggesting a structure of higher order within the mycomembrane, similar to microvesicles.

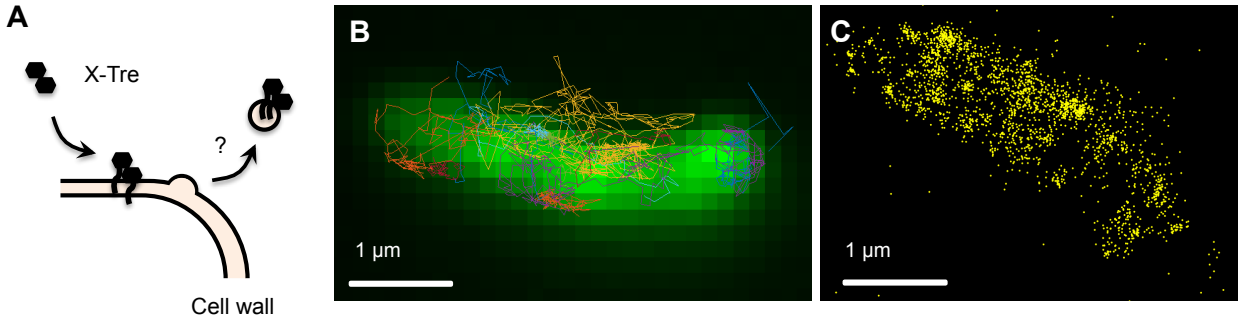

Figure 5.9 Super-resolution and single-molecule tracking of trehalose glycolipids in *M. marinum*. A) Metabolic engineering approach to study production of outer membrane vesicles. B) Single-molecule tracking in live Mm shows heterogeneous mobility of trehalose glycolipids (each track of a single molecule is represented in a different color). C) Super-resolution micrograph of an intact Mm cell demonstrates uneven distribution of trehalose glycolipids in the cell wall. Scale bar, 1 µm

Direct observation of punctate staining during of Mm cells grown in culture warranted further investigation. In 2011, Prados-Rosales *et al*. provided evidence of the immunostimulatory properties of pathogenic mycobacterial outer membrane vesicles (OMVs) released during infection and mediated by TLR2-dependent signaling.[55] More recent reports have contributed to the significance of OMVs by demonstrating genetic regulation of vesicle formation,[56] potential iron acquisition properties,[57] as well as promising vaccine developments.[58,59] The proteome of Mtb OMVs released in liquid culture was also published recently.[60] Importantly, vesiculogenesis and immune response regulator (virR) in Mtb, encoded by Rv0431, genetically controls OMV generation and protein composition, which is conserved in Mm (Mmar_0746, 83% homology to Mtb counterpart). Furthermore, the vesiculogenesis process is not restricted to mycobacteria as Gram-negative and -positive bacteria utilize it during pathogenesis.[61,62] We hypothesized that FlTre-labeled trehalose mycolates were accessing OMVs in the cell wall of *M. marinum* prior to release into the growth media, which would be in agreement with our glycolipid shedding hypothesis (Figure 5.10A).

Next, we examined more closely the composition of OMVs generated by pathogenic Mm in order to determine the abundance of trehalose mycolates by metabolic labeling in liquid culture. Bacterial cultures were grown to log-phase in the presence of FlTre reporters and vesicles were isolated as previously described.[55,63] Briefly, growth media supernatants were subjected to ultracentrifugation and dialysis procedures (Figure 5.10B). Vesicular fractions from Mm labeled with trehalose reporters exhibited fluorescent signal, which was completely absent from cells that were grown in the presence of vehicle (Figure 5.10C). Notably, this rigorous vesicle purification procedure excludes molecules smaller than 3 kDa, which reports on fluorophores tightly associated to these structures. These results provide evidence for the first time of trehalose mycolates being present in mycobacterial OMVs, which could go undetected by TLC and MS methods.

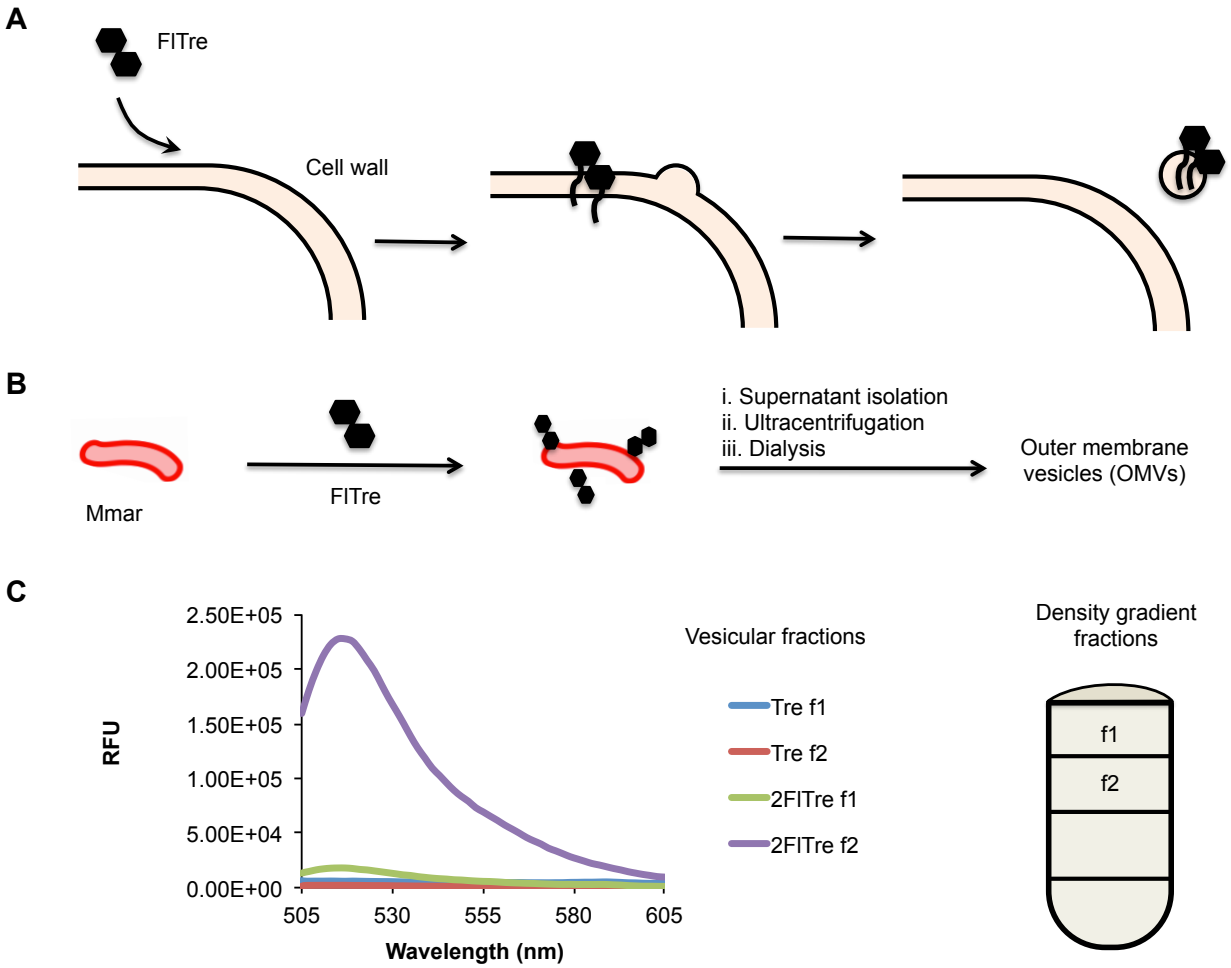

Figure 5.10 Membrane vesicles from *M. marinum* contain FlTre-labeled trehalose mycolates. (A) Proposed model for FlTre incorporation into mycobacterial membrane vesicles. (B) Experimental scheme for membrane vesicles isolated from liquid cultures of *M. marinum* after FlTre labeling. This protocol requires ultracentrifugation purification as well as dialysis of molecules smaller than 3 kDa. (C) Fluorimetry measurements of isolated fractions after purification steps show that only the second fraction contains labeled microvesicles.

Release of vesicles from bacteria has been hypothesized to occur by increased cytosolic turgor pressure or by disorder regions in the outer membrane that seed such structures. An alternative regulation of vesicle production could be achieved by modulating PG crosslinking, as diminished peptidoglycan (PG) density has been proposed to lead to increased release of OMVs.[61] We hypothesized that increasing concentrations of glycine could decrease PG crosslinking, as this step is commonly performed prior to challenging transformations by electroporation,[64] and increase glycolipid shedding. To this end, bacterial cells were labeled with FlTre analogs for several generations, washed and incubated under different conditions to promote vesiculogenesis. However, efforts towards modulating vesicle production with PG engineering tools such as glycine metabolic labeling proved unsuccessful in liquid culture for both *M. marinum* and *M. smegmatis* (Figure 5.11). We also endeavored to emulating host insults such as high osmotic stress found within the phagosomal compartment. For example,

concentrations on the order of 140 mM NaCl have been shown to modulate PG thickness in Mtb *in vitro*.[65] Addition of NaCl osmotic stress to live mycobacterial cultures did not significantly change glycolipid shedding (Figure 5.11). Collectively, efforts towards modulation of vesiculogenesis with small molecules did not increase glycolipid shedding under conditions tested.

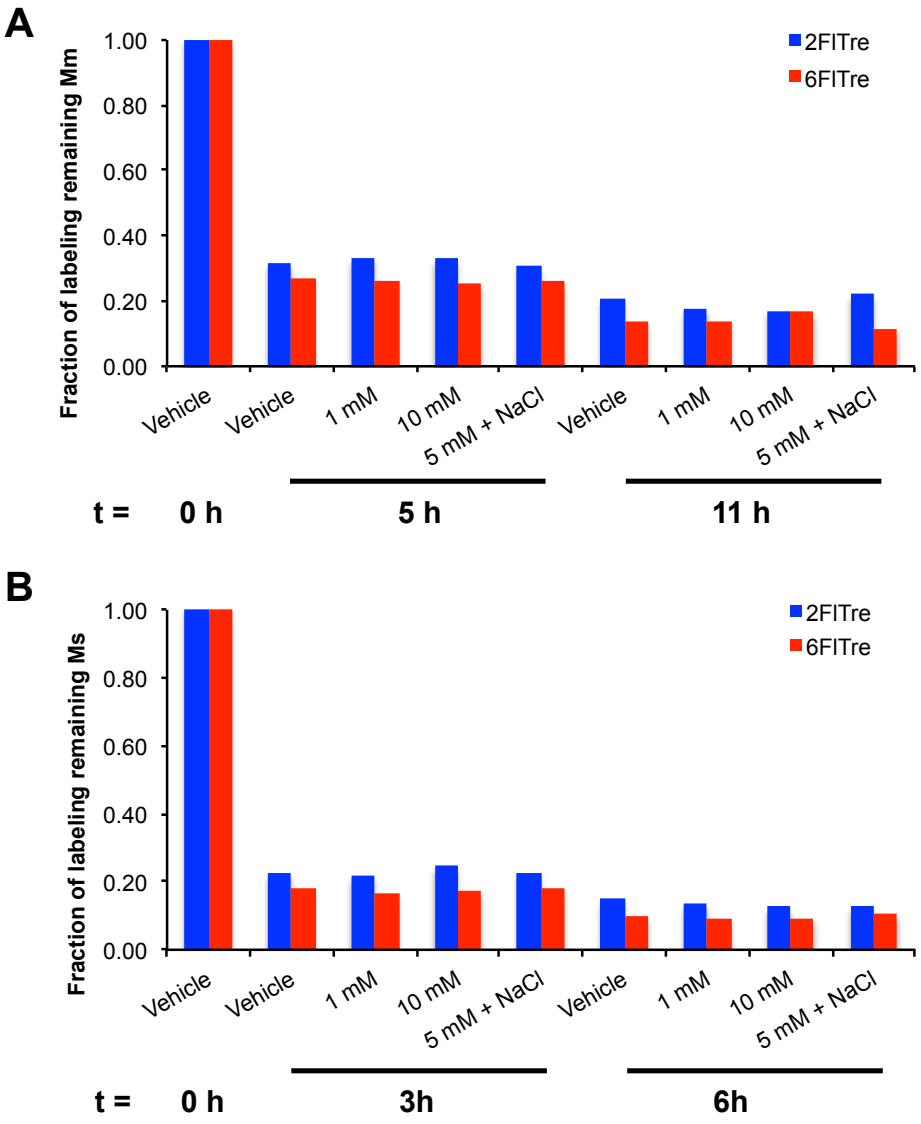

Figure 5.11 Non-genetic methods to potentially modulate OMV production in mycobacteria during growth *in vitro*. Cells were prelabeled with FlTre analogs for several generations, washed and treated with different conditions to promote vesicle formation, such as increasing concentrations of glycine and 140 mM NaCl. Results are shown for both *M. marinum* (A) and *M. smegmatis* (B), where the ratio of remaining label was determined by flow cytometry respective to t = 0 h for 3 technical replicates. Results are representative of at least two independent experiments.

We next considered additional host stresses that bacilli must endure to mount a successful macrophage infection. Both host and pathogen constantly experience a tug-of-war for essential nutrients and metabolites,[2] such as carbon sources and heavy metals. Pathogenic mycobacteria have also been show to modulate vesiculogenesis in iron-depleted environments, where siderophores have been identified in purified OMVs with potential roles in iron acquisition.[57] We labeled Mm cells with 6-TMR-Tre (see synthesis, characterization, and validation in Chapter 3) in rich media (7H9), and minimal media (only glycerol and glucose as carbon sources) in the presence and absence of iron (III). Metabolic labeling was evaluated at the 24 h timepoint by flow cytometry, after washing and fixing the cells. Surprisingly, carbon starvation resulted in increased 6-TMR-Tre labeling when compared to 7H9 rich media, while absence of iron had a more profound increase in labeling efficiency. These results suggest active remodeling of the cell wall under carbon starvation and iron depletion conditions *in vitro*.

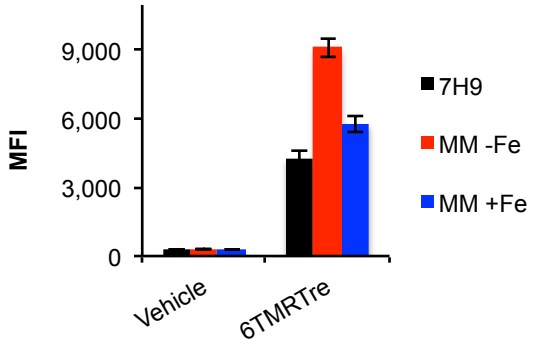

Figure 5.12 Metabolic labeling of *M. marinum* increases with carbon starvation and iron depletion in liquid culture. Cells were labeled with vehicle or 6-TMR-Tre for 24 h in 7H9 media or minimal medial in the presence or absence of iron (III). Metabolic labeling was assessed by flow cytometry after washing and fixation steps. Error bars depict standard deviation of three replicate experiments. Results are representative of at least two independent experiments. Mean fluorescence intensity (MFI)

Visualizing trehalose mycolates during infection in cellulo and in vivo

Selective visualization of defined classes of mycobacterial glycolipids in the context of infection remains unexplored, impeding advances toward unraveling their contributions as virulence factors without altering cell wall composition by genetic approaches. Earlier work by Russell and coworkers has provided insights into how mycobacterial cell wall components can be trafficked during infection in macrophages. Oxidation of mycobacterial surface components followed by labeling with hydrazide-functionalized fluorophores before infection facilitated their detection in endocytic compartments of macrophages.[11] A second example of glycolipid trafficking using this approach revealed that mycobacterial constituents can also be found in the extracellular vesicular fraction, implying involvement of a lysosomal exocytic pathway.[66] Notably, glycolipids released during infection of macrophages were characterized by metabolic labeling with ^{14}C-acetate, including TMM and TDM as components released into the extracellular matrix.[67] However, exclusive visualization of trehalose glycolipids during infection remains challenging.

Barry, Davis and coworkers utilized FITC-Tre to label cocultures of Mtb-infected murine macrophages and observed a relationship between extent of labeling and maturation of the phagolysosome.[14] Fluorescence colocalization studies indicated Mtb H37Rv cells were labeled more strongly when markers of phagosome maturation were absent in infected J774 macrophages after fixation.[14] These results highlighted a high degree of heterogeneity of Mtb cells inside of a single infected macrophage as well as cell-to-cell variability. We were interested in exploring *in cellulo* dynamics of trehalose mycolates in Mm within infected macrophages prior to investigating *in vivo* dynamics in the zebrafish model. Thus, we infected J774 macrophages with Mm-RFP at an MOI = 5, (multiplicity of infection) and treated the coculture with FlTre analogs to selectively label Mm cells (Figure 5.13A). Excess reporter was removed after washing and we visualized average population dynamics by confocal microscopy. Our results indicated that FlTre signal was associated with phagosomal compartments that did not contain Mm cells, which consistent with previous findings (data not shown).[11,66] Surprisingly, we found trehalose mycolates to be highly dynamic as significant changes in fluorescence intensity and total volume occurred for FlTre signal in the course of 4 h (Figure 5.13 B and C).

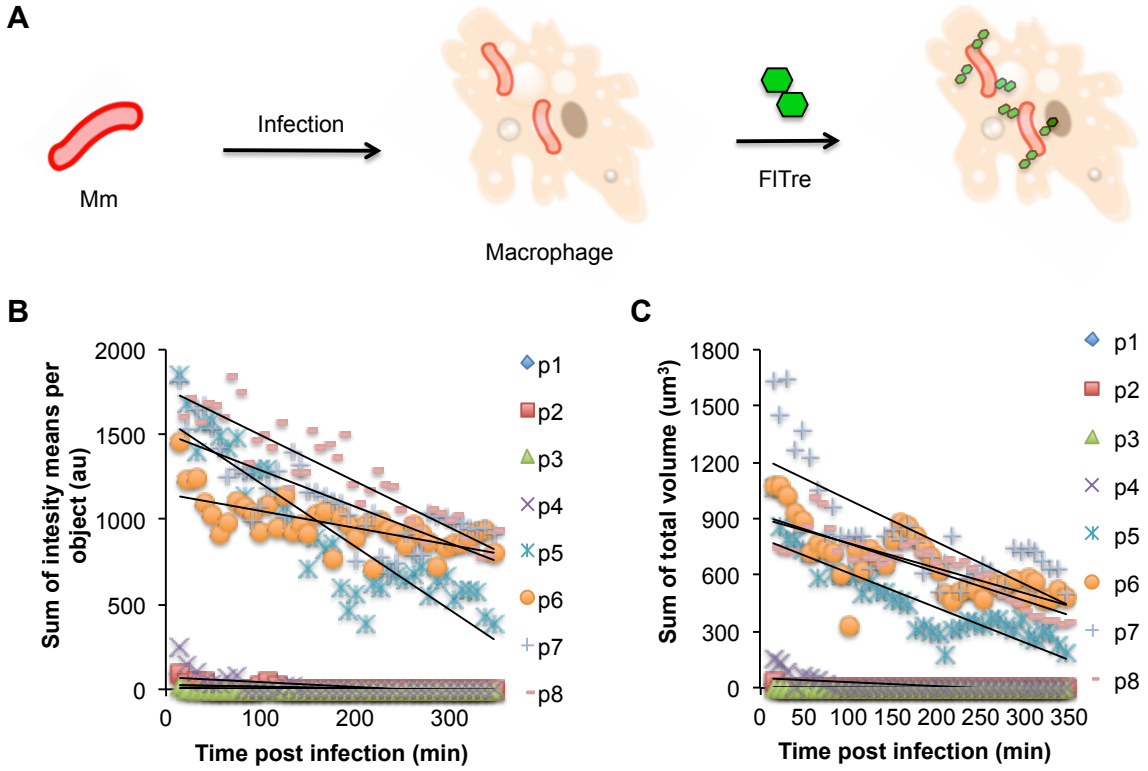

Figure 5.13 Trehalose mycolates are highly dynamic during infection of murine macrophages. A) Experimental scheme describing infection of J774 macrophages with Mm and treatment of co-culture with 100 µM 2-FlTre or vehicle for 32 h. Infected macrophages were visualized by live-cell imaging confocal microsocopy for 4 h. Four different fields were analyzed for vehicle (p1-p4) and FlTre (p5-p8) to quantify global fluorescence intensity (B) and volume (C) given by the green channel.

We hypothesize that this decrease in fluorescence is not due to fluorescein stability, as low pH should not significantly affect the quantum yield of the fluorophore.[68] In addition, we utilized acquisition settings that would minimize photobleaching of fluorescein. Our results suggested that trehalose mycolates are rather dynamic during *in cellulo* infection of live macrophages.

Next, we proceeded to implement a BCN-Tre reporter labeling strategy to visualize trehalose mycolates during infection. This approach would lend itself to an additional handle on temporal control with the delivery of a fluorogenic secondary labeling reagent. To this end, infected murine macrophages were treated with BCN-Tre analogs for 43 h, washed and treated with fluorogenic azido-coumarin[69] for 4h (Figure 5.14A). Similar to labeling with FlTre analogs, BCN-Tre showed differential metabolic incorporation by Mm cells within a single infected macrophage. Bacteria showed polar and side-wall labeling, but interestingly also showed punctate staining. This phenomenon was only observed for a small number of cells, as the size of these structures (50-250 nm) resides along the resolution limit for widefiled fluorescence microscopy. However, these labeled structures were clearly associated with the bacteria (Figure 5.14B), suggesting that they are Mm-derived. Interestingly, a recent report demonstrated that OMVs generated by Mtb are distinguishable from exosomes released from infected macrophages with gradient ultracentrifugation procedures.[70] These vesicle subtypes can be differentiated by the markers exposed on the surface as evidenced by immunostaining and western blotting. Taken together, metabolic labeling allowed us to visualize trehalose mycolate dynamics in real-time and reports on trafficking events as well as identification of OMV-like structures for the first time.

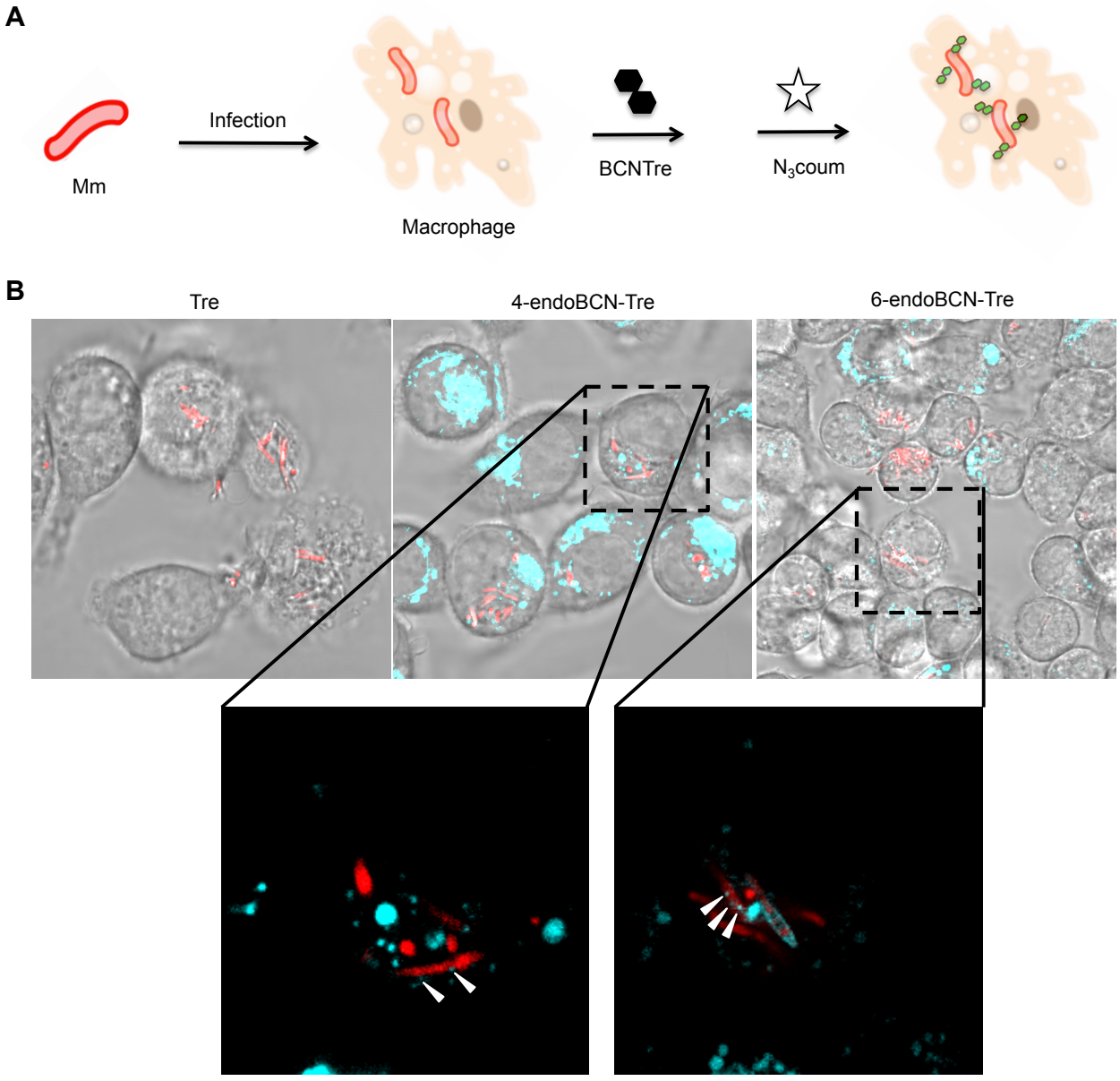

Figure 5.14 BCN-Tre metabolically labels Mm within infected macrophages. A) Experimental scheme depicting infection and labeling procedures. Infected co-cultures were labeled with 100 µM BCN-Tre analogs or vehicle for 43 h, washed and incubated with 10 µM azido-coumarin for 4 h prior to fluorescence imaging. B) Fluorescence microscopy images show heterogeneous labeling of phagocytosed bacteria (only one z-slice is shown). White arrowheads point at BCN-Tre labeled structures with a diameter that correlates with OMVs. Outer membrane vesicle (OMV)

Tissue-cultured phagocytic cells alone do not recapitulate host-pathogen interactions orchestrated during infection. The zebrafish has served as an important pathogenesis animal model that mirrors many aspects of human tuberculosis.[34,35] Notably, zebrafish larvae, up to 2 weeks post fertilization, have only developed innate immunity, which facilitates the dissection of innate versus adaptive immunity contributions during disease progression. In this regard, zebrafish embryos can be injected with a single-cell suspension of Mm cells into the hindbrain ventricle or caudal vein (Figure 5.15). In the former, delivery of bacteria to this cavity is desirable to visualize host-pathogen interactions during macrophage recruitment.[40] In the latter, bacteria in circulation can result in multiple granulomatous lesions more similar to chronic infection.

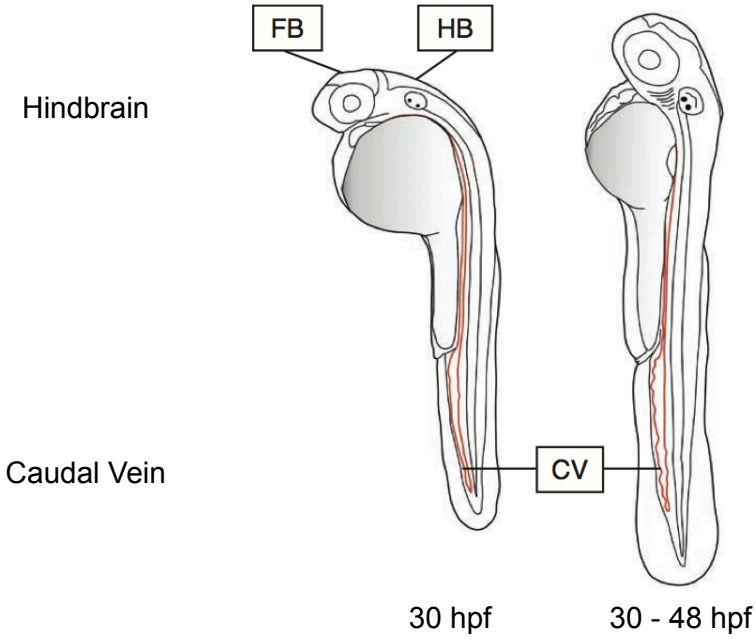

Figure 5.15. Larvae zebrafish tuberculosis pathogenesis model. Adapted with permission from Nature Publishing Group: Nature Protocols, reference 32, Copyright 2013.

We hypothesized that increased phenotypic heterogeneity in metabolic states[71] or growth states[72] in mycobacteria during infection could be captured by visualizing cell wall dynamics within infected zebrafish. Delivery of FlTre analogs by microcapillary injection would allow labeling of actively growing bacteria or cell wall remodeling dynamics, as trehalose is not metabolized by zebrafish. To this end, we co-injected 150-200 Mm cells and FlTre analogs (10 mM stock solution) into the caudal vein of zebrafish embryos at 30 h post fertilization (hpf) as shown in Figure 5.16A. Prior to injection, Mm cells were in contact with FlTre analogs for no more than 5 min, at which point we have not observed any metabolic incorporation by flow cytometry (data not shown). Infected embryos were analyzed at 48 hpf and showed selective Mm labeling. At this timepoint, heterogeneity in metabolic labeling of Mm could be a result of different growth states or accessibility of the probe itself (Figure 5.16). Importantly, injection of FlTre analogs into the caudal vein is cleared by the early kidney system and excess reporter accumulates in the pronephric ducts in a period of 12 h. Unfortunately, this time window might

contain interesting dynamics that we were unable to visualize with fluorescein-trehalose conjugates.

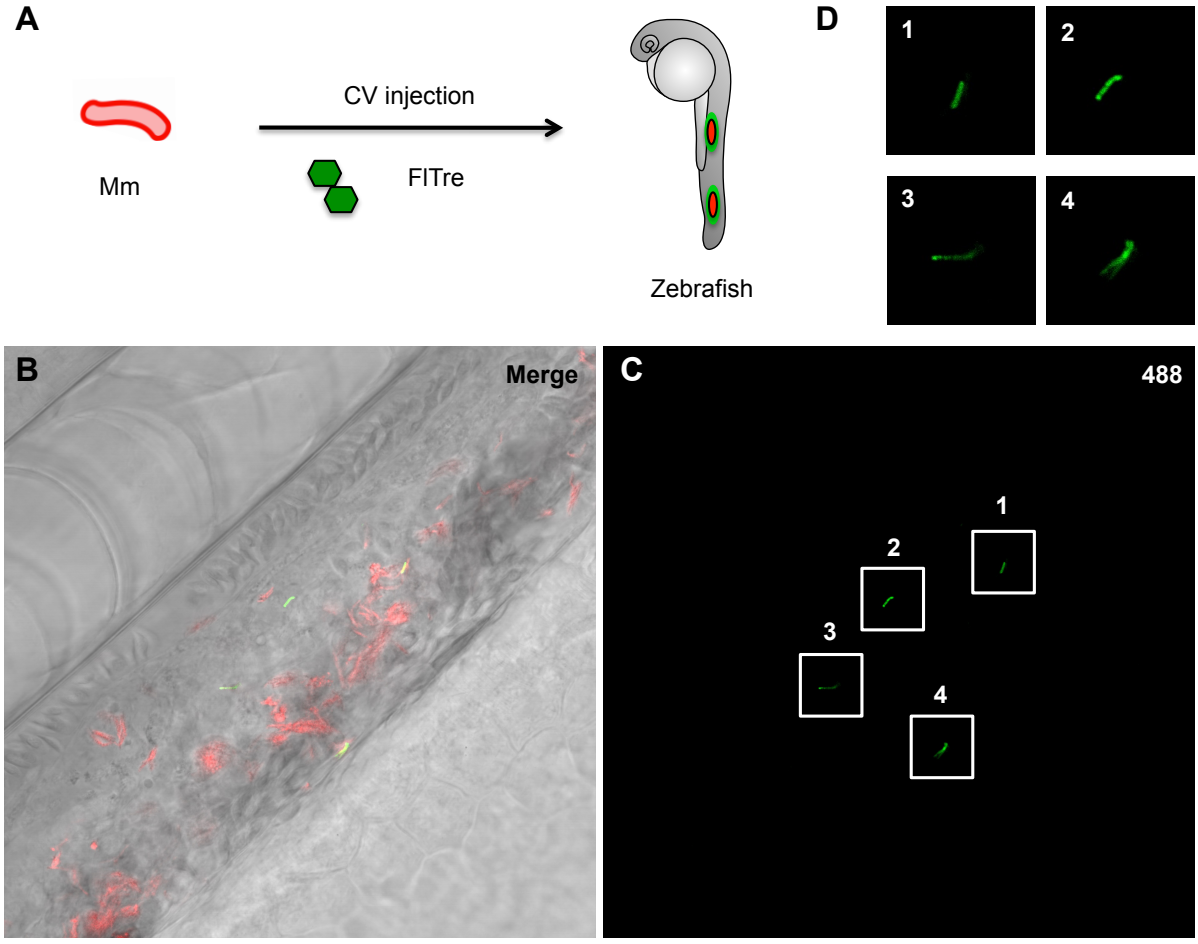

Figure 5.16 FlTre analogs metabolically label Mm during *in vivo* infection. A) Single-cell Mm suspension was co-injected with 2-FlTre reporter into the caudal vein (CV) at 30 hpf and embryos were visualized at 48 hpf by confocal microscopy. Fluorescence microscopy images reveal selective incorporation by Mm cells (constitutively expressing RFP) in the merge (B) and green (C) channels. Labeled Mm cells are highlighted in numbered white squares with expanded views in (D).

We also applied a BCN-Tre metabolic labeling strategy to visualize trehalose mycolates *in vivo*. Delivery of BCN-reactive fluorogenic probes[50,51,69] would allow minimization of background fluorescent signal stemming from excess probe that had not been incorporated. We screened fluorogenic probes and found that azido-coumarin presented increased autofluorescence at the required wavelengths. However, we were also discouraged by the limited cell permeability of CalFluors.[51] For this reason, we focused our efforts on utilizing a tetrazine-oregon green probe[50] that has been previously used for imaging glycans systemically in zebrafish.[49] We designed infection experiments to accommodate enough time for Mm cells to metabolize BCN-Tre prior to delivering the fluorogenic tetrazine probe. Along a similar vein to FlTre labeling of

Mm after caudal vein injection, Mm cells were coinjected with a stock BCN-Tre solution. After 2 days, embryos received a tertazine-oregon green injection and were imaged 18 h later (Figure 5.17A). Gratifyingly, injection of vehicle (trehalose) resulted in negligible fluorescence stemming from intrinsic background of fluorogenic probe. On the other hand, we were able to capture metabolic labeling of Mm for extracellular bacterial aggregates as shown in Figure 5.17B. We propose that a two-step labeling approach has limited accessibility for incorporation into intracellular bacteria. After comparing FlTre and BCN-Tre *in vivo* labeling, we obtained better temporal resolution with FlTre analogs by the one-step labeling strategy.

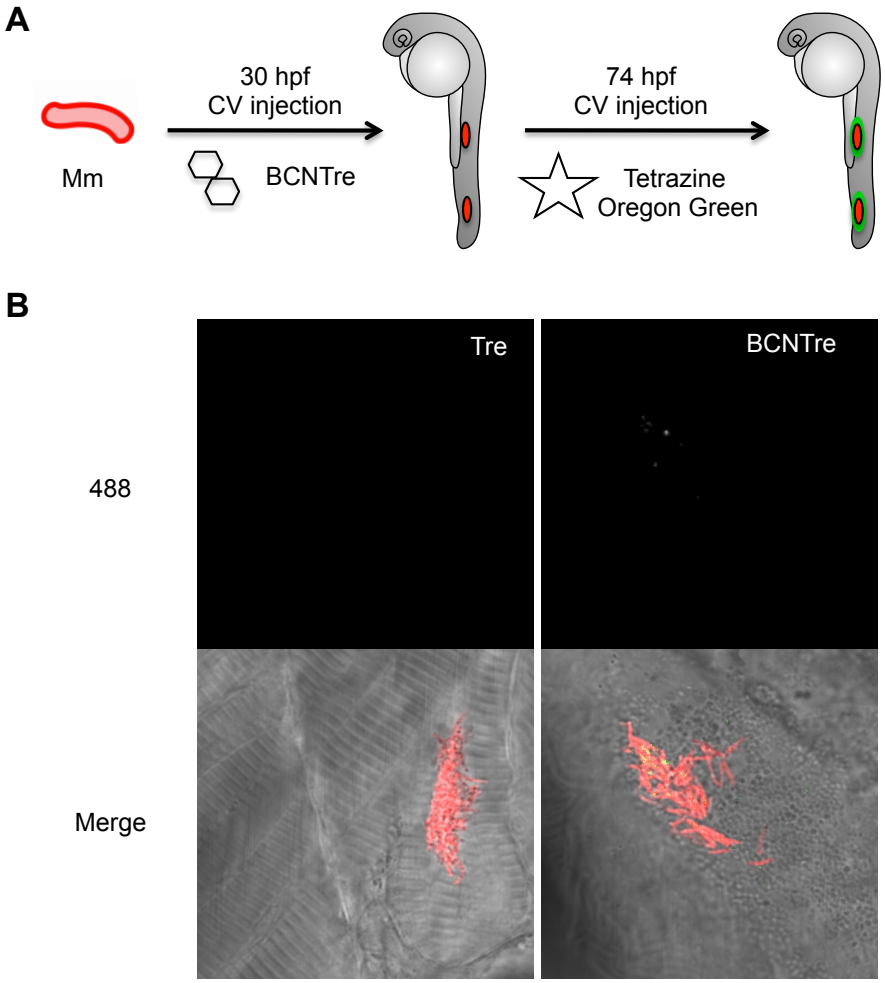

Figure 5.17 Visualization of trehalose mycolates with BCN-Tre and tetrazine-Oregon Green bioorthogonal pair *in vivo*. A) Zebrafish embryos were CV injected at 30 hpf with Mm and BCN-Tre. At 74 hpf, larvae were CV-injected with tetrazine-oregon green conjugate and visualized by confocal microscopy at 92 hpf. B) Fluorescence image showing BCN-Tre signal after reaction with fluorogenic probe for extracellular bacterial aggregates. Caudal vein (CV), hours post fertilization (hpf)

We were curious whether the release of microvesicles in real-time during *in vivo* infection could be captured by fluorescence imaging. We selected the hindbrain cavity to capture early interactions with recruited macrophages as well as visualization of a contained infection (approximately 15 nL volume). Specifically, we asked the question of whether macrophages played a role in responding to secreted OMVs, which can be achieved by monocyte depletion by anti-sense treatment (pu1 morphant)[40,73]. We hypothesized that Mm could decrease vesiculogenesis within an infected host, as markers from OMVs have been shown to produce a TLR2-mediated inflammation in mice.[55] To achieve this, we proceeded by prelabeling Mm cells prior to preparation of single-cell suspensions to obtain a homogenously labeled population for infection studies. Bacteria were injected into the hindbrain at 48 hpf and visualized by confocal microscopy for 12 h. In a similar fashion to caudal vein infections, trehalose mycolates were highly dynamic in the first 3 h (Figure 5.18A), for both wildtype and pu1 morphant embryos. We analyzed video-lapse microscopy images (every 8 min) in this 3 h time window to further characterize behavior of fluorescence signal that matched in size to those of OMVs. Extracted number of vesicles were normalized to bacterial burden by dividing it by bacterial volume as given by constitutively expressing Mm-RFP. Secreted OMVs significantly varied in the presence or absence of macrophages (Figure 5.18B), where wildtype embryos showed a fast decrease in vesicle release within the first 2 h. Bacteria injected into pu1 morphants maintained a rather constant rate of vesiculogenesis for the first 3 h, produced for 1 h longer than in wildtype embryos. This work suggests that microvesicles are released prior to macrophage recruitment and it is a bacteria-driven process. We propose that vesiculogenesis could be a potential signaling mechanism for bacteria to reside in the intracellular niche after macrophage phagcogytosis.

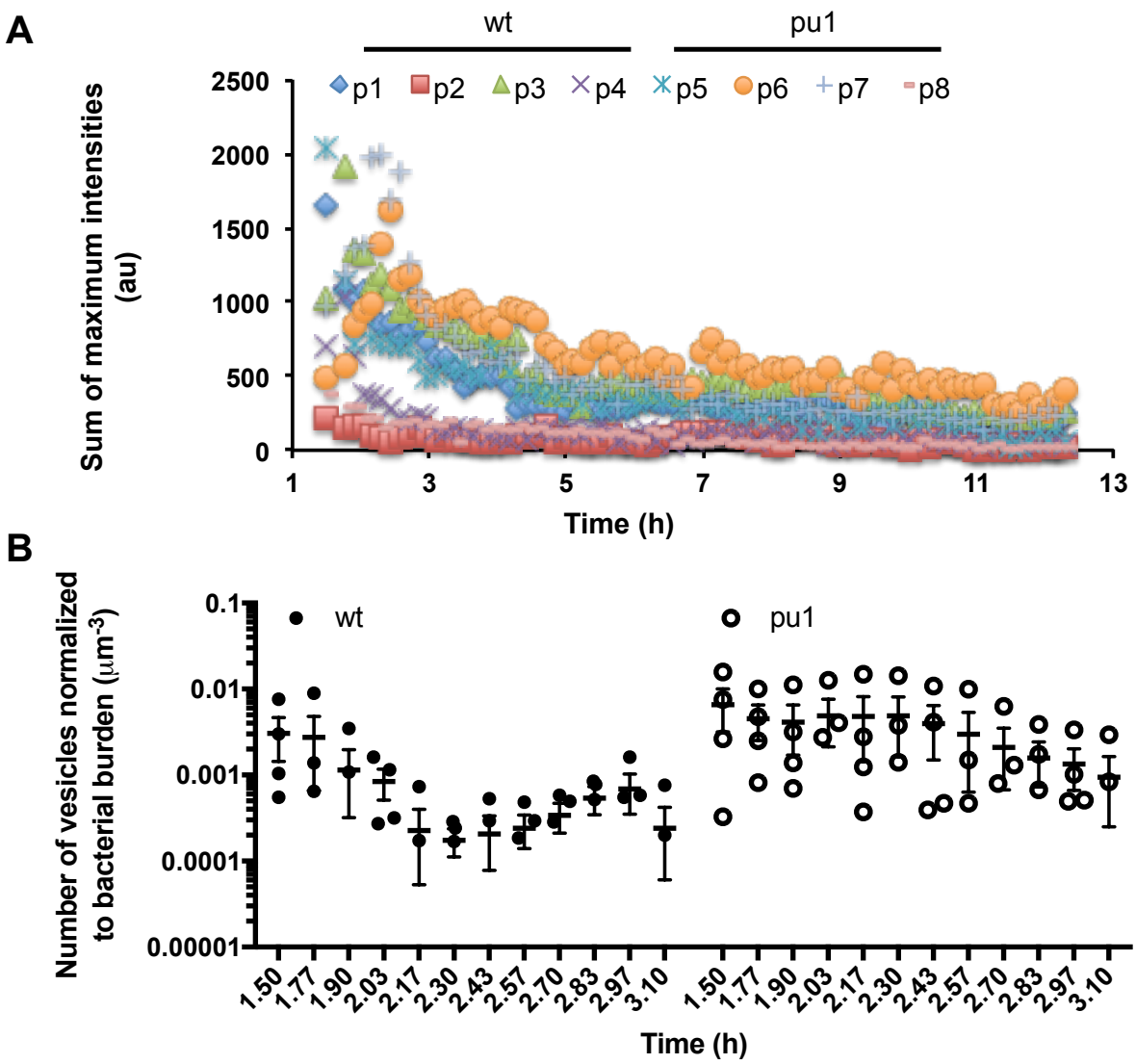

Figure 5.18 *In vivo* dynamics of trehalose mycolates during macrophage recruitment after hindbrain injection. A) Four infected embryos were analyzed for wildtype (p1-p4) and pu1 morphant (p5-p8) groups to quantify global maximum fluorescence intensity given by FlTre signal. B) Fluorescence intensities corresponding to vesicles (volume $\leq 3\ \mu m^{-3}$) were normalized to bacterial burden for dynamics captured every 8 min. Error bars represent mean ± SEM. Two-way ANOVA $p < 0.004$

CONCLUSION

Trehalose mycolates have remained elusive glycolipids in the context of infection due to the lack of biochemical tools to study them. Preparations of vesicles, emulsions or monolayers have shown that orientation and assembly of these amphiphiles can exert different responses by the immune system.[24,74–76] In contrast, we have shown that metabolic labeling of trehalose mycolates can be achieved selectively within the infected host counterparts with a panel of unnatural trehalose reporters. Our studies reveal interesting dynamics during infection *in cellulo* and *in vivo* that could only be visualized by harnessing the selectivity of mycobacterial trehalose metabolism. Notably, we have identified for the first time that trehalose mycolates are present in mycobacterial microvesicles. In combination with super resolution microscopy, we obtained a molecular view of these glycolipids residing in the cell wall. Additionally, our works points at OMVs playing an early role during pathogenesis in the Mm-zebrafish model that warrants further investigation.

With additional experiments, we anticipate determining whether the production of vesicle subtypes is host-protective or pathogen-driven by directly examining host-pathogen interactions. Thorough characterization of vesicles in combination with super resolution imaging would provide an accurate depiction of the observed trafficking during infection. Consequent insights could provide avenues for development of new therapeutics for the treatment of tuberculosis.

MATERIALS AND METHODS

General methods for synthesis

Materials and reagents were obtained from commercial sources without further purification unless otherwise noted. Anhydrous solvents were obtained either commercially or from an alumina column solvent purification system. All reactions were carried out in oven-dried glassware under nitrogen unless otherwise noted. Analytical TLC was performed on SiliCycle glass-backed silica gel 60 Å plates (thickness 250 μm) and detected by UV lamp or charring with 5% H_2SO_4 in MeOH. Column chromatography was performed using SiliCycle SiliaFlash P60 silica gel (40-63 μm). ^{1}H NMR spectra were recorded at 400, 500 or 600 MHz with chemical shifts in ppm referenced to solvent peaks. ^{13}C NMR spectra were recorded at 100 or 150 MHz with chemical shifts referenced to solvent peaks. NMR spectra were obtained on Bruker AVQ400, AVB-400, AV-500, or AV-600 instruments. Coupling constants (*J*) are reported in hertz (Hz). High-resolution electrospray ionization mass spectrometry (HR ESI MS) was performed at the UC Berkeley Mass Spectrometry Facility.

Reversed-phase HPLC was performed on a Varian Pro Star system with a Varian UV-Vis detector model 345 (210, 254 nm) on a Dynamax Microsorb C-18 preparative column (21.4 x 250 mm) at a flow rate of 20 mL/min or on an Agilent Eclipse XDB-C18 5μm semi-preparative column (9.4 x 250 mm) at a flow rate of 3 mL/min.

TreAz,[15] azido-coumarin,[69] tetrazine-oregon green conjugate[50] and endoBCN-p-nitrophenol[77] were synthesized as previously reported.

General procedure for the synthesis of BCN-trehalose analogs

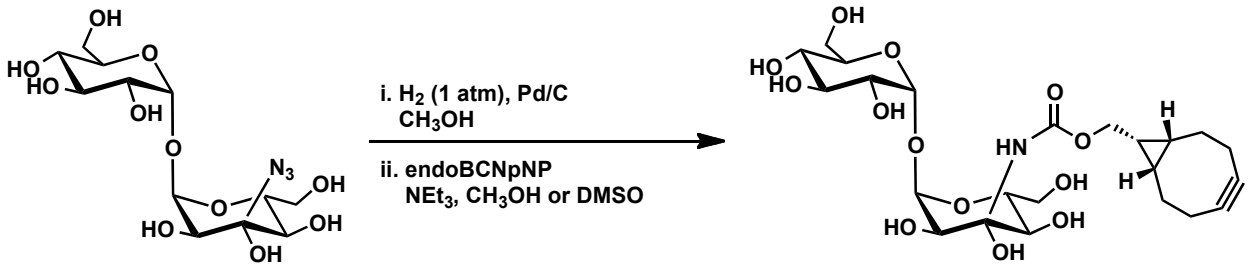

To a stirring solution of TreAz in anhydrous DMSO (at a final concentration of 20 mM) under argon atmosphere, 10% Pd/C was added to reaction mixture. A hydrogen-filled balloon was connected to the reaction flask to replace the argon atmosphere and stirred overnight at room temperature. The reaction mixture was filtered through celite and concentrated by rotary evaporation to afford the amine-trehalose product. Without further purification, amine-trehalose (1 equiv) was subjected to a reaction with BCN-p-nitrophenol (1.1 equiv) after dissolving in a DMSO and treating with NEt_3 (3.5 equiv). Reaction mixture was stirred overnight, followed by lyophilization of DMSO. White solids were purified by column chromatography.

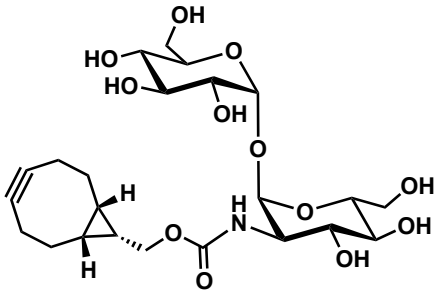

2-endoBCNTre

***N-(((1R,8S,9s)-bicyclo[6.1.0]non-4-yn-9-yl) methylcarbamate)-2-amino-2-deoxy-α,α-D-trehalose* (2-endoBCNTre, 5.1)** (3.2 mg, 92%) was obtained as a white solid. R_f = 0.51 (2:1 $CHCl_3$:MeOH, 5% H_2SO_4 in MeOH) ^{1}H NMR (500 MHz, D_2O): δ 0.82 (t, *J* = 10.0 Hz, 2H), 1.25 (q, 1H), 1.43 (d, *J* = 12.3 Hz, 2H), 2.00 – 2.17 (m, 5H), 2.55 (s, 2H), 3.22 – 3.34 (m, 2H), 3.44 – 3.61 (m, 6H), 3.61 – 3.78 (m, 6H), 4.04 (d, *J* = 8.2 Hz, 2H), 5.05 (t, 2H), 8.27 (s, 0H). ^{13}C NMR (125 MHz, D_2O): δ 17.26, 19.83, 20.83, 28.66, 38.80, 55.43, 60.58, 64.03, 68.23, 69.42, 69.69, 69.79, 71.24, 72.27, 72.61, 92.87, 93.30, 100.46, 159.33. HRMS (ESI): Calculated for $C_{23}H_{35}NO_{12}Na$ $[M\text{-}Na]^+$ 540.2051, found 540.2062.

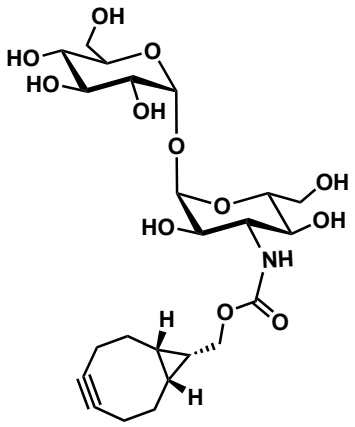

3-endoBCNTre

***N-(((1R,8S,9s)-bicyclo[6.1.0]non-4-yn-9-yl) methylcarbamate)-3-amino-3-deoxy-α,α-D-trehalose* (3-endoBCNTre, 5.2)** (5.2 mg, 77%) was obtained as a white solid. R_f = 0.60 (2:1 $CHCl_3$:MeOH, 5% H_2SO_4 in MeOH) ^{1}H NMR (500 MHz, D_2O): δ δ 0.82 (t, *J* = 10.0 Hz, 2H), 1.25 (q, 1H), 1.43 (d, *J* = 12.3 Hz, 2H), 2.00 – 2.17 (m, 5H), 2.55 (s, 2H), 3.22 – 3.34 (m, 2H), 3.44 – 3.61 (m, 6H), 3.61 – 3.78 (m, 6H), 4.04 (d, *J* = 8.2 Hz, 2H), 5.05 (t, 2H), 8.27 (s, 0H). ^{13}C NMR (125 MHz, D_2O): δ 17.26, 19.83, 20.83, 28.66, 38.80, 55.43, 60.58, 64.03, 68.23, 69.42, 69.69, 69.79, 71.24, 72.27, 72.61, 92.87, 93.30, 100.46, 159.33.. HRMS (ESI): Calculated for $C_{23}H_{35}NO_{12}Na$ $[M\text{-}Na]^+$ 540.2051, found 540.2060.

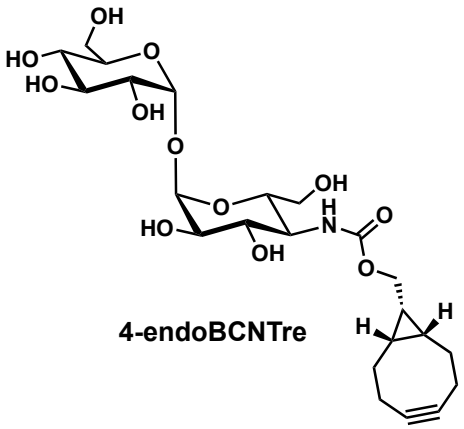

4-endoBCNTre

***N-(((1R,8S,9s)-bicyclo[6.1.0]non-4-yn-9-yl) methylcarbamate)-4-amino-4-deoxy-α,α-D-trehalose* (4-endoBCNTre, 5.3)** (5.6 mg, 72%) was obtained as a white solid. R_f = 0.52 (2:1 $CHCl_3$:MeOH, 5% H_2SO_4 in MeOH) ^{1}H NMR (500 MHz, D_2O): δ 0.96 (t, *J* = 10.0 Hz, 2H), 1.35 – 1.43 (m, 1H), 1.52 – 1.63 (m, 2H), 2.09 – 2.33 (m, 6H), 2.69 (s, 6H), 3.42 (t, *J* = 9.5 Hz, 1H), 3.51 (t, *J* = 10.3 Hz, 1H), 3.58 – 3.65 (m, 2H), 3.65 – 3.76 (m, 3H), 3.77 – 3.90 (m, 5H), 4.12 – 4.29 (m, 2H), 5.16 (d, *J* = 3.8 Hz, 1H), 5.20 (d, *J* = 3.8 Hz, 1H), 8.42 (s, 0H). ^{13}C NMR (125 MHz, D_2O): δ 17.10, 19.72, 20.69, 28.52, 28.55, 38.71, 53.14, 60.50, 60.80, 64.11, 69.65, 70.42, 70.97, 71.40, 72.14, 72.49, 93.22, 100.34, 158.59. HRMS (ESI): Calculated for $C_{23}H_{35}NO_{12}Na$ $[M\text{-}Na]^+$ 540.2051, found 540.2050

.

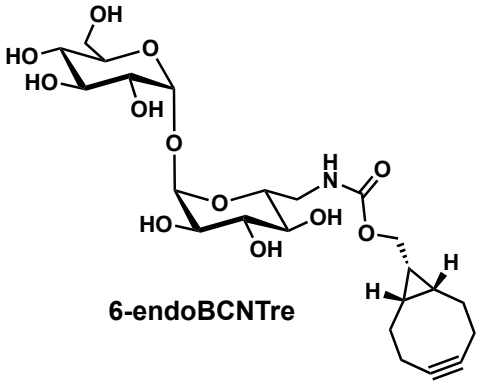

6-endoBCNTre

***N-(((1R,8S,9s)-bicyclo[6.1.0]non-4-yn-9-yl) methylcarbamate)-6-amino-6-deoxy-α,α-D-trehalose* (6-endoBCNTre, 5.4)** (4.1 mg, 72%) was obtained as a white solid. R_f = 0.58 (2:1 $CHCl_3$:MeOH, 5% H_2SO_4 in MeOH) ^{1}H NMR (500 MHz, D_2O): δ 0.81 (t, *J* = 10.0 Hz, 2H), 1.18 – 1.30 (m, 1H), 1.42 (d, *J* = 12.6 Hz, 2H), 2.00 – 2.17 (m, 5H), 3.16 (t, 2H), 3.25 (t, *J* = 9.5 Hz, 1H), 3.36 (d, *J* = 14.4 Hz, 1H), 3.41 (dd, *J* = 10.0, 3.8 Hz, 1H), 3.46 (dd, *J* = 9.9, 3.9 Hz, 2H), 3.51 – 3.59 (m, 3H), 3.59 – 3.70 (m, 5H), 3.96 – 4.10 (m, 2H), 4.97 (dd, *J* = 8.7, 3.9 Hz, 2H), 8.27 (s, 0H). ^{13}C NMR (125 MHz, D_2O): δ 17.21, 19.86, 19.88, 20.85, 28.69, 41.18, 60.64, 64.11, 69.70, 69.81, 71.08, 71.16, 71.24, 72.30, 72.50, 72.71, 93.08, 93.24, 100.44, 159.12, 171.17. HRMS (ESI): Calculated for $C_{23}H_{35}NO_{12}Na$ $[M\text{-}Na]^+$ 540.2051, found 540.2044.

Synthesis of 6-AF647-trehalose analog

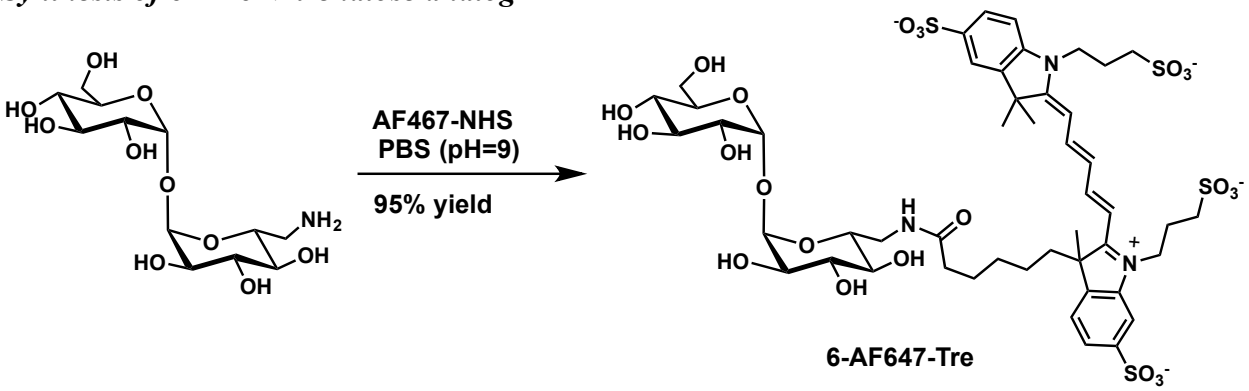

To a stirring solution of 6-Tre-NH_2 (0.58 mg, 1.7 umol, 2 equiv) in phosphate buffered solution (PBS with pH = 9), AF647-NHS (1 mg, 0.8 mmol, 1equiv) was added to flask. Reaction mixture was stirred overnight at room temperature, followed by concentration by rotary evaporation. Reverse-phase HPLC purification using a 5-100% MeCN/H_2O + 0.1% TFA gradient afforded desired product.

N-(6-oxohexyl-AlexaFluor647)-6-amino-6-deoxy-α,α-D-trehalose **(6-AF647-Tre, 5.5)** (0.9 mg, 95%) was obtained as a white solid. R_f = 0.31 (1:2:2 H_2O:EtOAc:IPA, 5% H_2SO_4 in MeOH) ^{1}H NMR (500 MHz, D_2O): δ 0.81 (t, *J* = 10.0 Hz, 2H), 1.18 – 1.30 (m, 1H), 1.42 (d, *J* = 12.6 Hz, 2H), 2.00 – 2.17 (m, 5H), 3.16 (t, 2H), 3.25 (t, *J* = 9.5 Hz, 1H), 3.36 (d, *J* = 14.4 Hz, 1H), 3.41 (dd, *J* = 10.0, 3.8 Hz, 1H), 3.46 (dd, *J* = 9.9, 3.9 Hz, 2H), 3.51 – 3.59 (m, 3H), 3.59 – 3.70 (m, 5H), 3.96 – 4.10 (m, 2H), 4.97 (dd, *J* = 8.7, 3.9 Hz, 2H), 8.27 (s, 0H). ^{13}C NMR (125 MHz, D_2O): δ 17.21, 19.86, 19.88, 20.85, 28.69, 41.18, 60.64, 64.11, 69.70, 69.81, 71.08, 71.16, 71.24, 72.30, 72.50, 72.71, 93.08, 93.24, 100.44, 159.12, 171.17. HRMS (ESI): Calculated for $C_{33}H_{35}N_2O_{15}S$ $[M-H]^{-2}$ 600.6361, found 600.6352.

Bacterial strains, media, and reagents

Bacterial species used in this work include *Mycobacterium marinum* strain M (ATCC BAA-535). *M. marinum* was cultured in Middlebrook 7H9 media supplemented with 10% OADC (oleic acid, albumin, dextrose, catalase), 0.5% glycerol, and 0.05% tween 80 at 37 ^{o}C. Minimal media with defined iron concentrations was prepared as previously described.[57] Briefly, minimal media (MM) was prepared by adding 0.5% asparagine, 0.5% KH_2PO_4, 0.2% glycerol, 10% ADN (0.5% BSA, 0.2% D-glucose, 0.085% NaCl), 0.5 mg/L $ZnCl_2$, 0.1 mg/L $MnSO_4$, 40 mg/L $MgSO_4$, and 50 mg/L $FeCl_3$ (if needed for iron supplementation to obtain 1 L of media. MM was subjected to iron depletion by incubation with Chelex resin 100 (following manufacturer's instructions) for 1 h stirring at room temperature with 25 g resin/L media. Resin was filtered after incubation and pH was adjusted to 6.8. At this stage, iron (III) was added back in for defined concentration.

Stock solutions of FlTre analogs were prepared at 10 mM in DMSO and stored at -20 ^{o}C. Other reagent stocks include ebselen (Cayman Chemical, 2 mg/mL in EtOH, stored at -20 ^{o}C), and FITC-Tre (Kerafast, 10 mM in DMSO, stored at -20 ^{o}C).

Bacterial metabolic labeling conditions
Frozen bacterial stocks were used to start stationary phase cultures, which were used to innoculate experimental cultures for all bacterial strains. Cells were grown in aerated culture tubes or 96-well plates with shaking until the desired optical density was achieved. Bacterial cultures in exponential growth phase were incubated with trehalose probes until designated end-point of the experiment. Bacterial cells were fixed prior to flow cytometry or fluorescence microscopy unless otherwise noted.

For metabolic labeling profile, *M. marinum* was incubated with 100 μM FlTre or BCNTre for time periods encompassing several doubling times 15- 24 h, unless otherwise noted.

For *in vitro* pulse-chase experiments, bacteria were labeled with 100 μM metabolic treahlose reporters. Trehalose competition experiments included co-incubation of native trehalose at 0, 0.5 or 5.0 mM with designated trehalose reporter in *M. marinum* for 4 h. Bacterial cells were co-treated with 100 μg/mL ebselen, for *M. marinum* (4 h), as well as with trehalose reporters.
Metabolic labeling in iron-defined conditions was performed for a period of 24 h incubation in rich media 7H9, MM without iron, or MM with iron supplementation.

Flow cytometry
Fluorescently labeled cells were analyzed in 96-well plate format in a BD Biosciences Accuri C6 flow cytometer equipped with a BD C-Sampler. Data was collected for 100,000 events at a rate of > 5,000 events/s for each sample. All flow cytometry experiments were performed in triplicate where results are representative of at least two independent experiments.

Macrophage infections with M. marinum
Cultures of *M. marinum* (3 mL, 50 ug/mL Hyg for fluorescent strains) were started at OD_{600} = 0.1-0.2 from frozen stocks and grown for two to two and a half doubling times. Bacteria were spun down and transferred to several wells of a 96-well plate (this is because in Falcon tubes a lot of cells were lost over the course of washing). Bacteria were washed 3 times with 7H9 + OADC + TW80 + glycerol (150 uL, 5 min at 3700 x g to pellet cells).

Prior to labeling, bacteria were passaged through a 27G needle. Labeled bacteria were washed 3 times with 7H9 + OADC + TW80 + glycerol and once with PBS (150 uL, 5 min @ 3700 x g to pellet cells). After resuspension in PBS, bacteria were passaged 10 times through a 27G needle. To pellet remaining clumps, bacteria were spun at 1000 rpm for 2 minutes. Supernatants were pooled from separate wells and single cells were quantified by measuring OD_{600}.

J774 or RAW264.7 were cultured in DMEM high glucose + 10 % fetal bovine serum (FBS), streptomycin (0.1 mg/ mL), and penicillin (100 units/ mL). Cells were seeded at least 16 hours prior to infection, to reach 2 x 10^5 cells/mL at the time of infection. Antibiotic medium was removed from macrophages immediately prior to infection. Cells were prepared by washing two times with media without antibiotics and infection took place in this medium.

Bacteria were added to the macrophages at MOI = 1, 5, 10 and allowed to infect over the course of 3 hours at 33 °C, 5 % CO_2. After infection, DMEM was replaced with DMEM + Gentamicin (200 μg/mL) and incubated for 30 minutes at 33 °C, 5% CO_2. Cells were washed two times with

DMEM high glucose + 10% FBS. For live cell imaging by confocal microscopy, cells were transferred to DMEM fluorobrite without phenol red in LabTech well slides.

Zebrafish husbandry and infections

Wildtype AB zebrafish were maintained as described.[32] Larvae were infected at 30-48 h post fertilization (hpf) via injection into the caudal vein or hindbrain ventricle. The number of embryos used in experiments was guided by prior results from our laboratory and our collaborator Prof. Lalita Ramakrishnan. Larvae were randomly allotted to different experimental groups or morphants. Zebrafish husbandry and all performed experiments were in compliance with the Institutional Animal Care and Use Committee approved protocols.

Single-cell supensions of *M. marinum* used of injection into the caudal vein or hindbrain were obtained as previously described.[32] For embryo infections, frozen stocks of single cell preparations of known titer were thawed prior microcapillary loading.[32,78]

Trehalose metabolic reporter labeling in vivo

Trehalose metabolic reporters were delivered into the caudal vein for better tissue distribution. Embryos of 30-96 hpf were injected with 3-5 nL of working stocks 10 mM FlTre in DMSO, 0.6 mM BCNTre in DMSO, 2.5 mM tetrazine-oregon green in water depending on the experimental setup.

Morpholino injections

Morpholinos (MO) were injected into yolk of 1-4 cell stage embryos. Pu1 morphants were obtained as previously described.[40,73] MO mix composition was given by 0.375 mM initiation MO and 0.025 mM exon MO. Phenol red was added to a final concentration of 2 mg/mL in 0.2 M KCl and 5 nL of pu1 MO mix were injected per embryo.

Fluorescence microscopy

Bacterial cultures (1-3 μL) were spotted on 1% agarose pads mounted on glass slides, installed coverslip, and sealed with nail polish. Fluorescence imaging was performed with a Nikon A1R resonant scanning confocal microscope using a CFI Plan Apo Lambda 60x oil objective. Images were captured with a Cool Snap HQ^2 (Photometrics) and processed with NIS Elements software. Acquisition and processing of images was performed identically for control and test samples.

Imaris image analysis

Confocal microscopy raw data was analyzed with Imaris v8.1.2 (Bitplane).

Super resolution fluorescence microscopy

Detection of these single molecules was performed by wide-field illumination. Every laser beam on the excitation pathway was circularly polarized with a quarter-wave plate and directed to an Olympus IX-71 imaging body with an oil-immersion UPlan-Apo objective with 1.4 NA and 100x magnification. A portion of the fluorescent emission is then collected with the same objective and is detected using an EMCCD camera. We used an electron-multiplication gain of 200 and 10 MHz pixel readout rate, where the exposure time is on the order of tens of milliseconds per frame. The size of each pixel on the chip is 16μm x 16μm and is cooled down to -70°C to suppress dark noise. The data were saved as *.TIF files.

For single-particle tracking experiments, all live-cell imaging was performed at 33°C inside an incubator. In addition, we add an imaging cocktail to our sample that includes glucose, pyranose oxidase, and catalase, which consumes oxygen and subsequently lengthens the lifetime of the fluorescent dye. Once a cell with Trehalose-AlexaFluor647 is detected using a 638 nm laser, we increase the intensity until most of the molecules have become photo-bleached. We then record single molecules diffusing along the cell membrane until there are none visible at an exposure rate of 50 ms/frame. In order to confirm that indeed we are observing a live cell, a 514 nm laser is used to detect green fluorescent protein (GFP) that is constitutively expressed by the bacterium or green cell tracker. Post-processing is done on acquired data afterwards to extract out relevant physical measurements (e.g. position, velocity, diffusion coefficients, etc).

For three-dimensional super-resolution microscopy, all imaging was performed at 25°C with fixed cells (2% paraformaldehyde for 20 min at room temperature). An imaging cocktail consisting of 1 M glucose, 2 mM cysteamine (MEA), 70 mg/mL pyranose oxidase, and 70 mg/mL catalase in PBS was used. In addition, cysteamine is known to react with AlexaFluor647, which facilitates its ability to become photoactivatable. We detect each AlexaFluor647 molecule attached to a trehalose reporter by increasing the intensity of the 638 nm laser. These fluorophores will blink in a stochastic manner and are detected at 35 ms/frame until most of them have become photobleached. However, since cysteamine is in solution, by exposing our cells to a 405 nm laser, we are able to photo-recover many of these molecules to obtain more localizations. These steps are repeated every hour since the reaction has a finite lifetime. In order to access the molecule's z-position, we optically transform the usual point spread function (PSF) into the double-helix PSF (DH-PSF), where we now have two lobes diametrically opposite to each other. When the object in view goes out of focus, the two lobes will then rotate about its center position. The center positions of each lobe of the DH-PSF is extracted by performing a double Gaussian fit and the midpoint of these two sets of X-Y coordinates is the XY position of the single molecule. The pitch of the two lobes gives the z-position and this is done for every molecule that is detected.

Isolation and purification of free glycolipids

Bacterial cultures incubated with trehalose probes were washed two times with corresponding growth media to remove excess reporter. Wet cell pellets were subjected to organic extraction by adding 1 mL 2:1 $CHCl_3$:MeOH and stirring vigorously in conical glass tubes overnight. Resulting heterogeneous mixture was centrifuged for 10 min at 3700 x g, clarified organic layer supernatant was saved and cell pellet was re-extracted twice with the same protocol. Combined organic layers recovered after centrifugation were concentrated and analyzed by HPTLC (Uniplate HPTLC-GHL, 5 x 5 cm, 150 μm thickness) developed with 65:25:4 $CHCl_3$:MeOH:H_2O. Fluorescently labeled glycolipids developed in HPTLC plates were imaged with typhoon scanner (Amersham Biosciences, Typhoon 9410). Free lipids were partially purified by preparative TLC (Analtech, 20 x 20 cm, 1 mm thickness).

Mass spectrometry validation of FlTre-labeled glycolipids

M. marinum bacterial cultures (200 mL) were grown 50 μM trehalose reporter until early stationary phase. Trehalose glycolipids were isolated as described above. Partially purified glycolipids were dissolved in 100 μL 2:1 $CHCl_3$:MeOH (HPLC grade) and filtered through a

0.45 μm PVDF membrane. Mass spectra were acquired on a Waters Q-tof Premier quadrupole time-of-flight mass spectrometer equipped with a nanoelectrospray ionization (nanoESI) source. Ions were formed in the positive ion mode from pulled borosilicate glass nanoESI tips. Mass spectra were recorded over the range mass-to-charge ratio (m/z) = 100 to 4000. Data acquisition was controlled using MassLynx software (version 4.1, Waters). This instrumentation is located in the QB3/Chemistry Mass Spectrometry Facility at the University of California, Berkeley.

Microvesicle purification

Microvesicles were isolated as previously described.[55,57,58,63]

Statistics

p-values between samples were calculated with paired student's t-test or two-way ANOVA as specified in figures.

SUPPLEMENTARY FIGURES

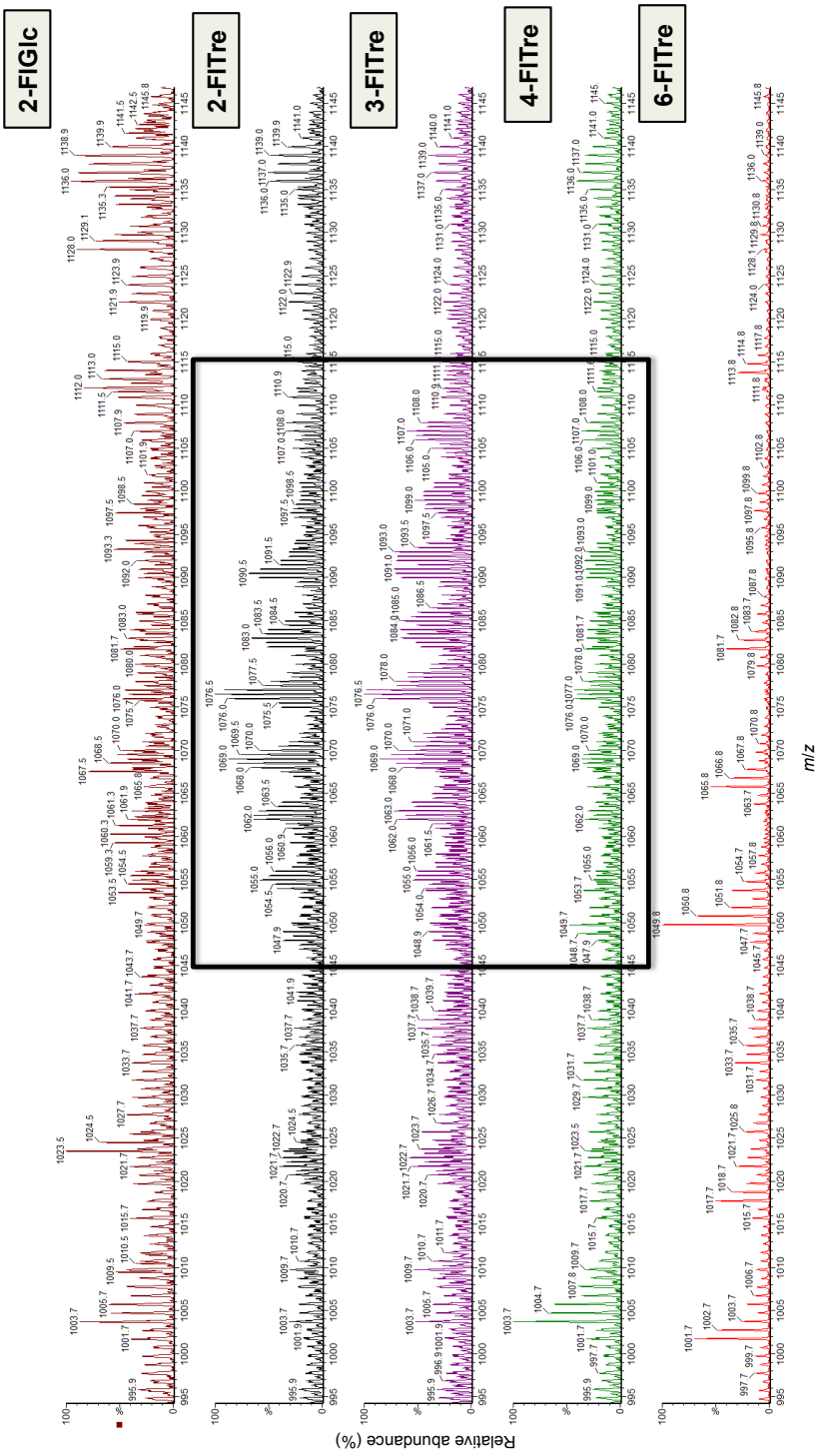

Figure 5.S1 Mass spectrometry validation of FlTre reporter incorporation by *M. marinum* into TMM. Partially purified glycolipids were subjected to mass spectrometry analysis. Nano-ESI Q-TOF mass spectra depicts native and FlTre-labeled trehalose monomycolate species in *M.*

marinum, plotting relative abundance (%) and m/z in *y* and *x*-axis, respectively. Black box denotes identified species corresponding to Fl-TMM. Electrospray ionization (ESI), quadrupole time-of-flight (Q-TOF), trehalose monomycolate (TMM)

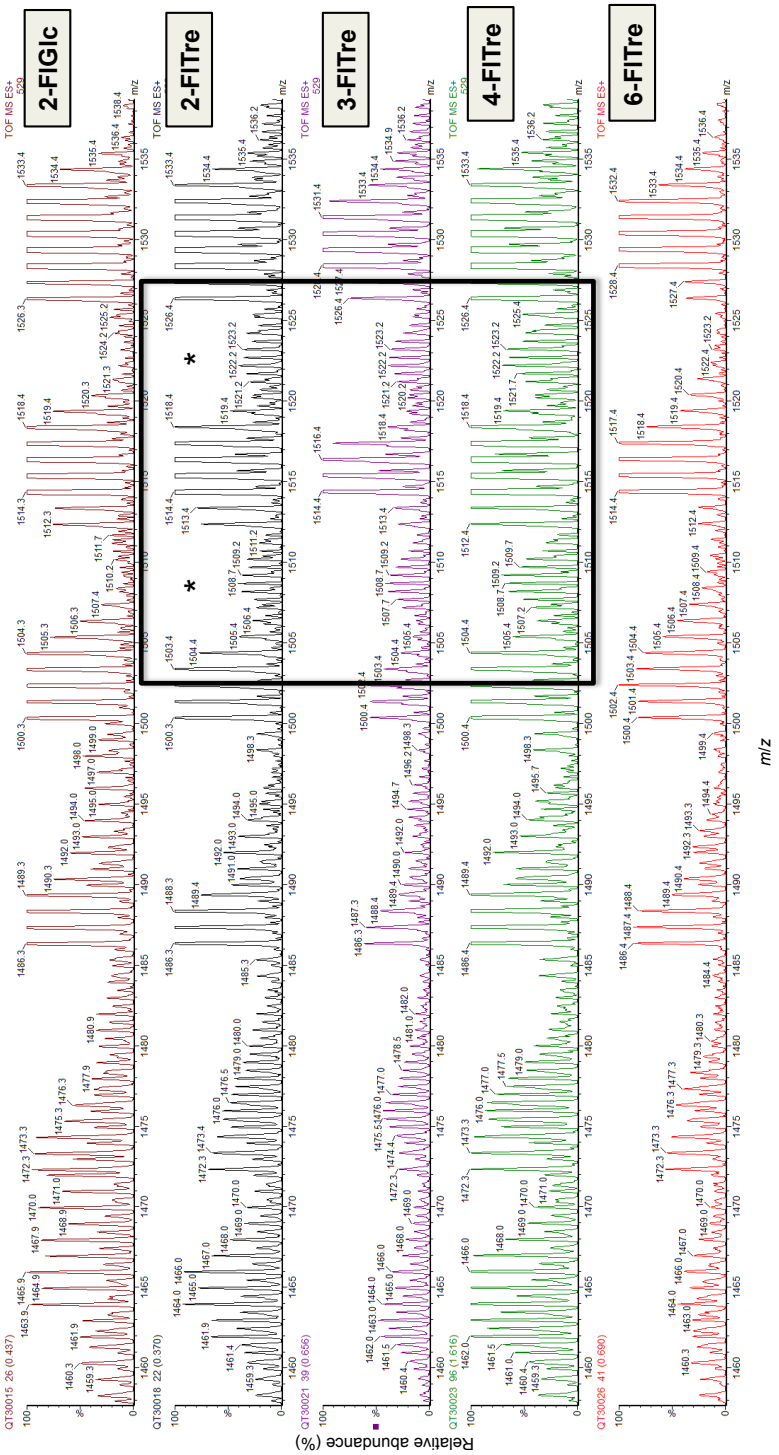

Figure 5.S2 Mass spectrometry validation of FlTre reporter incorporation by *M. marinum* into TDM. Partially purified glycolipids were subjected to mass spectrometry analysis. Nano-ESI Q-TOF mass spectra depicts native and FlTre-labeled trehalose dimycolate species in *M. marinum*, plotting relative abundance (%) and m/z in *y* and *x*-axis, respectively. Black box denotes identified species corresponding to Fl-TDM, in addition to black asterisks. Electrospray ionization (ESI), quadrupole time-of-flight (Q-TOF), trehalose dimycolate (TDM)

REFERENCES

1. Russell, D. G. Mycobacterium tuberculosis: here today, and here tomorrow. *Nat. Rev. Mol. Cell Biol.* **2,** 569–586 (2001).
2. Philips, J. A. & Ernst, J. D. Tuberculosis Pathogenesis and Immunity. *Annu. Rev. Pathol. Mech. Dis.* **7,** 353–384 (2012).
3. Jarlier, V. & Nikaido, H. Mycobacterial cell wall: Structure and role in natural resistance to antibiotics. *FEMS Microbiol. Lett.* **123,** 11–18 (1994).
4. Zhang, Y. The Magic Bullets and Tuberculosis Drug Targets. *Annu. Rev. Pharmacol. Toxicol.* **45,** 529–564 (2005).
5. Jankute, M., Cox, J. A. G., Harrison, J. & Besra, G. S. Assembly of the Mycobacterial Cell Wall. *Annu. Rev. Microbiol.* **69,** 405–423 (2015).
6. Marrakchi, H., Lanéelle, M.-A. & Daffé, M. Mycolic Acids: Structures, Biosynthesis, and Beyond. *Chem. Biol.* **21,** 67–85 (2014).
7. Russell, D. G., Mwandumba, H. C. & Rhoades, E. E. Mycobacterium and the coat of many lipids. *J. Cell Biol.* **158,** 421–426 (2002).
8. Takayama, K., Wang, C. & Besra, G. S. Pathway to Synthesis and Processing of Mycolic Acids in Mycobacterium tuberculosis. *Clin. Microbiol. Rev.* **18,** 81–101 (2005).
9. Neyrolles, O. & Guilhot, C. Recent advances in deciphering the contribution of Mycobacterium tuberculosis lipids to pathogenesis. *Tuberculosis* **91,** 187–195 (2011).
10. Cambier, C. J., Falkow, S. & Ramakrishnan, L. Host Evasion and Exploitation Schemes of Mycobacterium tuberculosis. *Cell* **159,** 1497–1509 (2014).
11. Beatty, W. L. *et al.* Trafficking and Release of Mycobacterial Lipids from Infected Macrophages. *Traffic* **1,** 235–247 (2000).
12. Hunter, R. L., Olsen, M. R., Jagannath, C. & Actor, J. K. Multiple roles of cord factor in the pathogenesis of primary, secondary, and cavitary tuberculosis, including a revised description of the pathology of secondary disease. *Ann. Clin. Lab. Sci.* **36,** 371–386 (2006).
13. Siegrist, M. S., Swarts, B. M., Fox, D. M., Lim, S. A. & Bertozzi, C. R. Illumination of growth, division and secretion by metabolic labeling of the bacterial cell surface. *FEMS Microbiol. Rev.* **39,** 184–202 (2015).
14. Backus, K. M. *et al.* Uptake of unnatural trehalose analogs as a reporter for Mycobacterium tuberculosis. *Nat. Chem. Biol.* **7,** 228–235 (2011).
15. Swarts, B. M. *et al.* Probing the Mycobacterial Trehalome with Bioorthogonal Chemistry. *J. Am. Chem. Soc.* **134,** 16123–16126 (2012).
16. Urbanek, B. L. *et al.* Chemoenzymatic Synthesis of Trehalose Analogues: Rapid Access to Chemical Probes for Investigating Mycobacteria. *ChemBioChem* **15,** 2066–2070 (2014).

17. Foley, H. N., Stewart, J. A., Kavunja, H. W., Rundell, S. R. & Swarts, B. M. Bioorthogonal Chemical Reporters for Selective In Situ Probing of Mycomembrane Components in Mycobacteria. *Angew. Chem. Int. Ed.* **55,** 2053–2057 (2016).
18. Rundell, S. R. *et al.* Deoxyfluoro-D-trehalose (FDTre) analogues as potential PET probes for imaging mycobacterial infection. *Org. Biomol. Chem.* **14,** 8598–8609 (2016).
19. Hunter, R. L., Olsen, M., Jagannath, C. & Actor, J. K. Trehalose 6,6′-Dimycolate and Lipid in the Pathogenesis of Caseating Granulomas of Tuberculosis in Mice. *Am. J. Pathol.* **168,** 1249–1261 (2006).
20. Khan, A. A., Stocker, B. L. & Timmer, M. S. M. Trehalose glycolipids—synthesis and biological activities. *Carbohydr. Res.* **356,** 25–36 (2012).
21. Welsh, K. J., Hunter, R. L. & Actor, J. K. Trehalose 6,6′-dimycolate – A coat to regulate tuberculosis immunopathogenesis. *Tuberculosis* **93, Supplement,** S3–S9 (2013).
22. Indrigo, J., Hunter, R. L. & Actor, J. K. Cord factor trehalose 6,6′-dimycolate (TDM) mediates trafficking events during mycobacterial infection of murine macrophages. *Microbiology* **149,** 2049–2059 (2003).
23. Gebhardt, H. *et al.* The key role of the mycolic acid content in the functionality of the cell wall permeability barrier in Corynebacterineae. *Microbiology* **153,** 1424–1434 (2007).
24. Harland, C. W., Rabuka, D., Bertozzi, C. R. & Parthasarathy, R. The Mycobacterium tuberculosis Virulence Factor Trehalose Dimycolate Imparts Desiccation Resistance to Model Mycobacterial Membranes. *Biophys. J.* **94,** 4718–4724 (2008).
25. Gupta, U. D. & Katoch, V. M. Animal models of tuberculosis. *Tuberculosis* **85,** 277–293 (2005).
26. Dharmadhikari, A. S. & Nardell, E. A. What Animal Models Teach Humans about Tuberculosis. *Am. J. Respir. Cell Mol. Biol.* **39,** 503–508 (2008).
27. Barry, C. E. *et al.* The spectrum of latent tuberculosis: rethinking the biology and intervention strategies. *Nat. Rev. Microbiol.* **7,** 845–855 (2009).
28. Flynn, J. L., Chan, J. & Lin, P. L. Macrophages and control of granulomatous inflammation in tuberculosis. *Mucosal Immunol.* **4,** 271–278 (2011).
29. Lin, P. L. *et al.* Sterilization of granulomas is common in active and latent tuberculosis despite within-host variability in bacterial killing. *Nat. Med.* **20,** 75–79 (2014).
30. Prouty, M. G., Correa, N. E., Barker, L. P., Jagadeeswaran, P. & Klose, K. E. Zebrafish-Mycobacterium marinum model for mycobacterial pathogenesis. *FEMS Microbiol. Lett.* **225,** 177–182 (2003).
31. Kaufmann, S. H. E. Immunopathology of mycobacterial diseases. *Semin. Immunopathol.* **38,** 135–138 (2016).
32. Takaki, K., Davis, J. M., Winglee, K. & Ramakrishnan, L. Evaluation of the pathogenesis and treatment of Mycobacterium marinum infection in zebrafish. *Nat. Protoc.* **8,** 1114–1124 (2013).
33. Stinear, T. P. *et al.* Insights from the complete genome sequence of Mycobacterium marinum on the evolution of Mycobacterium tuberculosis. *Genome Res.* **18,** 729–741 (2008).
34. Tobin, D. M. & Ramakrishnan, L. Comparative pathogenesis of Mycobacterium marinum and Mycobacterium tuberculosis. *Cell. Microbiol.* **10,** 1027–1039 (2008).
35. Cronan, M. R. & Tobin, D. M. Fit for consumption: zebrafish as a model for tuberculosis. *Dis. Model. Mech.* **7,** 777–784 (2014).
36. Berg, R. D. *et al.* Lysosomal Disorders Drive Susceptibility to Tuberculosis by Compromising Macrophage Migration. *Cell* **165,** 139–152 (2016).

37. Levitte, S. *et al.* Mycobacterial Acid Tolerance Enables Phagolysosomal Survival and Establishment of Tuberculous Infection In Vivo. *Cell Host Microbe* **20,** 250–258 (2016).
38. Davis, J. M. & Ramakrishnan, L. The Role of the Granuloma in Expansion and Dissemination of Early Tuberculous Infection. *Cell* **136,** 37–49 (2009).
39. Ramakrishnan, L. Revisiting the role of the granuloma in tuberculosis. *Nat. Rev. Immunol.* **12,** 352–366 (2012).
40. Cambier, C. J. *et al.* Mycobacteria manipulate macrophage recruitment through coordinated use of membrane lipids. *Nature* **505,** 218–222 (2014).
41. Daffé, M., Lanéelle, M. A. & Lacave, C. Structure and stereochemistry of mycolic acids of Mycobacterium marinum and Mycobacterium ulcerans. *Res. Microbiol.* **142,** 397–403 (1991).
42. Barry III, C. E. *et al.* Mycolic acids: structure, biosynthesis and physiological functions. *Prog. Lipid Res.* **37,** 143–179 (1998).
43. Volkman, H. E. *et al.* Tuberculous Granuloma Induction via Interaction of a Bacterial Secreted Protein with Host Epithelium. *Science* **327,** 466–469 (2010).
44. Meijer, A. H., van der Vaart, M. & Spaink, H. P. Real-time imaging and genetic dissection of host–microbe interactions in zebrafish. *Cell. Microbiol.* **16,** 39–49 (2014).
45. Dover, L. G., Cerdeño-Tárraga, A. M., Pallen, M. J., Parkhill, J. & Besra, G. S. Comparative cell wall core biosynthesis in the mycolated pathogens, Mycobacterium tuberculosis and Corynebacterium diphtheriae. *FEMS Microbiol. Rev.* **28,** 225–250 (2004).
46. Kalscheuer, R., Weinrick, B., Veeraraghavan, U., Besra, G. S. & Jacobs, W. R. Trehalose-recycling ABC transporter LpqY-SugA-SugB-SugC is essential for virulence of Mycobacterium tuberculosis. *Proc. Natl. Acad. Sci.* **107,** 21761–21766 (2010).
47. Favrot, L. *et al.* Mechanism of inhibition of Mycobacterium tuberculosis antigen 85 by ebselen. *Nat. Commun.* **4,** 2748 (2013).
48. Favrot, L., Lajiness, D. H. & Ronning, D. R. Inactivation of the Mycobacterium tuberculosis Antigen 85 Complex by Covalent, Allosteric Inhibitors. *J. Biol. Chem.* **289,** 25031–25040 (2014).
49. Agarwal, P., Beahm, B. J., Shieh, P. & Bertozzi, C. R. Systemic Fluorescence Imaging of Zebrafish Glycans with Bioorthogonal Chemistry. *Angew. Chem. Int. Ed.* **54,** 11504–11510 (2015).
50. Wu, H., Yang, J., Šečkutė, J. & Devaraj, N. K. In Situ Synthesis of Alkenyl Tetrazines for Highly Fluorogenic Bioorthogonal Live-Cell Imaging Probes. *Angew. Chem.* **126,** 5915–5919 (2014).
51. Shieh, P. *et al.* CalFluors: A Universal Motif for Fluorogenic Azide Probes across the Visible Spectrum. *J. Am. Chem. Soc.* **137,** 7145–7151 (2015).
52. Coltharp, C. & Xiao, J. Superresolution microscopy for microbiology. *Cell. Microbiol.* **14,** 1808–1818 (2012).
53. Gahlmann, A. & Moerner, W. E. Exploring bacterial cell biology with single-molecule tracking and super-resolution imaging. *Nat. Rev. Microbiol.* **12,** 9–22 (2014).
54. Milenkovic, L. *et al.* Single-molecule imaging of Hedgehog pathway protein Smoothened in primary cilia reveals binding events regulated by Patched1. *Proc. Natl. Acad. Sci.* **112,** 8320–8325 (2015).
55. Prados-Rosales, R. *et al.* Mycobacteria release active membrane vesicles that modulate immune responses in a TLR2-dependent manner in mice. *J. Clin. Invest.* **121,** 1471–1483 (2011).

56. Rath, P. *et al.* Genetic regulation of vesiculogenesis and immunomodulation in Mycobacterium tuberculosis. *Proc. Natl. Acad. Sci.* **110,** E4790–E4797 (2013).
57. Prados-Rosales, R. *et al.* Role for Mycobacterium tuberculosis Membrane Vesicles in Iron Acquisition. *J. Bacteriol.* **196,** 1250–1256 (2014).
58. Prados-Rosales, R. *et al.* Mycobacterial Membrane Vesicles Administered Systemically in Mice Induce a Protective Immune Response to Surface Compartments of Mycobacterium tuberculosis. *mBio* **5,** e01921–14 (2014).
59. Ziegenbalg, A. *et al.* Immunogenicity of mycobacterial vesicles in humans: Identification of a new tuberculosis antibody biomarker. *Tuberculosis* **93,** 448–455 (2013).
60. Lee, J. *et al.* Proteomic analysis of extracellular vesicles derived from Mycobacterium tuberculosis. *PROTEOMICS* **15,** 3331–3337 (2015).
61. Brown, L., Wolf, J. M., Prados-Rosales, R. & Casadevall, A. Through the wall: extracellular vesicles in Gram-positive bacteria, mycobacteria and fungi. *Nat. Rev. Microbiol.* **13,** 620–630 (2015).
62. Schwechheimer, C. & Kuehn, M. J. Outer-membrane vesicles from Gram-negative bacteria: biogenesis and functions. *Nat. Rev. Microbiol.* **13,** 605–619 (2015).
63. Rodriguez, G. M. & Prados-Rosales, R. Functions and importance of mycobacterial extracellular vesicles. *Appl. Microbiol. Biotechnol.* 1–6 (2016). doi:10.1007/s00253-016-7484-x
64. *Mycobacteria Protocols*. **1285,** (Springer New York, 2015).
65. Hatzios, S. K. *et al.* Osmosensory signaling in Mycobacterium tuberculosis mediated by a eukaryotic-like Ser/Thr protein kinase. *Proc. Natl. Acad. Sci.* **110,** E5069–E5077 (2013).
66. Beatty, W. L., Ullrich, H.-J. & Russell, D. G. Mycobacterial surface moieties are released from infected macrophages by a constitutive exocytic event. *Eur. J. Cell Biol.* **80,** 31–40 (2001).
67. Rhoades, E. *et al.* Identification and macrophage-activating activity of glycolipids released from intracellular Mycobacterium bovis BCG. *Mol. Microbiol.* **48,** 875–888 (2003).
68. Sjöback, R., Nygren, J. & Kubista, M. Absorption and fluorescence properties of fluorescein. *Spectrochim. Acta. A. Mol. Biomol. Spectrosc.* **51,** L7–L21 (1995).
69. Sivakumar, K. *et al.* A Fluorogenic 1,3-Dipolar Cycloaddition Reaction of 3-Azidocoumarins and Acetylenes. *Org. Lett.* **6,** 4603–4606 (2004).
70. Athman, J. J. *et al.* Bacterial Membrane Vesicles Mediate the Release of Mycobacterium tuberculosis Lipoglycans and Lipoproteins from Infected Macrophages. *J. Immunol.* **195,** 1044–1053 (2015).
71. Baek, S.-H., Li, A. H. & Sassetti, C. M. Metabolic Regulation of Mycobacterial Growth and Antibiotic Sensitivity. *PLOS Biol* **9,** e1001065 (2011).
72. Manina, G., Dhar, N. & McKinney, J. D. Stress and Host Immunity Amplify Mycobacterium tuberculosis Phenotypic Heterogeneity and Induce Nongrowing Metabolically Active Forms. *Cell Host Microbe* **17,** 32–46 (2015).
73. Adams, K. N. *et al.* Drug Tolerance in Replicating Mycobacteria Mediated by a Macrophage-Induced Efflux Mechanism. *Cell* **145,** 39–53 (2011).
74. Rath, P. *et al.* Cord factor (trehalose 6,6′-dimycolate) forms fully stable and non-permeable lipid bilayers required for a functional outer membrane. *Biochim. Biophys. Acta BBA - Biomembr.* **1828,** 2173–2181 (2013).

75. Schabbing, R. W., Garcia, A. & Hunter, R. L. Characterization of the trehalose 6,6'-dimycolate surface monolayer by scanning tunneling microscopy. *Infect. Immun.* **62,** 754–756 (1994).
76. Spargo, B. J., Crowe, L. M., Ioneda, T., Beaman, B. L. & Crowe, J. H. Cord factor (alpha,alpha-trehalose 6,6'-dimycolate) inhibits fusion between phospholipid vesicles. *Proc. Natl. Acad. Sci.* **88,** 737–740 (1991).
77. Dommerholt, J. *et al.* Readily Accessible Bicyclononynes for Bioorthogonal Labeling and Three-Dimensional Imaging of Living Cells. *Angew. Chem. Int. Ed.* **49,** 9422–9425 (2010).
78. Takaki, K., Cosma, C. L., Troll, M. A. & Ramakrishnan, L. An In Vivo Platform for Rapid High-Throughput Antitubercular Drug Discovery. *Cell Rep.* **2,** 175–184 (2012).

Appendix

^{1}H and ^{13}C NMR spectra

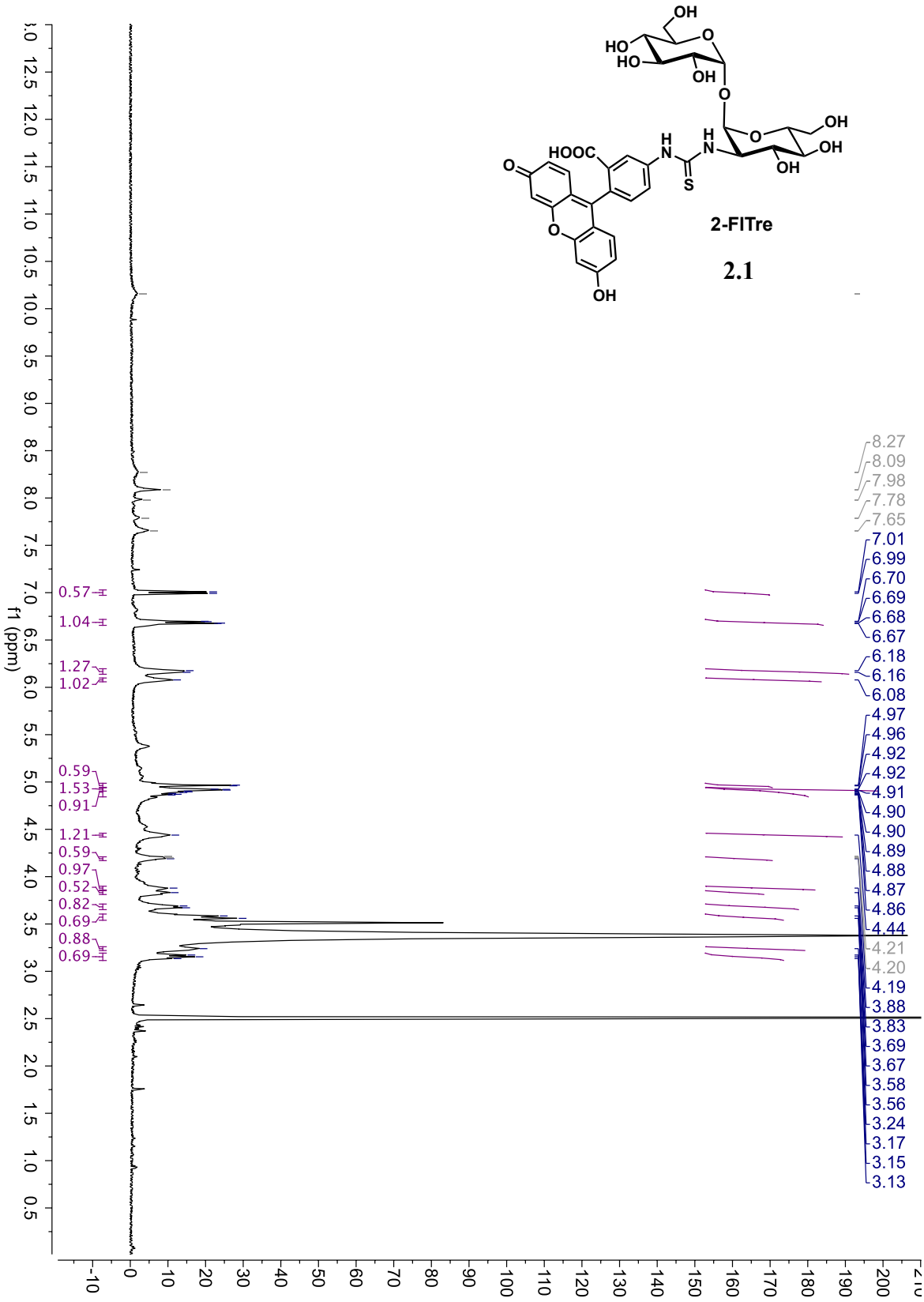
2-FITre
2.1
f1 (ppm)
0.57
1.04
1.27
1.02
0.59
1.53
0.91
1.21
0.59
0.97
0.52
0.82
0.69
0.88
0.69
8.27
8.09
7.98
7.78
7.65
7.01
6.99
6.70
6.69
6.68
6.67
6.18
6.16
6.08
4.97
4.96
4.92
4.92
4.91
4.90
4.90
4.89
4.88
4.87
4.86
4.44
4.21
4.20
4.19
3.88
3.83
3.69
3.67
3.58
3.56
3.24
3.17
3.15
3.13

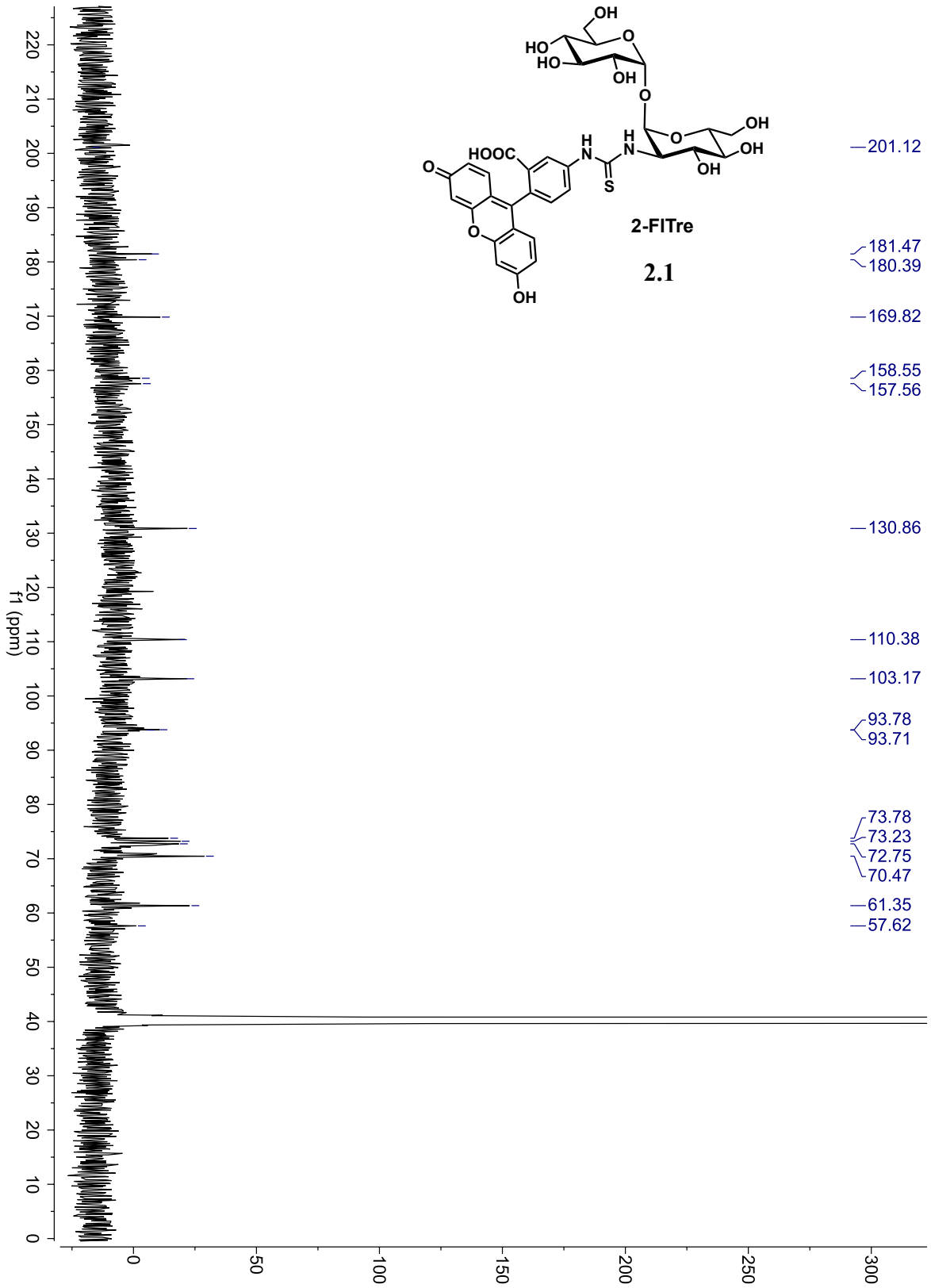
2-FITre
2.1
201.12
181.47
180.39
169.82
158.55
157.56
130.86
110.38
103.17
93.78
93.71
73.78
73.23
72.75
70.47
61.35
57.62
f1 (ppm)

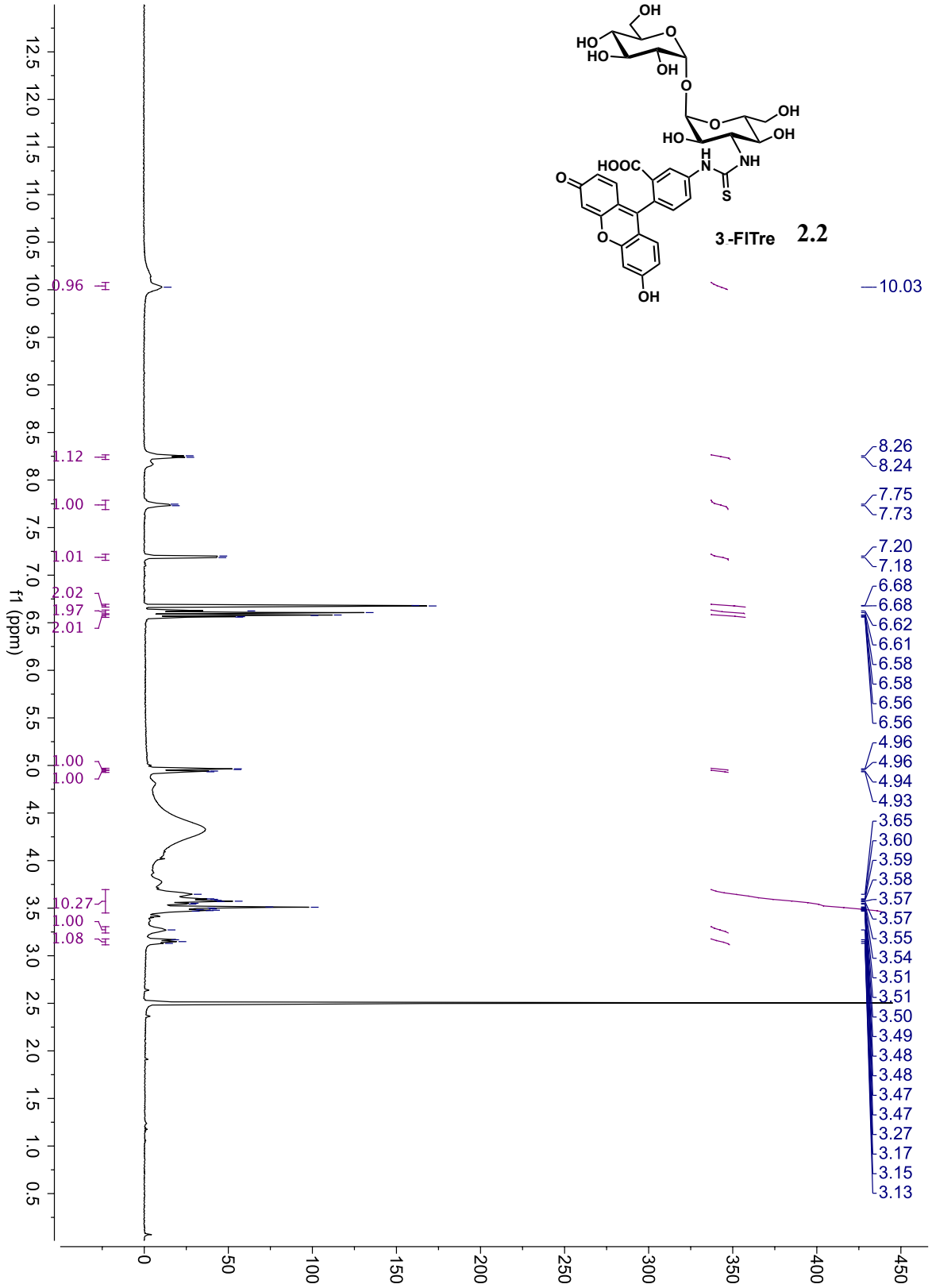
3-FITre
2.2
f1 (ppm)
0.96
1.12
1.00
1.01
2.02
1.97
2.01
1.00
1.00
10.27
1.00
1.08
10.03
8.26
8.24
7.75
7.73
7.20
7.18
6.68
6.68
6.62
6.61
6.58
6.58
6.56
6.56
4.96
4.96
4.94
4.93
3.65
3.60
3.59
3.58
3.57
3.57
3.55
3.54
3.51
3.51
3.50
3.49
3.48
3.48
3.47
3.47
3.27
3.17
3.15
3.13

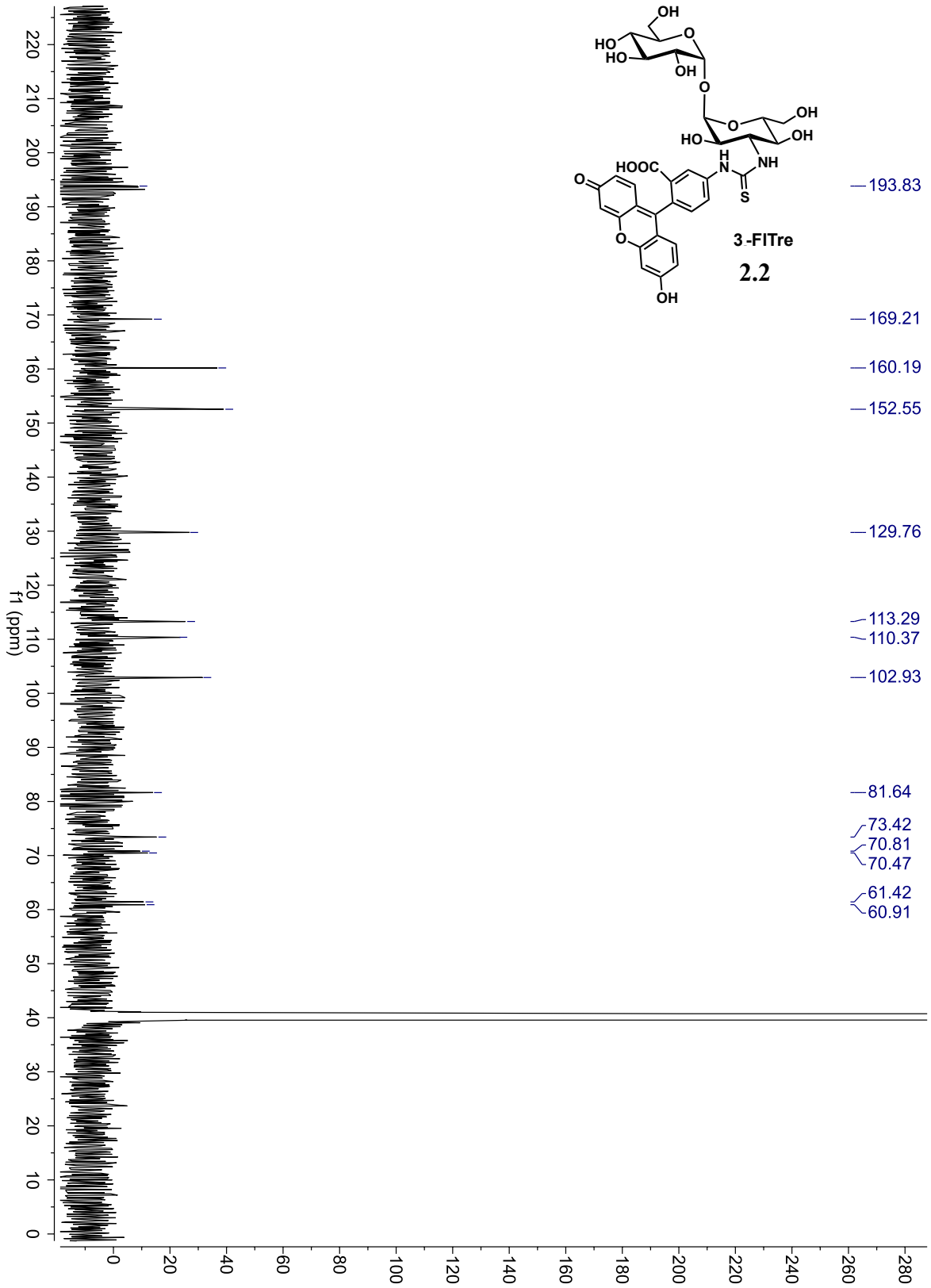
193.83
169.21
160.19
152.55
129.76
113.29
110.37
102.93
81.64
73.42
70.81
70.47
61.42
60.91
f1 (ppm)
3-FITre
2.2

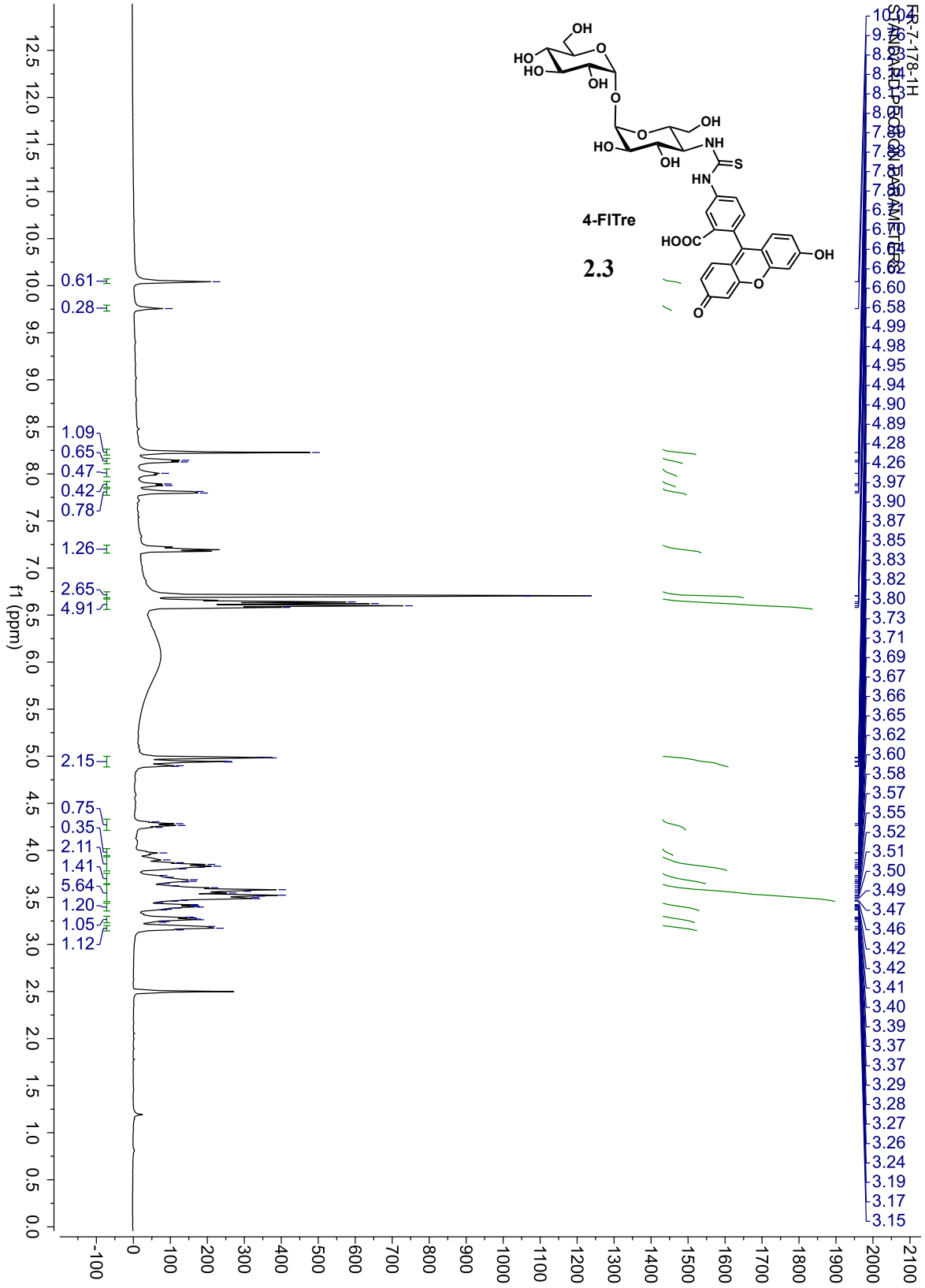
4-FITre
2.3
f1 (ppm)

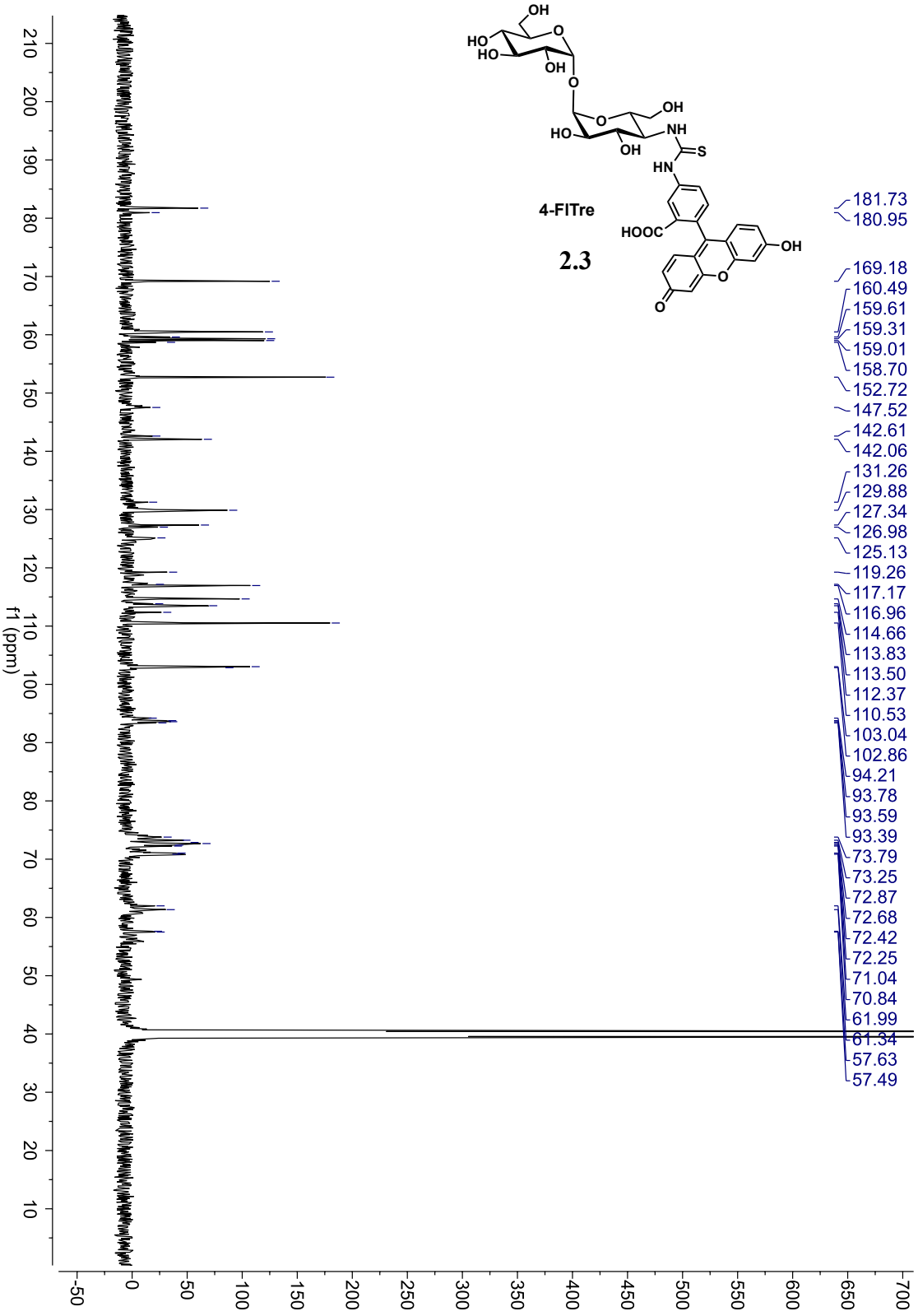
4-FITre
2.3
f1 (ppm)
181.73
180.95
169.18
160.49
159.61
159.31
159.01
158.70
152.72
147.52
142.61
142.06
131.26
129.88
127.34
126.98
125.13
119.26
117.17
116.96
114.66
113.83
113.50
112.37
110.53
103.04
102.86
94.21
93.78
93.59
93.39
73.79
73.25
72.87
72.68
72.42
72.25
71.04
70.84
61.99
61.34
57.63
57.49

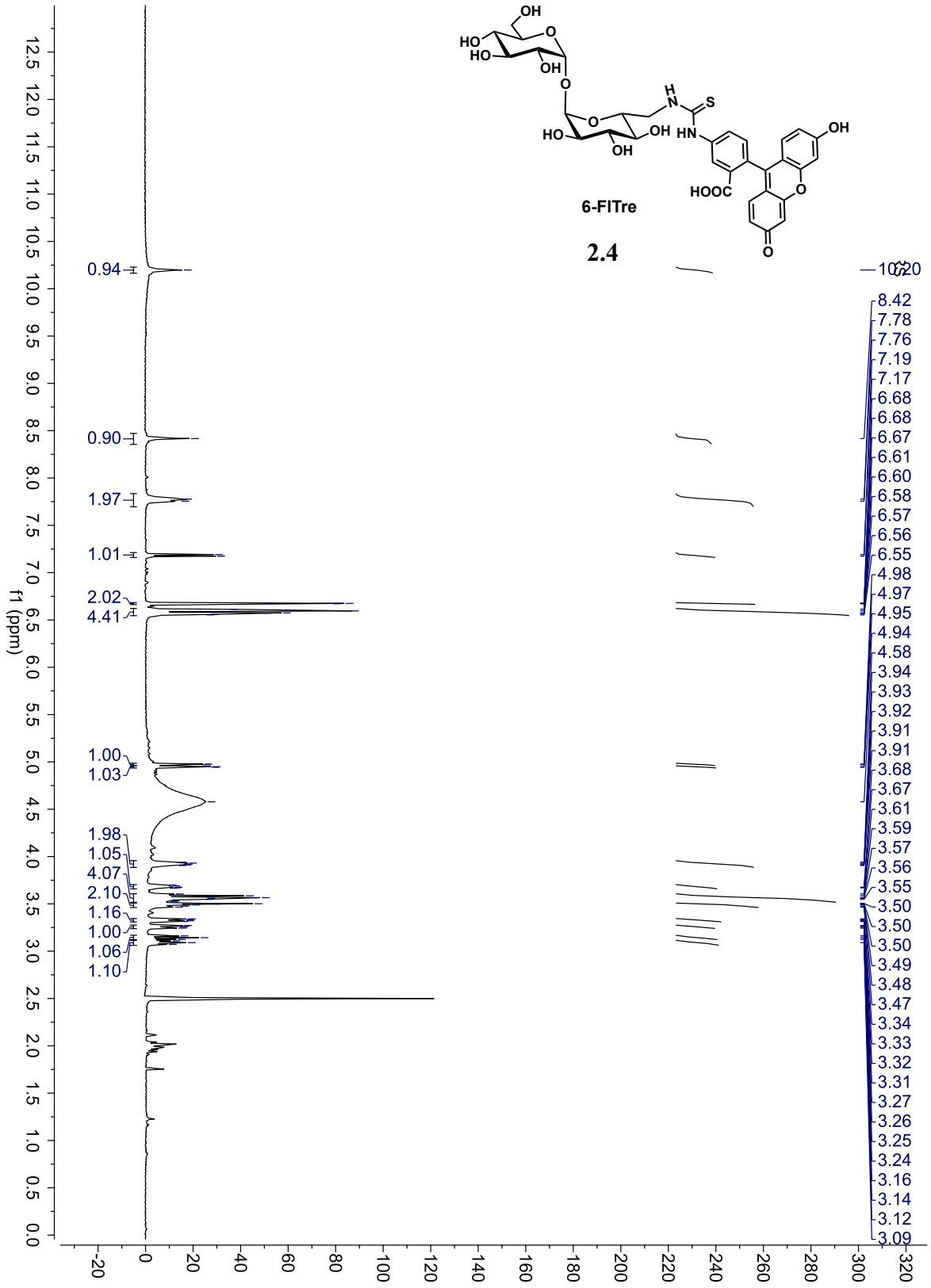
6-FITre
2.4
f1 (ppm)
0.94
0.90
1.97
1.01
2.02
4.41
1.00
1.03
1.98
1.05
4.07
2.10
1.16
1.00
1.06
1.10
10.20
8.42
7.78
7.76
7.19
7.17
6.68
6.68
6.67
6.61
6.60
6.58
6.57
6.56
6.55
4.98
4.97
4.95
4.94
4.58
3.94
3.93
3.92
3.91
3.91
3.68
3.67
3.61
3.59
3.57
3.56
3.55
3.50
3.50
3.50
3.49
3.48
3.47
3.34
3.33
3.32
3.31
3.27
3.26
3.25
3.24
3.16
3.14
3.12
3.09

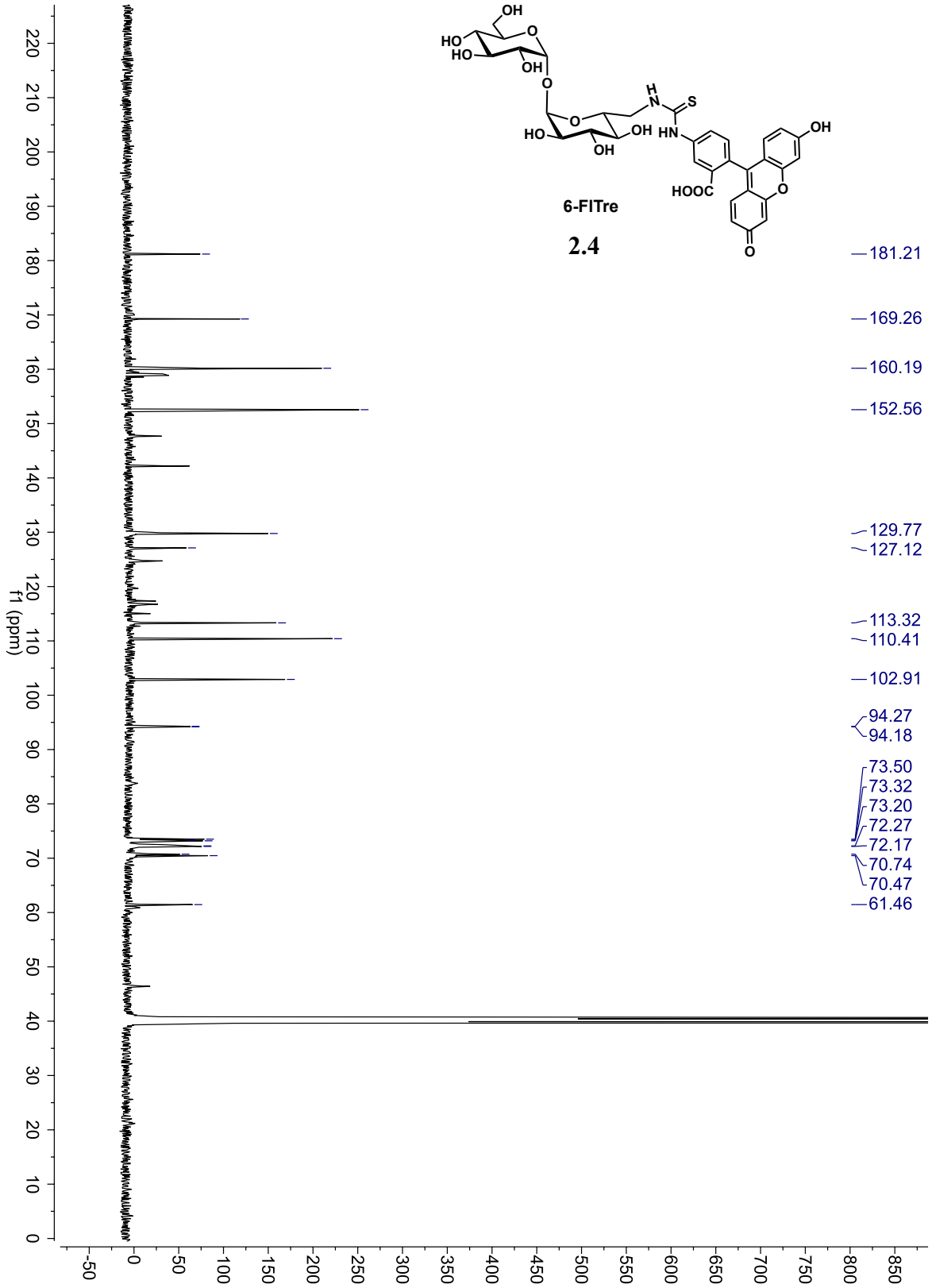
6-FITre
2.4
181.21
169.26
160.19
152.56
129.77
127.12
113.32
110.41
102.91
94.27
94.18
73.50
73.32
73.20
72.27
72.17
70.74
70.47
61.46
f1 (ppm)

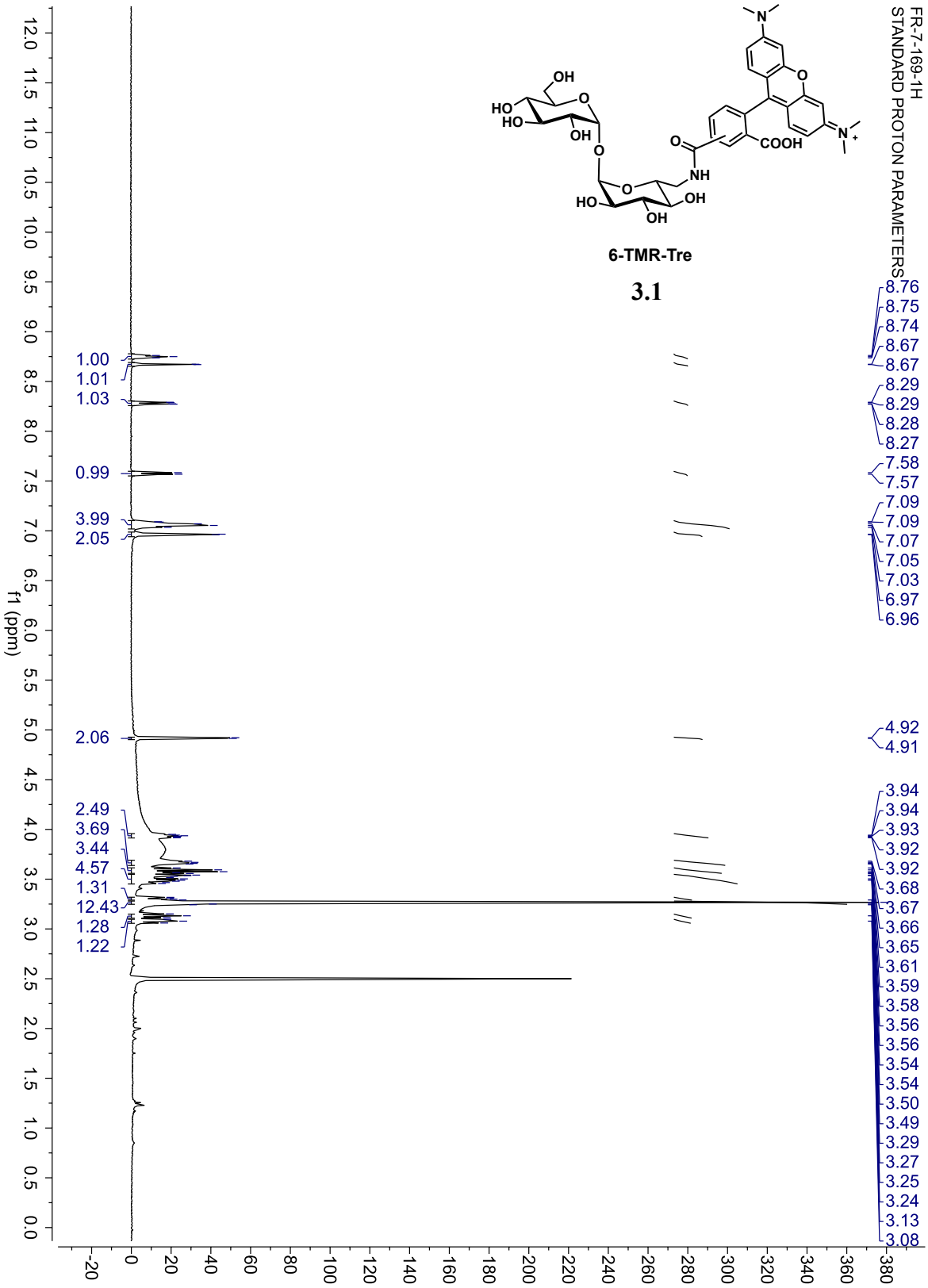
FR-7-169-1H
STANDARD PROTON PARAMETERS
6-TMR-Tre
3.1
f1 (ppm)
1.00
1.01
1.03
0.99
3.99
2.05
2.06
2.49
3.69
3.44
4.57
1.31
12.43
1.28
1.22
8.76
8.75
8.74
8.67
8.67
8.29
8.29
8.28
8.27
7.58
7.57
7.09
7.09
7.07
7.05
7.03
6.97
6.96
4.92
4.91
3.94
3.94
3.93
3.92
3.92
3.68
3.67
3.66
3.65
3.61
3.59
3.58
3.56
3.56
3.54
3.54
3.50
3.49
3.29
3.27
3.25
3.24
3.13
3.08

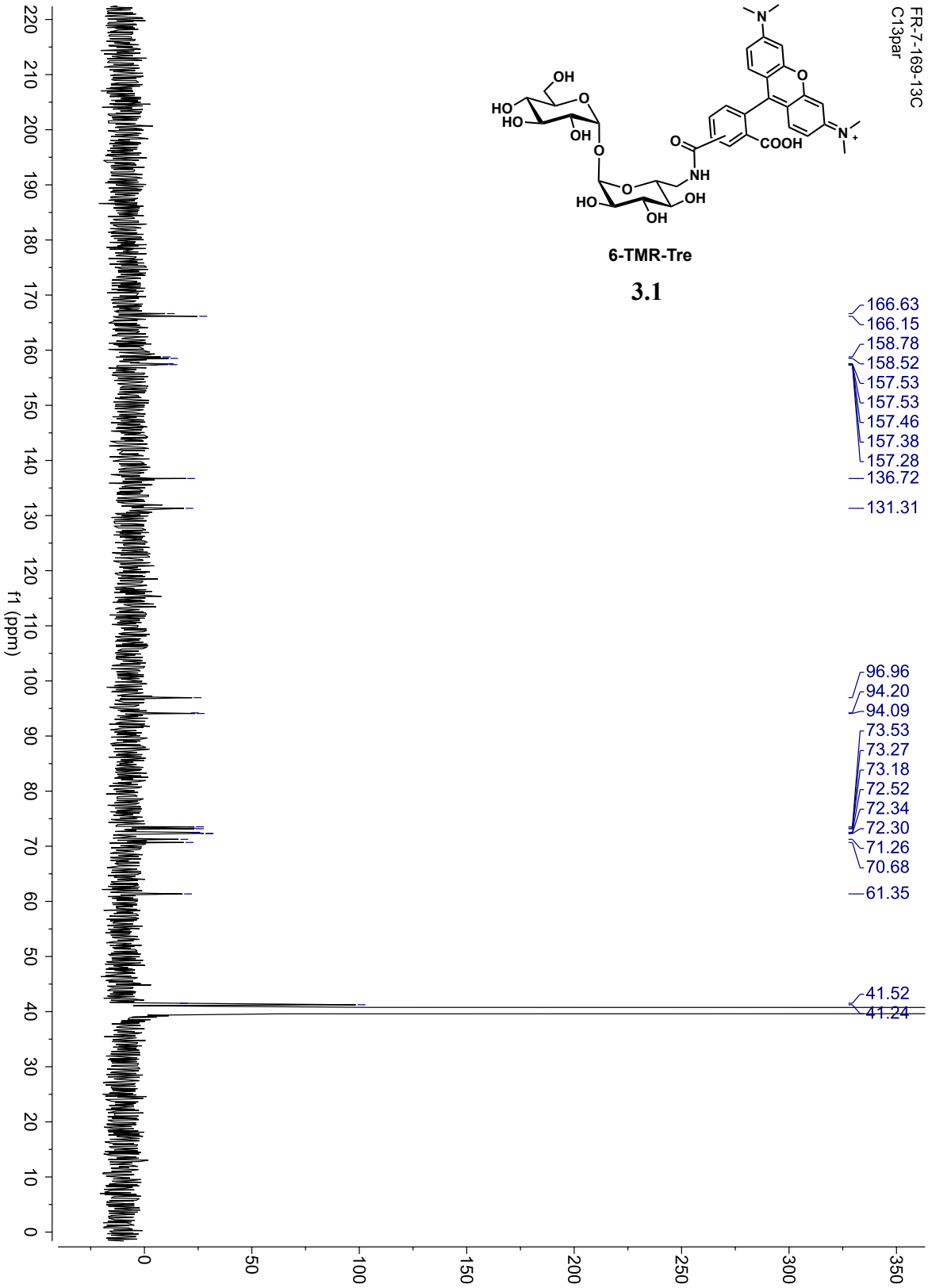
FR-7-169-13C
C13par
6-TMR-Tre
3.1
f1 (ppm)
166.63
166.15
158.78
158.52
157.53
157.53
157.46
157.38
157.28
136.72
131.31
96.96
94.20
94.09
73.53
73.27
73.18
72.52
72.34
72.30
71.26
70.68
61.35
41.52
41.24

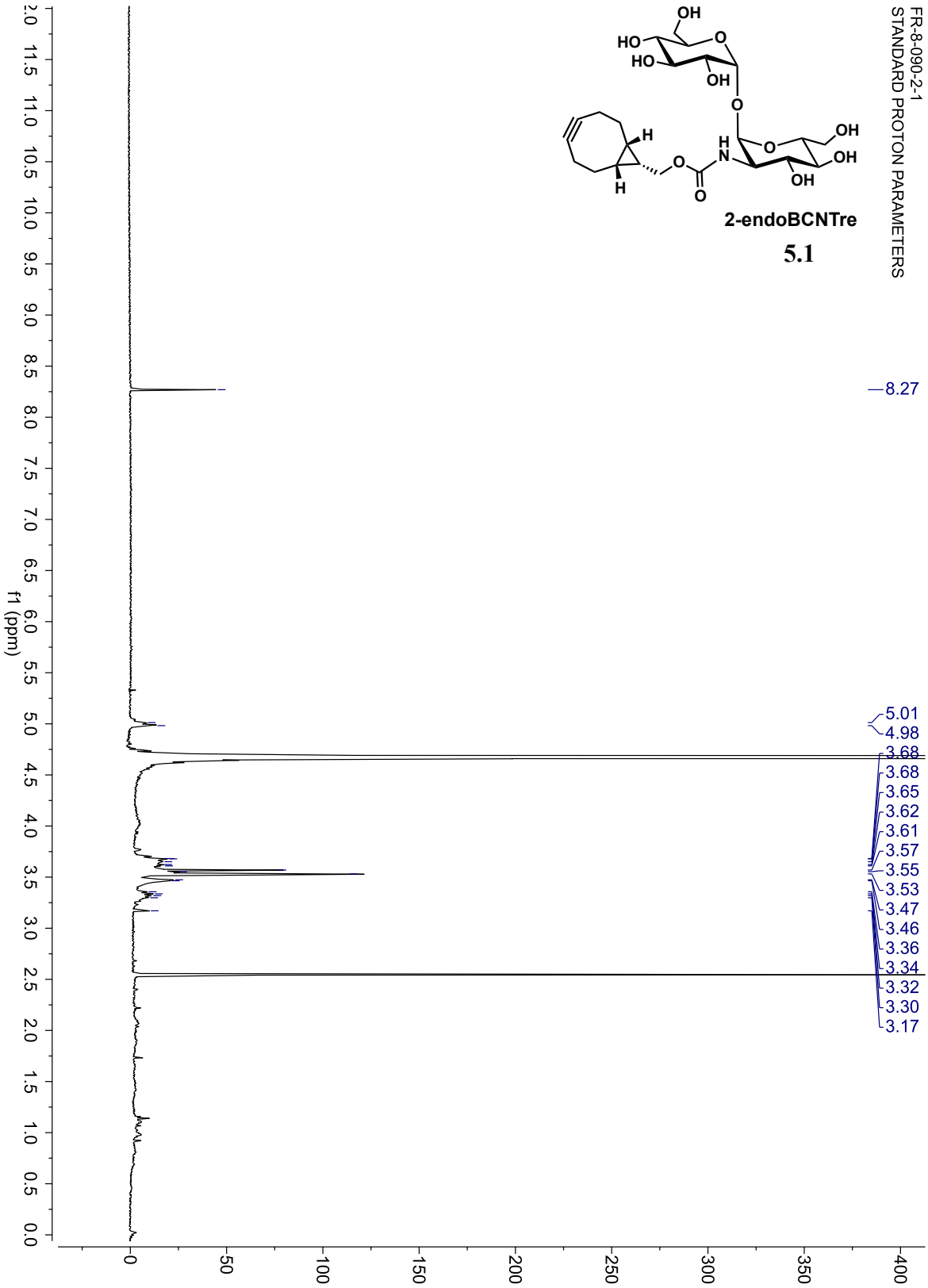
FR-8-090-2-1
STANDARD PROTON PARAMETERS
2-endoBCNTre
5.1
8.27
5.01
4.98
3.68
3.68
3.65
3.62
3.61
3.57
3.55
3.53
3.47
3.46
3.36
3.34
3.32
3.30
3.17
f1 (ppm)

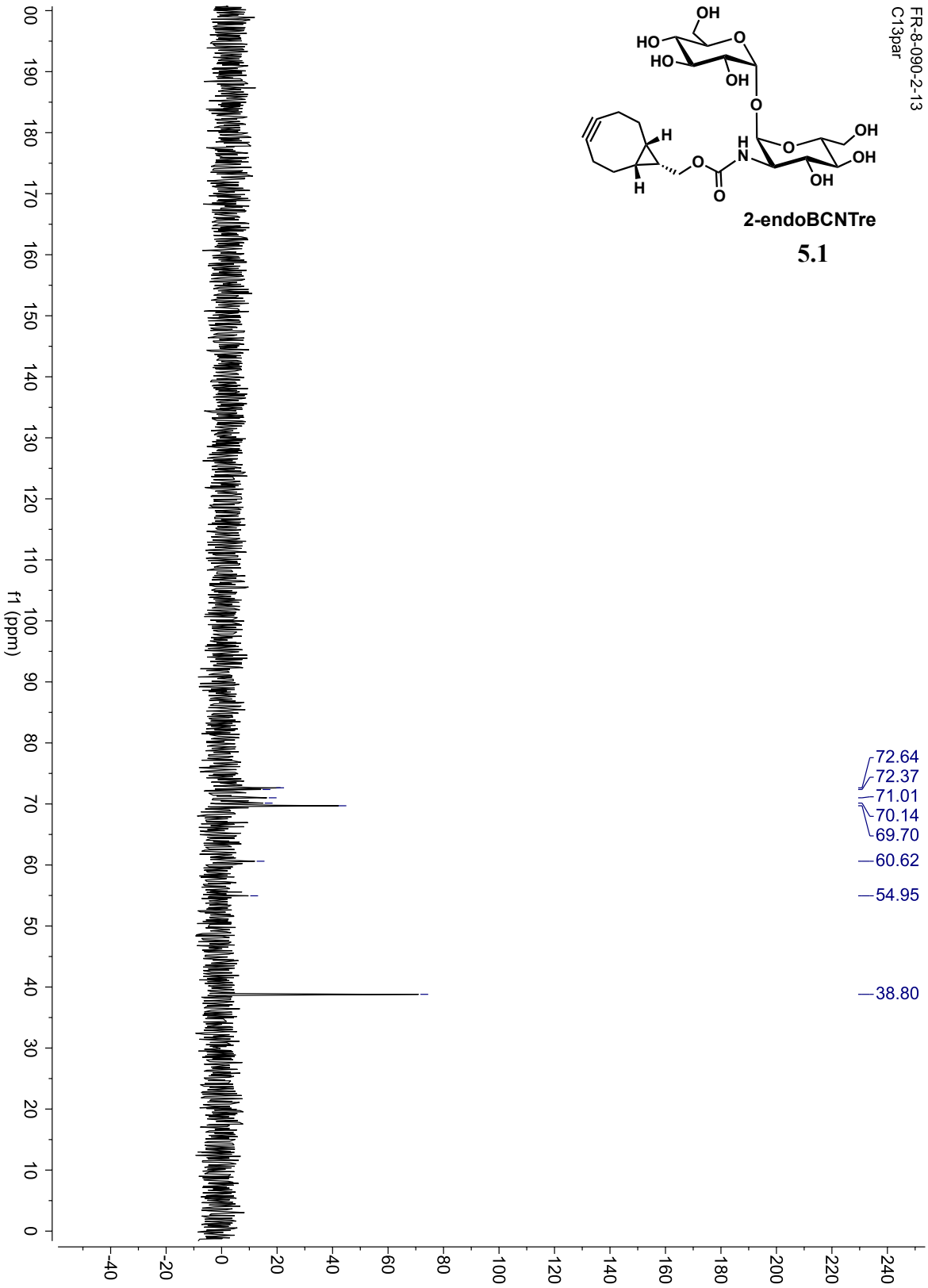
FR-8-090-2-13
C13par
2-endoBCNTre
5.1
72.64
72.37
71.01
70.14
69.70
60.62
54.95
38.80
f1 (ppm)

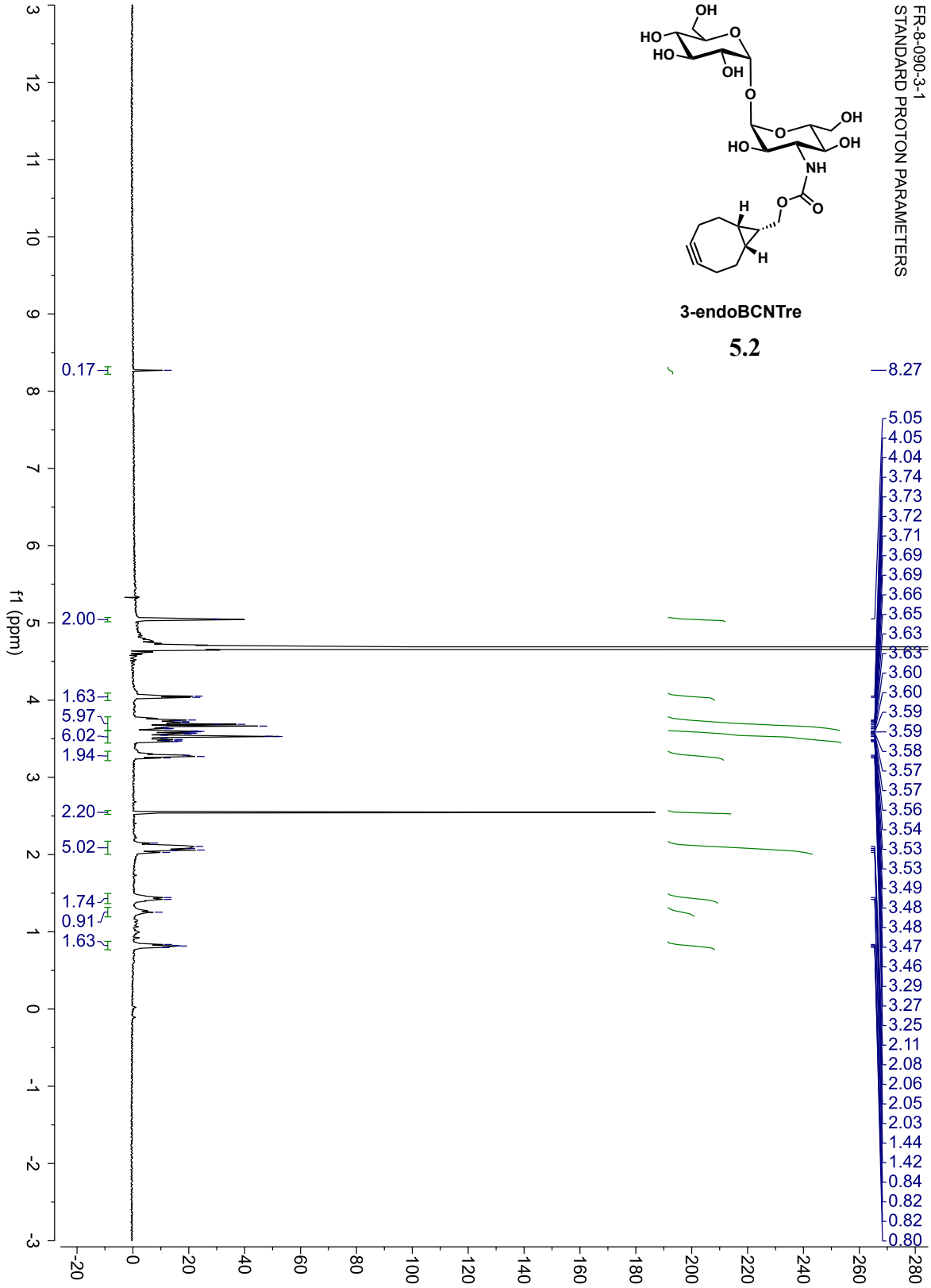
FR-8-090-3-1
STANDARD PROTON PARAMETERS
3-endoBCNTre
5.2
f1 (ppm)
0.17
2.00
1.63
5.97
6.02
1.94
2.20
5.02
1.74
0.91
1.63
8.27
5.05
4.05
4.04
3.74
3.73
3.72
3.71
3.69
3.69
3.66
3.65
3.63
3.63
3.60
3.60
3.59
3.59
3.58
3.57
3.57
3.56
3.54
3.53
3.53
3.49
3.48
3.48
3.47
3.46
3.29
3.27
3.25
2.11
2.08
2.06
2.05
2.03
1.44
1.42
0.84
0.82
0.82
0.80

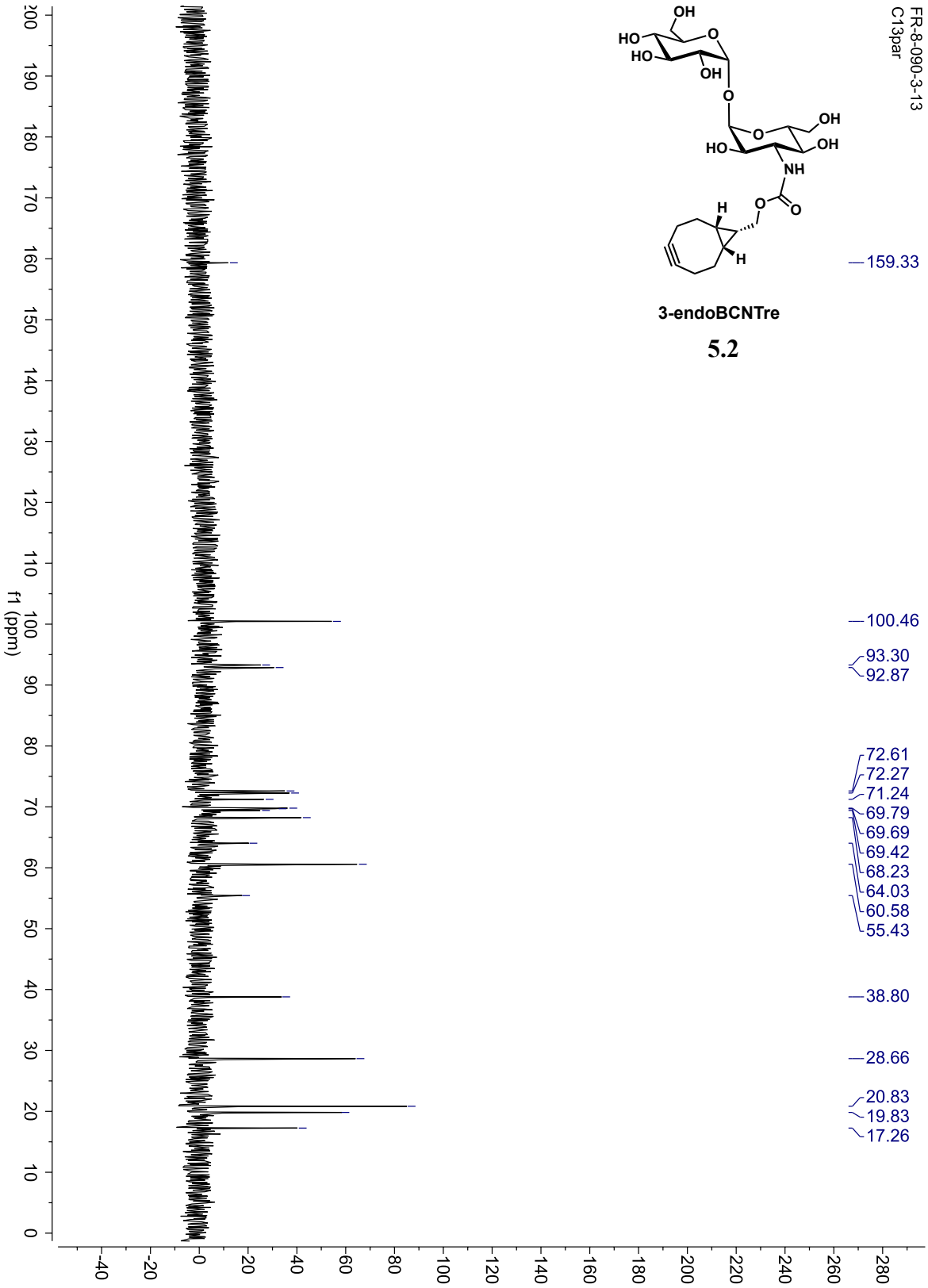
FR-8-090-3-13
C13par
3-endoBCNTre
5.2
159.33
100.46
93.30
92.87
72.61
72.27
71.24
69.79
69.69
69.42
68.23
64.03
60.58
55.43
38.80
28.66
20.83
19.83
17.26
f1 (ppm)

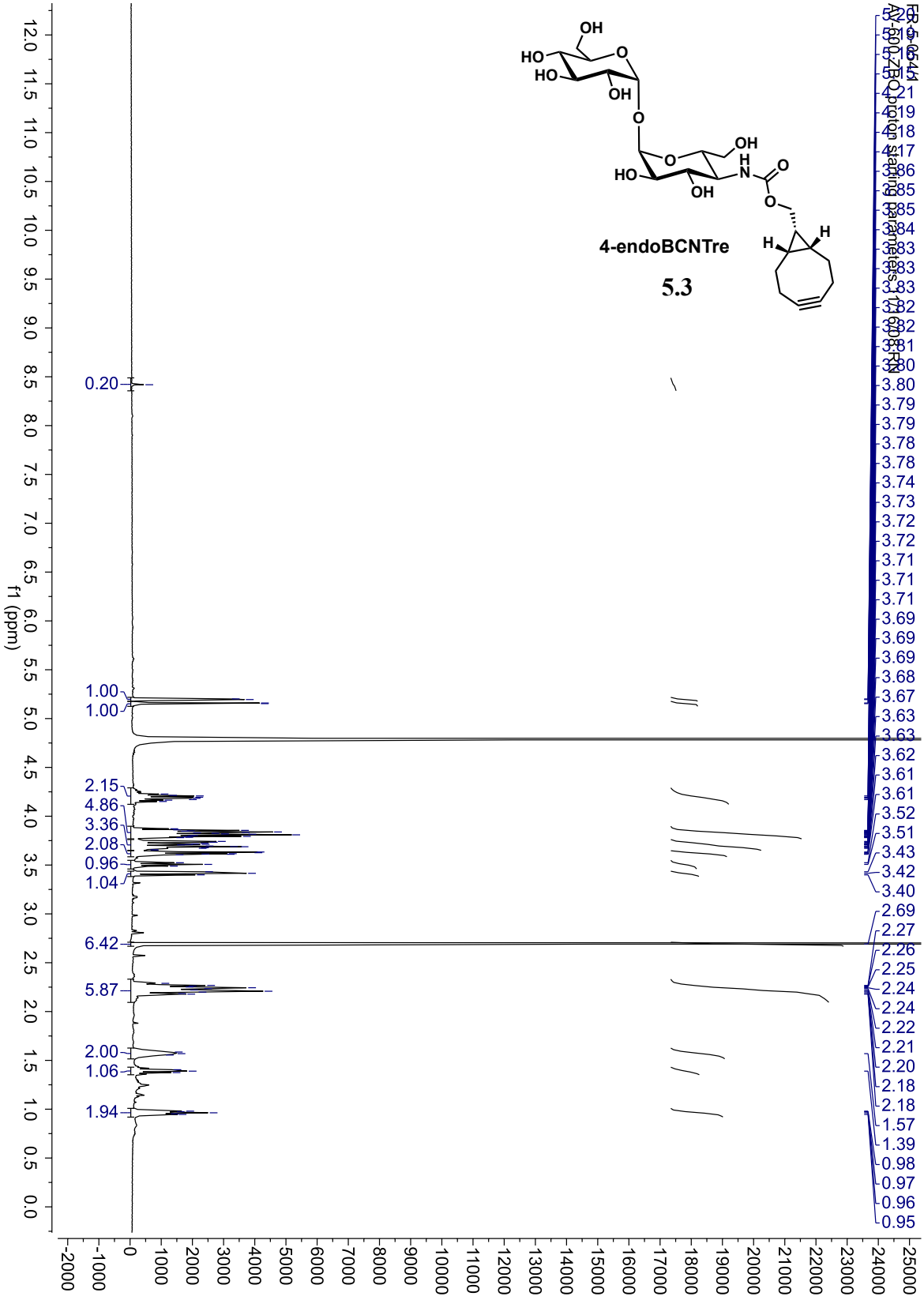
4-endoBCNTre
5.3
f1 (ppm)
0.20
1.00
1.00
2.15
4.86
3.36
2.08
0.96
1.04
6.42
5.87
2.00
1.06
1.94

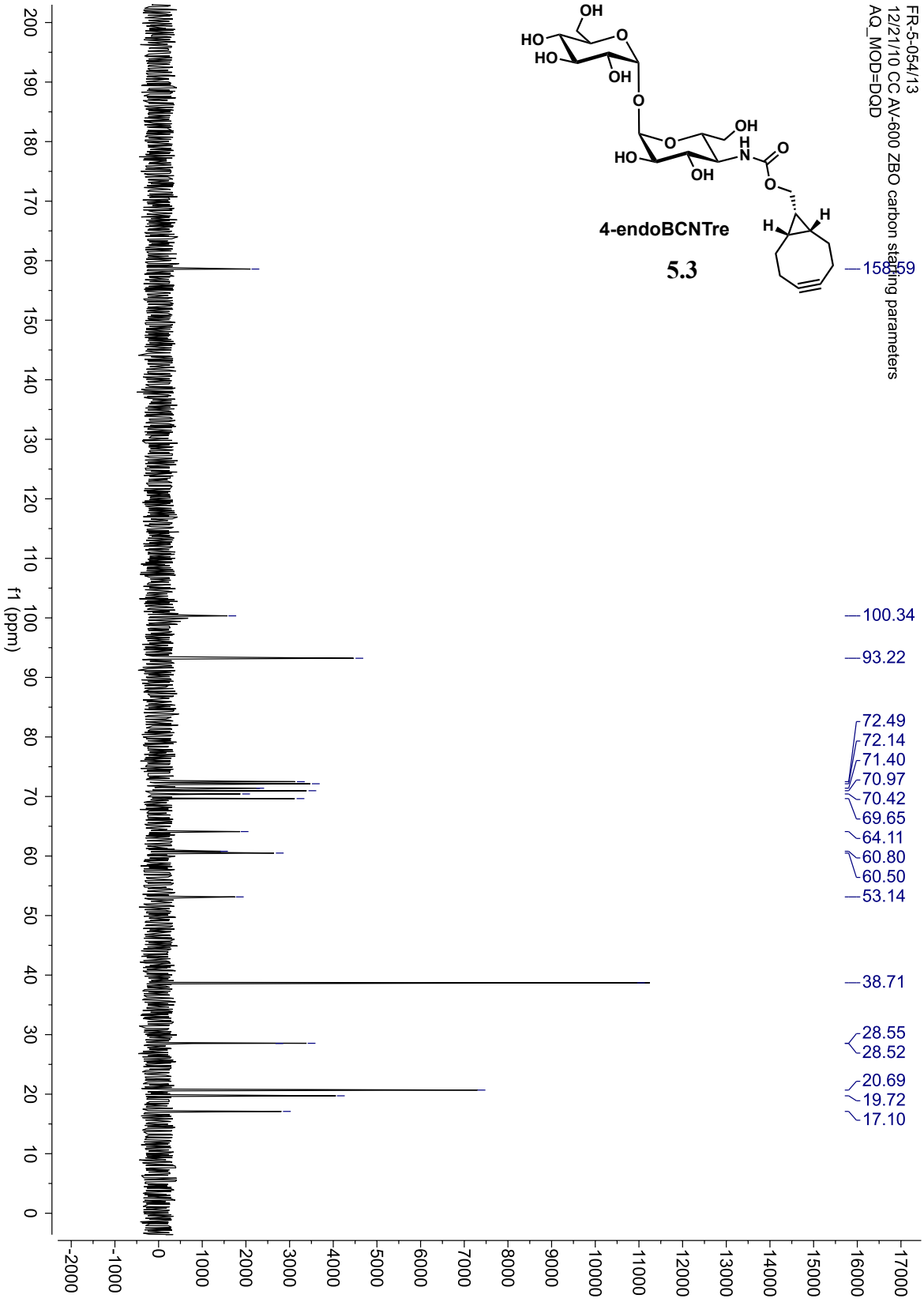
FR-5-054/13
12/21/10 CC AV-600 ZBO carbon standing parameters
AQ_MOD=DQD
4-endoBCNTre
5.3
158.59
100.34
93.22
72.49
72.14
71.40
70.97
70.42
69.65
64.11
60.80
60.50
53.14
38.71
28.55
28.52
20.69
19.72
17.10
f1 (ppm)

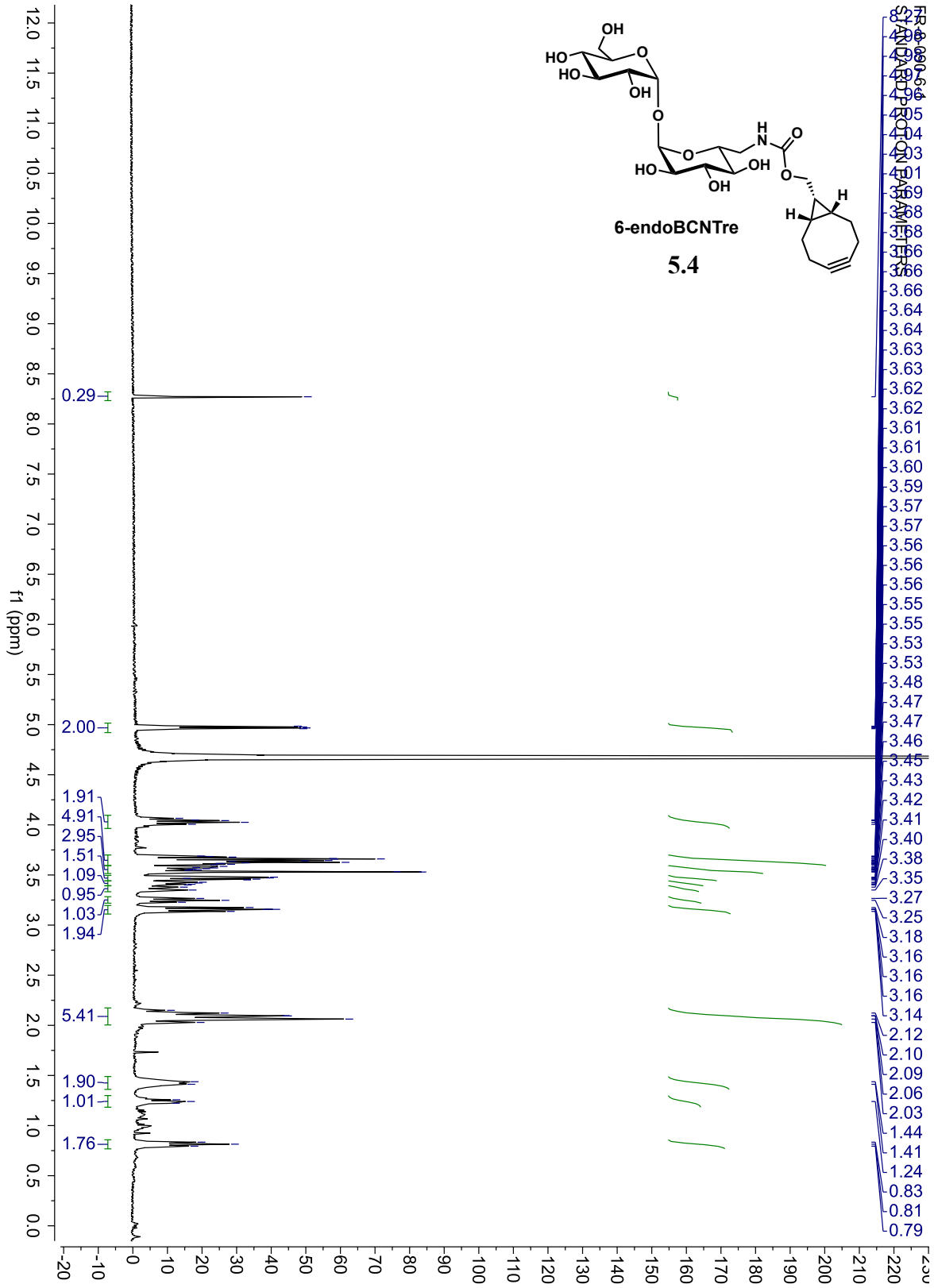
6-endoBCNTre
5.4
f1 (ppm)
0.29
2.00
1.91
4.91
2.95
1.51
1.09
0.95
1.03
1.94
5.41
1.90
1.01
1.76

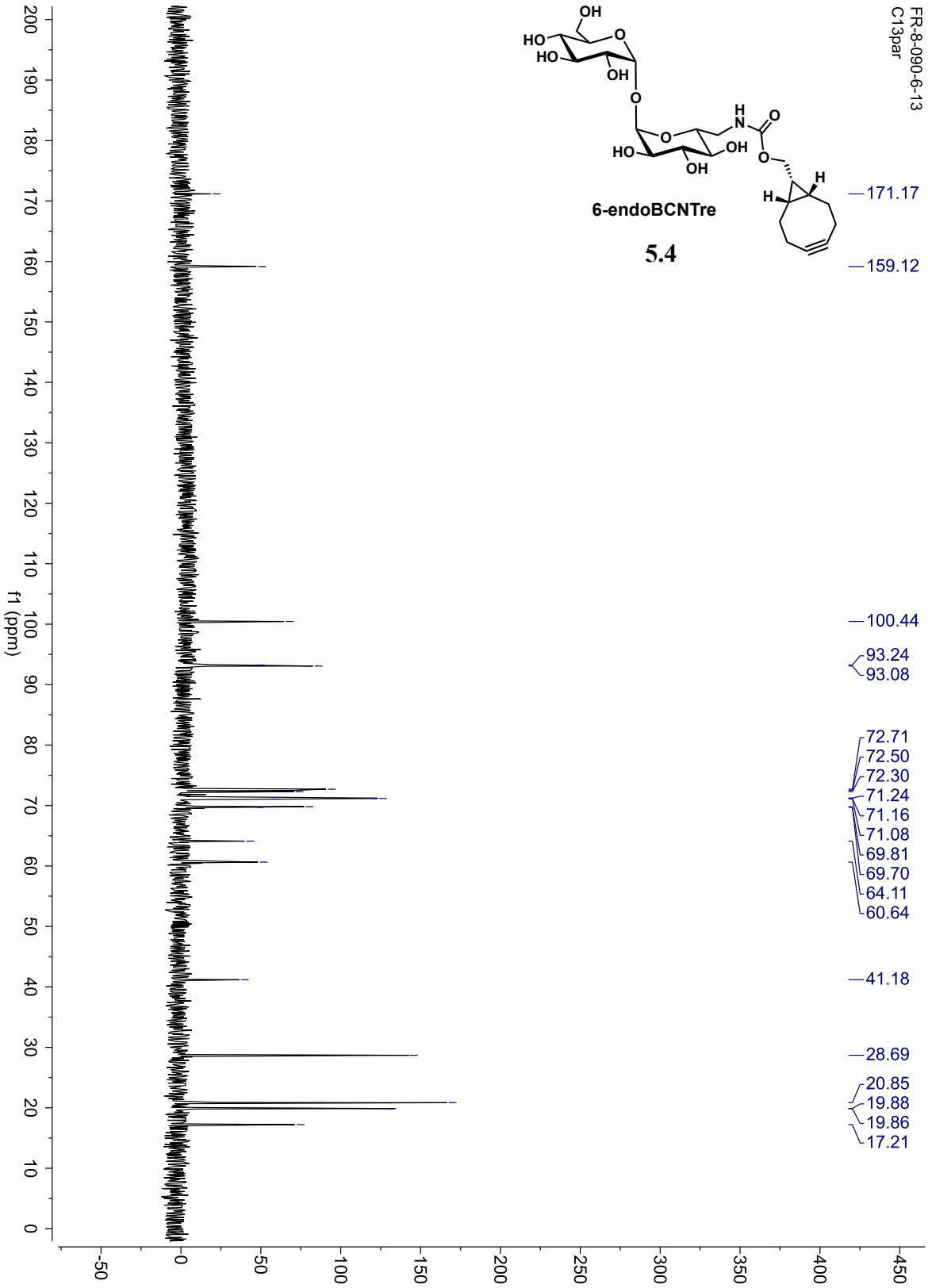
FR-8-090-6-13
C13par
6-endoBCNTre
5.4
171.17
159.12
100.44
93.24
93.08
72.71
72.50
72.30
71.24
71.16
71.08
69.81
69.70
64.11
60.64
41.18
28.69
20.85
19.88
19.86
17.21
f1 (ppm)